Model Updating of Modal Parameters from Experimental Data and Applications in Aerospace

Stefan Keye[†]

Centre for Numerical Modelling and Process Analysis
School of Computing and Mathematical Sciences
The University of Greenwich
London

A thesis submitted in partial fulfillment of
the requirements of the University of Greenwich
for the Degree of Doctor of Philosophy

August 27th, 2003

[†]Abteilung für Adaptive Struktursysteme, Institut für Strukturmechanik,
Deutsche Forschungsanstalt für Luft- und Raumfahrt (DLR), Braunschweig, Germany

Contents

Acknowledgements

My first and foremost appreciation goes to my supervisors Professor Mark Cross, Pro Vice Chancellor for Research and Director of the Centre for Numerical Modelling and Process Analysis at the University of Greenwich, and Dr. Avril Slone, Senior Research Fellow at the Centre for Numerical Modelling and Process Analysis, School of Computing and Mathematical Sciences, for their encouraging support and most valuable advice. I would also like to express my gratitude to Professors Christopher Bailey, School of Computing and Mathematical Sciences, and Grant Steven, School of Engineering, University of Durham, for their willingness to act as the internal and external examiners.

Furthermore, I wish to acknowledge the support and co-operation of Professor Heinz G. Hönlinger, Director of the Institute for Aeroelasticity, German Aerospace Research Establishment (DLR). Dr.-Ing. Ulrich Füllekrug, Head of the Department for Structural Dynamics, deserves particular recognition for his knowledgeable contributions. Special thanks go to my colleagues Dipl.-Ing. Manfred Degener, Head of the Ground Vibration Test Facility Working Group, for communicating his experienced advice, Hans-Jürgen Simm, Hubertus Giese, and Holger Haupt, Technicians in the Department for Structural Dynamics, for sharing their hands-on experience and their assistance during the experimental investigations, and Mrs. Christine Meyer, Institute for Aeroelasticity, for providing the drawings of the test structures.

Likewise, I want to convey my appreciation to Professor Dr.-Ing. Michael Link, Head of the Lightweight Structures and Structural Mechanics Laboratory, Universität Gesamthochschule Kassel, Germany, for numerous beneficial discussions and his substantial support.

Finally, I am exceptionally thankful to my dear wife Natascha. Her everlasting enthusiasm, sound optimism, and endless loyalty has given me the confidence to walk my way through the ups and downs involved with putting together this thesis.

Abstract

The research in this thesis is associated with different aspects of experimental analyses of structural dynamic systems and the correction of the corresponding mathematical models using the results of experimental investigations as a reference. A comprehensive finite-element model updating software technology is assembled and various novel features are implemented. The software technology is integrated into an experimental test facility for structural dynamic identification and used in a number of real life aerospace applications which illustrate the advantages of the new features.

To improve the quality of the experimental reference data a novel non-iterative method for the computation of optimised multi-point excitation force vectors for Phase Resonance Testing is introduced. The method is unique in that it is based entirely on experimental data, allows to determine both the locations and force components resulting in the highest phase purity, and enable to predict the corresponding mode indicator. A minimisation criterion for the real-part response of the test structure with respect to the total response is utilised and, unlike with the application of other methods, no further information such as a mass matrix from a finite-element model or assumptions on the structure's damping characteristics is required. Performance in comparison to existing methods is assessed in a numerical study using an analytical eleven-degrees-of-freedom model. Successful applications to a simple laboratory satellite structure and under realistic test conditions during the Ground Vibration Test on the European Space Agency's Polar Platform are described. Considerable improvements are achieved with respect to the phase purity of the identified mode shapes as compared to other methods or manual tuning

strategies as well as the time and effort involved in the application during Ground Vibration Testing.

Various aspects regarding the application of iterative model updating methods to aerospace-related test structures and live experimental data are discussed. A new iterative correction parameter selection technique enabling to create a physically correct updated analytical model and a novel approach for the correction of structural components with viscous material properties are proposed. A finite-element model of the GARTEUR SM-AG19 laboratory test structure is updated using experimental modal data from a Ground Vibration Test. In order to assess the accuracy and physical consistency of the updated model a novel approach is applied where only a fraction of the mode shapes and natural frequencies from the experimental data base is used in the model correction process and analytical and experimental modal data beyond the range utilised for updating are correlated.

To evaluate the influence of experimental errors on the accuracy of finite-element model corrections a numerical simulation procedure is developed. The effects of measurement uncertainties on the substructure correction factors, natural frequency deviations, and mode shape correlation are investigated using simulated experimental modal data. Various numerical models are generated to study the effects of modelling error magnitudes and locations. As a result, the correction parameter uncertainty increases with the magnitude of the experimental errors and decreases with the number of modes involved in the updating process. Frequency errors, however, since they are not averaged during updating, must be measured with an adequately high precision.

Next, the updating procedure is applied to an authentic industrial aerospace structure. The finite-element model of the EC 135 helicopter is utilised and a novel technique for the parameterisation of substructures with non-isotropic material properties is suggested. Experimental modal parameters are extracted from frequency responses recorded during a Shake Test on the EC 135-S01 prototype. In this test case, the correction process involves the handling of a high degree of modal and spatial incompleteness in the experi-

mental reference data. Accordingly, new effective strategies for the selection of updating parameters are developed which are both physically significant and likewise have a sufficient sensitivity with respect to the analytical modal parameters.

Finally, possible advantages of model updating in association with a model-based method for the identification and localisation of structural damage are investigated. A new technique for identifying and locating delamination damages in carbon fibre reinforced polymers is introduced. The method is based on a correlation of damage-induced modal damping variations from an elasto-mechanic structure to the corresponding data from a numerical model in order to derive information on the damage location. Using a numerical model enables the location of damages in a three-dimensional structure from experimental data obtained with only a single response sensor. To acquire sufficiently accurate experimental data a novel criterion for the determination of most appropriate actuator and sensor positions and a polynomial curve fitting technique are suggested. It will be shown that in order to achieve a good location precision the numerical model must retain a high degree of accuracy and physical consistency.

Nomenclature

Matrices and Tensors

$\mathbf{D}$	damping matrix
$\mathbf{E}$	elasticity matrix
$\mathbf{G}$	Jacobian matrix
$\mathbf{H}$	admittance matrix
$\mathbf{K}$	stiffness matrix
$\mathbf{L}$	matrix of differential operators
$\mathbf{M}$	mass matrix
$\mathbf{T}$	matrix of outward normal operators
$\mathbf{U}$	structural response matrix
$\mathbf{W}$	weighting matrix
Φ	modal matrix
$\boldsymbol{\sigma}$	stress tensor

Vectors

$\mathbf{b}$	body force vector
$\mathbf{f}$	global force vector, excitation force vector
$\mathbf{n}$	outward unit normal vector
$\mathbf{p}$	correction parameter vector
$\mathbf{t}$	traction vector
$\mathbf{u}$	displacement vector, structural response vector
$\mathbf{x}$	location vector
$\mathbf{z}$	state vector

$\boldsymbol{\delta}$	simulated experimental error
$\boldsymbol{\epsilon}$	strain vector
$\boldsymbol{\varepsilon}$	error vector
$\boldsymbol{\phi}$, $\boldsymbol{\varphi}$	eigenvectors

Scalars

C	correlation criterion
D	generalised damping
E	Young's modulus
F	Fourier transformation of excitation force
G	shear modulus
I	second moment of area
J	objective function
J	second moment of inertia
K	generalised stiffness
M	generalised mass
N	shape function
N	number of samples
S	parameter sensitivity
T	time period
U	voltage
U	Fourier transformation of structural response
a_0, a_j, b_j	Fourier coefficients
a, b, c	polynomial coefficients
d	viscous damping coefficient
f	excitation force
f	frequency
h	thickness
k	stiffness
m	mass
n	sample number

t	time co-ordinate
u	displacement, structural response
x, y, z	location co-ordinates
α	stiffness correction factor
β	mass correction factor
ϵ	strain component
ζ	proportionality constant
η	damping factor
κ	proportionality constant
λ	eigenvalue
μ	proportionality constant
ν	Poisson's ratio
ρ	material density
σ	stress component
ω	angular frequency

Subscripts and Superscripts

0	initial value or quantity
C	number of exciter configurations
D	damaged state
H	healthy state
I, J	number of substructures
K	number of correction parameters
M	number of degrees of freedom
N	number of modes or samples
T	w.r.t. traction
U	w.r.t. displacement
a	analytical quantity
c	exciter configuration
e	experimental quantity
i, j	components, node numbers, substructures

k	correction parameter
m	degree of freedom
n	mode, resonance, time step
p	w.r.t. correction parameter vector
p	prescribed quantity
r, s, t	mode, resonance
x, y, z	components w.r.t. co-ordinate system
ε	w.r.t. error vector
κ	iteration step
λ	w.r.t. eigenvalues
ξ	modelling error
φ	w.r.t. eigenvectors

abs	absolute
freq	frequency
max	largest value
min	smallest value
norm	normalisation quantity
opt	optimised
rel	relative
tor	torsion

Operators and Symbols

Γ	surface
Ω	domain
∇	nabla operator
$\dot{(\,)}$	1^{st} derivative w.r.t. time
$\ddot{(\,)}$	2^{nd} derivative w.r.t. time
$\lvert\ \rvert$	L_2-norm, determinant
$(\,)^{-1}$	inverse
$(\,)^{T}$	transpose

$\tilde{(\,)}$	approximate or erroneous quantity
$\hat{(\,)}$	amplitude
$\Delta(\,)$	deviation
$\delta(\,)$	virtual quantity
$\Re(\,)$	real part
$\Im(\,)$	imaginary part

Other Abbreviations

DoF	degree of freedom
FRF	Frequency Response Function
MAC	Modal Assurance Criterion
MIF	Mode Indicator Function
PRM	Phase Resonance Method
RBM	rigid body mode
SVD	Singular Value Decomposition

List of Tables

List of Figures

Chapter 1

Introduction

1.1 Background

Free harmonic oscillations of an elastic structure are completely determined by four modal parameters, the natural frequency, a damping parameter, the generalised mass, and the mode shape [136]. A thorough knowledge of these modal parameters is a proven and efficient approach to understand and characterise the dynamic behaviour of an elastic structure in a structural dynamic investigation. An accurate mathematical model constitutes a sound foundation for all forms of structural dynamic investigations, including

- the computation of forced dynamic responses,
- the assessment of structural modifications,
- the coupling of sub-components,
- the analysis of fluid-structure interactions, or
- the design of control algorithms.

Consequently, the identification of modal parameters is of major importance throughout the entire development phase of a structure.

In the past, engineers had to completely rely on the experimental identification of modal parameters [136], whereas today, modal parameters are

identified by means of both analytical methods [138] (in the design stage using mathematical models based on construction documents) and experimental techniques [138] (after completion of a prototype in a vibration test). The development of the finite-element method has allowed this procedure to be established for complex aerospace structures also. The numerical determination of dynamic properties of a structure based on the finite-element method now is a customary and readily applicable procedure [136].

The comparison and evaluation of analytical and experimental results enables the high degree of consistency and accuracy required with aerospace structures. In practice, however, differences are most likely to occur between the computed and the measured natural frequencies and mode shapes which hamper a direct correlation of results. The discrepancies are a result of the numerical model's sensitivity to structural modifications and modelling errors.

An obvious approach to obtain a more accurate representation of the actual structure is to combine the observations and results from experimental and numerical investigation approaches in order to correct the numerical model.

The grade of improvement that can be achieved through the application of model updating techniques is essentially determined by both the quality and quantity of the experimental data. As a result, experimental identification techniques play an important role in the optimisation process.

Additionally, the quality of the updated model essentially depends on the consistency between the selected correction parameters and the actual modelling errors, the parameter sensitivity with respect to the analytical modal properties, and the processing of experimental and analytical data in order to derive the necessary parameter modifications.

Accordingly, creating physically realistic and trustworthy mathematical models involves the optimisation of the experimental data quality, knowledge on the influence of experimental errors on the model corrections, and the selection of appropriate updating and process control parameters.

This thesis concerns the development of methods and application strategies which improve the data quality of experimental modal identification procedures

and allow model updating techniques to be applied to large industrial finite-element models in order to meet the requirements imposed by the increasing dynamic complexity of future aerospace structures.

1.2 Introduction to Structural Dynamics

1.2.1 Introduction

This section develops the basic equations of motion of a linear, time-invariant, viscously damped, elastic system. The spatial discretisation of the structural domain follows the displacement matrix formulation which is commonly found in standard works on structural dynamics using the finite-element method [170].

1.2.2 Governing Equations

The universal law governing a solid continuum undergoing motion is given by Cauchy's equation

$$\mathbf{b} + \nabla \cdot \boldsymbol{\sigma}_{ij} = \rho \ddot{\mathbf{u}} \,, \tag{1.1}$$

where $\mathbf{b}$ is the body force vector, $\boldsymbol{\sigma}_{ij}$ is the stress tensor, ρ is the material density, and $\ddot{\mathbf{u}}$ is acceleration. In the theory of elasticity eq. (1.1) is variously described as the stress equation of small motions [47], the equation of equilibrium [159], or the equation of motion [63]. The term equation of dynamic equilibrium will be employed hereafter to distinguish the dynamic problems considered in this research from static structural problems.

Eq. (1.1) does not contain an explicit mechanism for the dissipation of energy. This problem is most commonly solved by adding an ideal linear viscous damper [14, 30, 71] which opposes structural motion with a force proportional to velocity. Thus, the equation of dynamic equilibrium becomes

$$\mathbf{b} + \nabla \cdot \boldsymbol{\sigma}_{ij} = \rho \ddot{\mathbf{u}} + d\dot{\mathbf{u}} \,, \tag{1.2}$$

where the constant d is the coefficient of viscous damping and $\dot{\mathbf{u}}$ is velocity.

1.2.3 Constitutive Relationship for Stress and Strain

Based on the assumptions that:

- the stress applied to any solid is proportional to the strain it produces within the elastic limit for that solid (the ratio of longitudinal stress to strain being equal to Young's modulus of elasticity) and

- the total effect of a combination of loads applied to a body is the sum of the individual loads applied separately, provided that these effects are directly proportional to the loads which produced them and that the strains produced are small,

the generalised form of Hooke's law yields constitutive relationships between stresses and strains for the two fundamental cases of plane stress and plane strain. For the two-dimensional problem of an isotropic homogeneous material undergoing loading in the x, y-plane, where thermal effects are neglected and the strains are small [170], the following two cases are considered:

1. **Plane Stress.** Only the three components of stress and strain in the x, y-plane have to be taken into account as, by definition, all other components of stress are zero, i.e. $\sigma_{xz} = \sigma_{yz} = \sigma_z \equiv 0$. Hence, the stress vector is defined as $\boldsymbol{\sigma} = [\sigma_x, \sigma_y, \sigma_{xy}]^{\mathrm{T}}$ and the stress-strain relationship is expressed in matrix form as

$$\begin{pmatrix} \sigma_x \\ \sigma_y \\ \sigma_{xy} \end{pmatrix} = \frac{E}{(1-\nu^2)} \begin{pmatrix} 1 & \nu & 0 \\ \nu & 1 & 0 \\ 0 & 0 & \frac{1-\nu}{2} \end{pmatrix} \begin{pmatrix} \epsilon_x \\ \epsilon_y \\ \epsilon_{xy} \end{pmatrix}, \tag{1.3}$$

   where E and ν are Young's modulus and Poisson's ratio, respectively.

2. **Plane Strain.** In this case $\epsilon_{xz} = \epsilon_{yz} = \epsilon_z \equiv 0$. However, a normal stress component exists in addition to the other three stress components. Hence, the stress vector becomes $\boldsymbol{\sigma} = [\sigma_x, \sigma_y, \sigma_z, \sigma_{xy}]^{\mathrm{T}}$ and the stress-

strain relationship is expressed in matrix form as

$$\begin{pmatrix} \sigma_x \\ \sigma_y \\ \sigma_z \\ \sigma_{xy} \end{pmatrix} = \frac{E}{(1+\nu)(1-2\nu)} \begin{pmatrix} 1-\nu & \nu & \nu & 0 \\ \nu & 1-\nu & \nu & 0 \\ \nu & \nu & 1 & 0 \\ 0 & 0 & 0 & \frac{1-2\nu}{2} \end{pmatrix} \begin{pmatrix} \epsilon_x \\ \epsilon_y \\ \epsilon_z \\ \epsilon_{xy} \end{pmatrix} . \tag{1.4}$$

Thus, the constitutive relationship for an isotropic homogeneous material subjected to linear elastic strains is

$$\boldsymbol{\sigma} - \mathbf{E}(\boldsymbol{\epsilon} - \boldsymbol{\epsilon}_0) = \mathbf{0} \qquad \text{in } \Omega \ , \tag{1.5}$$

where the elastic strain at any instant in time may be represented by the difference of total strains $\boldsymbol{\epsilon}$ and initial strains $\boldsymbol{\epsilon}_0$. The augmented forms of the elasticity matrix [170] are defined as

$$\mathbf{E} = \frac{E}{(1-\nu^2)} \begin{pmatrix} 1 & \nu & 0 & 0 \\ \nu & 1 & 0 & 0 \\ 0 & 0 & 0 & 0 \\ 0 & 0 & 0 & \frac{1-\nu}{2} \end{pmatrix} \tag{1.6}$$

for plane stress and

$$\mathbf{E} = \frac{E}{(1+\nu)(1-2\nu)} \begin{pmatrix} 1-\nu & \nu & \nu & 0 \\ \nu & 1-\nu & \nu & 0 \\ \nu & \nu & 1 & 0 \\ 0 & 0 & 0 & \frac{1-2\nu}{2} \end{pmatrix} \tag{1.7}$$

for plane strain.

1.2.4 Displacement Formulation

This work is based on a linear strain-displacement formulation using the assumption that the strains remain small.[1] As a result, the strains may be

[1]This assumption is considered to be valid for strains in the order of a few percent [47].

decomposed into a product of the matrix of linear operators $\mathbf{L}$ and the displacement vector $\mathbf{u}$ which enables the strains to be defined in the general displacement form as

$$\boldsymbol{\epsilon} = \begin{pmatrix} \epsilon_x \\ \epsilon_y \\ \epsilon_z \\ \epsilon_{xy} \end{pmatrix} = \begin{pmatrix} \frac{\partial}{\partial x}(u_x) \\ \frac{\partial}{\partial y}(u_y) \\ 0 \\ \frac{\partial}{\partial y}(u_x) + \frac{\partial}{\partial x}(u_y) \end{pmatrix} = \begin{pmatrix} \frac{\partial}{\partial x} & 0 \\ 0 & \frac{\partial}{\partial y} \\ 0 & 0 \\ \frac{\partial}{\partial y} & \frac{\partial}{\partial x} \end{pmatrix} \begin{pmatrix} u_x \\ u_y \end{pmatrix} = \mathbf{L}\,\mathbf{u} \quad (1.8)$$

with

$$\mathbf{L} = \begin{pmatrix} \frac{\partial}{\partial x} & 0 \\ 0 & \frac{\partial}{\partial y} \\ 0 & 0 \\ \frac{\partial}{\partial y} & \frac{\partial}{\partial x} \end{pmatrix} . \quad (1.9)$$

From eq. (1.8) the strain-displacement relation is given by

$$\boldsymbol{\epsilon} - \mathbf{L}\mathbf{u} = \mathbf{0} \qquad \text{in } \Omega \ . \quad (1.10)$$

The boundary conditions on the surface Γ of the structural domain Ω are described in terms of prescribed displacements $\mathbf{u}_p$ on Γ_U and prescribed tractions $\mathbf{t}_p$ on Γ_T as follows:

$$\begin{aligned} \mathbf{u} - \mathbf{u}_p &= \mathbf{0} \qquad \text{on } \Gamma_U \ , \\ \mathbf{T}\boldsymbol{\sigma} - \mathbf{t}_p &= \mathbf{0} \qquad \text{on } \Gamma_T \ . \end{aligned} \quad (1.11)$$

The structural boundary is the union of the prescribed displacement and traction boundaries, i.e. $\Gamma = \Gamma_U \cup \Gamma_T$, and

$$\mathbf{T} = \begin{pmatrix} n_x & 0 & 0 & n_y \\ 0 & n_y & 0 & n_x \end{pmatrix} \quad (1.12)$$

is the matrix of outward normal operators, where $\mathbf{n}$ is the outward unit normal vector to the domain boundary with components n_x and n_y.

Applying the constitutive stress-strain equation (1.5) and the strain-displacement relation (1.10) to the traction boundary condition, eq. (1.11), gives the displacement formulation of the boundary conditions

$$\mathbf{T}\left(\mathbf{E}\,\mathbf{L}\,\mathbf{u} - \mathbf{E}\,\boldsymbol{\epsilon}_0\right) - \mathbf{t}_p = \mathbf{0} \qquad \text{on } \Gamma_T \ . \quad (1.13)$$

Using the same substitutions the equation of dynamic equilibrium (1.2) becomes

$$\mathbf{L}^{\mathrm{T}}\left(\mathbf{E}\,\mathbf{L}\,\mathbf{u}-\mathbf{E}\,\boldsymbol{\epsilon}_0\right)+\mathbf{b}-\rho\,\ddot{\mathbf{u}}-d\,\dot{\mathbf{u}}=\mathbf{0}\qquad\text{in }\Omega\,. \tag{1.14}$$

This form is known as the displacement formulation of the equation of motion. As a result, the general governing equation of motion of a solid continuum is given by

$$\rho\,\ddot{\mathbf{u}}+d\,\dot{\mathbf{u}}-\mathbf{L}^{\mathrm{T}}\left(\mathbf{E}\,\mathbf{L}\,\mathbf{u}-\mathbf{E}\,\boldsymbol{\epsilon}_0\right)-\mathbf{b}=\mathbf{0}\qquad\text{in }\Omega \tag{1.15}$$

with the boundary conditions

$$\begin{aligned}\mathbf{u}-\mathbf{u}_p&=\mathbf{0}\qquad\text{on }\Gamma_U\,,\\ \mathbf{T}\left(\mathbf{E}\,\mathbf{L}\,\mathbf{u}-\mathbf{E}\,\boldsymbol{\epsilon}_0\right)-\mathbf{t}_p&=\mathbf{0}\qquad\text{on }\Gamma_T\,.\end{aligned} \tag{1.16}$$

1.2.5 Discretisation of the Displacement Equations

Applying the method of weighted residuals to eqs. (1.15) and (1.16) leads to

$$\begin{aligned}&\int_\Omega \mathbf{W}^{\mathrm{T}}\left[\mathbf{L}^{\mathrm{T}}\left(\mathbf{E}\,\mathbf{L}\,\mathbf{u}-\mathbf{E}\,\boldsymbol{\epsilon}_0\right)+\mathbf{b}-\rho\,\ddot{\mathbf{u}}-d\,\dot{\mathbf{u}}\right]\mathrm{d}\Omega\\ +\;&\oint_{\Gamma_T}\mathbf{W}_T^{\mathrm{T}}\left[\mathbf{T}\left(\mathbf{E}\,\mathbf{L}\,\mathbf{u}-\mathbf{E}\,\boldsymbol{\epsilon}_0\right)-\mathbf{t}_p\right]\mathrm{d}\Gamma+\oint_{\Gamma_U}\mathbf{W}_U^{\mathrm{T}}\left(\mathbf{u}-\mathbf{u}_p\right)\mathrm{d}\Gamma=\mathbf{0}\,,\end{aligned} \tag{1.17}$$

where $\mathbf{W}$ denotes the weighting functions.

In order to satisfy the kinetic boundary condition $\mathbf{W}_U$ must be equal to zero on Γ_U [170]. Additionally, since the weighting functions are arbitrary, $\mathbf{W}_T=-\mathbf{W}$ may be assumed. Therefore,

$$\begin{aligned}&\int_\Omega \mathbf{W}^{\mathrm{T}}\,\mathbf{L}^{\mathrm{T}}\left(\mathbf{E}\,\mathbf{L}\,\mathbf{u}-\mathbf{E}\,\boldsymbol{\epsilon}_0\right)\mathrm{d}\Omega+\int_\Omega \mathbf{W}^{\mathrm{T}}\left(\mathbf{b}-\rho\,\ddot{\mathbf{u}}-d\,\dot{\mathbf{u}}\right)\mathrm{d}\Omega\\ -\;&\oint_{\Gamma_T}\mathbf{W}^{\mathrm{T}}\,\mathbf{T}\left(\mathbf{E}\,\mathbf{L}\,\mathbf{u}-\mathbf{E}\,\boldsymbol{\epsilon}_0\right)\mathrm{d}\Gamma+\oint_{\Gamma_T}\mathbf{W}^{\mathrm{T}}\,\mathbf{t}_p\,\mathrm{d}\Gamma=\mathbf{0}\,.\end{aligned} \tag{1.18}$$

Since the surface of the structure is the union of the prescribed traction and displacement surfaces the first of the integrals along the traction surface in eq. (1.18) may be replaced with an integral along the surface and an integral along the prescribed displacement boundary, thus removing the displacements from the integral on the traction boundary. On rearrangement this gives:

$$\int_\Omega \mathbf{W}^{\mathrm{T}}\,\mathbf{L}^{\mathrm{T}}\left(\mathbf{E}\,\mathbf{L}\,\mathbf{u}-\mathbf{E}\,\boldsymbol{\epsilon}_0\right)\mathrm{d}\Omega+\int_\Omega \mathbf{W}^{\mathrm{T}}\left(\mathbf{b}-\rho\,\ddot{\mathbf{u}}-d\,\dot{\mathbf{u}}\right)\mathrm{d}\Omega$$

$$
\begin{aligned}
&- \oint_{\Gamma} \mathbf{W}^{\mathrm{T}}\,\mathbf{T}\,(\mathbf{E}\,\mathbf{L}\,\mathbf{u} - \mathbf{E}\,\boldsymbol{\epsilon}_0)\,\mathrm{d}\Gamma + \oint_{\Gamma_U} \mathbf{W}^{\mathrm{T}}\,\mathbf{T}\,(\mathbf{E}\,\mathbf{L}\,\mathbf{u} + \mathbf{E}\,\boldsymbol{\epsilon}_0)\,\mathrm{d}\Gamma \\
&+ \oint_{\Gamma_T} \mathbf{W}^{\mathrm{T}}\,\mathbf{t}_p\,\mathrm{d}\Gamma = \mathbf{0}\ . \qquad (1.19)
\end{aligned}
$$

The application of Green's First Theorem to the first two integrals in eq. (1.19) results in

$$
\begin{aligned}
&- \int_{\Omega} (\mathbf{L}\,\mathbf{W})^{\mathrm{T}}\,(\mathbf{E}\,\mathbf{L}\,\mathbf{u} - \mathbf{E}\,\boldsymbol{\epsilon}_0)\,\mathrm{d}\Omega + \int_{\Omega} \mathbf{W}^{\mathrm{T}}\,(\mathbf{b} - \rho\,\ddot{\mathbf{u}} - d\,\dot{\mathbf{u}})\,\mathrm{d}\Omega \\
&+ \oint_{\Gamma_U} \mathbf{W}^{\mathrm{T}}\,\mathbf{T}\,(\mathbf{E}\,\mathbf{L}\,\mathbf{u} - \mathbf{E}\,\boldsymbol{\epsilon}_0)\,\mathrm{d}\Gamma + \oint_{\Gamma_T} \mathbf{W}^{\mathrm{T}}\,\mathbf{t}_p\,\mathrm{d}\Gamma = \mathbf{0}\ . \qquad (1.20)
\end{aligned}
$$

Eq. (1.20) permits discontinuous first derivatives of the displacements, thus being the weak form of eq. (1.17). Additionally, by choosing the weighting functions to be equal to the vector of virtual displacements, i.e. $\mathbf{W} = [\delta u_x, \delta u_y, \delta u_z]^{\mathrm{T}}$, eq. (1.20) becomes equivalent to the Principle of Virtual Displacements formulation [170].

For the finite-element method of spatial discretisation the unknown displacements $\mathbf{u}$ may be approximated by

$$
\mathbf{u} \simeq \tilde{\mathbf{u}} = \mathrm{N}_j \cdot \tilde{\mathbf{u}}_j\ , \qquad (1.21)
$$

where N_j is a set of shape functions and $\tilde{\mathbf{u}}_j$ are the displacements evaluated at the nodes j. Selecting an appropriate set of weighting functions $\mathbf{W}_i$ and applying the constitutive equation

$$
\boldsymbol{\sigma}_0 = \mathbf{E}\,\boldsymbol{\epsilon}_0 \qquad (1.22)
$$

eq. (1.20) may be written as

$$
\begin{aligned}
&\int_{\Omega} \mathbf{W}_i^{\mathrm{T}} \rho\,\mathrm{N}_j\,\ddot{\tilde{\mathbf{u}}}\,\mathrm{d}\Omega + \int_{\Omega} \mathbf{W}_i^{\mathrm{T}} d\,\mathrm{N}_j\,\dot{\tilde{\mathbf{u}}}\,\mathrm{d}\Omega + \int_{\Omega} (\mathbf{L}\,\mathbf{W}_i)^{\mathrm{T}}\,\mathbf{E}\,\mathbf{L}\,\mathrm{N}_j\,\tilde{\mathbf{u}}\,\mathrm{d}\Omega \\
&\qquad - \oint_{\Gamma_{U,i}} \mathbf{W}_i^{\mathrm{T}}\,\mathbf{T}\,\mathbf{E}\,\mathbf{L}\,\mathrm{N}_j\,\tilde{\mathbf{u}}\,\mathrm{d}\Gamma = \\
&\int_{\Omega} \mathbf{W}_i^{\mathrm{T}}\,\mathbf{b}_0\,\mathrm{d}\Omega + \oint_{\Gamma_{T,i}} \mathbf{W}_i^{\mathrm{T}}\,\mathbf{t}_p\,\mathrm{d}\Gamma + \int_{\Omega} (\mathbf{L}\,\mathbf{W}_i)^{\mathrm{T}}\,\boldsymbol{\sigma}_0\,\mathrm{d}\Omega - \oint_{\Gamma_{U,i}} \mathbf{W}_i^{\mathrm{T}}\,\mathbf{T}\,\boldsymbol{\sigma}_0\,\mathrm{d}\Gamma\ . \qquad (1.23)
\end{aligned}
$$

1.2.6 The Equations of Motion

Using eq. (1.21) to approximate the displacements and combining all terms in eq. (1.23) yields the well-known compact matrix form of the second-order

differential equations of motion of an elastic system

$$\mathbf{M}\,\ddot{\tilde{\mathbf{u}}}(t) + \mathbf{D}\,\dot{\tilde{\mathbf{u}}}(t) + \mathbf{K}\,\tilde{\mathbf{u}}(t) = \mathbf{f}(t) \tag{1.24}$$

with

$$\mathbf{M}_{ij} = \int_\Omega \mathbf{W}_i^{\mathrm{T}} \rho\, \mathrm{N}_j \,\mathrm{d}\Omega\,, \tag{1.25}$$

$$\mathbf{D}_{ij} = \int_\Omega \mathbf{W}_i^{\mathrm{T}} d\, \mathrm{N}_j \,\mathrm{d}\Omega\,, \tag{1.26}$$

$$\mathbf{K}_{ij} = \int_\Omega (\mathbf{L}\,\mathbf{W}_i)^{\mathrm{T}}\, \mathbf{E}\,\mathbf{L}\,\mathrm{N}_j \,\mathrm{d}\Omega - \oint_{\Gamma_{U,i}} \mathbf{W}_i^{\mathrm{T}}\,\mathbf{T}\,\mathbf{E}\,\mathbf{L}\,\mathrm{N}_j \,\mathrm{d}\Gamma\,, \tag{1.27}$$

$$\begin{aligned}\mathbf{f}_i = &\int_\Omega \mathbf{W}_i^{\mathrm{T}}\,\mathbf{b}_0 \,\mathrm{d}\Omega + \oint_{\Gamma_{T,i}} \mathbf{W}_i^{\mathrm{T}}\,\mathbf{t}_p \,\mathrm{d}\Gamma \\ &+ \int_\Omega (\mathbf{L}\,\mathbf{W}_i)^{\mathrm{T}}\,\boldsymbol{\sigma}_0 \,\mathrm{d}\Omega - \oint_{\Gamma_{U,i}} \mathbf{W}_i^{\mathrm{T}}\,\mathbf{T}\,\boldsymbol{\sigma}_0 \,\mathrm{d}\Gamma\,.\end{aligned} \tag{1.28}$$

In eq. (1.24) $\tilde{\mathbf{u}}(t)$ is the global approximation to the vector of displacements[2], $\mathbf{M}$, $\mathbf{D}$, and $\mathbf{K}$ are the mass, viscous damping, and stiffness matrices, respectively, and $\mathbf{f}(t)$ is the equivalent global force vector.

1.2.7 Damping

Damping is the ability of a structure to dissipate energy and the basic mechanisms by which damping is introduced into an elastic structure are:

1. **Structural Damping.** The friction between two contacting surfaces generates structural damping.

2. **Material or Hysteretic Damping.** Internal energy dissipation of the materials is responsible for material damping.

Fluid damping caused by dynamic drag, where energy is dissipated by the viscous and pressure drag on the surface of a structure as it moves relative to a surrounding fluid, is not significant with structural dynamic applications and therefore will not be regarded here. Typical aerospace materials like refined metals or carbon fibres also have low internal material damping. Hence,

[2]For simplicity reasons the tilda symbol will be omitted further on.

structural damping remains as the primary mechanism for the dissipation of energy in aerospace structures.

In practice the physical damping of a structure ensures that its response to an expected excitation does not exceed acceptable limits. Increased damping reduces the response amplitudes such that vibrations and dynamic stresses are decreased. Hence, fatigue is lowered and the life of the structure is prolonged.

1.2.7.1 Structural Damping

Structural damping is most effective at low frequencies and the corresponding lower modes of vibration since it is only at these frequencies that the vibration amplitudes are large enough to create significant slip and energy dissipation between contacting surfaces. However, the structural damping inherent in a system generally is not known as knowledge of the associated physical dissipative mechanisms is limited. Thus, structural damping is commonly modelled by an ideal viscous damper which opposes the motion of the structure by a force proportional to the velocity of the structure.

1.2.7.2 Rayleigh Damping

Rayleigh damping [145] represents viscous damping as a linear combination of the stiffness and mass matrices

$$\mathbf{D} = \mu \mathbf{M} + \kappa \mathbf{K} \ , \tag{1.29}$$

where μ and κ are the stiffness and mass proportional damping constants. Eq. (1.29) is usually referred to as proportional damping approach. While there is no physical justification for this widely used approximation no significantly better linear model appears to be available so far [120].

Viscous damping may be introduced by means of specifying the viscous damping ratio η which relates to the damping constants and frequency of vibration through

$$\eta = \frac{1}{2}\left(\kappa\omega + \frac{\mu}{\omega}\right) \ . \tag{1.30}$$

The damping constants are determined by choosing η at two different frequencies ω_1 and ω_2 and solving the resulting pair of simultaneous equations for μ

and κ, where ω_1 and ω_2 are taken at the structure's lowest and highest natural frequencies of interest, respectively.

Hence, for general Rayleigh damping the amount of damping is controlled at these two frequencies but it is not controlled for any other modes. For stiffness proportional damping the damping ratio is directly proportional to the frequency of vibration. As a result, the highest modes of the system will be the most strongly damped. For mass proportional damping the damping ratio is inversely proportional to the frequency. Thus, the lowest modes will be damped most heavily.

1.2.8 Free Vibrations of the Undamped System

Free vibrations of the elastic system represented by eq. (1.24) occur when no external forces are applied within the time range of observation, i.e. $\mathbf{f}(t) \equiv \mathbf{0}$. The following sections cover analytical solutions for free vibrations of discrete elastic structures. First, the (unrealistic) undamped system is considered. The results, however, will be useful for the later modal treatment of real structures. Next, a generally damped system is studied.

Disregarding the damping forces $\mathbf{D}\,\dot{\mathbf{u}}(t)$ in eq. (1.24) yields the equilibrium equations for free vibrations of an undamped system

$$\mathbf{M}\,\ddot{\mathbf{u}}(t) + \mathbf{K}\,\mathbf{u}(t) = \mathbf{0}\ . \tag{1.31}$$

A fundamental solution for eq. (1.31) is given by

$$\mathbf{u}(t) = \boldsymbol{\varphi}\, e^{i\omega t}\ , \tag{1.32}$$

where $\boldsymbol{\varphi}$ is a time-invariant vector of deflection amplitudes and ω is an angular frequency. Introducing eq. (1.32) into eq. (1.31) leads to

$$(-\omega^2\,\mathbf{M} + \mathbf{K})\,\boldsymbol{\varphi} = \mathbf{0}\ . \tag{1.33}$$

Eq. (1.33) is referred to as the general eigenvalue problem.

The fundamental solution, eq. (1.32), describes harmonic oscillations of the structure represented by the system matrices $\mathbf{M}$ and $\mathbf{K}$. The vibrations are

a distinctive property of the structure as they are solely determined by the equilibrium of elastic forces and inertia forces which is maintained at each degree of freedom (DoF) and for every point in time.

1.2.8.1 Eigenvectors and Eigenvalues

Non-trivial solutions for eq. (1.33) are obtained when the determinant of coefficients of the homogeneous equation system vanishes:

$$|-\omega^2 \mathbf{M} + \mathbf{K}| \equiv 0 \,. \tag{1.34}$$

Eq. (1.34) results in a polynomial in ω^2, the characteristic equation, the roots of which are called eigenvalues.[3] Introducing a particular eigenvalue ω^2 into eq. (1.33) allows to compute the corresponding eigenvector $\boldsymbol{\varphi}$.

While the system matrices $\mathbf{M}$ and $\mathbf{K}$ represent the spatial model of the discrete elastic system the eigenvalues and eigenvectors constitute the modal model which contains the complete free vibration solution and helps to understand and control the dynamic phenomena encountered with vibration problems.

1.2.8.2 Characteristic Eigenvector Properties

The eigenvectors $\boldsymbol{\varphi}_n$ with $n = 1, \ldots, N$ comprise various specific characteristics which will become useful in Chapter 3.

Generalised Quantities. When ω_n^2 and $\boldsymbol{\varphi}_n$ are a solution of eq. (1.33), then

$$(-\omega_n^2 \mathbf{M} + \mathbf{K})\, \boldsymbol{\varphi}_n = \mathbf{0} \,. \tag{1.35}$$

Left hand multiplication with $\boldsymbol{\varphi}_n^{\mathrm{T}}$ gives

$$-\omega_n^2\, \boldsymbol{\varphi}_n^{\mathrm{T}} \mathbf{M}\, \boldsymbol{\varphi}_n + \boldsymbol{\varphi}_n^{\mathrm{T}} \mathbf{K}\, \boldsymbol{\varphi}_n = 0 \,. \tag{1.36}$$

The expression

$$M_n = \boldsymbol{\varphi}_n^{\mathrm{T}} \mathbf{M}\, \boldsymbol{\varphi}_n \tag{1.37}$$

[3] With large structural systems the common practice is to directly derive a numerical solution from eq. (1.33).

represents the kinetic energy accumulated in mode n. M_n is called the generalised mass. The second expression in eq. (1.36), i.e.

$$K_n = \boldsymbol{\varphi}_n^{\mathrm{T}} \mathbf{K} \boldsymbol{\varphi}_n \ , \tag{1.38}$$

is the potential or deformation energy contained in mode shape n which is entitled the generalised stiffness. Both the absolute values of M_n and K_n depend on the normalisation of $\boldsymbol{\varphi}_n$.

Eq. (1.36) may be rewritten to yield the Rayleigh quotient

$$\omega_n^2 = \frac{\boldsymbol{\varphi}_n^{\mathrm{T}} \mathbf{K} \boldsymbol{\varphi}_n}{\boldsymbol{\varphi}_n^{\mathrm{T}} \mathbf{M} \boldsymbol{\varphi}_n} \ . \tag{1.39}$$

Orthogonality. Assuming ω_r^2 and $\boldsymbol{\varphi}_r$ to be a solution of eq. (1.35), left hand multiplication with $\boldsymbol{\varphi}_s^{\mathrm{T}}$ leads to the scalar expression

$$-\omega_r^2 \, \boldsymbol{\varphi}_s^{\mathrm{T}} \mathbf{M} \boldsymbol{\varphi}_r + \boldsymbol{\varphi}_s^{\mathrm{T}} \mathbf{K} \boldsymbol{\varphi}_r = 0 \ . \tag{1.40}$$

Likewise, if ω_s^2 and $\boldsymbol{\varphi}_s$ are a solution of eq. (1.35), pre-multiplication with $\boldsymbol{\varphi}_r^{\mathrm{T}}$ returns

$$-\omega_s^2 \, \boldsymbol{\varphi}_r^{\mathrm{T}} \mathbf{M} \boldsymbol{\varphi}_s + \boldsymbol{\varphi}_r^{\mathrm{T}} \mathbf{K} \boldsymbol{\varphi}_s = 0 \ . \tag{1.41}$$

Computing the transpose of eq. (1.41)

$$-\omega_s^2 \, \boldsymbol{\varphi}_s^{\mathrm{T}} \mathbf{M} \boldsymbol{\varphi}_r + \boldsymbol{\varphi}_s^{\mathrm{T}} \mathbf{K} \boldsymbol{\varphi}_r = 0 \ , \tag{1.42}$$

where $\mathbf{M}^{\mathrm{T}} = \mathbf{M}$ and $\mathbf{K}^{\mathrm{T}} = \mathbf{K}$, and subtracting eq. (1.40) results in

$$(\omega_r^2 - \omega_s^2) \, \boldsymbol{\varphi}_s^{\mathrm{T}} \mathbf{M} \boldsymbol{\varphi}_r = 0 \ . \tag{1.43}$$

For $\omega_r^2 \neq \omega_s^2$

$$\boldsymbol{\varphi}_s^{\mathrm{T}} \mathbf{M} \boldsymbol{\varphi}_r = 0 \ . \tag{1.44}$$

Additionally, introducing eq. (1.44) into eq. (1.42) gives

$$\boldsymbol{\varphi}_s^{\mathrm{T}} \mathbf{K} \boldsymbol{\varphi}_r = 0 \ . \tag{1.45}$$

Eqs. (1.44) and (1.45) state that the eigenvectors of the undamped system are orthogonal with respect to both the mass and stiffness matrix. The according physical interpretation is, that no energy is transferred between mode shape $\boldsymbol{\varphi}_s$ and the inertia forces $-\omega_r^2 \mathbf{M} \boldsymbol{\varphi}_r$ or elastic forces $\mathbf{K} \boldsymbol{\varphi}_r$ of mode r, i.e. each mode shape is completely uncoupled from all other vibration modes and therefore may be individually identified during an experimental analysis.

1.2.9 Free Vibrations of the Damped System

Free vibrations of a damped system are described by

$$\mathbf{M}\,\ddot{\mathbf{u}}(t) + \mathbf{D}\,\dot{\mathbf{u}}(t) + \mathbf{K}\,\mathbf{u}(t) = \mathbf{0}\ . \tag{1.46}$$

Again, the fundamental solution approach, eq. (1.32), is used. Introducing into eq. (1.46) yields the non-linear quadratic eigenvalue problem

$$(-\omega^2\,\mathbf{M} + i\omega\,\mathbf{D} + \mathbf{K})\,\boldsymbol{\varphi} = \mathbf{0}\ . \tag{1.47}$$

As outlined in Section 1.2.8.1, non-trivial solutions are obtained when the determinant of coefficients of the homogeneous equation system vanishes:

$$|-\omega^2\,\mathbf{M} + i\omega\,\mathbf{D} + \mathbf{K}| \equiv 0\ . \tag{1.48}$$

In this case, however, the eigenvalues computed from eq. (1.48) are either real or take the form of conjugate complex pairs, where the imaginary part is the frequency of oscillation and the real part describes the decay behaviour of the respective mode shape. With stable, damped, elastic structures the real parts of the complex eigenvalues are always negative [55].

Again, the associated eigenvectors $\boldsymbol{\varphi}_n$ are obtained by individually introducing the eigenvalues ω_n^2 into eq. (1.47). In the most general case the eigenvectors are complex which conveys the physical situation that the structure's individual degrees of freedom do not oscillate in phase. An orthogonality relation of the eigenvectors $\boldsymbol{\varphi}$ with respect to the system matrices $\mathbf{M}$ and $\mathbf{K}$ does not exist here, i.e. a coupling of all modes is constituted by the system's internal damping forces.

1.3 Model Updating Methods

1.3.1 Historical Perspective

The initial impulse to assemble physical parameter matrices from measured modal quantities has been given by RODDEN [146] in 1967. One of the first

systematic approaches, where an incomplete set of measured natural frequencies and mode shapes of a structure was used to improve stiffness and mass characteristics of a finite-element model, has been published by BERMAN and FLANNELLY [12] in 1971. In 1974, iterative procedures have been suggested by COLLINS, HART, HASSELMANN, and KENNEDY [26]. Other basic contributions have been made by NATKE, COLLMANN, and ZIMMERMANN [128] (1974), NATKE [122] (1977), BARUCH [7, 8] (1978 & 1982), and BERMAN and WEI [13] (1981). Further methods for the correction of numerical models based on experimental data have been proposed, [59, 114, 24, 23, 25, 129, 166, 169]. Comparative investigations and individual results [123, 129, 166, 18, 148, 106] have shown that the updated numerical models occasionally yield similar modal parameters but do not maintain the physical significance of the corresponding mass and stiffness matrices.[4] On the other hand, the expectations and hopes were directed towards unveiling the modelling imprecision and errors of the numerical structural dynamic models. This objective has been achieved by coupling a physically significant mathematical model and the experimental modal parameters with the purpose of generating a model which incorporates the observations and results of both the analysis and experiment.

Early applications of computational model updating techniques to large structures, e.g. the Skylab space station (DEMCHAK and HARCROW [37]) or the Vereinigte Flugzeugwerke VFW 614 passenger aircraft (ZIMMERMANN, COLLMANN, and NATKE [171]), date back to the 1970's. During the last decade, applications to increasingly complex aerospace and automotive structures have been published. Some examples are listed in Table 1.1.

1.3.2 Iterative Updating Methods

With the iterative updating methods discussed here the correlation between measured modal data $\mathbf{z}_e$ and the corresponding numerical modal predictions

[4]The general correlation between the existence of a unique consistent solution and the physical meaning of the identified model parameters has been addressed by BERMAN and FLANNELLY [12] and BERMAN [11, 10].

Author(s)	Year	Ref.	Structure
Brughmans, Leuridan, Hrycko, Wyzykowski	1990	[17]	Boeing DeHavilland, DASH 8-300A Aircraft
Brughmans, Leuridan, Blauwkamp	1993	[16]	General Motors, 1991 Saturn Automobile Body
Caesar, Eckert, Wöhler	1994	[20]	European Space Agency (ESA) CLUSTER Satellites
Schedlinski, Link, Schönrock	1998	[151]	BMW Rolls Royce Jet Engine, Intermediate Casing
Link, Hanke	1998	[103]	BMW Rolls Royce Jet Engine, High Pressure Turbine Casing & Rear Bearing Support Structure
Schedlinski	2000	[149]	BMW Automotive Transmission

Table 1.1: Model Updating Applications to Large-Scale Structures

$\mathbf{z}_a$ is determined by a penalty function of the form

$$\boldsymbol{\varepsilon} = \mathbf{z}_e - \mathbf{z}_a \tag{1.49}$$

with

$$\mathbf{z}_e^{\mathrm{T}} = [\, \lambda_{e,1}\,,\, \boldsymbol{\varphi}_{e,1}^{\mathrm{T}}\,,\, \lambda_{e,2}\,,\, \boldsymbol{\varphi}_{e,2}^{\mathrm{T}}\,,\, \ldots\,,\, \lambda_{e,N}\,,\, \boldsymbol{\varphi}_{e,N}^{\mathrm{T}}\,]^{\mathrm{T}} \tag{1.50}$$

and

$$\mathbf{z}_a^{\mathrm{T}} = [\, \lambda_{a,1}\,,\, \boldsymbol{\varphi}_{a,1}^{\mathrm{T}}\,,\, \lambda_{a,2}\,,\, \boldsymbol{\varphi}_{a,2}^{\mathrm{T}}\,,\, \ldots\,,\, \lambda_{a,N}\,,\, \boldsymbol{\varphi}_{a,N}^{\mathrm{T}}\,]^{\mathrm{T}}\,. \tag{1.51}$$

Depending on the individual optimisation objective the penalty functions may also contain Frequency Response Functions (FRF) [29, 52, 124, 117, 50, 152], which requires damping to be included in numerical model, or force residuals [29, 48, 9]. The majority of these approaches were discussed in the 1980's.

The state vector $\mathbf{z}_a$ relates the penalty function to the numerical model properties. As a result, eq. (1.49) is a – generally – non-linear function of the mathematical model's mass and stiffness properties. A linearised approximation, which is usually derived from a truncated Taylor series expansion, allows to express the penalty function in terms of the unknown model parameters $\mathbf{p}$ and a sensitivity matrix $\mathbf{G}$

$$\Delta\boldsymbol{\varepsilon} \approx \mathbf{G} \cdot \Delta\mathbf{p}\,. \tag{1.52}$$

The sensitivity matrix $\mathbf{G}$ contains the derivatives of the analytical eigenvalues and eigenvectors with respect to the correction factors $\mathbf{p}$. Various methods have been proposed to compute the sensitivities from the modal data of the initial finite-element model. For the undamped structural eigenvalue problem expressions have been derived for the first derivatives of the eigenvalues by LINK [99] and for the eigenvectors by FOX and KAPOOR [49] and NELSON [130]. OJALVO [142], MILLS-CURRAN [112, 113], and DAILEY [31] have extended NELSON's method to deal with the case of repeated or closely spaced eigenvalues.

Due to the non-linearity of both the penalty function and sensitivity matrix with respect to the analytical mass and stiffness properties the minimisation of $\Delta\boldsymbol{\varepsilon}$, eq. (1.52), and computation of the related model parameters from

$$\Delta\mathbf{p} = (\mathbf{G}^{\mathrm{T}}\,\mathbf{G})^{-1}\,\mathbf{G}^{\mathrm{T}} \cdot \Delta\boldsymbol{\varepsilon} \tag{1.53}$$

involves an iterative solution procedure and a numerical modal analysis at every iteration step. The model updating method applied within the scope of this research is introduced in Section 3.2.

1.3.2.1 Definition of Substructures

In most practical cases the number of model parameters (the mass and stiffness values at each degree of freedom) will vastly exceed the number of measurements (the natural frequencies and mode shape deflection components). This leads to an under-determined equation system for the computation of the unknown model parameters and does not allow for a direct estimation of physical mass and stiffness properties. However, if a number of physical degrees of freedom are combined to form a group or substructure and the mass and stiffness properties of the analytical model are utilised as initial data a correction factor may be determined for each substructure and a rank deficiency of $\mathbf{G}^{\mathrm{T}}\,\mathbf{G}$ is avoided. The parameters $\mathbf{p}$ now represent the correction factors for the individual substructures. To reduce the influence of noise in the measured data the number of correction parameters is usually chosen to be smaller than

the number of measurements. The resulting equation system becomes overdetermined and is solved by least squares approximations. This approach has been originally proposed by NATKE [128] in (1974).

Iterative methods enable a wide choice of model properties to be corrected. The definition of substructures, however, requires a profound knowledge of the actual modelling uncertainties. Otherwise, the updated model may well reproduce the experimental results but the modifications do not necessarily comprise the desired physical significance.

1.3.3 Comparison of Analytical and Experimental Data

1.3.3.1 Mode Shape Allocation

With the comparison of numerical and measured modal data in eq. (1.49) it is essential to correctly identify and individually allocated each analytical eigenvector and associated eigenfrequency in $\mathbf{z}_a$ to the corresponding experimental mode shape and natural frequency in $\mathbf{z}_e$. Simply arranging the eigenfrequencies in ascending order does not necessarily ensure the comparison of identical mode shapes since the order of modes obtained from the test and numerical estimates may be different due to errors in the mathematical model and because the experimental data base may be incomplete, i.e. not all modes in the frequency range under investigation have been identified in the test (cf. Section 2.3.2). Further problems arise from the damping not being included in the mathematical model and errors in the measured data.

Initially, the problem has been addressed by ALLEMANG and BROWN [1] who have suggested a Modal Assurance Criterion

$$\mathbf{MAC}_{rs} = \frac{|\boldsymbol{\varphi}_{a,r}^{\mathrm{T}} \cdot \boldsymbol{\varphi}_{e,s}|^2}{(\boldsymbol{\varphi}_{a,r}^{\mathrm{T}} \cdot \boldsymbol{\varphi}_{a,r})(\boldsymbol{\varphi}_{e,s}^{\mathrm{T}} \cdot \boldsymbol{\varphi}_{e,s})} \qquad \text{for } r, s = 1, \ldots, N \tag{1.54}$$

to estimate the degree of correlation between analytical and experimental mode shape vectors. The **MAC** essentially is the normalised scalar product of the vectors $\boldsymbol{\varphi}_{a,r}$ and $\boldsymbol{\varphi}_{e,s}$. Values close to one indicate a good correlation of the two vectors while small values imply them to be orthogonal. Since a true

orthogonality relation only exists with respect to the mass or stiffness matrix, eqs. (1.44) and (1.45), the **MAC** for dissimilar eigenvectors will not necessarily be exactly zero.[5]

1.3.3.2 Model Reduction and Mode Shape Expansion Techniques

The eigenvector and mode shape components must be identical in number and location to allow a direct comparison in eqs. (1.49) and (1.54). Adversely, the number of components in the experimental mode shape vectors usually is some orders of magnitude smaller than the number of degrees of freedom in the numerical model. Equal vector sizes may be achieved by either reducing the system matrices to the measured degrees of freedom or expanding the measured mode shapes to the size of the analytical model.

Model Reduction Methods. A simple and most popular method has been introduced by GUYAN [57] who has derived a transformation between the full state vector and the master co-ordinates by neglecting the inertia terms of the slave degrees of freedom in the equations of motion (1.24). Disregarding the inertia terms causes the eigenfrequencies of the reduced model to be higher than those of the full model. The static reduction may be modified to include inertia forces at an appropriately chosen frequency ω_0. An improvement to GUYAN's static reduction method, where the inertia terms are included as pseudo static forces, has been introduced by O'CALLAHAN [139]. O'CALLAHAN, AVITABILE, and RIEMER [140] have used the computed eigenvectors to assemble a transformation between the master and slave co-ordinates. The reduced model exactly reproduces all eigenvectors and eigenfrequencies used in the transformation.

Mode Shape Expansion Methods. Mode shape expansion methods utilise the numerical model to obtain the missing information by either using the equations of motion to derive a relation between the unknown and the mea-

[5] In addition, the Co-Ordinate Modal Assurance Criterion [94] may be used to determine the correlation between two measurement locations for all the paired mode shapes.

sured deflection components [88][6] or expressing the measured mode shape as linear combination of the analytical eigenvectors [141, 108].

A comparison of reduction methods is provided in [5] and [6]. GYSIN [58] and IMREGUN and EWINS [67] have given examples of the practical application of mode shape expansion methods. IBRAHIM [66] has discussed model reduction techniques and eigenvector expansion methods in the context of modal and FRF sensitivity techniques.

1.4 Thesis Outline

The main objectives of this thesis are:

- The development of a method, which improves data quality and helps to reduce testing time with experimental modal identification techniques, namely the Phase Resonance Method, in order to meet the requirements imposed by the increasing dynamic complexity, i.e. high modal density, non-proportional damping, or restricted accessibility, of future aerospace structures. This includes the implementation of the approach into the Ground Vibration Test Facility operated by the German Aerospace Research Establishment (DLR) and a performance evaluation on aerospace structures of varying dimensions.

- The development of techniques and application strategies which allow model updating to be applied to large-scale industrial finite-element models. Here, the foremost concerns are the handling of experimental modal data exposed to random measurement errors, noise, modal and spatial incompleteness, or low phase purity of the measured mode shapes and the identification of updating parameters which are coherent with the actual modelling errors in the analytical system matrices thus leading to a physically consistent updated numerical model. Again, performance is evaluated on aerospace structures of varying size and complexity. Additionally, the advantages of model updating in other fields of application

[6]This method is equivalent to an inverse Guyan reduction.

are demonstrated. The problem of detecting structural damage is chosen for this purpose and the advantages of model updating on the damage localisation accuracy are investigated.

The subjects of research are arranged as follows:

Chapter 2 provides an introduction to the standard experimental modal identification techniques used. Two analysis methods, allowing to transform measured time domain response data into frequency domain modal parameters, are described. The main test hardware components for data acquisition are introduced and the experimental errors originating from both analysis methods and measurement techniques are reviewed. Finally, the Ground Vibration Test Facility operated by DLR's Institute for Aeroelasticity is introduced.

In Section 3.2 the basic model updating method is set out. The algorithm used here has been established in publications by NATKE [126] and LINK [106, 99]. The model optimisation process is based on the minimisation of a residual involving measured and analytical modal data, where the latter are non-linear functions of the model's mass and stiffness properties. Linearisation of the residual using a truncated Taylor series expansion and introducing a Jacobian matrix allows to compute the unknown correction parameters. In order to reduce the influence of noise in the experimental data the number of parameters should always be smaller than the number of measurements. This results in an over-determined equation system which is solved in a least squares sense.

In Section 3.3 a new model-based method for the localisation of structural damage is introduced. The method uses measured Frequency Response Functions (FRF) and modal data from a finite-element model to derive information on the damage location on the structure under investigation. A localisation criterion based on a correlation of measured and analytical damage-induced damping deviations is proposed. Experimental modal damping factors are obtained from fitting the measured FRFs to quadratic polynomials. A standard Rayleigh damping approach and an analytical damage model are used to generate numerical damping factors for the healthy and damaged states.

A novel method for the computation of optimised excitation force vectors for Phase Resonance Testing is proposed in Section 3.4. Unlike other approaches, no numerical data or preliminary assessments on the structural damping are needed. The method processes measured structural responses from harmonic single-point excitations at selected exciter locations. A new feature is the superposition of the measured responses such that the real-part response is minimised with respect to the total response. In the associated eigenvalue problem the eigenvector related to the smallest eigenvalue is used to compute the unknown force vector components for an optimised multi-point excitation. A further novel element is the option to calculate a Mode Indicator Function (MIF) from the corresponding structural response which allows for an a-priori assessment of the mode isolation quality and selection of the most promising exciter configuration.

Section 4.2 gives an overview of principal aspects related to the practical application of the model updating method set out in Section 3.2. A laboratory test structure has been selected for simplicity. Experimental modal data were identified from the structural model and the generation of a finite-element model suitable for model updating is described. The problem of finding updating parameters which are consistent to the errors in the mathematical model and additionally satisfy existing mathematical constraints is discussed and a new knowledge-based strategy for selecting a set of physically significant correction parameters is introduced. To demonstrate the performance of the updating method the model correction process is restricted to a fraction of the modal parameters from the experimental data base and an original attempt is made to use the resulting validated model to predict the remaining modal data and FRFs.

In Section 4.3 a simulation study is developed to investigate the influence of errors resulting from inaccuracies in the test hardware and experimental identification methods on the accuracy of the model corrections. Different representative categories of experimental uncertainties are numerically modelled and added to simulated experimental modal data. Error magnitudes are

varied and the effect on substructure correction factors, frequency deviations, and mode shape correlation is investigated. Different numerical models are used to evaluate the role of modelling error magnitudes and locations.

An application to a large-scale industrial finite-element model of the EC 135 helicopter [39] is described in Section 5.2. The initial finite-element model has been provided by Eurocopter Deutschland [38] and experimental modal data have been extracted from a Shake Test on the EC 135-S01 prototype. With the fundamental importance of parameter selection in mind and to ensure a significant influence on the helicopter's overall dynamic characteristics preference regarding the selection of updating substructures is given to those components which constitute the aircraft backbone structure. To avoid inconsistencies of the material parameters and enable an efficient parameterisation in the MSC/NASTRAN^{TM} finite-element code a novel technique for the parameterisation of non-isotropic material regions is proposed.

In Section 5.3 the beneficial effects of model updating on the localisation accuracy of the damage localisation method introduced in Section 3.3 is demonstrated. The finite-element model of a basic aircraft component is updated using experimental mode shapes and natural frequencies from the undamaged test structure and the damage localisation accuracy obtained with the initial and updated models are compared. Preliminary investigations involve an optimisation of positions for the excitation device and response sensor in order to maximise the amount of data acquired from the test structure and an assessment of the method's spatial resolution.

Finally, in Section 5.4 the method for the computation of optimised excitation force vectors introduced in Section 3.4 is evaluated with respect to performance as compared to other force tuning approaches and the potential to improve the quality of experimental modal data. Of particular interest with regard to the modal testing of complex aerospace structures are the capabilities of handling a high modal density, non-proportional damping, and restricted accessibility to the test structure. A mathematical model is used for comparison with other methods. To assess effects not represented within the analytical

model, like structural non-linearity, eigenfrequency shifts due to incomplete excitation, or systematic and experimental errors, the method is applied to a laboratory test structure. The performance under realistic test conditions is investigated during the Ground Vibration Test on the Polar Platform (PPF) [144] space structure.

Chapter 2

Experimental Identification Techniques

The experimental identification of a structure's characteristic dynamic response is a vitally important step in finite-element model updating. The measurement and analysis techniques comprised in this chapter provide the experimental modal reference data which is used to modify the analytical system matrices in order to adjust the model's numerical dynamic response to the measured response of the real world structure.

The following sections cover the two main categories of analysis methods for transforming measured time domain structural responses into frequency domain data, describe the core components of standard data acquisition and pre-processing hardware, discuss the most significant sources of experimental errors, and introduce the Ground Vibration Test Facility operated by DLR's Institute for Aeroelasticity [68].

A comprehensive introduction to modal testing has been given by EWINS [44]. ALLEMANG, BROWN, and ROST [2] and SNOEYS, SAS, HEYLEN, and VAN DER AUWERAER [156] have also discussed various aspects of vibration testing.

2.1 Analysis Methods

Although modal parameters can be identified directly from the measured excitation $\mathbf{f}(t)$ and structural response $\mathbf{u}(t)$, eq. (1.24), processing time domain data generally is not practical for typical structural systems because of the quantity of the experimental data involved and the computational effort and due to the difficult interpretation of the results. Therefore, the first step in the extraction of modal parameters from an experimental structural response is to convert the measured signal into the frequency domain where it is described by its constituent frequencies and corresponding magnitudes. This is usually achieved by means of a Fourier series expansion

$$u(t_n) = \frac{a_0}{2} + \sum_{j=1}^{N/2} \left(a_j \cdot \cos \frac{2\pi j\, t_n}{T} + b_j \cdot \sin \frac{2\pi j\, t_n}{T} \right) , \tag{2.1}$$

where the periodic response $u(t_n)$, which is sampled at N discrete steps over a time period T, is represented by a finite number of spectral coefficients

$$\begin{aligned} a_0 &= \frac{1}{N} \sum_{n=1}^{N} u(t_n) , \\ a_\mathrm{j} &= \frac{1}{N} \sum_{n=1}^{N} u(t_n) \cdot \cos \frac{2\pi j\, n}{N} , \\ b_\mathrm{j} &= \frac{1}{N} \sum_{n=1}^{N} u(t_n) \cdot \sin \frac{2\pi j\, n}{N} . \end{aligned} \tag{2.2}$$

Likewise, the transformation can be applied to the excitation force signal to compute the Frequency Response Function (FRF)

$$\mathrm{FRF}(\omega) = U(\omega)/F(\omega) , \tag{2.3}$$

where $U(\omega)$ and $F(\omega)$ are the Fourier transformations of the response and excitation force, respectively. Most post-processing methods use the Frequency Response Functions as input to compute experimental eigenfrequencies and mode shapes. They are commonly classified into Phase Separation Techniques and Phase Resonance Techniques [135].

2.1.1 Phase Separation Techniques

Phase separation methods [105, 92, 162] can work with either broadband (random or impact) or single frequency (sine-sweep or step-sine) excitation signals. The real-part (in-phase with the excitation signal) and imaginary-part (in quadrature to the excitation signal) of the complex structural responses are measured and correlated to the excitation forces to compute FRFs. The experimental FRFs are fitted to a polynomial, where the frequency is used as variable. The polynomial coefficients are obtained from least squares approximation techniques. When all measured FRFs are used the methods produce global estimates of the natural frequencies and damping ratios.

A major problem with phase separation techniques is to determine the actual number of modes in the frequency range under investigation when the natural frequencies are closely spaced or in the presence of noise in the measured structural response signals. Also, local modes which only appear in a few FRFs may be difficult to identify.

A phase separation technique is used in Section 5.2 to extract experimental modal data from measured structural responses.

2.1.2 Phase Resonance Techniques

Classical phase resonance techniques are the most frequently applied testing methods in aerospace. Their historical development can be traced back to the 1920's [53]. The methods are considered to be established and reliable.

The basic idea of phase resonance techniques is to balance the structure's internal damping forces $\mathbf{D}\,\dot{\mathbf{u}}(t)$ in eq. (1.24) by applying a suitable external excitation $\mathbf{f}(t)$. As a result, the structure oscillates in a pure natural mode which allows to directly identify the modal parameters of the corresponding undamped system.

Phase Resonance Methods (PRM) work with single frequency excitations which enables them to apply high excitation energy levels to the test structure resulting in high signal to noise ratios. The methods can separate closely spaced natural frequencies through the use of phase-coherent multi-point exci-

tation force vectors. The force components are individually tuned for each of the neighbouring mode shapes in order to amplify the response of one mode while the other mode is simultaneously suppressed. Furthermore, Phase Resonance Methods are essential for the investigation of non-linear systems.

The methods main disadvantage is the time-consuming force tuning process. To save precious testing time and exploit the full potential of the Phase Resonance Method, especially with respect to the quality of the experimental data, a systematic approach for tuning the excitation force vectors is proposed in Section 3.4, where an in-depth theoretical treatment of the Phase Resonance Method is provided. The force tuning method is tested and compared to other force tuning techniques in Section 5.4. The Phase Resonance Method is used to identify the experimental modal reference data for model updating in Sections 4.2, 5.2, and 5.4.

2.2 Test Hardware

The test hardware enables the acquisition of the input data needed by the experimental modal analysis methods which were delineated in the previous section. The test hardware basically consists of three main components:

- excitation devices to apply excitation forces $\mathbf{f}(t)$ to the test structure,
- sensors to measure the corresponding dynamic structural response $\mathbf{u}(t)$, and
- equipment to record and process the measured data.

2.2.1 Excitation Devices

Electromagnetic shakers are most commonly used as excitation devices in Phase Resonance Testing.[1] Because of their advantages as to operation and handling they were chosen for all experimental investigations in Sections 4.2,

[1]Other possible excitation devices are impact hammers, hydraulic shakers, or devices incorporating rotating eccentric masses.

5.2, and 5.4. Shakers provide an output force proportional to a specified electric input current. The input current generates a proportional magnetic field in a cylindrical moving coil which is located in a static, homogeneous, outer magnetic field. The axial force generated in the moving coil by the superposition of magnetic fields is proportional to the input current. A stinger is used to feed the excitation force into the structure. Having a low bending stiffness the stinger ensures that structural movements at the excitation point are not constrained by the shaker. It should be noted, however, that the masses of the moving coil and stinger and the stiffness of the coil suspension result in a local perturbation of the structure.

2.2.2 Response Sensors

With the exception of extremely low frequencies the structural response is usually measured in terms of accelerations which are more convenient to convert into an electric signal than deflections or strains. Acceleration sensors basically consist of a seismic mass mounted on an elastic suspension. When the sensor is subjected to an acceleration the seismic mass executes forced vibrations at the frequency of excitation. The deflection amplitude is proportional to the external acceleration when the eigenfrequency of the sensor element is high compared to the excitation frequency.

The majority of transducers uses the piezoelectric effect [120], where a mechanical strain generates an electric charge. A signal conditioning unit converts the charge into a proportional voltage for further processing. Other transducer types use inductive or magneto-resistive principles to transform accelerations into electric signals.

As in the case of attaching shakers the mounting of sensors adds mass to the structure and changes the modal parameters. The sensor masses are considered as being part of the structure in any subsequent analysis. If the additional sensor masses are not acceptable, e.g. with light-weight structures or high accelerations, remote sensing devices such as optical or inductive transducers must be used.

Except for the investigations performed in Section 5.3, where a piezoelectric sensor and a laser Doppler scanning vibrometer were utilised, all structural responses throughout this thesis were measured using magneto-resistive sensors. They are described in more detail in Section 2.4.1.

2.2.3 Recording and Processing Equipment

The initial stage in a post-processing chain is to amplify the transducer output signals to an appropriate voltage range, usually ± 5 V or ± 10 V, to reduce the sensitivity to perturbations which are likely to occur in the further processing steps. Some types of sensors, like strain gauges or magneto-resistive accelerometers, may also require a phantom power supply. The next step is to remove any noise and disturbances beyond the frequency range of interest by appropriate filtering.

Today, all subsequent processing steps are commonly performed digitally. The analog data is sampled at discrete time steps by an analog-to-digital converter. The sampling rate required to retrieve the analog signal from the digital data must be at least twice the maximum frequency of the analog signal. This condition is known as Shannon's sampling theorem. Higher-order low pass filters are used to remove all frequencies beyond half the sampling rate from the analog signal and prevent aliasing effects. Aliasing would cause frequencies above half the sampling rate to appear as spurious low frequencies in a subsequent digital-to-analog conversion.

The measured data is now prepared to be analysed by appropriate computer hardware using the methods introduced in Section 2.1. A mobile data acquisition and signal processing facility [32, 34] which is particularly designed for vibration testing of large aerospace structures is described in detail in the next section.

2.2.4 Suspension Systems

Additionally, the suspension system which supports the test structure and defines the test boundary conditions may be regarded as part of the test set-

up. To acquire significant results the test should as closely as possible simulate the operating conditions of the respective structure.

For aircraft the free flight or so-called 'free-free' boundary conditions are approximated by a low-frequency suspension. The frequencies of the rigid body modes (RBM) of the suspended structure should be sufficiently smaller than the lowest elastic mode. A problem with these suspensions is their low stiffness resulting in large static deflections due to the structure's weight. Free-free boundary conditions were chosen for the test cases investigated in Sections 4.2 and 5.2.

The most critical operating conditions for satellites, i.e. the highest structural loads, occur during lift-off when the satellite is mounted to the payload bay of a launch vehicle. Typically, the launcher has a considerably larger mass and stiffness and primarily behaves like a seismic foundation. Therefore, satellites are usually fixed at their base during vibration testing. This set-up was used with the test cases described in Sections 5.3 and 5.4.

2.3 Experimental Errors

Limitations of the test hardware and experimental identification methods discussed in the previous sections lead to inevitable imperfections in the measured modal data. With respect to model updating applications the most significant errors are the phase purity of the measured mode shapes, modal and spatial incompleteness, and measurement noise. A short review of publications dealing with the problems of complex modes and incomplete data is provided in the following sections. Random measurement errors have been considered by various authors [62, 41, 42, 19]. Systematic studies, however, have not been performed in the past. An investigation on the influence of experimental errors on the finite-element model corrections is provided in Section 4.3.

2.3.1 Complex Mode Shapes

A fundamental inconsistency between the numerical analysis and modal identification test arises from the damping distribution in the test structure which leads to complex experimental mode shapes. With the exception of Phase Resonance Testing [27] any realistic structure will exhibit complex modes, unless an appropriated multi-point excitation is used in the identification process. The problem has been reviewed by CAUGHEY and O'KELLY [21] and MITCHELL [115]. According to NIEDBAL [136] a comparison of real analytical and complex experimental modes must be avoided since it is likely to prevent any model improvements based on measured modal parameters. Therefore, the measured complex mode shapes should be converted into real modes [133, 135]. IBRAHIM [65] has presented a method to transform complex modes into real modes by directly solving the equilibrium equations for the undamped system to obtain an estimate for $\mathbf{M}^{-1}\mathbf{K}$ which may then be used to compute the eigenvalue problem of the damped system. The method works well for weakly damped structures with phase angles close to zero or 180 degrees. Another method proposed by NIEDBAL [134] involves writing the complex mode shapes in terms of the real mode shapes using a complex transformation. The transformation matrix is computed from the real and imaginary components of the complex mode shapes. The errors introduced by some of the mode shape conversion methods were analysed by SESTIERI and IBRAHIM [153].

2.3.2 Modal and Spatial Incompleteness

The second problem is the incompleteness of the experimental modal data with respect to both the number of identified mode shapes and the number of measured degrees of freedom. Modal incompleteness is due to the fact that the number of measured mode shapes is limited, mainly by the frequency range of the test hardware and the critical modal density of the experimental modal analysis methods.[2] Spatial incompleteness is caused by the number of

[2] A useful comparison of measured and analytical modal data may additionally be restricted by the accuracy of the mathematical model.

measured structural response components being smaller than the number of degrees of freedom in the numerical model.

The improvement of the stiffness and flexibility matrix based on an incomplete number of measured natural frequencies using weighted least squares has been investigated by NATKE, COLLMANN, and ZIMMERMANN [128]. Problems associated with the derivation of analytical model properties from incomplete data have also been addressed by BERMAN and FLANNELLY [12], BERMAN [11], NATKE [124], and MOTTERSHEAD [116].

2.4 The Ground Vibration Test Facility

The Ground Vibration Test Facility, Figure 2.1, operated by DLR's Institute for Aeroelasticity forms a central part of the framework within which this research is conducted. The facility comprises the test hardware required to carry out experimental vibration analyses on complex aerospace structures. In recent years, the test facility was used for modal identification and dynamic qualification tests on most major European military and civil fixed wing aircraft, helicopters, satellites, and other space structures. To allow for world wide operation the measurement equipment is installed in two mobile, air-conditioned, standard freight containers. Approximately 800 sensor channels and 24 independent excitation channels are available. Excitation, vibration recording, and data processing are controlled by a process computer.

2.4.1 Excitation

Five electromagnetic exciter types of various sizes and force amplitude levels are available. 24 excitation channels are controlled simultaneously by the test facility. On most structures only a few excitation points are needed to isolate a mode shape, yet, the large number of excitation channels helps to avoid the time-consuming rearrangement of shakers during a test.

The shakers were modified by DLR in order to minimise their vibrating mass, grounded stiffness, and internal friction. This diminishes any interaction

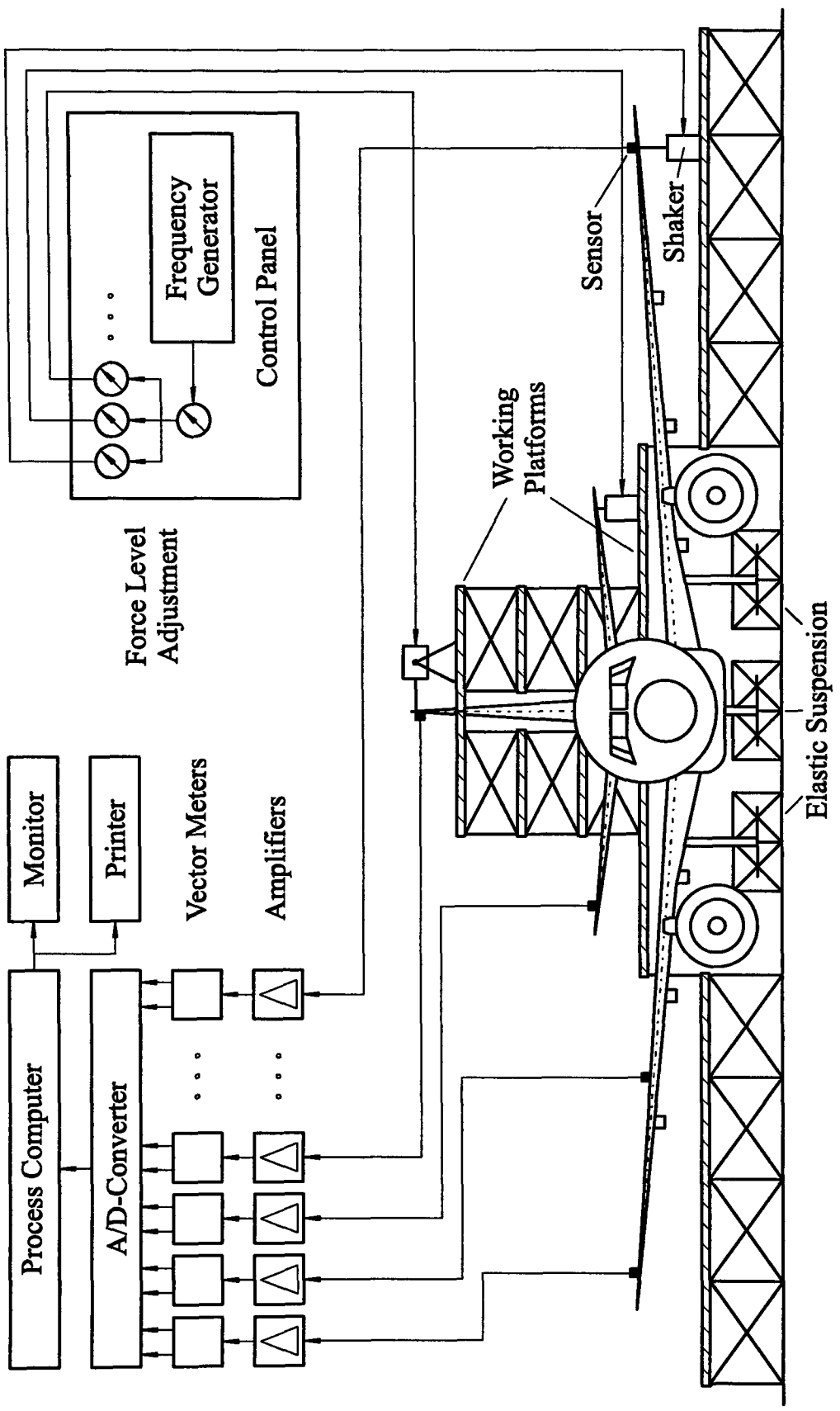

Figure 2.1: Ground Vibration Test Facility operated by DLR

Parameter	Value
Type	DLR
Quantity	12
max. Force	16 N
max. Stroke	±10 mm
Vibrating Mass	83 g
Height	190 mm
Diameter	95 mm
Exciter Mass	4 kg

Table 2.1: Exciter Specifications

between the shaker and test structure and allows to determine the excitation force directly by measuring the voice coil current. The technical data of the shakers are given in Table 2.1.

Each exciter is mounted on a tripod of variable height. A slide bearing support decouples the shaker from the tripod stiffness. The support can be rotated around two perpendicular axes allowing for a free excitation force orientation in space. Lightweight rods link the shakers to the excitation points on the structure. The excitation forces are transferred to the structure by vacuum shoes or, for special applications, custom made adapters.

A digital high resolution frequency generator provides the harmonic input signal for the amplifiers which drive the shakers. All shakers are operated at the same frequency and phase angle. Force levels for each individual excitation channel are set on a control board. For multi-point excitations all force levels can be adjusted proportionally to conveniently investigate non-linearity effects.

2.4.2 Vibration Measurement

The test structure's dynamic response is measured by magneto-resistive acceleration sensors. The sensors were developed by DLR and are specifically designed for low-frequency applications and good linearity. They were manufactured under license by Georg Wazau Meß- und Prüfsysteme GmbH, Berlin, Germany. Table 2.2 lists the key specifications.

Parameter	Value
Type	Wazau (DLR)
Quantity	800
Measuring Range	± 1000 m/s^2
Sensitivity	~ 0.5 mV/$\frac{\text{m}}{\text{s}^2}$
Resolution	0.01 m/s^2
Frequency Range	0-300 Hz
Resonance Frequency	> 600 Hz
Amplitude Linearity	< 2 %
Transverse Sensitivity	< 2 %
Temperature Sensitivity	~ 0.1 %/°C
max. Acceleration	± 5000 m/s^2
Length	30 mm
Diameter	8 mm
Mass	8 g

Table 2.2: Sensor Specifications

Two-sided adhesive tape is used to attach the sensors to the test structure. The actual sensor element rotates in an outer holder to allow its individual measurement direction to be aligned independent of the local surface orientation.

2.4.3 Data Processing

A SUN 20/2 workstation is used to control the excitation frequency and force amplitudes and to process the sensor data. Every sensor signal is split into its real (in phase with the excitation reference signal) and imaginary (± 90 degrees phase shift to the excitation signal) component by means of vector meters. The signals are then fed into a set of multi-channel A/D-converters and stored on the workstation's internal hard disk drive.

The control software was developed by DLR to meet the particular requirements of Modal Survey Testing which include an automated data acquisition, online post-processing, display of results, and data storage. The following functions are implemented:

- automated sine-sweep excitation in a given frequency band,
- display of Mode Indicator Function (MIF), eq. (3.54), versus excitation frequency,
- recording of Frequency Response Functions (FRF),
- acquisition of mode shape deflection amplitudes, generalised masses, and modal damping factors, and
- online display of mode shapes (static/animated).

The Ground Vibration Test Facility was used as data acquisition system for the majority of test cases discussed in Chapters 4 and 5. Normal modes and Frequency Response Functions were measured on the structural model (SM) used by the GARTEUR[3] Action Group 19, Section 4.2. A Shake Test and modal identification were performed on the prototype of the Eurocopter EC 135 helicopter in Section 5.2. Modal parameters of a laboratory test structure, Section 5.4.2, and the Polar Platform satellite developed by the European Space Agency (ESA), Section 5.4.3, were identified. Table 2.3 gives an overview of the applications within the scope of this thesis.

[3]Group for Aeronautical Research and Technology in Europe

Table 2.3: Overview of Applications using the Ground Vibration Test Facility

Test Case	Test Method	No. of Sensors	No. of Exciters	Frequency Range		No. of Modes
				f_{min}/[Hz]	f_{max}/[Hz]	
GARTEUR SM-AG19	Ground Vibration Test	24	12	0	150	14
	Shake Test	24	2	4	65	-
EC 135-S01	Shake Test	64	5	5	35	15
Laboratory Test Structure	Ground Vibration Test	101	7	10	210	18
Polar Platform Satellite	Ground Vibration Test	575	99	0	180	109

Chapter 3

Development of Procedures

3.1 Introduction

In this chapter the procedures utilised for the improvement of numerical models using experimental modal data, the localisation of structural damage, and the experimental identification of natural frequencies and mode shapes are developed.

The theoretical background of the model updating method introduced by NATKE [126] and LINK [106, 99] is outlined in Section 3.2. The method performs an implicit estimation of analytical model parameters based on a least squares approximation to experimental modal data. It is assumed that the system is passive and linear and that the analytical system matrices are real, symmetric, and positive definite. The existing finite-element analysis [101, 102] and model optimisation [100] computer codes are used. This enables to focus attention on the application-related aspects of the updating problem which will be discussed in Chapters 4 and 5.

In Section 3.3 a novel concept for the identification and localisation of delamination damages in carbon fibre reinforced polymers (CFRP) is introduced. The method is based on the observation of damage-induced modal damping variations and a correlation of measured data to an analytical model. The approach is unique in that it allows to locate damage in a three-dimensional structure using data from only a single structural response sensor. A technique to

accurately measure the damage-induced deviations of modal damping factors is developed and a correlation coefficient for modal vector analysis is adapted to enable the identification and localisation of the damage. In Section 5.3 a stringer-stiffened aircraft panel is used as a test structure to generate experimental data for an undamaged and damaged case and to assess the proposed concept.

A new method for the computation of optimised multi-point excitation force vectors, which are needed for an accurate and consistent identification of the natural modes of complex structures in Phase Resonance Testing, cf. Section 2.1.2, is presented in Section 3.4. The method performs a superposition of structural responses from a series of preliminary sweep runs in different exciter configurations in order to minimise the real-part response with respect to the total response. Unlike other approaches, it does not rely on numerical data or assessments on the structural damping. Optimised excitation forces are determined in a non-iterative procedure and the associated achievable phase purity is assessed. The updating algorithm is shown in Figure 3.1 and various test cases are discussed in Section 5.4.

3.2 Model Updating Method

As with all model updating techniques, the main objective of the iterative method used here is to improve the correlation between experimental data from a test structure and the corresponding analytical model. This is achieved through a variation of model parameters in order to minimise a penalty function, which describes the deviations between measured and computed data. The model parameters are associated with properties of structural components which due to inaccurate modelling require correction. As a result of the penalty function's non-linearity with respect to the model parameters, the optimisation problem needs to be linearised and solved using an iterative procedure.

A major advantage of iterative updating techniques, as opposed to direct methods, is their capability to maintain the initial coincidence between degrees of freedom within the system matrices. This allows for model corrections which do not only reproduce the experimental data but also are capable to improve the analytical model's physical significance and provide valuable information on the modelling of complicated details.

3.2.1 Basic Equations

In order to attain a selective correction of those model components which are assumed to contain modelling errors the system matrices of the initial finite-element model $\mathbf{K}_0$ and $\mathbf{M}_0$ are superimposed with a set of submatrices $\mathbf{K}_i$ and $\mathbf{M}_j$, representing the uncertain model regions and properties, to define the improved mass and stiffness matrices

$$\begin{aligned} \mathbf{K} &= \mathbf{K}_0 + \sum_{i=1}^{I} \alpha_i \mathbf{K}_i \ , \\ \mathbf{M} &= \mathbf{M}_0 + \sum_{j=1}^{J} \beta_j \mathbf{M}_j \ . \end{aligned} \tag{3.1}$$

Any structural modification to the original model is introduced through discrete correction factors α_i and β_j for each submatrix.

The submatrices $\mathbf{K}_i$ and $\mathbf{M}_j$ may consist of individual or groups of finite elements. Due to the manifold connections between each submatrix and the adjacent finite-element mesh the submatrices can not be extracted directly from the full system matrices but have to be individually built as separate models.

As to start the optimisation from the original analytical model the initial values for the correction factors α_i and β_j are set to zero. For physically meaningful corrections α_i and β_j must assume values larger than minus one. Otherwise, the stiffness or mass within the corresponding substructure vanishes or becomes negative.

A residual or error vector constitutes the penalty function for the model corrections

$$\boldsymbol{\varepsilon}(\mathbf{p}) = \mathbf{z}_e - \mathbf{z}_a(\mathbf{p}) \ . \tag{3.2}$$

The state vector $\mathbf{z}_e$ contains experimental data (e.g. modal, frequency response, or force residuals) while $\mathbf{z}_a(\mathbf{p})$ is the vector of corresponding analytical model data, therefore being a function of the correction factors

$$\mathbf{p}^{\mathrm{T}} = (\ldots , \alpha_i , \ldots , \beta_j , \ldots) \ . \tag{3.3}$$

The residual vector represents the optimisation criterion for the model corrections. The best approximation to measured reference data corresponds to a minimum of the residual. A range of possible choices for residuals will be discussed in more detail in Section 3.2.2.

The objective of the updating process is to find the correction factors α_i and β_j which minimise the error vector, eq. (3.2). The minimisation usually requires a least squares approximation of analytical to experimental data because the system to be solved is over-determined, i.e. the number of components in ε exceeds the number of parameters in p. This leads to an objective function

$$\mathrm{J}(\mathbf{p}) = \boldsymbol{\varepsilon}^{\mathrm{T}} \, \mathbf{W}_{\varepsilon} \, \boldsymbol{\varepsilon} + \mathbf{p}^{\mathrm{T}} \, \mathbf{W}_{\mathrm{p}} \, \mathbf{p} \ , \tag{3.4}$$

where $\mathbf{W}_{\varepsilon}$ and $\mathbf{W}_{\mathrm{p}}$ are regular symmetric matrices for the residual and the parameter vectors, respectively. An appropriate choice of the weighting matri-

ces allows to focus the optimisation process on particularly important experimental data or substructures [118, 126, 99]. Minimising the objective function, eq. (3.4), simultaneously reduces the deviations between experimental and analytical data and constrains parameter variations throughout the iteration by means of which the solution process is stabilised.

To find a minimum for the objective function the partial derivatives of $\mathrm{J}(\mathbf{p})$ with respect to the correction factors need to be computed. This requires the residual, eq. (3.2), to be linearised in $\mathbf{p}$ by means of a truncated Taylor series expansion:

$$\boldsymbol{\varepsilon}(\mathbf{p}_{\kappa+1}) \approx \boldsymbol{\varepsilon}(\mathbf{p}_{\kappa}) + \left.\frac{\partial\, \boldsymbol{\varepsilon}(\mathbf{p})}{\partial\, \mathbf{p}^{\mathrm{T}}}\right|_{\mathbf{p}=\mathbf{p}_{\kappa}} (\mathbf{p}_{\kappa+1} - \mathbf{p}_{\kappa}) \;, \tag{3.5}$$

where subscript κ denotes the iteration step and

$$\boldsymbol{\varepsilon}(\mathbf{p}_{\kappa}) = \mathbf{z}_e - \mathbf{z}_a(\mathbf{p}_{\kappa}) \;.$$

Introducing the Jacobian matrix

$$\mathbf{G}_{\kappa} = \left.\frac{\partial\, \mathbf{z}_a(\mathbf{p})}{\partial\, \mathbf{p}^{\mathrm{T}}}\right|_{\mathbf{p}=\mathbf{p}_{\kappa}} \tag{3.6}$$

and

$$\Delta\mathbf{p} = \mathbf{p}_{\kappa+1} - \mathbf{p}_{\kappa} \tag{3.7}$$

eq. (3.5) may be rewritten as

$$\boldsymbol{\varepsilon}(\mathbf{p}_{\kappa+1}) \approx \boldsymbol{\varepsilon}(\mathbf{p}_{\kappa}) - \mathbf{G}_{\kappa} \cdot \Delta\mathbf{p} \;. \tag{3.8}$$

The Jacobian matrix $\mathbf{G}_{\kappa}$ describes the influence of correction factor changes on the analytical data. Therefore, it is frequently called sensitivity matrix or gradient matrix. The modified objective function now reads

$$\mathrm{J}(\Delta\mathbf{p}) = (\boldsymbol{\varepsilon}_{\kappa}^{\mathrm{T}} - \Delta\mathbf{p}^{\mathrm{T}}\, \mathbf{G}_{\kappa}^{\mathrm{T}}) \cdot \mathbf{W}_{\varepsilon} \cdot (\boldsymbol{\varepsilon}_{\kappa} - \mathbf{G}_{\kappa}\, \Delta\mathbf{p}) + \Delta\mathbf{p}^{\mathrm{T}}\, \mathbf{W}_{\mathrm{p}}\, \Delta\mathbf{p} \;. \tag{3.9}$$

With the necessary conditions for the minimisation

$$\frac{\partial\, \mathrm{J}(\Delta\mathbf{p})}{\partial\, \Delta\mathbf{p}} = \mathbf{0} \tag{3.10}$$

eq. (3.9) becomes

$$\frac{\partial\, \mathrm{J}(\Delta\mathbf{p})}{\partial\, \Delta\mathbf{p}} \;=\; \frac{\partial}{\partial\, \Delta\mathbf{p}} (\boldsymbol{\varepsilon}_{\kappa}^{\mathrm{T}}\, \mathbf{W}_{\varepsilon}\, \boldsymbol{\varepsilon}_{\kappa}) - 2\, \frac{\partial\, \Delta\mathbf{p}^{\mathrm{T}}}{\partial\, \Delta\mathbf{p}} (\mathbf{G}_{\kappa}^{\mathrm{T}}\, \mathbf{W}_{\varepsilon}\, \boldsymbol{\varepsilon}_{\kappa})$$

$$
\begin{aligned}
&+ \frac{\partial \Delta\mathbf{p}^{\mathrm{T}}}{\partial \Delta\mathbf{p}} \left(\mathbf{G}_{\kappa}^{\mathrm{T}} \mathbf{W}_{\varepsilon} \mathbf{G}_{\kappa}\right) \Delta\mathbf{p} + \frac{\partial \Delta\mathbf{p}^{\mathrm{T}}}{\partial \Delta\mathbf{p}} \left(\mathbf{G}_{\kappa}^{\mathrm{T}} \mathbf{W}_{\varepsilon} \mathbf{G}_{\kappa}\right)^{\mathrm{T}} \Delta\mathbf{p} \\
&+ \frac{\partial \Delta\mathbf{p}^{\mathrm{T}}}{\partial \Delta\mathbf{p}} \mathbf{W}_{\mathrm{p}} \Delta\mathbf{p} + \frac{\partial \Delta\mathbf{p}^{\mathrm{T}}}{\partial \Delta\mathbf{p}} \mathbf{W}_{\mathrm{p}}^{\mathrm{T}} \Delta\mathbf{p} \\
= \; & -2\, \mathbf{G}_{\kappa}^{\mathrm{T}} \mathbf{W}_{\varepsilon}\, \boldsymbol{\varepsilon}_{\kappa} + 2\, \mathbf{G}_{\kappa}^{\mathrm{T}} \mathbf{W}_{\varepsilon} \mathbf{G}_{\kappa} \Delta\mathbf{p} + 2\, \mathbf{W}_{\mathrm{p}} \Delta\mathbf{p} = \mathbf{0} \; .
\end{aligned}
$$

Solving for $\Delta\mathbf{p}$ yields a linear system of equations for the unknown correction factors:

$$
\Delta\mathbf{p} = \left(\mathbf{G}_{\kappa}^{\mathrm{T}} \mathbf{W}_{\varepsilon} \mathbf{G}_{\kappa} + \mathbf{W}_{\mathrm{p}}\right)^{-1} \cdot \mathbf{G}_{\kappa}^{\mathrm{T}} \mathbf{W}_{\varepsilon}\, \boldsymbol{\varepsilon}_{\kappa} \; . \tag{3.11}
$$

The quality of the solution will essentially depend on the choice of correction parameters, the weighting, and the residuals [107].

3.2.2 Error Vector and Gradient Matrix

Computing the correction factors from eq. (3.11) requires the Jacobian matrix and error vector to be determined and the weighting matrices $\mathbf{W}_{\varepsilon}$ and $\mathbf{W}_{\mathrm{p}}$ to be chosen appropriately. The residual is selected according to the given updating problem and controls the nature and amount of experimental data by which the analytical model is updated. Possible choices are eigenvalue and eigenvector residuals as well as force or response residuals. Within the scope of this thesis further considerations will concentrate on corrections based on modal data. Therefore, only the expressions for eigenvalue and eigenvector residuals will be developed in detail. A comprehensive collection and discussion of residuals is given in [126].

In the following sections an undamped system with real eigenvectors and eigenvalues will be assumed. In addition, a precise allocation between measured quantities and the corresponding numerical model quantities as outlined in Section 1.3.3 must be established.[1]

[1]The allocation of experimental and analytical data may change as the correction proceeds. It has to be checked within each iteration step.

3.2.2.1 Eigenvalue Residuals

Updating the analytical model in order to reproduce measured natural frequencies requires a residual of the form:

$$\boldsymbol{\varepsilon}_\lambda = \begin{pmatrix} \lambda_{e,1} - \lambda_{a,1}(\mathbf{p}) \\ \lambda_{e,2} - \lambda_{a,2}(\mathbf{p}) \\ \vdots \\ \lambda_{e,N} - \lambda_{a,N}(\mathbf{p}) \end{pmatrix} , \tag{3.12}$$

where $\lambda_{e,n}$ are the squares of experimental eigenfrequencies and $\lambda_{a,n}$ are analytical eigenvalues. To ensure a correct allocation of corresponding measured and analytical values the respective mode shapes and eigenvectors have to be considered. Pairing of natural frequencies and eigenvalues in ascending order alone does not necessarily lead to a comparison of equal modes (cf. Section 1.3.3).

The associated gradient matrix

$$\mathbf{G}_\lambda = \begin{bmatrix} \frac{\partial \lambda_{a,1}}{\partial p_1} & \frac{\partial \lambda_{a,1}}{\partial p_2} & \cdots & \frac{\partial \lambda_{a,1}}{\partial p_K} \\ \frac{\partial \lambda_{a,2}}{\partial p_1} & \frac{\partial \lambda_{a,2}}{\partial p_2} & \cdots & \frac{\partial \lambda_{a,2}}{\partial p_K} \\ \vdots & \vdots & \ddots & \vdots \\ \frac{\partial \lambda_{a,N}}{\partial p_1} & \frac{\partial \lambda_{a,N}}{\partial p_2} & \cdots & \frac{\partial \lambda_{a,N}}{\partial p_K} \end{bmatrix} \tag{3.13}$$

is derived from the eigenvalue problem for the updated analytical model

$$(-\lambda_a \mathbf{M} + \mathbf{K})\, \boldsymbol{\varphi}_a = \mathbf{0} \, . \tag{3.14}$$

Partial differentiation with respect to the correction factors yields

$$\left(-\frac{\partial \lambda_a}{\partial p_k}\mathbf{M} - \lambda_a \frac{\partial \mathbf{M}}{\partial p_k} + \frac{\partial \mathbf{K}}{\partial p_k}\right) \boldsymbol{\varphi}_a + (-\lambda_a \mathbf{M} + \mathbf{K}) \frac{\partial \boldsymbol{\varphi}_a}{\partial p_k} = \mathbf{0} \, . \tag{3.15}$$

Eqs. (3.15) contain the required derivatives $\partial \lambda_a / \partial p_k$ and additionally the eigenvector derivatives $\partial \boldsymbol{\varphi}_a / \partial p_k$ which will be used in Section 3.2.2.2. Left hand multiplication with $\boldsymbol{\varphi}_a^{\mathrm{T}}$ and writing eqs. (3.15) for the r^{th} eigenvalue results in

$$\begin{aligned} -\frac{\partial \lambda_{a,r}}{\partial p_k} \boldsymbol{\varphi}_{a,r}^{\mathrm{T}} \mathbf{M} \boldsymbol{\varphi}_{a,r} - \lambda_{a,r} \boldsymbol{\varphi}_{a,r}^{\mathrm{T}} \frac{\partial \mathbf{M}}{\partial p_k} \boldsymbol{\varphi}_{a,r} + \boldsymbol{\varphi}_{a,r}^{\mathrm{T}} \frac{\partial \mathbf{K}}{\partial p_k} \boldsymbol{\varphi}_{a,r} \\ + \boldsymbol{\varphi}_{a,r}^{\mathrm{T}} (-\lambda_{a,r} \mathbf{M} + \mathbf{K}) \frac{\partial \boldsymbol{\varphi}_{a,r}}{\partial p_k} = 0 \, . \end{aligned} \tag{3.16}$$

With the generalised mass, eq. (1.37), of mode r

$$M_{a,r} = \boldsymbol{\varphi}_{a,r}^{\mathrm{T}} \, \mathbf{M} \, \boldsymbol{\varphi}_{a,r} \tag{3.17}$$

and taking into account the symmetry of the system matrices

$$\boldsymbol{\varphi}_{a,r}^{\mathrm{T}} (-\lambda_{a,r} \, \mathbf{M} + \mathbf{K}) = \mathbf{0}^{\mathrm{T}}$$

the eigenvalue derivatives are:

$$\frac{\partial \, \lambda_{a,r}}{\partial \, p_k} = \frac{1}{M_{a,r}} \left(-\lambda_{a,r} \, \boldsymbol{\varphi}_{a,r}^{\mathrm{T}} \frac{\partial \, \mathbf{M}}{\partial \, p_k} \, \boldsymbol{\varphi}_{a,r} + \boldsymbol{\varphi}_{a,r}^{\mathrm{T}} \frac{\partial \, \mathbf{K}}{\partial \, p_k} \, \boldsymbol{\varphi}_{a,r} \right) \, . \tag{3.18}$$

Using eqs. (3.1) the final expressions for stiffness matrix corrections

$$\frac{\partial \, \lambda_{a,r}}{\partial \, \alpha_i} = \frac{1}{M_{a,r}} \, \boldsymbol{\varphi}_{a,r}^{\mathrm{T}} \, \mathbf{K}_i \, \boldsymbol{\varphi}_{a,r} \tag{3.19}$$

and for mass matrix corrections

$$\frac{\partial \, \lambda_{a,r}}{\partial \, \beta_j} = -\frac{1}{M_{a,r}} \, \lambda_{a,r} \, \boldsymbol{\varphi}_{a,r}^{\mathrm{T}} \, \mathbf{M}_j \, \boldsymbol{\varphi}_{a,r} \tag{3.20}$$

are obtained.

Eqs. (3.19) and (3.20) require an eigenvalue solution in order to determine the derivatives with respect to the correction factors. For each mode r the gradients for stiffness corrections $\partial \, \lambda_a / \partial \, \alpha_i$ are proportional to the substructure's potential energy $\boldsymbol{\varphi}_{a,r}^{\mathrm{T}} \, \mathbf{K}_i \, \boldsymbol{\varphi}_{a,r}$ and the gradients for mass corrections $\partial \, \lambda_a / \partial \, \beta_j$ are proportional to the substructure's kinetic energy $\boldsymbol{\varphi}_{a,r}^{\mathrm{T}} \, \mathbf{M}_j \, \boldsymbol{\varphi}_{a,r}$, respectively.

3.2.2.2 Eigenvector Residuals

Updating the system matrices with experimental eigenfrequencies also provides corrected eigenvectors. Their accuracy, however, is usually lower as if they were directly involved in the optimisation process. To generate an analytical model that properly reproduces measured mode shapes a modified residual is used:

$$\boldsymbol{\varepsilon}_{\varphi} = \begin{pmatrix} \boldsymbol{\varphi}_{e,1} - \boldsymbol{\varphi}_{a,1}(\mathbf{p}) \\ \boldsymbol{\varphi}_{e,2} - \boldsymbol{\varphi}_{a,2}(\mathbf{p}) \\ \vdots \\ \boldsymbol{\varphi}_{e,N} - \boldsymbol{\varphi}_{a,N}(\mathbf{p}) \end{pmatrix} \, . \tag{3.21}$$

Correctly computing the differences in eq. (3.21) requires all vectors $\boldsymbol{\varphi}_{e,n}$ and $\boldsymbol{\varphi}_{a,n}$ to be normalised in the same way.

Due to the limited number of sensors on the test structure the experimental mode shapes usually contain a smaller number of deflection components than the eigenvectors from the analytical model. As a result, the error vector does only include the degrees of freedom corresponding to the measurement locations whereas at all other degrees of freedom no conditions have to be fulfilled.

The eigenvector derivatives in the gradient matrix

$$\mathbf{G}_{\varphi} = \begin{bmatrix} \frac{\partial \boldsymbol{\varphi}_{a,1}}{\partial p_1} & \frac{\partial \boldsymbol{\varphi}_{a,1}}{\partial p_2} & \cdots & \frac{\partial \boldsymbol{\varphi}_{a,1}}{\partial p_K} \\ \frac{\partial \boldsymbol{\varphi}_{a,2}}{\partial p_1} & \frac{\partial \boldsymbol{\varphi}_{a,2}}{\partial p_2} & \cdots & \frac{\partial \boldsymbol{\varphi}_{a,2}}{\partial p_K} \\ \vdots & \vdots & \ddots & \vdots \\ \frac{\partial \boldsymbol{\varphi}_{a,N}}{\partial p_1} & \frac{\partial \boldsymbol{\varphi}_{a,N}}{\partial p_2} & \cdots & \frac{\partial \boldsymbol{\varphi}_{a,N}}{\partial p_K} \end{bmatrix} \tag{3.22}$$

are approximated by a series expansion of all eigenvectors

$$\frac{\partial \boldsymbol{\varphi}_{a,r}}{\partial p_k} = \sum_{s=1}^{N_a} c_s \, \boldsymbol{\varphi}_{a,s} \; . \tag{3.23}$$

To compute the coefficients c_s eq. (3.15) again is written for mode r and multiplied by $\boldsymbol{\varphi}_{a,t}^{\mathrm{T}}$, where $r \neq t$

$$\begin{aligned} -\frac{\partial \lambda_{a,r}}{\partial p_k} \boldsymbol{\varphi}_{a,t}^{\mathrm{T}} \mathbf{M} \boldsymbol{\varphi}_{a,r} + \boldsymbol{\varphi}_{a,t}^{\mathrm{T}} \left(-\lambda_{a,r} \frac{\partial \mathbf{M}}{\partial p_k} + \frac{\partial \mathbf{K}}{\partial p_k} \right) \boldsymbol{\varphi}_{a,r} \\ + \boldsymbol{\varphi}_{a,t}^{\mathrm{T}} \left(-\lambda_{a,r} \mathbf{M} + \mathbf{K} \right) \frac{\partial \boldsymbol{\varphi}_{a,r}}{\partial p_k} \;\; = \;\; 0 \; . \end{aligned} \tag{3.24}$$

Applying eq. (3.23) while keeping in mind the eigenvector's orthogonality with respect to the mass matrix yields

$$\boldsymbol{\varphi}_{a,t}^{\mathrm{T}} \left(-\lambda_{a,r} \mathbf{M} + \mathbf{K} \right) \cdot \sum_{s=1}^{N_a} c_s \, \boldsymbol{\varphi}_{a,s} = -\boldsymbol{\varphi}_{a,t}^{\mathrm{T}} \left(-\lambda_{a,r} \frac{\partial \mathbf{M}}{\partial p_k} + \frac{\partial \mathbf{K}}{\partial p_k} \right) \boldsymbol{\varphi}_{a,r} \; . \tag{3.25}$$

Because of

$$\boldsymbol{\varphi}_{a,t}^{\mathrm{T}} (-\lambda_{a,r} \mathbf{M} + \mathbf{K}) \, c_s \, \boldsymbol{\varphi}_{a,s} = 0 \qquad \text{for } s \neq t$$

eq. (3.25) reduces to

$$(-\lambda_{a,r} \, \boldsymbol{\varphi}_{a,t}^{\mathrm{T}} \mathbf{M} \, \boldsymbol{\varphi}_{a,t} + \boldsymbol{\varphi}_{a,t}^{\mathrm{T}} \mathbf{K} \, \boldsymbol{\varphi}_{a,t}) \cdot c_t = -\boldsymbol{\varphi}_{a,t}^{\mathrm{T}} \left(-\lambda_{a,r} \frac{\partial \mathbf{M}}{\partial p_k} + \frac{\partial \mathbf{K}}{\partial p_k} \right) \boldsymbol{\varphi}_{a,r} \; . \tag{3.26}$$

Using the generalised quantities, eqs. (1.37) and (1.38),

$$M_{a,t} = \boldsymbol{\varphi}_{a,t}^{\mathrm{T}}\,\mathbf{M}\,\boldsymbol{\varphi}_{a,t} \qquad \text{and} \qquad K_{a,t} = \boldsymbol{\varphi}_{a,t}^{\mathrm{T}}\,\mathbf{K}\,\boldsymbol{\varphi}_{a,t} \tag{3.27}$$

and $\lambda_{a,t} = K_{a,t}/M_{a,t}$ the coefficients for $\lambda_{a,t} \neq \lambda_{a,r}$ are

$$c_t = -\frac{1}{(\lambda_{a,t} - \lambda_{a,r})M_{a,t}}\,\boldsymbol{\varphi}_{a,t}^{\mathrm{T}}\left(-\lambda_{a,r}\frac{\partial\,\mathbf{M}}{\partial\,p_k} + \frac{\partial\,\mathbf{K}}{\partial\,p_k}\right)\boldsymbol{\varphi}_{a,r}\ . \tag{3.28}$$

In order to avoid a division by zero no repeated eigenvalues are permitted in eq. (3.28).

The remaining coefficient c_r is derived from the expression for the generalised mass, eq. (3.17), by partial differentiation with respect to the correction factors:

$$2\,\boldsymbol{\varphi}_{a,r}^{\mathrm{T}}\,\mathbf{M}\,\frac{\partial\,\boldsymbol{\varphi}_{a,r}}{\partial\,p_k} + \boldsymbol{\varphi}_{a,r}^{\mathrm{T}}\frac{\partial\,\mathbf{M}}{\partial\,p_k}\,\boldsymbol{\varphi}_{a,r} = 0\ .$$

Replacing the partial derivatives by the series expansion, eq. (3.23), gives

$$2\,\boldsymbol{\varphi}_{a,r}^{\mathrm{T}}\,\mathbf{M}\cdot\sum_{s=1}^{N_a} c_s\,\boldsymbol{\varphi}_{a,s} + \boldsymbol{\varphi}_{a,r}^{\mathrm{T}}\frac{\partial\,\mathbf{M}}{\partial\,p_k}\,\boldsymbol{\varphi}_{a,r} = 0$$

and because of

$$2\,\boldsymbol{\varphi}_{a,r}^{\mathrm{T}}\,\mathbf{M}\,c_s\,\boldsymbol{\varphi}_{a,s} = 0 \qquad \text{for } r \neq s$$

the last coefficient is

$$c_r = -\frac{1}{2M_{a,r}}\,\boldsymbol{\varphi}_{a,r}^{\mathrm{T}}\frac{\partial\,\mathbf{M}}{\partial\,p_k}\,\boldsymbol{\varphi}_{a,r}\ . \tag{3.29}$$

With eqs. (3.28) and (3.29) all coefficients for eq. (3.23) are determined and the partial derivatives can be computed. For $p_k = \alpha_i$ eq. (3.23) becomes

$$\frac{\partial\,\boldsymbol{\varphi}_{a,r}}{\partial\,\alpha_i} = \sum_{s=1}^{N_a} c_s\,\boldsymbol{\varphi}_{a,s}\ . \tag{3.30}$$

Using eq. (3.1) to simplify eqs. (3.28) and (3.29) gives

$$c_s = \begin{cases} \frac{-1}{(\lambda_{a,s}-\lambda_{a,r})M_{a,s}}\,\boldsymbol{\varphi}_{a,s}^{\mathrm{T}}\,\mathbf{K}_i\,\boldsymbol{\varphi}_{a,r} & \text{for } r \neq s \\ 0 & \text{for } r = s \end{cases}\ .$$

Similarly, for $p_k = \beta_j$ eq. (3.23) becomes

$$\frac{\partial\,\boldsymbol{\varphi}_{a,r}}{\partial\,\beta_j} = \sum_{s=1}^{N_a} c_s\,\boldsymbol{\varphi}_{a,s}\ , \tag{3.31}$$

where

$$c_s = \begin{cases} \frac{\lambda_{a,r}}{(\lambda_{a,s}-\lambda_{a,r})M_{a,s}}\, \boldsymbol{\varphi}_{a,s}^{\mathrm{T}}\, \mathbf{M}_j\, \boldsymbol{\varphi}_{a,r} & \text{for } r \neq s \\ -\frac{1}{2M_{a,s}}\, \boldsymbol{\varphi}_{a,s}^{\mathrm{T}}\, \mathbf{M}_j\, \boldsymbol{\varphi}_{a,s} & \text{for } r = s \end{cases}$$

again using eq. (3.23) for simplification.

Analogous to Section 3.2.2.1 a solution of the eigenvalue problem from the analytical model is required. Starting from this eigenvalue solution all partial eigenvector derivatives needed to assemble the gradient matrix are given by eqs. (3.30) and (3.31).

3.2.2.3 Combined Eigenvalue and Eigenvector Residuals

Since an updated numerical model is usually expected to match both the experimental eigenfrequencies and the mode shapes the error vectors, eqs. (3.12) and (3.21), and gradient matrices, eqs. (3.13) and (3.22), are used to form joint expressions

$$\boldsymbol{\varepsilon} = \begin{pmatrix} \boldsymbol{\varepsilon}_\lambda \\ \boldsymbol{\varepsilon}_\varphi \end{pmatrix} \tag{3.32}$$

and

$$\mathbf{G} = \begin{bmatrix} \mathbf{G}_\lambda \\ \mathbf{G}_\varphi \end{bmatrix} . \tag{3.33}$$

Introducing eqs. (3.32) and (3.33) into eq. (3.11) unfortunately reveals that the products $\mathbf{G}^{\mathrm{T}}\, \mathbf{W}_\varepsilon\, \mathbf{G}$ and $\mathbf{G}^{\mathrm{T}}\, \mathbf{W}_\varepsilon\, \boldsymbol{\varepsilon}$ contain elements of dissimilar dimensions. To retain eqs. (3.32) and (3.33) in the given form the frequency differences in eq. (3.12) and the modal vector differences in eq. (3.21) are replaced with normalised expressions

$$(\lambda_{e,n} - \lambda_{a,n})/\lambda_{norm} \qquad \text{and} \qquad (\boldsymbol{\varphi}_{e,n} - \boldsymbol{\varphi}_{a,n})/\varphi_{norm} \ ,$$

respectively, where $1/\lambda_{norm}$ and $1/\varphi_{norm}$ are suitable normalisation factors, e.g. the largest observed deviations between analytical and experimental data. Partial differentiation with respect to the correction factors according to eq. (3.6) reproduces identical normalisation factors $1/\lambda_{norm}$ and $1/\varphi_{norm}$ in the respective gradient matrix terms. As a result, the correction factors can be computed from eq. (3.11).

3.2.3 Summary

This section has developed the procedures which will be applied in the process of improving finite-element models using experimental modal data as a reference.

The initial numerical model is parameterised by means of a superposition of the original system matrices and a set of correction submatrices which characterise the supposedly erroneous model regions, eq. (3.1), and enable a selective correction of existing modelling errors. The numerical model optimisation is controlled through a residual vector, eq. (3.2), containing the experimental and corresponding analytical vibration data toward which the model shall be improved. Since, in most cases the system to be solved is over-determined, i.e. the number of measurements exceeds the number of correction parameters, a least squares approximation, eq. (3.4), is utilised to find a minimum of the residual. As a result, a linear system of equations for the unknown correction factors, eq. (3.11), is obtained. Solving eq. (3.11) involves the definition of appropriate weighting matrices and the computation of a Jacobian matrix from analytical modal data, eqs. (3.13) and (3.22). Due to the residual's non-linearity with respect to the correction factors the model optimisation problem needs to be solved by means of an iterative procedure. The algorithm, made available as a computer code [100] from the Lightweight Structures and Structural Mechanics Laboratory, University of Kassel [96], is sketched in Figure 3.1.

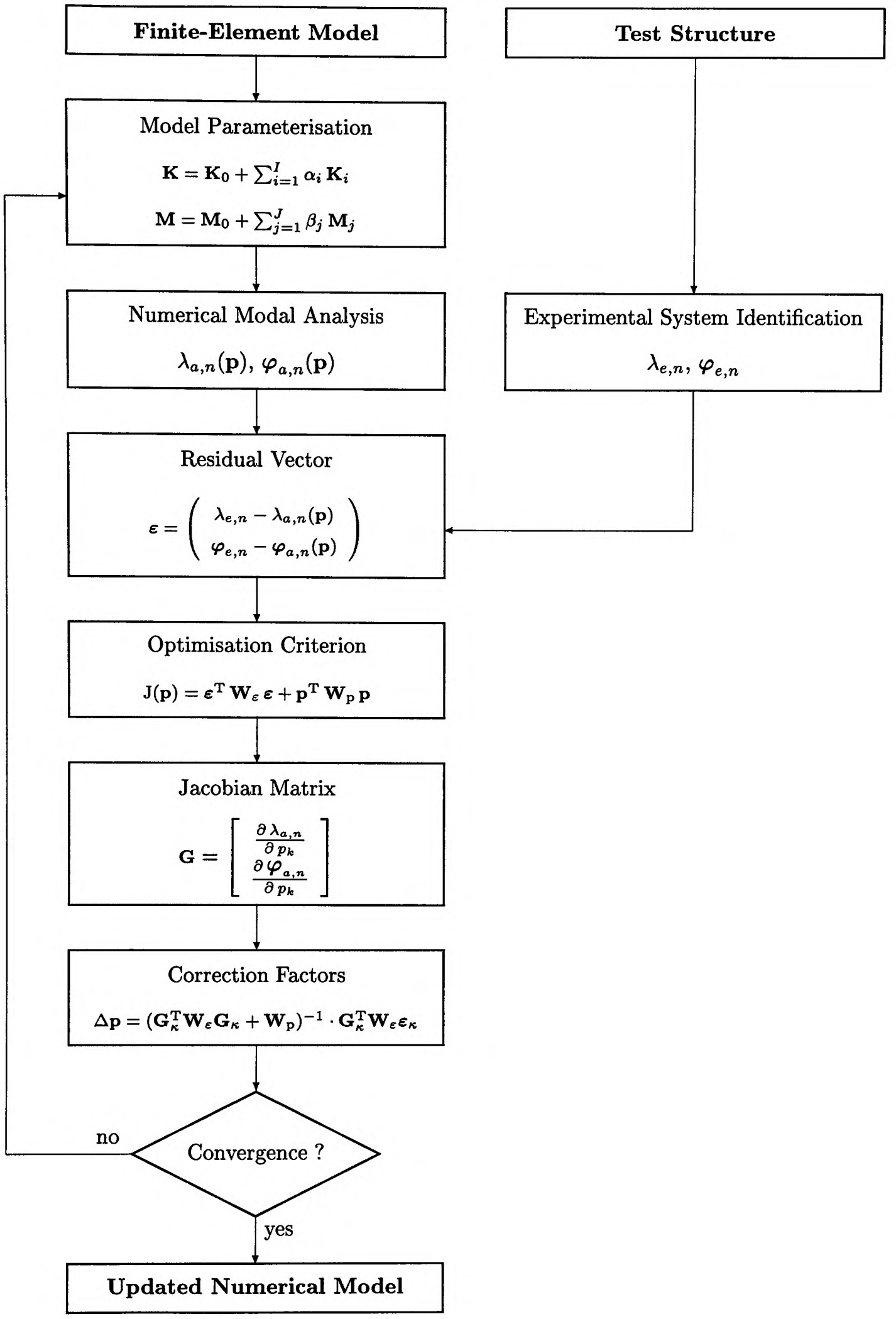

Figure 3.1: Updating Algorithm

3.3 Localisation of Structural Damage

The occurrence of structural damage in elasto-mechanic structures is directly related to changes in their dynamic characteristics. Solving the inverse problem, i.e. deriving reliable information on the damage location and size from experimental vibration data, has been a subject of research for decades. The initial impetus has come from the offshore industry [163, 110, 168, 28, 70] where the harsh mechanical and chemical environment requires a permanent observation of the structural integrity. Some contributions have also been made recently by the civil engineering community, e.g. [54, 45, 147]. Here, the surveillance of bridges and buildings and the assessment of earthquake damage are the most important subjects.

Major applications for damage detection methods are emerging in aerospace owing to the high operational safety standards and low level of redundancy in light-weight structures. Modal approaches appear particularly attractive since, as a result of a local event (the damage), the structure's dynamic characteristics are affected globally. This allows to identify a damage from measurements in remote undamaged areas. Therefore, modal approaches are most suitable when the structural accessibility is limited and when no a-priori knowledge on the possible damage location is available.

Hence, the key task of modal damage diagnoses is to observe global phenomena and to identify the associated local events. The identification process usually involves a mathematical model of the examined structure. Using this model the relation between a damage and variations of the dynamic properties is inverted mathematically. For most practical applications, however, only a finite-element model is available. In this case, information on the damage location is obtained from a comparison between analytical and experimental quantities.

3.3.1 Introduction

Among the most attractive new materials for aerospace applications are fibre reinforced polymers. Unfortunately, these fibre materials respond highly sensitive to surface impacts caused for example by projectiles or during maintenance. If the energy of the impacting object exceeds a specific threshold the internal bonding between adjacent fibre layers is destroyed over a certain area around the impact location. In the delamination region the unbonded fibre layers are free to glide along the fibre plane directions which leads to a local reduction in shear stiffness and additional friction.

Generally, the damaged component's surface is left intact and the delamination remains invisible. Appropriate conventional inspection techniques are usually based on ultrasonic wave scan methods. Being time consuming and cost intensive the aircraft industry now is strongly interested in alternative methods.

Regarding the structures dynamic behaviour the decreased shear stiffness causes the natural frequencies to decline and the additional friction is perceived as an increased modal damping. Minor alterations also occur in the mode shapes. Yet, the influence of the damage is mainly restricted to its immediate vicinity and decreases rapidly with distance from the damage location [127]. Due to this, the monitoring of mode shape deflections would require a high sensor density which apparently is not very suitable for aerospace applications.

Despite some promising results [164, 111] the sensitivity of natural frequencies with respect to general structural damage typically is rather low. With delamination damages in particular, however, the increased damping is clearly observable [69]. Nonetheless, the amount of additional friction generated by the delamination depends on the distribution of shear deformations over the damaged area. Since the distribution of shear deformations varies within the global deflection field the increase of damping is a function of the damage location and depends on the mode shape.

Simple as it appears, no working method currently exists for structures exceeding the complexity of simple beams, especially when the experimental

data is incomplete and contains measurement errors [22, 51, 165]. As in most inverse problems ill-conditioning is a major concern. To avoid this it is essential to limit the localisation problem to its basic aspects, that is to reduce the number of unknown quantities such that only a minimum number of parameters need to be determined. Therefore, the investigations will be focussed on a single concentrated damage and linear behaviour is assumed before and after damage has occurred.

The localisation method proposed here [86, 87, 82] is based on observing the differences of modal damping between a healthy, i.e. undamaged, and a damaged configuration for a range of mode shapes and a subsequent comparison of experimental and analytical data. Regarding the monitored test article this involves measuring the structural response and extracting damping factors (Section 3.3.2) for both the healthy and the damaged state. For the respective numerical model a damping distribution must be modelled (Section 3.3.3) and a realistic finite-element model of the delamination damage has to be generated in order to derive analytical data for the healthy and the damaged state. The damage location, being unknown at this point, is the variable of the localisation problem. Comparing experimental and analytical damage-induced damping deviations for a sufficient number of mode shapes (Section 3.3.4) reveals that the correlation varies with the damage position in the finite-element model. The highest degree of similarity is associated with a coincidence of the damage position in the finite-element model and the real damage location on the test structure. The correlation coefficient is therefore used as the criterion to determine the damage location.

In Section 5.3 an application to to a stringer-stiffened fuselage panel made of carbon fibre reinforced polymers (CFRP) is described and the advantages of using an updated finite-element model are emphasised.

3.3.2 Extraction of Experimental Damping Parameters

The extraction of experimental damping values from measured frequency response data is based on a polynomial curve fit. Assuming the damping to be

sufficiently low and the resonance frequencies to be adequately spaced the measured structural response in the vicinity of a resonance n is approximated by a proportionally damped one-degree-of-freedom system with mass m, damping factor $\eta_{e,n}$, and eigenfrequency ω_n. The system's response to a stationary harmonic excitation force $\mathrm{f}(\omega)$ is given by

$$u_e(\omega) = \frac{\mathrm{f}(\omega)}{m(-\omega^2 + 2i\eta_{e,n}\omega_n\omega + \omega_n^2)} \,. \tag{3.34}$$

If $\mathrm{f}(\omega) = const.$ the inverse response is a quadratic polynomial in ω

$$\frac{1}{u_e(\omega)} = \underbrace{-\frac{m}{\mathrm{f}}}_{a_n} \cdot \omega^2 + \underbrace{2i\eta_{e,n}\frac{m}{\mathrm{f}}\omega_n}_{b_n} \cdot \omega + \underbrace{\frac{m}{\mathrm{f}}\omega_n^2}_{c_n} \tag{3.35}$$

with the coefficients

$$a_n = -\frac{m}{\mathrm{f}} \,, \qquad b_n = 2i\eta_{e,n}\frac{m}{\mathrm{f}}\omega_n \,, \qquad \text{and} \qquad c_n = \frac{m}{\mathrm{f}}\omega_n^2 \,. \tag{3.36}$$

Solving for $\eta_{e,n}$ yields the unknown damping factor:

$$\eta_{e,n} = \frac{-b_n}{2i\omega_n \cdot a_n} \qquad \text{or} \qquad \eta_{e,n} = \frac{\omega_n \cdot b_n}{2i \cdot c_n} \,. \tag{3.37}$$

The coefficients a_n, b_n, and c_n are easily obtained from a polynomial curve fit around the resonance frequency ω_n.

3.3.3 Analytical Damping Model

Eqs. (3.37) allow to compute modal damping factors from experimental frequency response data. To derive the corresponding quantities from the analytical model a damping matrix is assembled from a linear superposition of the mass and stiffness matrices as outlined in Section 1.2.7.2. Rewriting eq. (1.29) using the generalised properties from eqs. (1.37) and (1.38) results in

$$D_n = \mu \cdot M_n + \kappa \cdot K_n \,. \tag{3.38}$$

The damping factor of a given mode n is defined as

$$\eta_{a,n} = \frac{D_n}{2\sqrt{K_n M_n}} \tag{3.39}$$

or, using eq. (3.38),

$$\eta_{a,n} = \frac{\mu}{2\,\omega_n} + \frac{\kappa\,\omega_n}{2} \,. \tag{3.40}$$

The proportionality constants μ and κ are chosen such that the $\eta_{a,n}$ from the finite-element model provide the most accurate approximation to the measured modal damping values $\eta_{e,n}$ of the undamaged structure in a least squares sense.

3.3.4 Correlation of Experimental and Analytical Data

The correlation of experimental and analytical data is based on the damage-induced differences of the damping factors obtained from eqs. (3.37) and (3.40). The deviation of measured damping factors is

$$\Delta\eta_{e,n}(\mathbf{x}_e) = \frac{\eta^{\mathrm{D}}_{e,n}(\mathbf{x}_e) - \eta^{\mathrm{H}}_{e,n}}{\eta^{\mathrm{H}}_{e,n}} \,, \tag{3.41}$$

where $\eta^{\mathrm{H}}_{e,n}$ denotes the measured damping value of mode n for the healthy structure, whereas $\eta^{\mathrm{D}}_{e,n}(\mathbf{x}_e)$ is the corresponding value after damage has occurred. The (unknown) damage location is described by the vector $\mathbf{x}_e$. For analytical damping deviations

$$\Delta\eta_{a,n}(\mathbf{x}_a) = \frac{\eta^{\mathrm{D}}_{a,n}(\mathbf{x}_a) - \eta^{\mathrm{H}}_{a,n}}{\eta^{\mathrm{H}}_{a,n}} \tag{3.42}$$

with $\mathbf{x}_a$ being the location vector for the modelled damage. Computing the deviations according to eqs. (3.41) and (3.42) requires response measurements on the healthy and the damaged structure and computing analytical damping factors for the healthy and damaged states, respectively.

Writing the modal damping deviations from a set of N measured modes as a vector results in

$$\Delta\boldsymbol{\eta}_e(\mathbf{x}_e) = \begin{pmatrix} \Delta\eta_{e,1}(\mathbf{x}_e) \\ \Delta\eta_{e,2}(\mathbf{x}_e) \\ \vdots \\ \Delta\eta_{a,N}(\mathbf{x}_e) \end{pmatrix} \tag{3.43}$$

and, for the appropriate computed modes,

$$\Delta\boldsymbol{\eta}_a(\mathbf{x}_a) = \begin{pmatrix} \Delta\eta_{a,1}(\mathbf{x}_a) \\ \Delta\eta_{a,2}(\mathbf{x}_a) \\ \vdots \\ \Delta\eta_{a,N}(\mathbf{x}_a) \end{pmatrix} . \tag{3.44}$$

The experimental and analytical damping deviations are compared through a correlation coefficient for modal vector analysis [1]:

$$C(\mathbf{x}_a, \mathbf{x}_e) = \frac{(\Delta\boldsymbol{\eta}_a^{\mathrm{T}}(\mathbf{x}_a) \cdot \Delta\boldsymbol{\eta}_e(\mathbf{x}_e))^2}{(\Delta\boldsymbol{\eta}_a^{\mathrm{T}}(\mathbf{x}_a) \cdot \Delta\boldsymbol{\eta}_a(\mathbf{x}_a)) \cdot (\Delta\boldsymbol{\eta}_e^{\mathrm{T}}(\mathbf{x}_e) \cdot \Delta\boldsymbol{\eta}_e(\mathbf{x}_e))} . \tag{3.45}$$

As the damage position in the finite-element model is varied the correlation between numerical and experimental data will also vary. Assuming that a sufficient number of modes is considered the correlation coefficient C will have a unique maximum exactly when, and only when, $\mathbf{x}_a$ approaches $\mathbf{x}_e$:

$$C(\mathbf{x}_a, \mathbf{x}_e) \rightarrow \max. \qquad \Leftrightarrow \qquad \mathbf{x}_a \rightarrow \mathbf{x}_e . \tag{3.46}$$

If $C(\mathbf{x}_a, \mathbf{x}_e)$ has more than one local maximum the number of mode shapes needs to be increased to refine the spatial resolution.

Eq. (3.46) is the criterion to locate the damage on the test structure. It allows to identify a local event (the damage) from observing global characteristics, in this case the deviations of modal damping, at arbitrary sensor locations.

3.3.5 Summary

A new concept for identifying and localising delamination damages in CFRP is introduced. Processing damage-induced modal damping variations and correlating the experimental data to a mathematical model enables locating damage in a three-dimensional structure using a single structural response sensor. The method involves a novel technique for the extraction of modal damping factors from a measured structural response, a standard approach for the modelling of damping in the numerical model, and a newly developed localisation criterion based on the correlation of experimental and analytical data.

In order to obtain sufficiently accurate modal damping measurements the structural response around each resonance frequency is approximated by a proportionally damped one-degree-of-freedom system. Now, the inverse of the response, eq. (3.35), is expressed as a quadratic polynomial in ω and the damping factors can be computed from the coefficients of a polynomial curve fit.

The associated analytical modal damping factors are derived from a proportional damping approach, eq. (1.29), where a damping matrix is assembled from a linear superposition of mass and stiffness matrices given from the existing numerical model.

Damage localisation is based on a comparison of measured and computed damage-induced modal damping variations utilising a correlation coefficient for modal vector analysis, eq. (3.45). The location of the structural damage is associated with the maximum in the correlation coefficient. An overview of the individual working phases is provided by the flow chart in Figure 3.2.

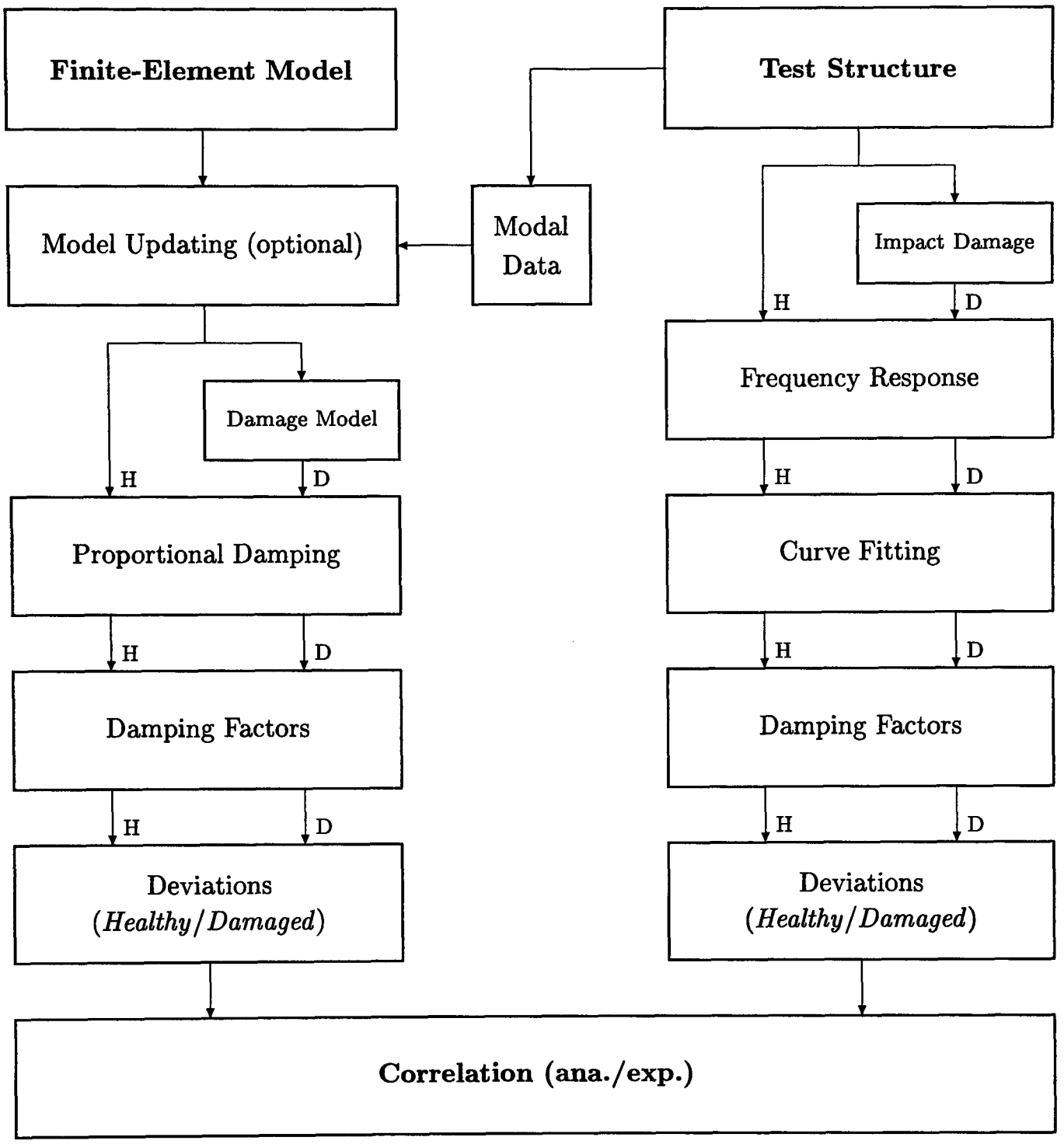

Figure 3.2: Flow Chart of Damage Localisation Procedure

3.4 Optimised Excitation Forces

Ground Vibration or Modal Survey Testing is a commonly applied procedure to investigate the dynamic characteristics of aerospace structures [44]. Typical applications for the experimental data gained from these tests are aeroelastic stability calculations, response analyses, and numerical model corrections [136]. Today, the Phase Resonance Method (PRM) provides a reliable tool for the experimental identification of the dynamic behaviour of elasto-mechanic structures [53]. Especially the method's ability to directly identify normal modes makes Phase Resonance Testing particularly suitable for acquiring the experimental reference data for model updating [136].

The PRM involves a direct measurement of modal parameters and therefore allows for high-quality test results [120]. This, however, is associated with a major disadvantage: Phase resonance testing requires the use of an appropriated excitation force vector to balance the test structure's internal damping forces. The force tuning process results in an extended test duration as compared to other methods [132]. Further problems arise from the restricted accessibility of modern space structures due to their increasing complexity and dimensions [133].

Several systematic approaches for tuning the excitation forces have been suggested in the past, all having individual advantages and specific drawbacks. LEWIS and WRISLEY [93] have assumed the shaker force at a given location to be proportional to the product of local mass and deflection. TRAILL-NASH [161] has performed a superposition of structural responses to fulfil the phase resonance criterion. ASHER [4] has derived an admittance matrix from measured structural responses to compute the unknown excitation force components. ANDERSON [3] has used the inverse of the modal force matrix. HUNT, VOLD, PETERSON, and WILLIAMS [64] and NIEDBAL and KLUSOWSKI [137] have applied different criteria to minimise the real-part response with respect to the total response.

The method proposed here [73, 84] is based entirely on experimental data. It does not require any additional information such as a mass matrix from a

finite-element model or assumptions on the structural damping. The locations and force components, which most appropriately match the phase resonance criterion, are determined in a single step and the corresponding Mode Indicator Function (MIF), eq. (3.54), is predicted. By applying the pre-computed force vector the time-consuming mode tuning process becomes dispensable and the test duration is reduced considerably while an optimum modal data quality is assured.

The following sections provide a brief introduction to the PRM and give a theoretical outline of the force tuning procedure. Applications to a laboratory test structure and to the European Space Agency's (ESA) Polar Platform satellite are described in Sections 5.4.2 and 5.4.3, respectively.

3.4.1 The Phase Resonance Method

Starting from the dynamic equilibrium equations (1.24) introduced in Section 1.2.6

$$\mathbf{M}\,\ddot{\mathbf{u}}(t) + \mathbf{D}\,\dot{\mathbf{u}}(t) + \mathbf{K}\,\mathbf{u}(t) = \mathbf{f}(t) \tag{3.47}$$

the structural response to a forced sinusoidal excitation with all force components in phase such that:

$$\mathbf{f}(t) = \hat{\mathbf{f}}\, e^{i\omega t} \tag{3.48}$$

is given by

$$\mathbf{u}(t) = \hat{\mathbf{u}}\, e^{i\omega t} = \left(\Re(\hat{\mathbf{u}}) + i\,\Im(\hat{\mathbf{u}})\right)\, e^{i\omega t} \tag{3.49}$$

with $\hat{\mathbf{f}}$ as a vector of excitation force components, $\hat{\mathbf{u}}$ as the vector of complex response amplitudes, and $\Re(\hat{\mathbf{u}})$ and $\Im(\hat{\mathbf{u}})$ as the corresponding real and imaginary components. Introducing eqs. (3.48) and (3.49) into the equations of motion the real and imaginary parts of eq. (3.47) become

$$(-\omega^2\mathbf{M} + \mathbf{K})\,\Re(\hat{\mathbf{u}}) - \omega\mathbf{D}\,\Im(\hat{\mathbf{u}}) = \hat{\mathbf{f}}\ , \tag{3.50}$$

$$\omega\,\mathbf{D}\,\Re(\hat{\mathbf{u}}) + (-\omega^2\mathbf{M} + \mathbf{K})\,\Im(\hat{\mathbf{u}}) = \mathbf{0}\ . \tag{3.51}$$

Claiming the real part of the response vector $\Re(\hat{\mathbf{u}})$ to be zero, which constitutes the necessary condition for the excitation of a normal mode, yields

$$-\omega\,\mathbf{D}\,\Im(\hat{\mathbf{u}}) = \hat{\mathbf{f}}\ , \tag{3.52}$$

$$(-\omega^2\mathbf{M}+\mathbf{K})\,\Im(\hat{\mathbf{u}})=\mathbf{0}\;. \tag{3.53}$$

Hence, the real-part response vanishes precisely when the external excitation force is in balance with the internal damping forces of the test article, eq. (3.52), and when the imaginary response and excitation frequency fulfil the eigenproblem of the undamped system, eq. (3.53). In the close vicinity of a resonance the structure behaves like a one-degree-of-freedom system.[2]

From the physical view point the damping forces in eq. (3.47) cause a coupling of all existing eigenvectors. As a result, the structural response for each frequency is given by a superposition of all mode shapes. Compensating the damping forces by means of an excitation force vector according to eq. (3.52) removes the coupling and allows the system to oscillate in a single mode.

Accordingly, the test procedure is to adjust the individual excitation force components to the (unknown) damping forces and to simultaneously tune the excitation frequency until all real parts of the dynamic response are zero. Now, the eigenfrequency and natural mode shape may be recorded.

In order to check the phase resonance criterion $\Re(\hat{\mathbf{u}})=\mathbf{0}$ efficiently the Mode Indicator Function (MIF) proposed in [15] is used, where:

$$\mathrm{MIF}=1-\frac{\sum_{m=1}^{M}|\Re(\hat{\mathbf{u}}_m)||\hat{\mathbf{u}}_m|}{\sum_{m=1}^{M}|\hat{\mathbf{u}}_m|^2}\;. \tag{3.54}$$

When all real-part responses vanish and the test structure vibrates in a normal mode the mode indicator approaches a value of one.[3] The Mode Indicator Function has a highly sensitive response to phase purity and has proven to be a powerful tool in conveniently identifying and isolating the normal modes of a complex structure.

Despite of the time-consuming force tuning process the Phase Resonance Method features several substantial advantages compared to other experimental modal analysis methods:

---

[2] In particular, this requires a proportional damping of the form $\mathbf{D}=\mu\cdot\mathbf{M}+\kappa\cdot\mathbf{K}$, eq. (1.29).

[3] Following a common practice the MIF-values will hereafter be multiplied by a factor of 10^3, i.e. $0\leq\mathrm{MIF}\leq 1{,}000$.

- Mode shapes are measured directly without the need for any off-line post-processing.

- The results are available immediately and are verified while the test is still in progress.

- The method provides a high level of accuracy and the risk of missing a particular mode is small.

Since the selection of exciter configurations and tuning of force vector components constitute a major fraction of the total test duration various systematic techniques, which allow the process to be automated, have been developed in the past. Today, the results of Modal Survey Tests are regularly used for updating of numerical models and the capability to improve the quality of the experimental modal data has become a new substantial aspect of all force tuning procedures. Typical contemporary aerospace structures usually possess a complex dynamic behaviour and a high modal density. As a result, suitable excitation force tuning methods are subject to the following requirements:

- The method must allow for a separation of mode shapes with closely spaced eigenfrequencies (e.g. symmetric/anti-symmetric wing bending modes of an aircraft). This involves a deliberate excitation of the chosen mode shape and simultaneously a suppression of the adjacent mode or modes.

- The excitation force vectors are incomplete, i.e. the number of force components is much smaller than the number of structural degrees of freedom.

- Due to potential restrictions regarding the application of excitation forces and the limited accessibility of structural components the force components are prescribed by the user.

- An acquisition of all modal parameters in a given frequency range must be possible.

- Minor deviations from the theoretical assumptions inherent in the Phase Resonance Method (e.g. non-linearities or an inhomogeneous damping distribution) must be tolerated.

3.4.2 Computation of Optimised Excitation Forces

The excitation force vector for each individual mode shape needs to be adjusted according to eq. (3.52). As a result of the damping being continuously distributed over the structure only an approximate solution for a discrete force vector matching the phase resonance criterion may be found. However, experience gained during numerous modal identification tests of different structures of varying nature and complexity has shown[4] that in practical use a few appropriately placed exciters are sufficient. Still, the individual force amplitude components have to be tuned to the point where a good mode isolation is attained.

The first step in a Ground Vibration Test employing the Phase Resonance Method usually is to obtain response data from several sine-sweep runs at different exciter locations. The mode isolation process is then started based on the measured Mode Indicator Function values. The proposed method performs a superposition of structural responses from the different sweep runs so that a minimisation of the real-part response with respect to the total response is achieved. For each resonance r, i.e. each maximum of the MIF, the real and imaginary response vector components $\Re(\hat{\mathbf{u}}^c)_r$ and $\Im(\hat{\mathbf{u}}^c)_r$ for the exciter configuration c and the associated force vector $\hat{\mathbf{f}}_r^c$ are recorded. The different response vectors are written as matrices

$$\Re(\hat{\mathbf{U}})_r = [\, \Re(\hat{\mathbf{u}})_r^1, \ldots, \Re(\hat{\mathbf{u}})_r^c, \ldots, \Re(\hat{\mathbf{u}})_r^C \,] \tag{3.55}$$

and

$$\Im(\hat{\mathbf{U}})_r = [\, \Im(\hat{\mathbf{u}})_r^1, \ldots, \Im(\hat{\mathbf{u}})_r^c, \ldots, \Im(\hat{\mathbf{u}})_r^C \,] \,. \tag{3.56}$$

For each mode a force vector must be found so that the real-part response is

[4] According to DLR's Ground Vibration Test Facility operation personnel.

minimised with respect to the total response:

$$\min \frac{\left(\Re(\hat{\mathbf{U}})_r^{\mathrm{T}} \cdot \Re(\hat{\mathbf{U}})_r\right) \cdot \boldsymbol{\phi}_r}{\left(\Re(\hat{\mathbf{U}})_r^{\mathrm{T}} \cdot \Re(\hat{\mathbf{U}})_r + \Im(\hat{\mathbf{U}})_r^{\mathrm{T}} \cdot \Im(\hat{\mathbf{U}})_r\right) \cdot \boldsymbol{\phi}_r} = \lambda_r \ . \tag{3.57}$$

$\boldsymbol{\phi}_r$ and λ_r are the eigenvector and eigenvalue of the corresponding eigenvalue problem [64] which for non-trivial solutions is given by

$$\left(-\lambda_r \left(\Re(\hat{\mathbf{U}})_r^{\mathrm{T}} \cdot \Re(\hat{\mathbf{U}})_r + \Im(\hat{\mathbf{U}})_r^{\mathrm{T}} \cdot \Im(\hat{\mathbf{U}})_r\right) + \Re(\hat{\mathbf{U}})_r^{\mathrm{T}} \cdot \Re(\hat{\mathbf{U}})_r\right) \boldsymbol{\phi}_r = \mathbf{0} \ . \tag{3.58}$$

The eigenvector related to the smallest eigenvalue yields the optimised excitation force vector

$$\hat{\mathbf{f}}_{r,opt} = [\ \hat{\mathbf{f}}_r^1, \ \ldots \ \hat{\mathbf{f}}_r^c, \ \ldots \ \hat{\mathbf{f}}_r^C\ ] \cdot \boldsymbol{\phi}_r \ . \tag{3.59}$$

From the associated structural responses[5]

$$\Re(\hat{\mathbf{u}})_{r,opt} = \Re(\hat{\mathbf{U}})_r \cdot \boldsymbol{\phi}_r \tag{3.60}$$

and

$$\Im(\hat{\mathbf{u}})_{r,opt} = \Im(\hat{\mathbf{U}})_r \cdot \boldsymbol{\phi}_r \tag{3.61}$$

a theoretical prediction to the MIF, eq. (3.54), to be achieved in the subsequent identification process using the optimised multi-point excitation is computed.

The method may be accordingly applied to a subset of the C exciter configurations to compute the optimised force vectors and corresponding MIFs for any possible combination of exciter configurations from the given set of locations. Thus, the best combination and minimum number of exciters is determined and the definition of fixed exciter locations prior to the tuning process is no longer necessary.

3.4.3 Summary

In this section a novel approach for the computation of optimised multi-point excitation force vectors in Phase Resonance Testing is proposed. Structural response run data, which are readily available from preliminary sine-sweep runs

[5]Strictly speaking, the superposition of structural responses in eqs. (3.60) and (3.61) requires the structure to behave linearly and all responses $\Re(\hat{\mathbf{u}})_r^c$ and $\Im(\hat{\mathbf{u}})_r^c$ to have exactly the same frequencies.

on the test structure, are processed and a superposition of structural responses is performed in order to minimise the real-part response with respect to the total response, eq. (3.57). In the equivalent eigenvalue problem, eq. (3.58), the eigenvector corresponding to the smallest eigenvalue yields the optimised force vector components, eq. (3.59). A Mode Indicator Function, eq. (3.54), is predicted from the associated structural responses, providing a measure to pre-evaluate the specific exciter configuration. The method allows to find the most suitable combination and minimum number of excitation points from a given set of possible configurations. The general force tuning procedure is shown in Figure 3.3.

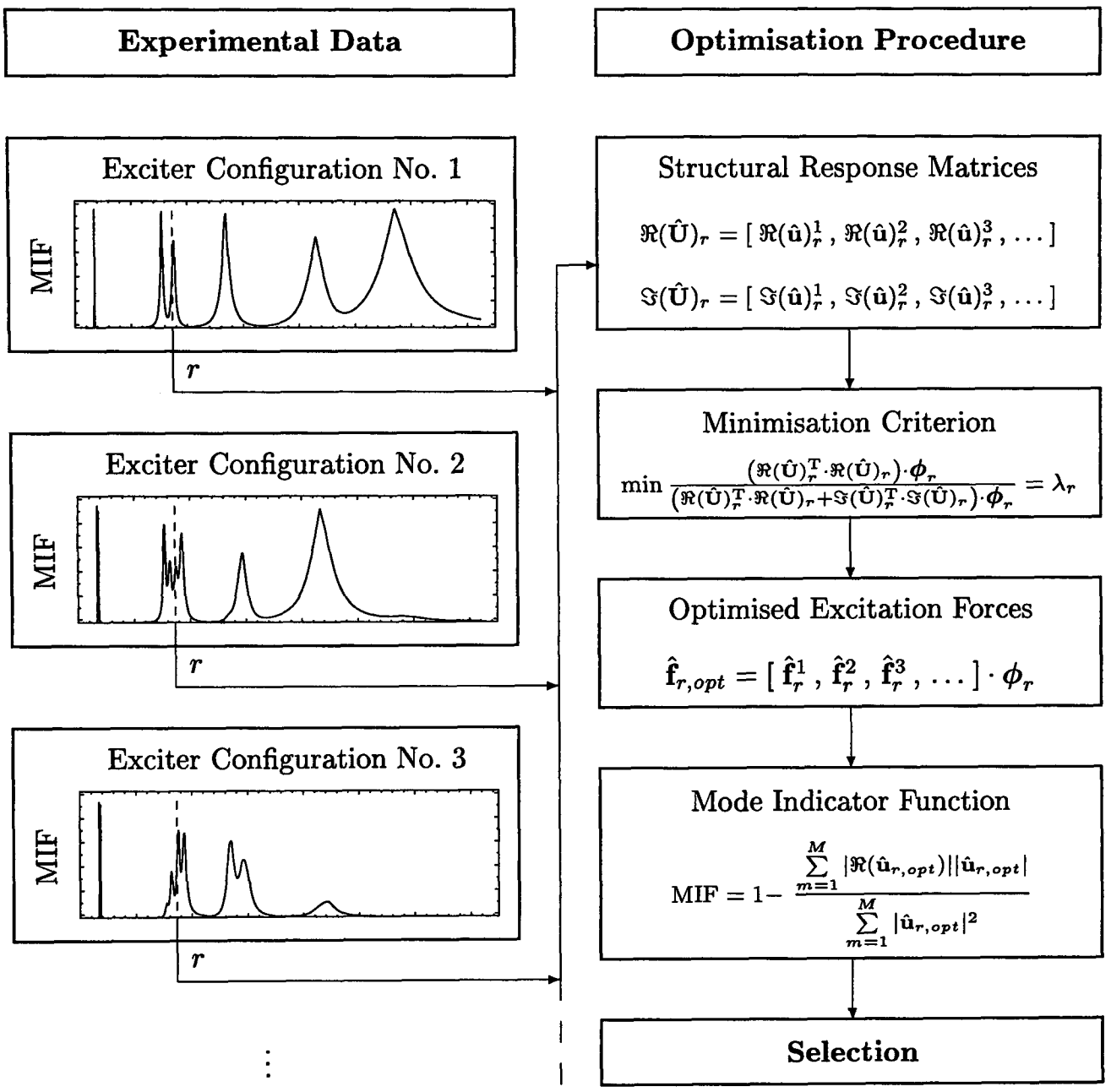

Figure 3.3: Force Optimisation Algorithm

3.5 Closure

In the foregoing sections the basic theoretical environment for the test cases to be discussed in the successive chapters has been introduced.

The iterative updating procedure for numerical structural models is based on a least squares approximation to measured modal data. Parameterised submatrices, representing the erroneous model regions, allow for a selective correction of existing modelling errors in the original system matrices. The method has been introduced by NATKE [126] and LINK [106, 99] and existing computer codes [101, 102, 100] are utilised.

Next, a new approach for the localisation of delamination damages in CFRP has been proposed. The experimental identification of damage-induced modal damping variations and a correlation of the measured data to an analytical model are the novel features which enable the localisation of a single concentrated structural damage in a three-dimensional structure using data from a single response sensor. Techniques for the accurate determination of modal damping factors from the measured structural response and the localisation of the structural damage based on a correlation of experimental and analytical damping variations have been developed.

Finally, a novel method to determine optimised multi-point excitation force vectors for Phase Resonance Testing has been introduced. As opposed to earlier approaches, no supplementary analytical data, estimations on the structural damping, or iterative algorithms are involved. Structural responses from preliminary sine-sweep runs on the test structure are processed and the real-part response components are minimised with respect to the total responses in a linear superposition. The associated eigenvalue problem now yields the optimised excitation force components. The corresponding structural response is used to assess the achievable phase purity and to select the most suitable combination and minimum number of excitation points.

Chapter 4

Accuracy of Model Updating Methods

4.1 Introduction

The test cases to be discussed in this chapter permit the validation of the model correction method developed in Section 3.2 and allow the introduction of novel techniques associated with their application to structural dynamic systems.

In Section 4.2 the GARTEUR SM-AG19 structural model is chosen to relate the model updating method to a practical application. A novel iterative procedure for the selection of correction parameters is presented and the effects of different parameter sets on both the results of model validation and the newly introduced numerical prediction of modal data, i.e. the comparison of analytical and experimental eigenfrequencies and mode shapes which were not used in the preceding updating process, are investigated. Additionally, a technique for updating substructures with viscous material properties is suggested. The results illustrate the importance of parameter selection when a physically consistent updated model is sought.

Next, the problem of experimental errors is addressed in a numerical study. An analytical model of a laboratory test structure is utilised and a simulation procedure is developed to evaluate the accuracy of the model corrections un-

der the influence of experimental errors in Section 4.3. The study shows that the resulting correction parameter uncertainties grow progressively with the magnitude of the experimental errors. However, the uncertainties may be partially reduced by increasing the number of mode shapes used in the updating process.

4.2 Prediction of Modal Data

The first complex real world case study is intended to give an overview of application-related aspects of the model updating method described in Section 3.2 and to highlight the importance of parameter selection to create a physically consistent updated model. For clarity and a sound physical understanding a simple laboratory test structure is selected. For further orientation some selected problems associated with the application of iterative model correction methods are discussed in [77].

The GARTEUR SM-AG19 structural model is chosen as a test structure for the following investigations. A finite-element model is generated and experimental modal and frequency response data are made available from a structural dynamic identification test performed on the structural model. The problem of finding suitable updating parameters for the model corrections is discussed in detail and two sets of updating parameters for the GARTEUR SM-AG19 finite-element model are investigated. To assess the updating method's capability to create a consistent analytical model, i.e. a model that is able to predict modal and frequency response data which were not used in the preceding validation process, the updating process is restricted to a fraction of the mode shapes and corresponding natural frequencies in the experimental data base. Following the initial model validation phase the updated model is utilised to predict the remaining eigenvectors and eigenfrequencies which were not considered in the model corrections. Finally, Frequency Response Functions (FRF) for a given loading condition are computed from the updated analytical model and the results are compared to the measured response data.

The work described here was DLR's contribution [78] to an updating benchmark study which had been defined by the COST[1] F3 Working Group on Finite-Element Model Updating Methods.

[1] European Cooperative on Science and Technology

4.2.1 Test Structure

The test structure, Figure 4.1, is assembled from six aluminium beams with different rectangular cross sections. The structure is intended to represent a simplified aircraft with its main components fuselage (1), wings (2), and tail (3). Specifications are listed in Table 4.1. The total mass is 44 kg and the overall dimensions are 1.5 m (length) by 2.0 m (wing span). The distance between the fuselage front and the wing leading edge is 0.55 m. Realistic damping levels are obtained through the use of a visco-elastic self-adhesive tape (8) of 50 μm thickness and 76 mm width which is bonded to the upper wing surface over a length of 1.7 m and aligned along the trailing edge. To achieve sufficient levels of shear deformation within the visco-elastic layer the tape's upper surface is covered by an aluminium plate of 1.1 mm thickness and 76.2 mm width. The structure is equipped with 24 acceleration sensors and a low frequency bungee cord suspension ensures correct so-called 'free-free' boundary conditions during Ground Vibration Testing.

4.2.2 Finite-Element Model

The computer code MATFEM [102] is used for the finite-element analysis. A numerical model with 104 beam elements, Figure 4.2, is generated. The beam elements have two nodes with 6 degrees of freedom (DoF) each and are based on Timoshenko beam theory [157, 158]. The main structural components, i.e. fuselage, wing, and tail, are linked by rigid body elements. Special care was taken to accurately model the stiffening effects caused by the joints between fuselage and wing as well as tail and tailplane, respectively (cf. Section 4.2.4.2). For the damping layer stiffness and mass distribution initial estimations based on the manufacturer's specifications are used. Due to the high modal deflection amplitudes and low mass in some structural regions, e.g. at the wing tips, a detailed mass matrix, taking into account all connecting bolts and the acceleration sensor masses, is assembled. In order to correctly reflect the test boundary conditions the measured rigid body modes (RBM), Table 4.2, are used to tune the model's elastic suspension. The actual sensor positions, e.g.

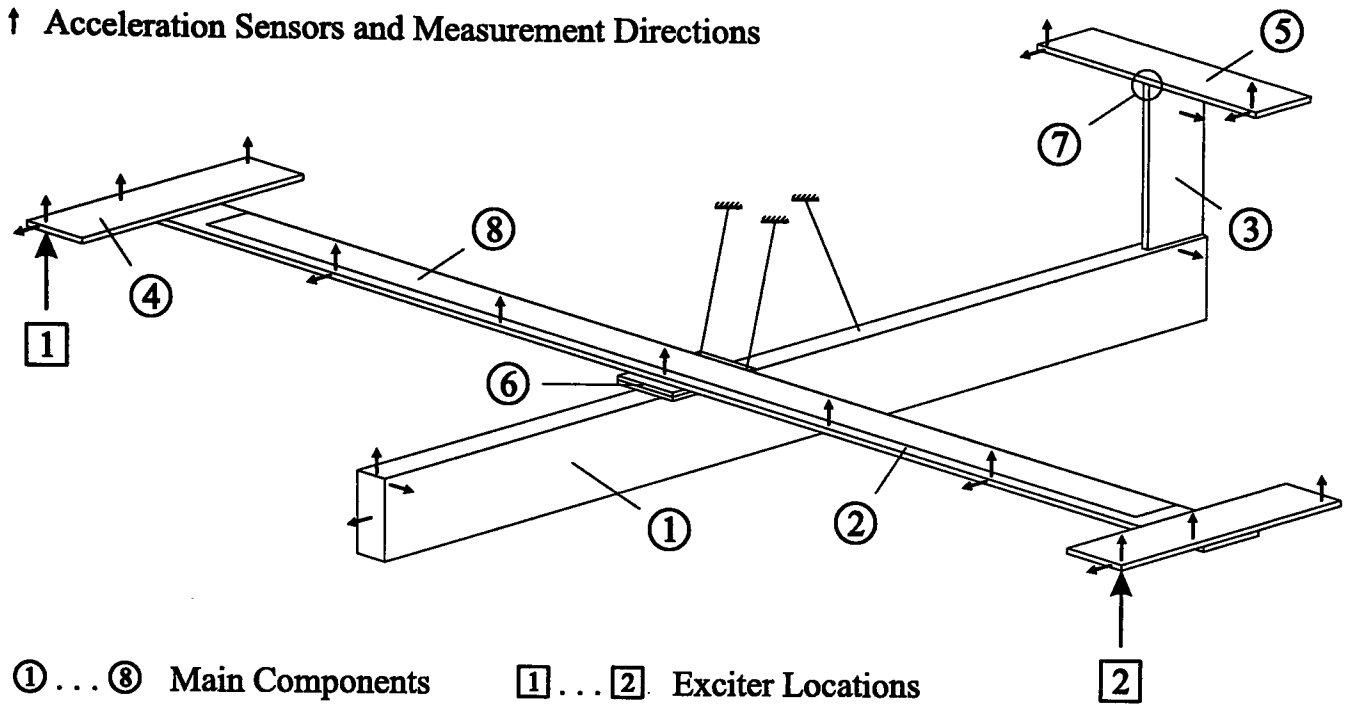

Figure 4.1: The GARTEUR SM-AG19 Structure

General Specifications:		
Density		2.70×10^3 kg/m^3
Young's Modulus		7.20×10^{10} N/m^2
Lumped Masses:		
Fuselage Suspension		0.250 kg
Fuselage-Wing-Joint (6)		1.573 kg
Tail-Tailplane-Joint (7)		0.400 kg
Shaker @ Right Wing		0.200 kg
Shaker @ Left Wing		0.200 kg
Beam Dimensions:		
Cross Section:	Fuselage (1)	0.05×0.15 m^2
	all others	0.10×0.01 m^2
Length:	Fuselage (1)	1.50 m
	Wings (2)	2.00 m
	Tail (3)	0.30 m
	Drums (4) & Tailplane (5)	0.40 m

Table 4.1: Specifications of the GARTEUR SM-AG19 Test Structure

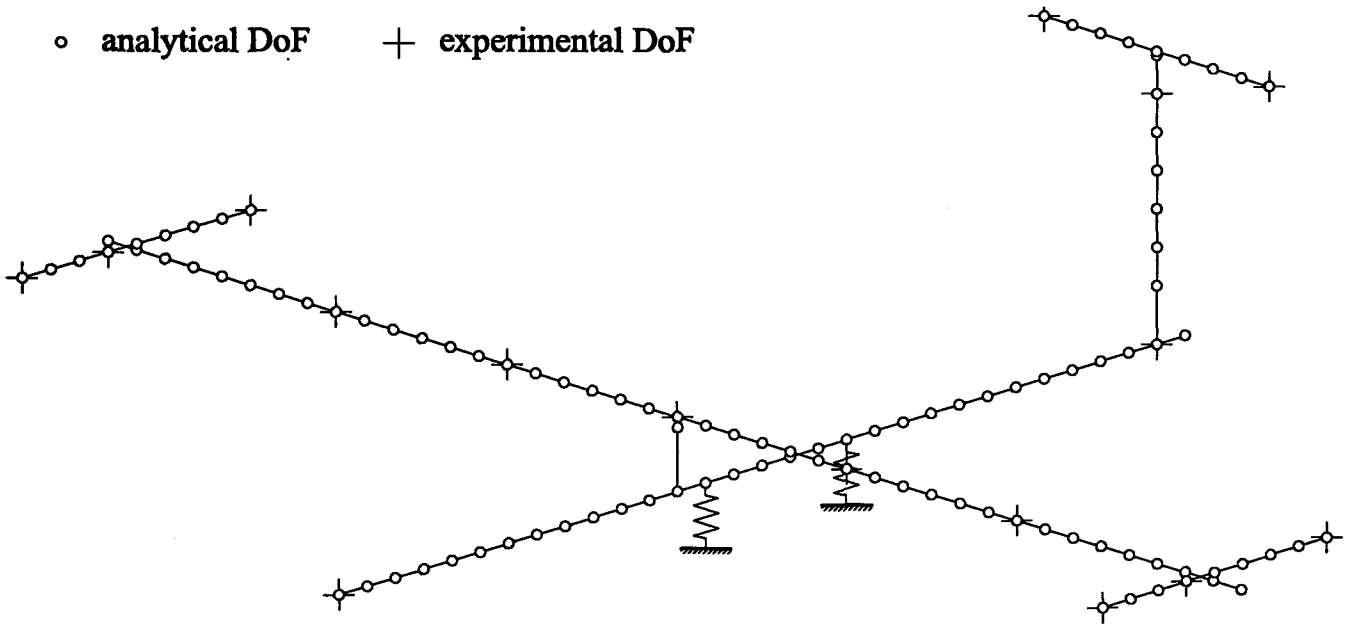

Figure 4.2: GARTEUR SM-AG19 Finite-Element Model

Mode No.	Mode Shape	Frequency	MIF
RBM 1	Roll	0.52 Hz	966
RBM 2	Pitch	0.62 Hz	934
RBM 3	Heave	1.84 Hz	965

Table 4.2: GARTEUR SM-AG19 Rigid Body Modes

at the wing leading and trailing edges, are realised through supplementary offset nodes.

4.2.3 Experimental and Analytical Modal Data

The experimental data base available for model validation and comparison contains 14 normal modes with eigenfrequencies between 6.38 Hz and 151.32 Hz. Additionally, 24 Frequency Response Functions (FRFs) for two different excitation points at the right and left wing tip (represented by symbols [1] and [2] in Figure 4.1), respectively, were recorded in a frequency range from 4 Hz to 65 Hz. All experiments were carried out by DEGENER [36] using DLR's Ground Vibration Test Facility (cf. Section 2.4).

In this study only modes numbered 1 to 9 are used to validate the initial finite-element model. They will hereafter be called the active modes. The remaining passive modes numbered 10 to 14 and the FRFs constitute a reference

for comparison to the corresponding predictions to be made with the validated numerical model.

To provide an overview of the structure's dynamic characteristics the analytical eigenvectors for modes numbered 1 to 14 are plotted in Figure 4.3. In Table 4.3 the analytical eigenfrequencies $f_{a,n}$ for the initial finite-element model, the measured natural frequencies $f_{e,n}$, the frequency deviations

$$\Delta f_n = \frac{f_{a,n} - f_{e,n}}{f_{e,n}} \qquad \text{for } n = 1\,,\,\ldots\,,\,N \quad , \tag{4.1}$$

and the degree of correlation between computed eigenvectors $\varphi_{a,r}$ and measured mode shapes $\varphi_{e,s}$ based on the Modal Assurance Criterion (**MAC**) suggested by ALLEMANG and BROWN [1]

$$\mathbf{MAC}_{rs} = \frac{|\varphi_{a,r}^{\mathrm{T}} \cdot \varphi_{e,s}|^2}{(\varphi_{a,r}^{\mathrm{T}} \cdot \varphi_{a,r})(\varphi_{e,s}^{\mathrm{T}} \cdot \varphi_{e,s})} \qquad \text{for } r, s = 1\,,\,\ldots\,,\,N \tag{4.2}$$

are summarised. The highest frequency deviations are found in the first symmetric wing torsion ($\Delta f_4 = -2.60$ %) and the second anti-symmetric wing bending ($\Delta f_9 = +2.91$ %). With the exception of the two wing torsion modes the mode correlation yields **MAC**-values[2] higher than 90 %.

4.2.4 Parameter Selection

The selection of correction parameters is a fundamental step for successfully updating a finite-element model. To obtain an improved numerical model of the structure under investigation the submatrices $\mathbf{K}_i$ and $\mathbf{M}_j$ in eqs. (3.1) should coincide as closely as possible with the existing modelling errors. This allows to build a physically consistent updated numerical model that enables

- to introduce structural changes and obtain reliable results without the need for repeating both the modal identification test and updating procedure, or
- to predict modal data beyond the frequency range covered during structural identification which is not considered in the updating process.

[2] **MAC**-values are usually specified in percent.

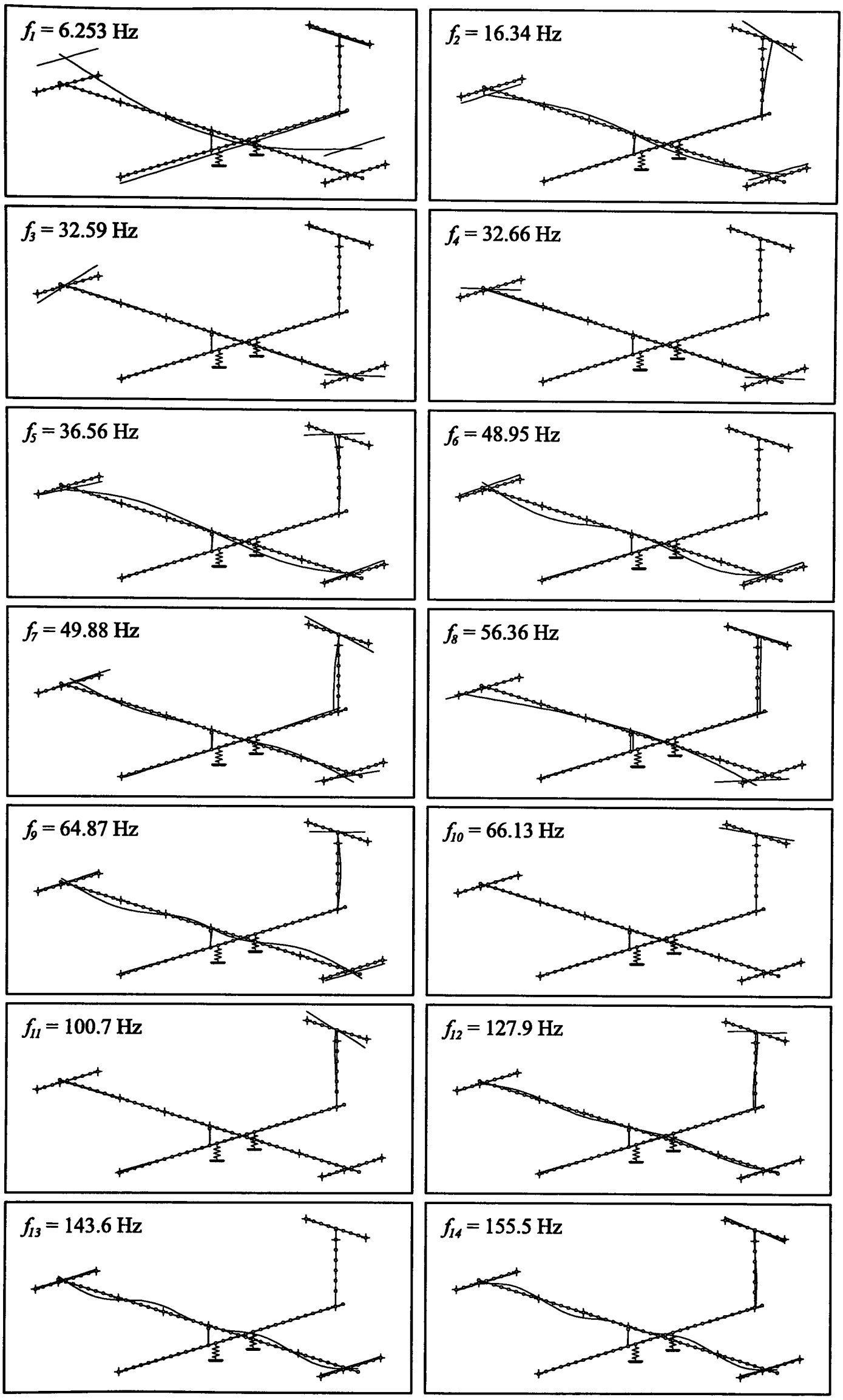

Figure 4.3: Analytical Modal Data of the GARTEUR SM-AG19 Structure

Table 4.3: GARTEUR SM-AG19 Modal Data

Mode No.	Mode Shape	$f_{a,n}$/[Hz]	$f_{e,n}$/[Hz]	Δf_n/[%]	$\mathbf{MAC}_{rs}$/[%]$^{+)}$
1	1st Symmetric Wing Bending	6.253	6.376	−1.93	99.96
2	Fuselage Rotation	16.34	16.10	+1.47	97.46
3	1st Anti-Symmetric Wing Torsion	32.59	33.13	−1.63	76.40
4	1st Symmetric Wing Torsion	32.66	33.53	−2.60	83.20
5	1st Anti-Symmetric Wing Bending	36.56	35.65	+2.57	93.25
6	2nd Symmetric Wing Bending	48.95	48.38	+1.17	99.51
7	1st Anti-Symmetric In-Plane Bending	49.88	49.43	+0.89	97.60
8	1st Symmetric In-Plane Bending	56.36	55.08	+2.33	99.38
9	2nd Anti-Symmetric Wing Bending	64.87	63.04	+2.91	96.20
10	Tail Torsion	66.13	66.50	−0.56	99.93
11	Lateral Fuselage Bending	100.7	102.9	−2.11	99.81
12	2nd Tail Bending	127.9	130.5	−2.01	98.83
13	3rd Symmetric Wing Bending	143.6	141.4	+1.56	97.44
14	3rd Anti-Symmetric Wing Bending	155.5	151.3	+2.79	94.59

$^{+)}$ $r = s = 1, \ldots, N$

Otherwise, the numerical model would solely be improved with respect to it's ability to reproduce the experimental data, but the computed correction factors would not necessarily contain any physical meaning.

On the other hand, the analytical eigenvectors and eigenfrequencies should be sufficiently sensitive to the correction parameters. If the numerical data is insensitive to a chosen parameter the updating algorithm does preferably use the more sensitive parameters which allow to minimise the residual with smaller changes of the correction factors, cf. eq. (3.4). As a result, the updated value of the insensitive parameter may become highly uncertain.

Finally, since the experimental modal data in most cases contains a limited amount of information the number of parameters should be kept as small as possible in order to retain an over-determined system, eq. (3.11), and to avoid problems of ill-conditioning.[3]

Numerous systematic modelling error localisation methods have been published over the years. FISSETTE and IBRAHIM [48] have used a force balance method to identify inaccurately modelled regions within the analytical model's system matrices, SHEPARD and MILANI [154] have suggested a frequency-based procedure based on a Rayleigh quotient. TO, LIN, and EWINS [160] have recommended an eigendynamic constraint method which is using the structural eigenvalue problem, eq. (3.14), and the orthogonality of the eigenvectors with respect to the mass matrix to locate modelling errors. LIEVEN and EWINS [95] have created pseudo-flexibility and pseudo-intertance matrices with correlating analytical and measured modes and have used the Singular Value Decomposition (SVD) approach to produce incomplete pseudo-inverse stiffness and mass matrices. The mass and stiffness errors are located from the difference between the experimental and analytical pseudo-inverses. LALLEMENT and PIRANDA [89] have proposed a best subspace method that searches for the linear combinations of columns in the gradient matrix $\mathbf{G}$ which establish the best representation of the measured data $\mathbf{z}_e$. This allows for a selection of those sub-

[3]Ill-conditioning or a rank deficiency also occur when one or more updating parameters can be expressed as a linear combination of the other parameters. Problems of ill-conditioning related to model updating from vibration measurements were addressed in detail in [118].

structures which are most likely to represent the dominant modelling errors. LINK and SANTIAGO [104] have suggested the use of energy functions based on the substructures $\mathbf{K}_i$ and $\mathbf{M}_j$ in eqs. (3.1). Further methods for reducing the number of updating parameters are described in [90], [97], and [127]. An extensive review of various error localisation and regularisation techniques for model updating has been given by NATKE [125].

4.2.4.1 General Procedure

The systematic localisation methods for finite-element modelling errors yield useful results for simple structures and in the absence of systematic and discretisation errors and measurement noise. The limited spatial and frequency resolution of the experimental data, however, establishes principal restrictions to the perceptible size and localisation accuracy of any modelling error.

Methods which use the experimental mode shapes usually require the number and locations of the measured degrees of freedom to be identical to the degrees of freedom in the analytical model. Since this is rarely the case in practical applications[4] the experimental mode shapes need to be expanded to the size of the full analytical eigenvectors which is likely to cause additional uncertainties introduced by the expansion methods used.

Numerical studies [120] have shown that even with faults of considerable size and magnitude the results produced by systematic modelling error localisation methods are of limited reliability and should be considered with great care. Therefore, owing to the importance of parameter selection in the model updating method, a novel iterative procedure [74] based on both physical knowledge and mathematical constraints is suggested here and will be applied to all updating case studies in Chapters 4 and 5. The new method combines mathematical and physical requirements to find a set of correction parameters which establish a well-conditioned optimisation problem ensuring good convergence and trustworthy updating results and leading to an updated analytical model of improved physical significance.

[4]Especially the rotational degrees of freedom, being difficult to measure, are commonly not considered in a vibration test.

As a first step, information on uncertain or erroneous substructures is derived from the simplifying assumptions made during the finite-element modelling phase. Generally, all material parameters and geometric properties should be reviewed and doubtful quantities be identified. Apparent candidates for updating parameters are adhesive, bolted, welded, or clamped joints. Being the structural link between individual components these elements have a significant influence on the overall dynamic behaviour of the entire structure. Due to limitations as to the total number of degrees of freedom in the finite-element model these components usually are not modelled in full detail. As a substitute, experience-based assessments are made on a reduced effective stiffness in the joint region. For applications with moderate accuracy requirements this methodology is more than adequate, but when a high-precision model is needed the estimated stiffness should be parameterised to allow for correction. The same applies to the boundary conditions where in most cases the actual finite stiffness of a rigid or free suspension is not known exactly.

After defining all prospective updating parameters from a physical point of view, their influence on the model's modal properties is evaluated by means of the L_2-norm of the individual columns in the gradient matrix $\mathbf{G}$, eqs. (3.13) and (3.22),

$$S_{\lambda,k} = \left| \begin{array}{c} \frac{\partial \lambda_{a,1}}{\partial p_k} \\ \frac{\partial \lambda_{a,2}}{\partial p_k} \\ \vdots \\ \frac{\partial \lambda_{a,N}}{\partial p_k} \end{array} \right| \quad \text{and} \quad S_{\varphi,k} = \left| \begin{array}{c} \frac{\partial \boldsymbol{\varphi}_{a,1}}{\partial p_k} \\ \frac{\partial \boldsymbol{\varphi}_{a,2}}{\partial p_k} \\ \vdots \\ \frac{\partial \boldsymbol{\varphi}_{a,N}}{\partial p_k} \end{array} \right| . \tag{4.3}$$

For simplicity and because the absolute values are of no practical importance both the eigenvalue sensitivities $S_{\lambda,k}$ and eigenvector sensitivities $S_{\varphi,k}$ are commonly scaled such that their largest values are equal to one. In the second step, parameters with high eigenvalue and/or eigenvector sensitivities should be preferred for further consideration. If a parameter's sensitivity is insufficient[5] it should either be omitted or redefined. The latter was demonstrated by MOTTERSHEAD, FRISWELL, and BRANDON [121], who have shown that

[5]Experience has shown that parameters with sensitivities below 0.1 should not be used.

by appropriately modifying an updating parameter it's sensitivity can often be increased without losing the parameter's physical significance.

Finally, in the third step the set of potential updating parameters is checked for convergence and the ability to produce accurate results. Test runs are performed using an erroneous numerical model with simulated structural errors and 'experimental' mode shapes and natural frequencies which are generated from the analytical modal data, Figure 4.4. For the 'experimental' mode shapes only those eigenvector components are taken into account which correspond to sensor locations on the test structure. The modes used for the simulation are identical to the modes available in the experimental data base. Then, artificial modelling errors are introduced into the system matrices to generate an inaccurate numerical model. The modelling errors exactly equal the updating parameters, that is the substructures and properties to be modified which have been defined so far. Assuming these conditions are given and that the updating problem is well-posed, the correction algorithm should completely eliminate the artificial modelling inaccuracies during the test run. As a result, the correction factors must converge to the inverse of the mass/stiffness reduction previously introduced through the modelling errors. If a parameter does not approach the exact correction factor value or convergence problems arise the selection of parameters should be modified. Alternate methods for examining the information content of the selected substructures were proposed by ZURMÜHL [172] and LAWSON and HANSON [91].

4.2.4.2 Parameter Selection for the GARTEUR Test Structure

The fundamental uncertainties in the finite-element model are assumed to be located in (cf. Figure 4.1) the fuselage-wing joint (6), the tail-tailplane joint (7), and in the viscous damping layer (8). Additionally, non-symmetric deflections were observed with some mode shapes during Ground Vibration Testing which indicate a geometric asymmetry in the test structure. Additional information on possible modelling errors can be derived from the mode shapes with high deviations between analytical and experimental eigenfrequencies, Table 4.3

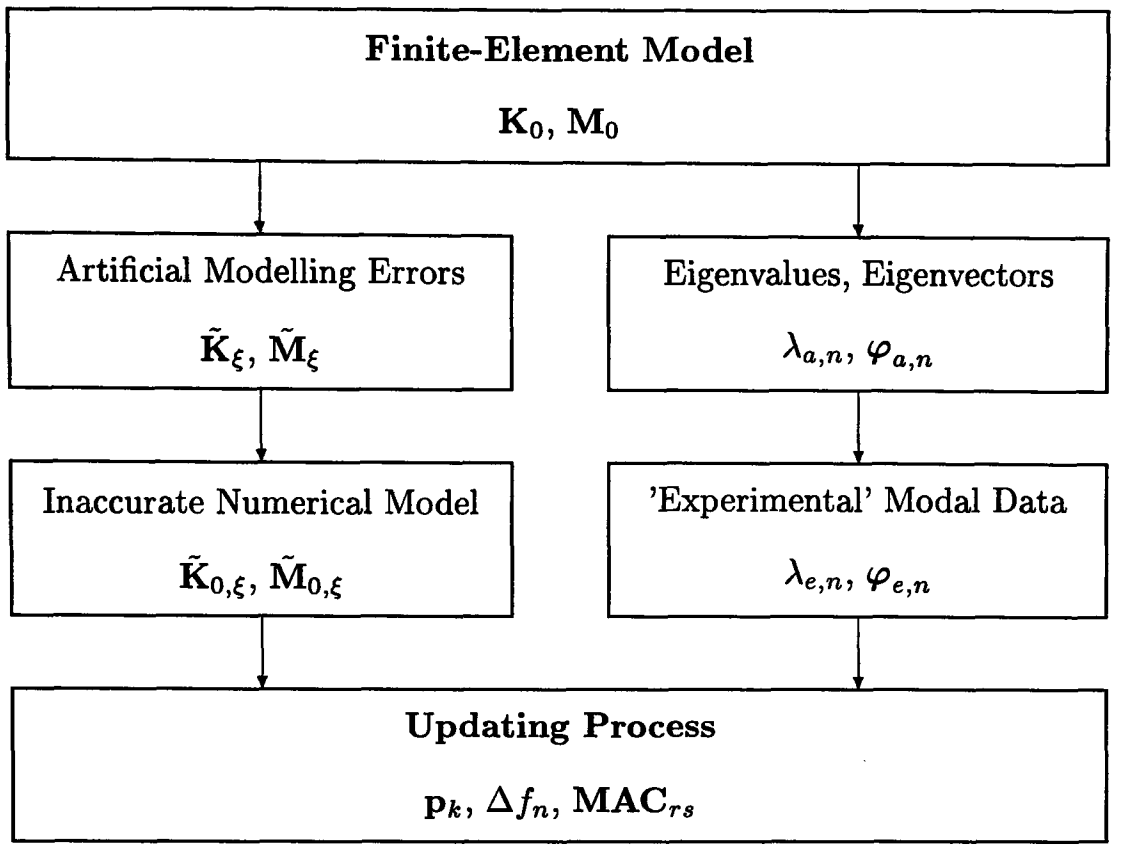

Figure 4.4: Test Procedure for Updating Parameters

and Figure 4.3. Stiffness modelling errors are usually located in areas of high strain whereas mass modelling errors are found in regions of large deflections.

Fuselage-Wing Joint & Tail-Tailplane Joint. Preliminary parameter studies revealed that changes in the joint stiffnesses (components number 6 and number 7 in Figure 4.1) do not have a significant influence on the model's modal parameters in the frequency range under consideration. The local joint stiffnesses are found to be several orders of magnitude higher than the adjacent distributed stiffness of the fuselage, wing, and tail structure, respectively.[6] The global vibration modes and frequencies, however, are dominated by the considerably lower distributed bending and torsion stiffness. Therefore, the model's dynamic characteristics do not respond to a variation of the joint stiffness. As a result, a representation through rigid body elements in the numerical model appears to be sufficiently accurate and a parameterisation is not necessary.

[6] An initially suspected compliance in the joints on the test structure which would have affected the numerical modelling was not confirmed.

Damping Layer Stiffness & Mass. The damping layer viscosity results in a frequency-dependent shear modulus which increases from approximately 240 N/m^2 at 6 Hz to 1200 N/m^2 at 150 Hz. Accordingly, the wing bending stiffness is a function of frequency as well. Since the finite-element code used for this study can not handle frequency-dependent material properties the frequency-dependence is substituted by variation with location.

This is based on the fact that the additional damping layer stiffness solely becomes effective when the wings are subjected to a bending deflection. This occurs for only a small number of discrete frequencies, those corresponding to the six wing bending modes.[7] All other frequencies are not regarded in the updating process. An individual stiffness correction for each bending mode is achieved by splitting the wing bending stiffness parameter I_{min} into multiple separate sections, which correspond to the regions of highest strains in the wing bending modes (numbered 1, 2, 5, 6, 9, 13 and 14; cf. Figures 4.3 and 4.5). The resulting correction parameters, Figure 4.6, as they are sufficiently uncoupled, enable an individual stiffness correction for each bending mode and allow to approximately model and update the frequency-dependent stiffening effect induced by the visco-elastic damping layer.

Non-Symmetric Deflections. The asymmetric deflection amplitudes observed during Ground Vibration Testing (most obvious for the two wing torsion modes at $f_{e,3} = 33.13$ Hz and $f_{e,4} = 33.53$ Hz) are considered through independent correction parameters for the right and left wing sides.

Final Parameter Selection. Two different sets of correction parameters, Table 4.4, are defined in order to investigate their effects on both the validation and prediction results. Parameter set number 1 is intended to provide the most accurate validated model with respect to the active frequency range, i.e. the model that gives the best correlation to the measured modal data. This set is assembled using the procedure described in Section 4.2.4.1. Set number 2 incorporates only those correction parameters which are supposed

[7]The influence on the two in-plane bending modes was found to be negligible.

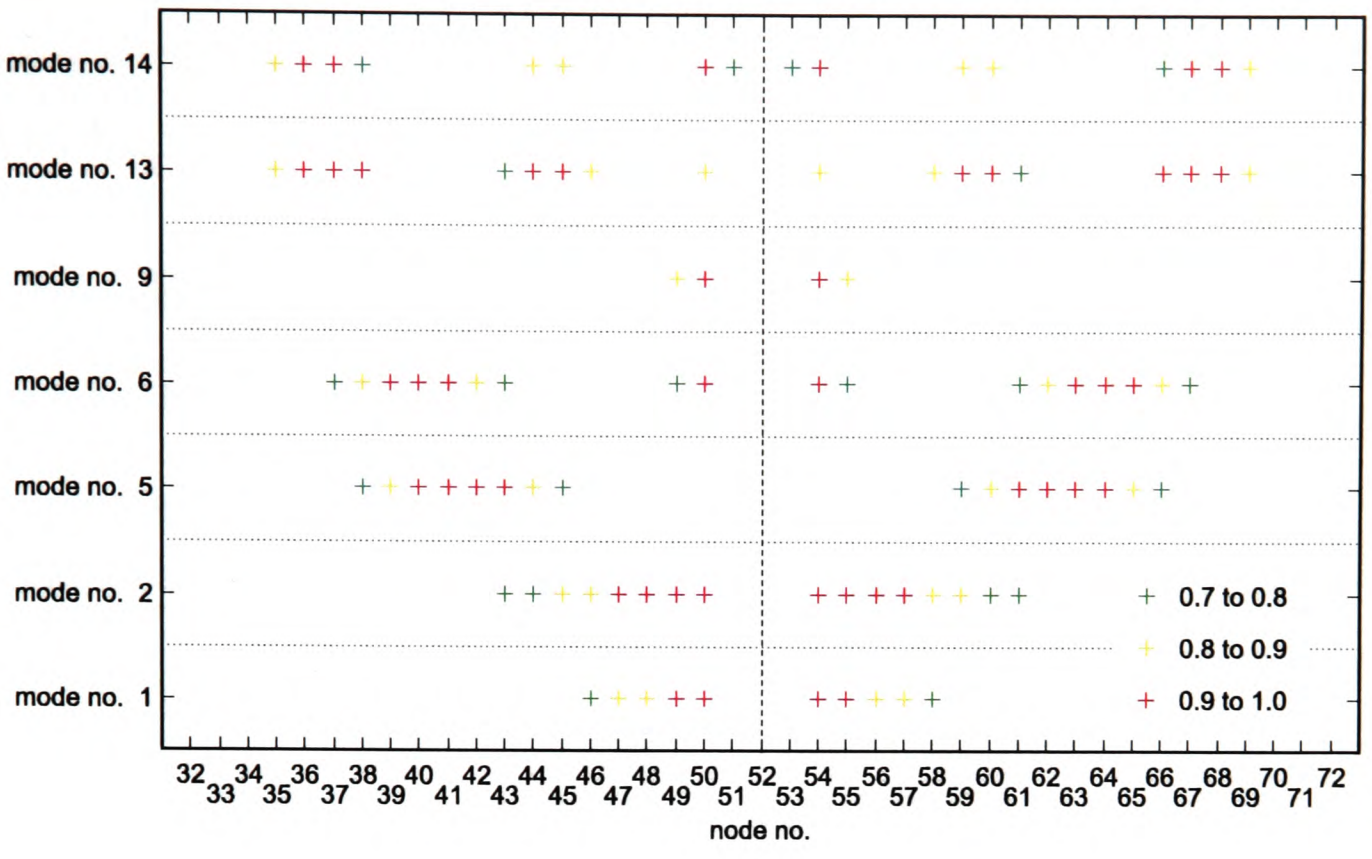

Figure 4.5: Normalised Span-Wise Strains for Wing Bending Modes

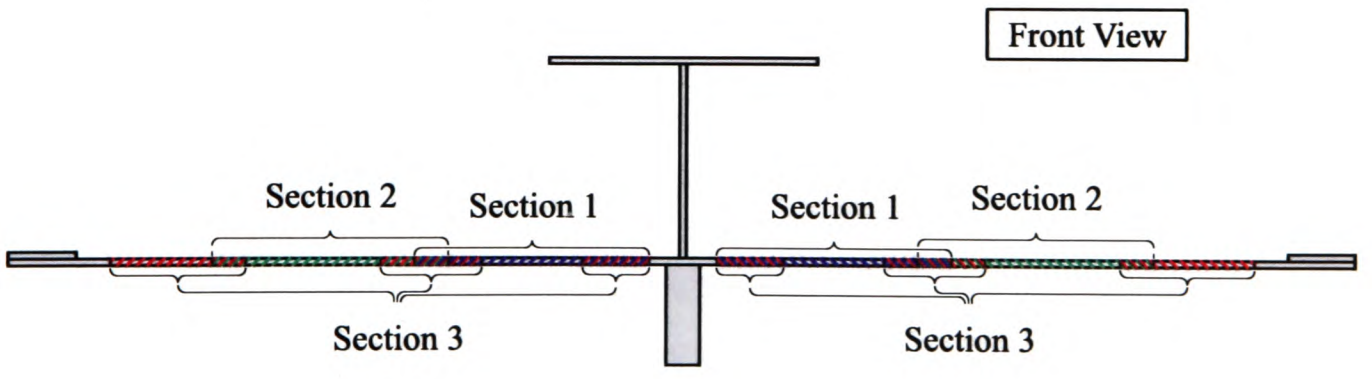

Figure 4.6: Piecewise Correction of Wing Bending Stiffness

to be consistent with the actual modelling uncertainties. This parameter set is primarily designed to provide a physically significant analytical model which is essential for a reliable prediction of the passive modal data and frequency response. For both sets the parameter sensitivities according to eqs. (4.3) are plotted in Figures 4.7 and 4.8.

4.2.5 Results

4.2.5.1 Model Validation

The updating results for both parameter sets are listed in Table 4.4. Using set number 1 the correction factors converge[8] after 2 (Shaker Masses) to 22 (Right Wing, Sections 3, Figure 4.6) iteration steps, Figure 4.9. With set number 2 a stable solution is achieved within only 1 to 4 iterations, Figure 4.10. However, some transient oscillation occurs (Wings (I_{min}), Right Wing (m), Left Wing (m)), which needs approximately 12 to 14 iterations to decay.

In Figures 4.11 to 4.14 the deviations between measured and computed eigenfrequencies, eq. (4.1), and mode correlation, eq. (4.2), are plotted as a function of iteration step. Faster convergence as compared to the correction factors occurs which is due to the fact that the parameter sensitivities vary as the correction proceeds. The residual frequency deviations lie below ± 0.25 % for parameter set number 1 and below ± 1.5 % for parameter set number 2. Regarding the final **MAC**-values both parameter sets give almost similar results.

Using the updating parameters from set number 1 some inconsistencies with respect to the correction factors are found:

- Due to the frequency-dependent stiffening effect of the damping layer the wing bending stiffness parameters number 4 and number 5 (Right Wing, Sections 3 and Left Wing, Sections 3) which correspond to the high-strain areas for the higher bending modes are expected to yield larger correction factors than parameter number 3 (Wings, Sections 2) for the lower bending modes.

[8] Convergence is assumed to be reached when $\alpha_\kappa - \alpha_{\kappa-1} \leq 10^{-3}$.

Table 4.4: Updating Parameter Sets for the GARTEUR SM-AG19 Structure

Set No. 1				Set No. 2			
No.	**Location**	**Parameter**	$\mathbf{p}_k/[\%]^{*)}$	**No.**	**Location**	**Parameter**	$\mathbf{p}_k/[\%]^{**)}$
1	Wings	I_{max}	−3.29	1	Wings	I_{max}	−3.45
2	Wings, Sections 1	I_{min}	+4.30				
3	Wings, Sections 2	I_{min}	+12.2				
4	Right Wing, Sections 3	I_{min}	−7.53				
5	Left Wing, Sections 3	I_{min}	−7.54				
				2	Wings	I_{min}	+1.82
6	Right Wing	I_{tor}	+3.15	3	Right Wing	I_{tor}	+3.61
7	Left Wing	I_{tor}	+3.18	4	Left Wing	I_{tor}	+2.81
8	Tail & Tailplane	$I_{tor} \propto m$	+9.21				
				5	Tail	I_{min}	−5.41
9	Fuselage	m	−2.76				
10	Right Wing	m	+6.70	6	Right Wing	m	+2.65
11	Left Wing	m	+8.72	7	Left Wing	m	+3.25
12	Shaker @ Right Wing	m	−2.74				
13	Shaker @ Left Wing	m	+1.85				
				8	Tail	m	−0.15
*) after 32 iterations				**) after 16 iterations			

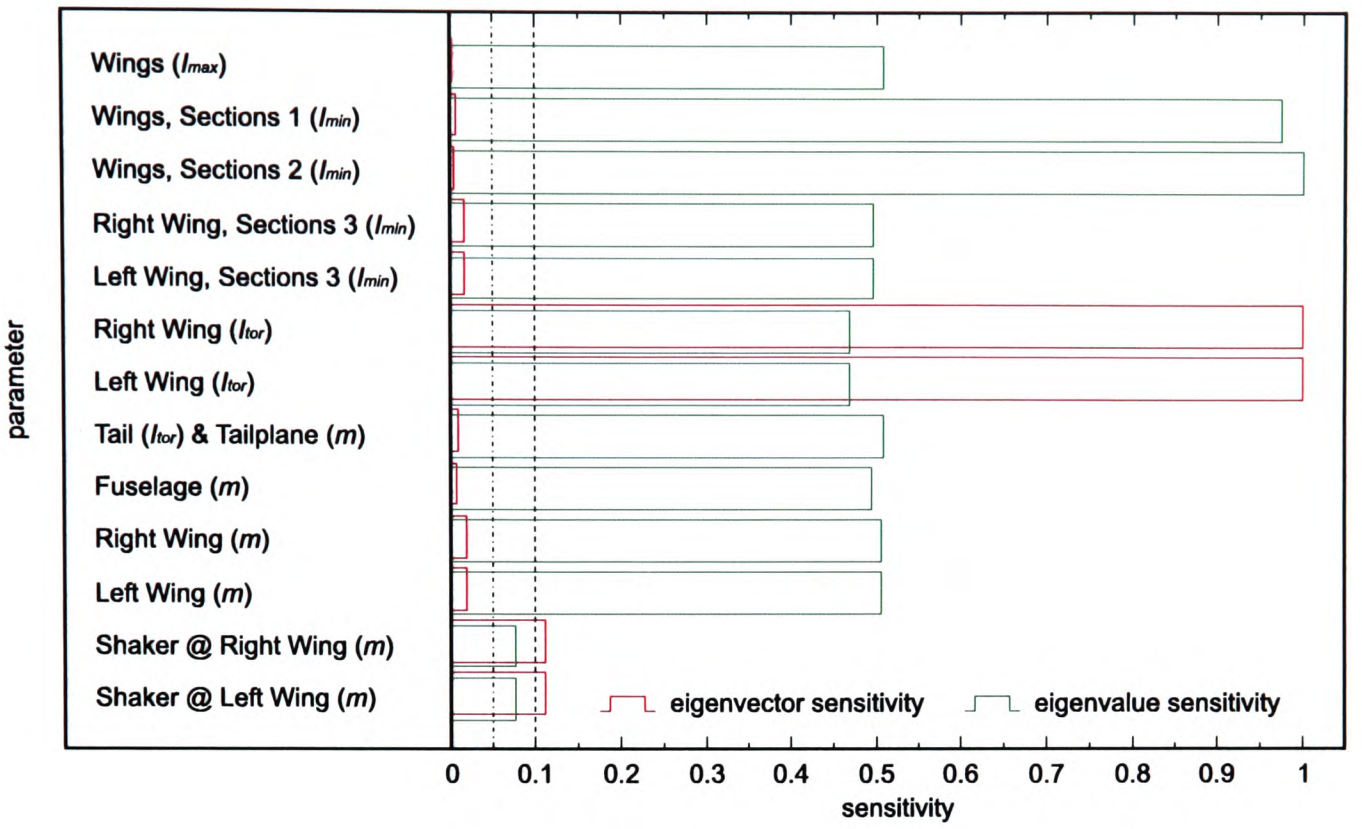

Figure 4.7: Parameter Sensitivities for Parameter Set Number 1

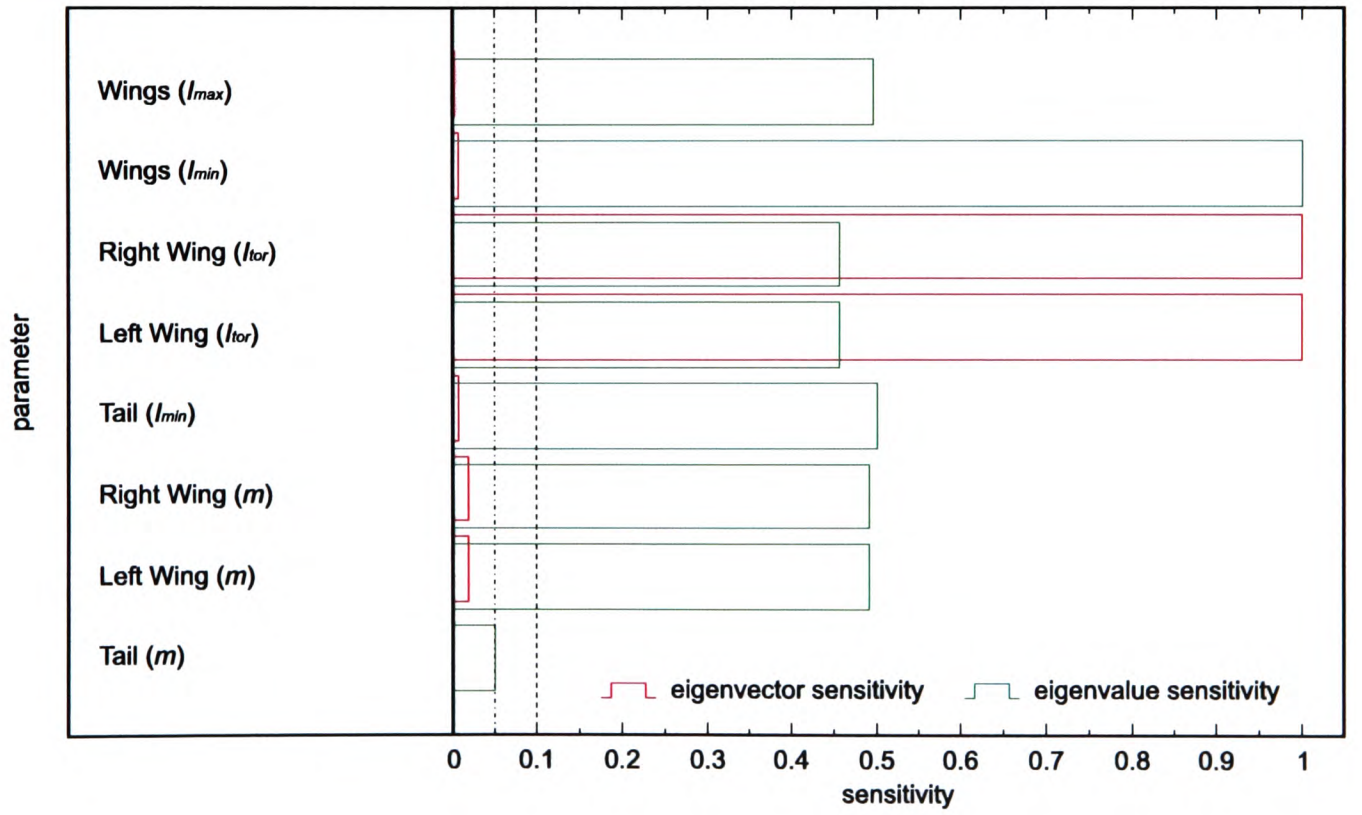

Figure 4.8: Parameter Sensitivities for Parameter Set Number 2

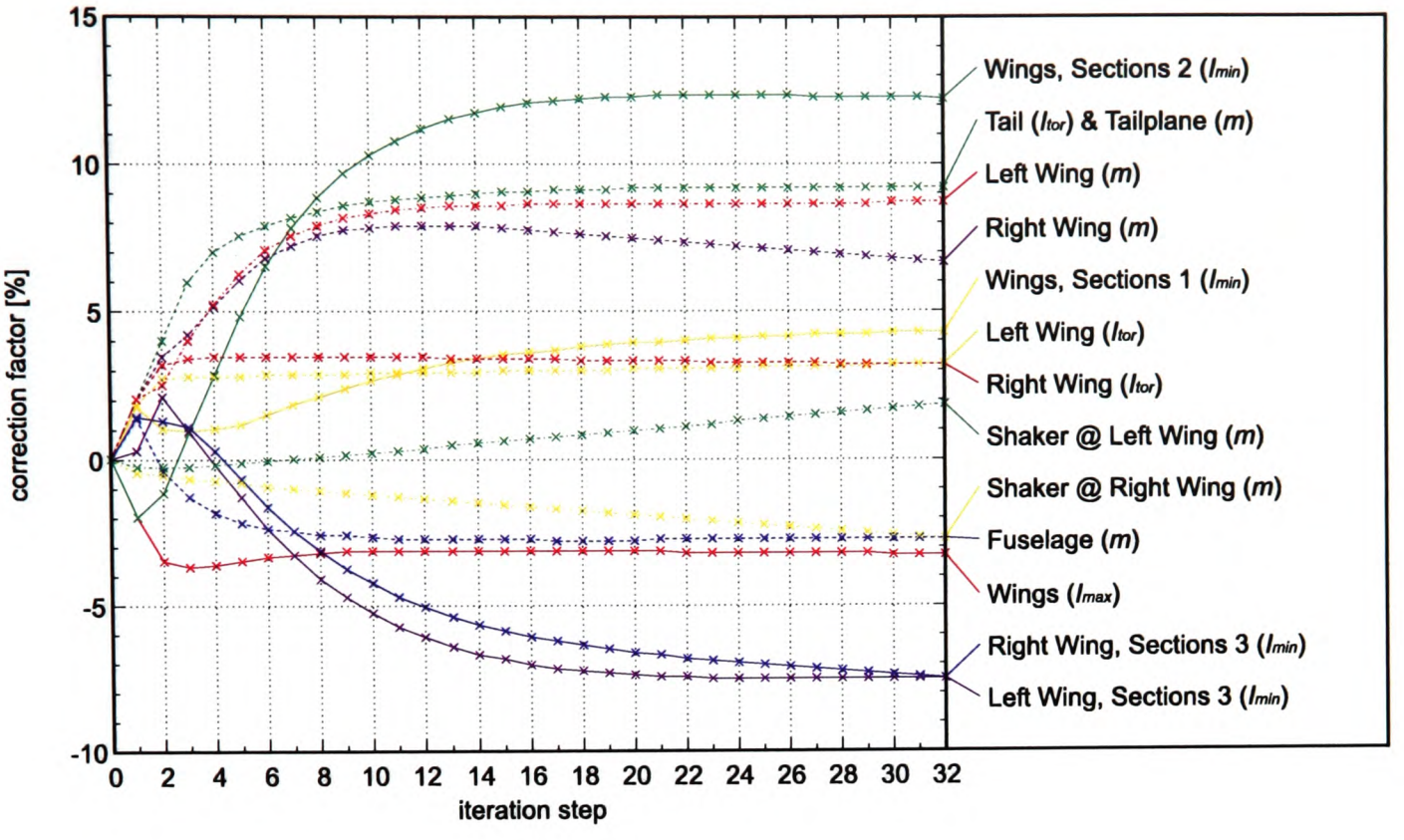

Figure 4.9: Convergence of Correction Factors for Parameter Set Number 1

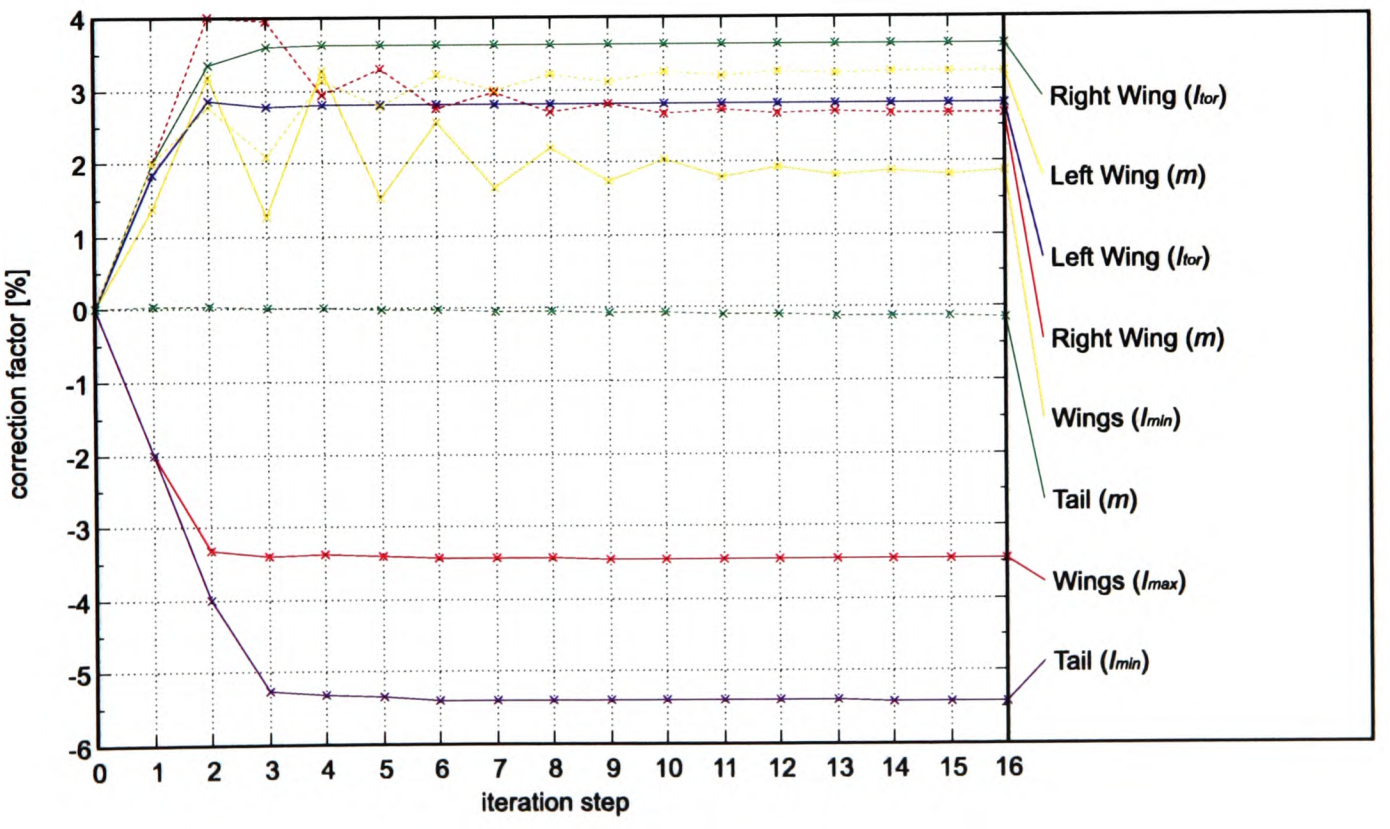

Figure 4.10: Convergence of Correction Factors for Parameter Set Number 2

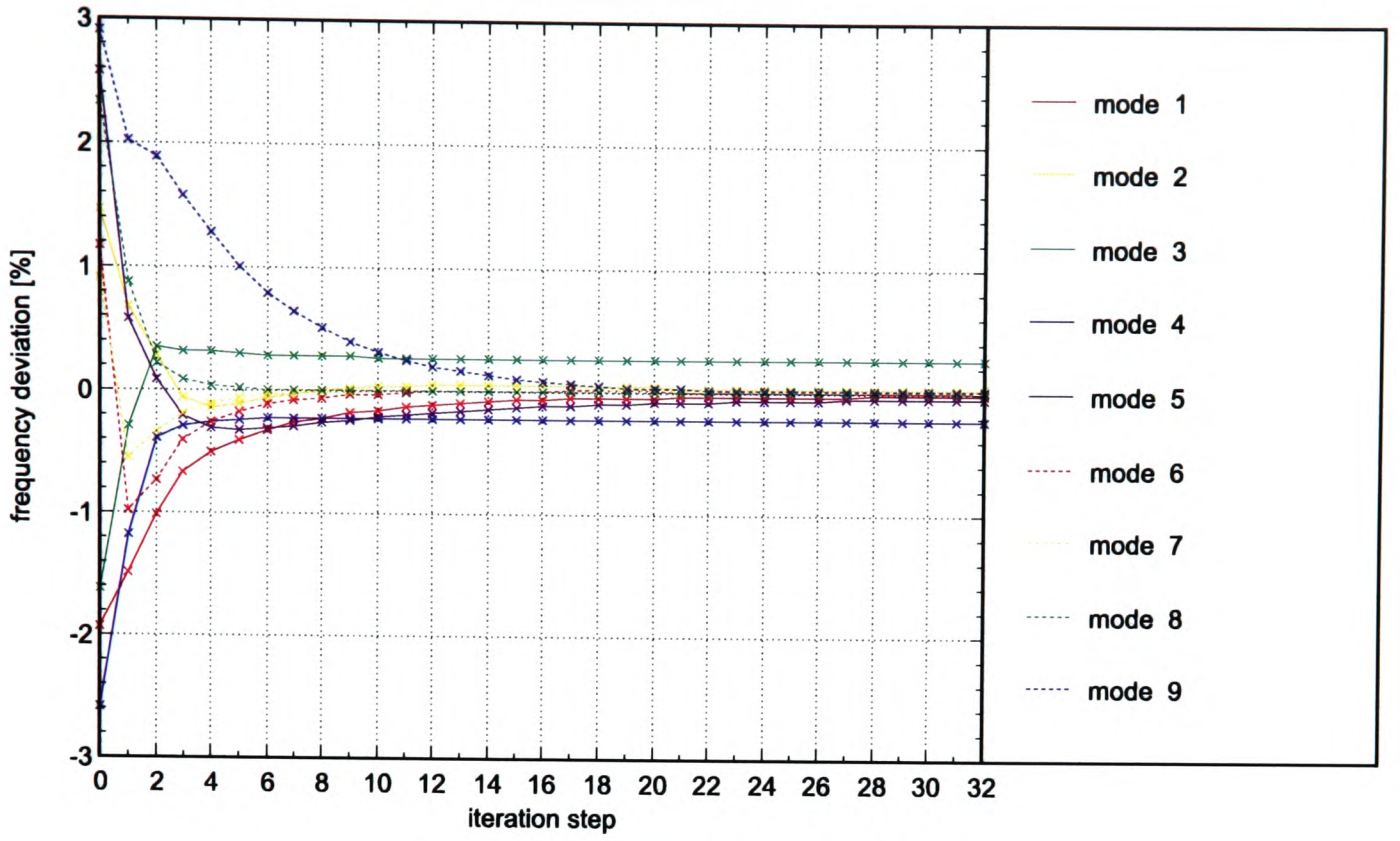

Figure 4.11: Convergence of Frequency Deviations for Parameter Set Number 1

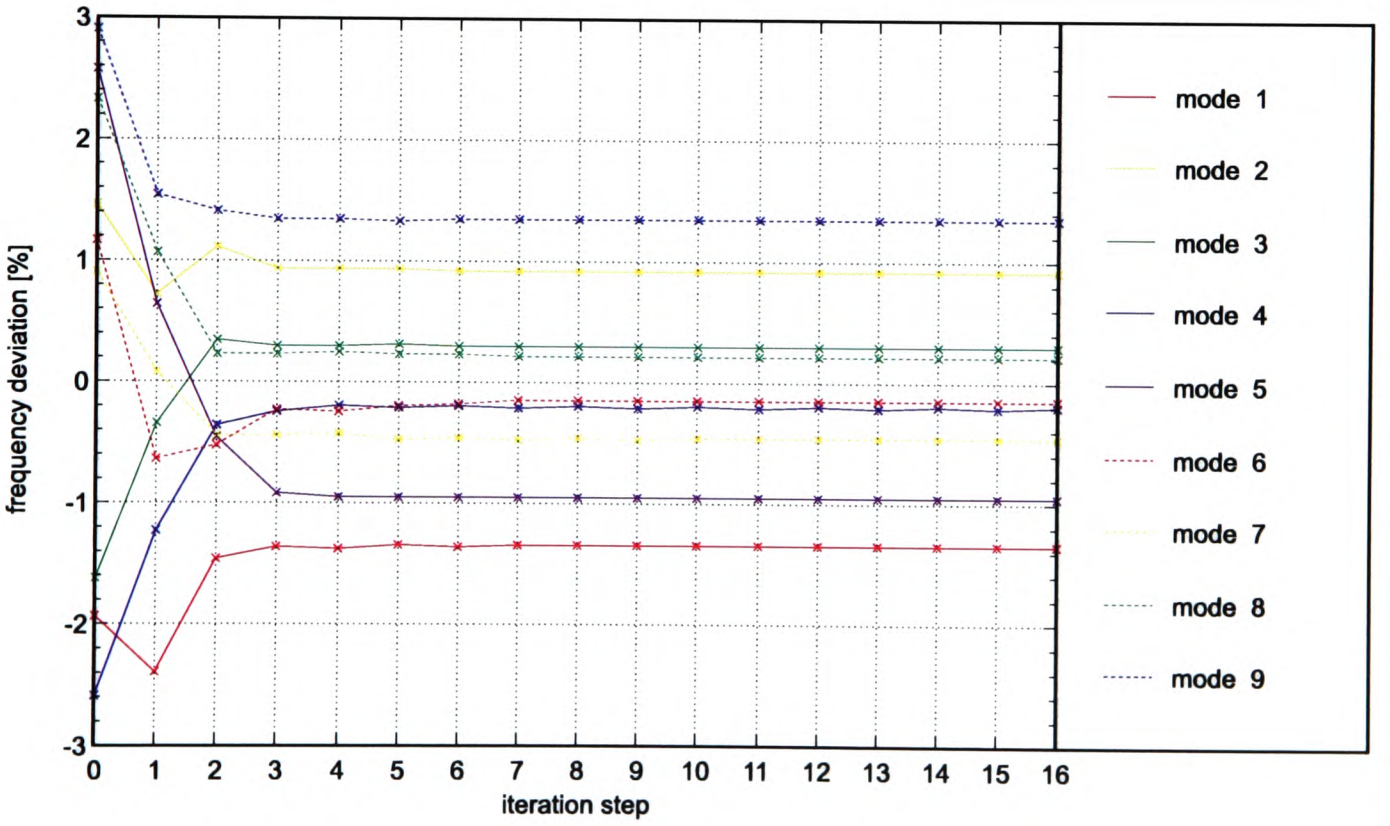

Figure 4.12: Convergence of Frequency Deviations for Parameter Set Number 2

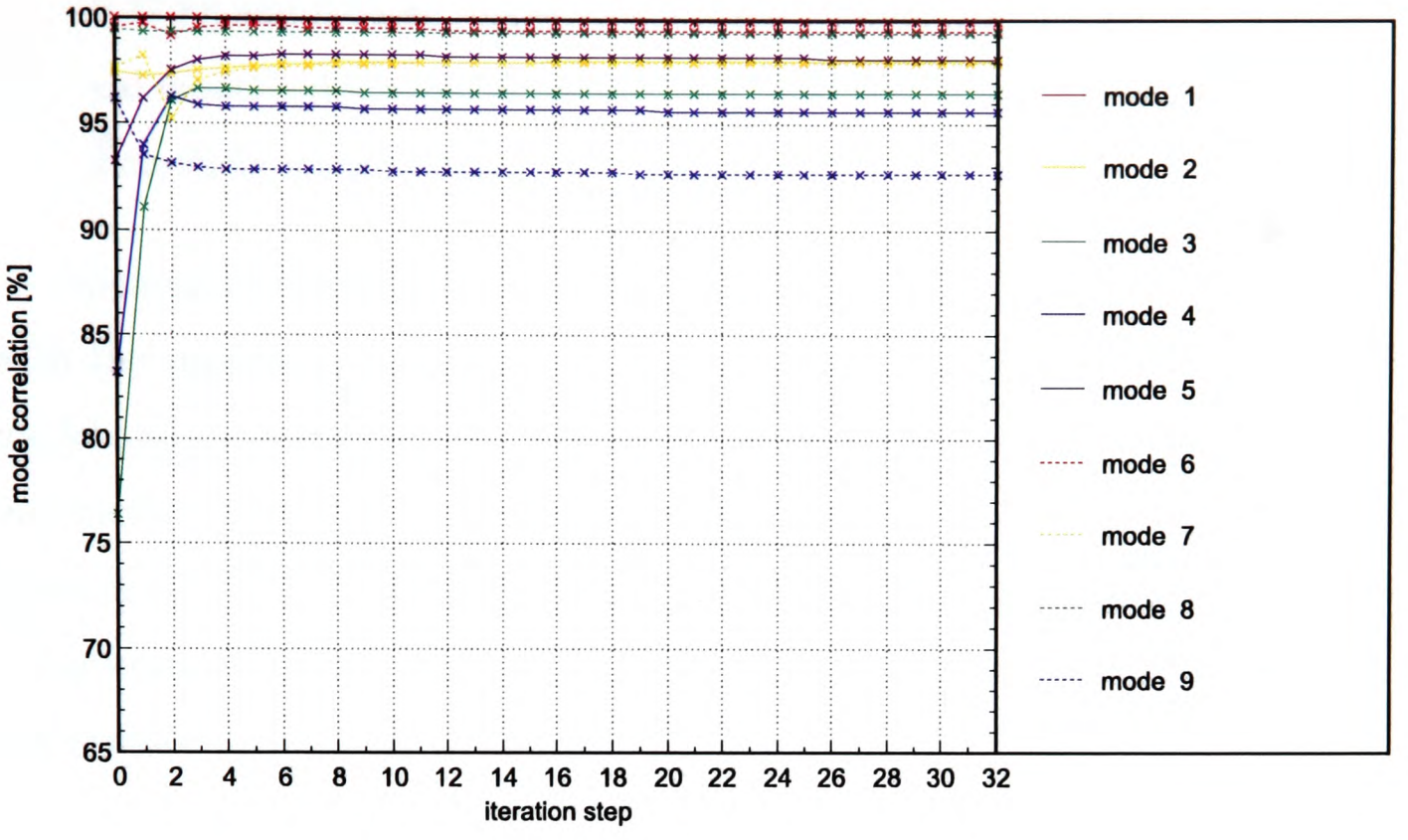

Figure 4.13: Convergence of **MAC**-Values for Parameter Set Number 1

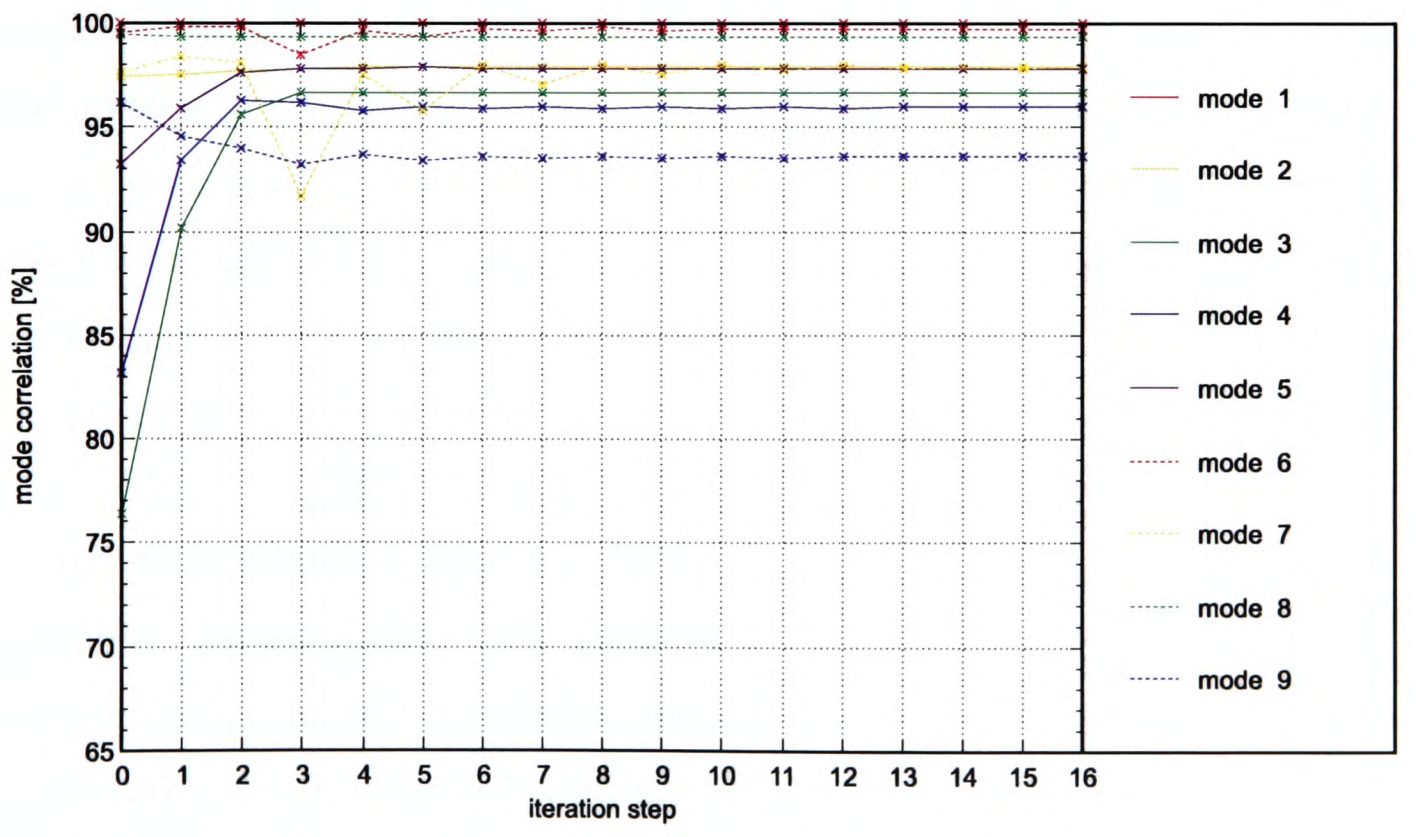

Figure 4.14: Convergence of **MAC**-Values for Parameter Set Number 2

- The mass correction factors for parameters number 10 and number 11 (Right Wing and Left Wing) are equivalent to additional masses of 0.37 kg and 0.48 kg, respectively. They considerably exceed the analytical model's estimated accuracy limits and therefore must be regarded as extremely questionable.

Apparently, the substructures in set number 1 are not sufficiently consistent with the regions where actual discrepancies exist between the finite-element model and the test structure. The updating procedure, however, uses all given parameters, regardless of their physical justification, to minimise the residual given in eq. (3.2). As a result, a high-quality solution regarding the frequency deviations and mode correlations may be obtained but the validated model is not necessarily coherent to the physical structure.

4.2.5.2 Modal Data Prediction

Following the model validation process eigenfrequencies and mode shapes beyond the frequency range used for the model corrections are computed from the updated finite-element model. Again, the model's predictive capabilities are assessed in terms of frequency deviations, Figures 4.15 and 4.16, and mode correlation, Figures 4.17 and 4.18, for both the active and passive modes and with respect to the experimental reference data.

For parameter set number 1 a very good correction in the active frequency range ($\Delta f_n < \pm 0.25$ %) is achieved, but for the passive modes numbered 10 to 14 the frequency deviations generally increase as compared to the initial finite-element model. This supports the assumption previously stated in Section 4.2.5.1 that the corrections introduced by the selected updating parameters are not fully consistent with the modelling errors. The results are fairly similar to those found with direct updating methods which exactly reproduce the test data but fail to predict higher eigenfrequencies and mode shapes.

Because of the smaller number of correction parameters parameter set number 2 yields less accurate corrections for the active modes ($\Delta f_n < \pm 1.5$ %). The results for the passive mode shapes, however, appear more reasonable.

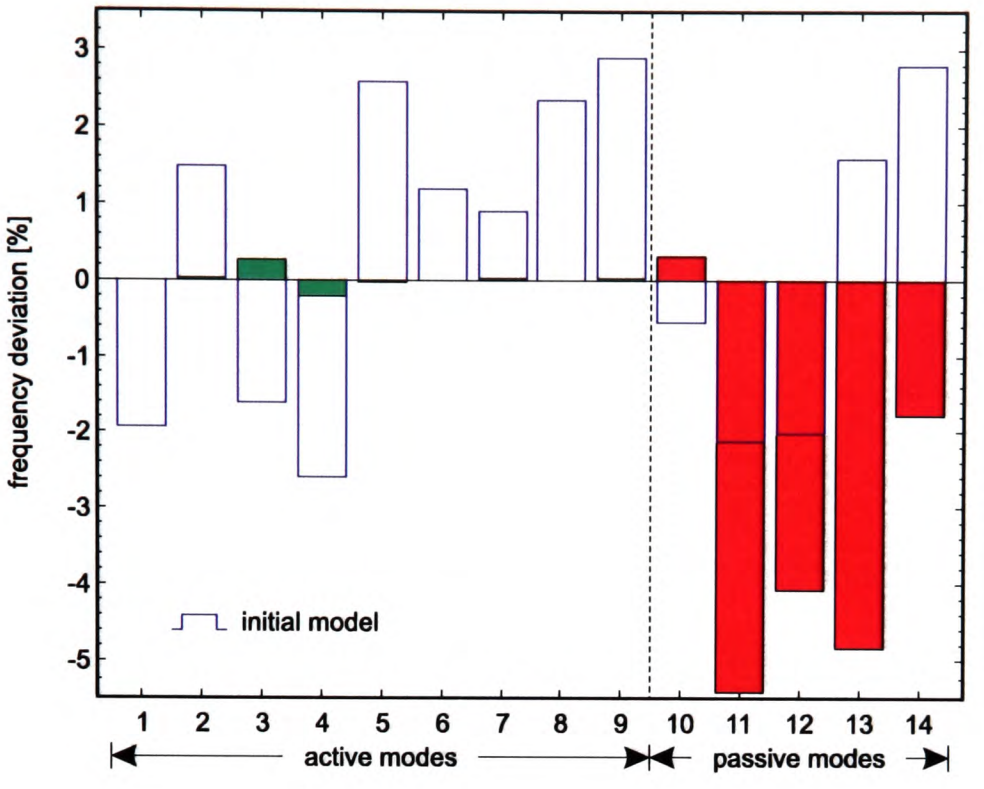

Figure 4.15: Frequency Deviations for Active and Passive Modes (Parameter Set Number 1)

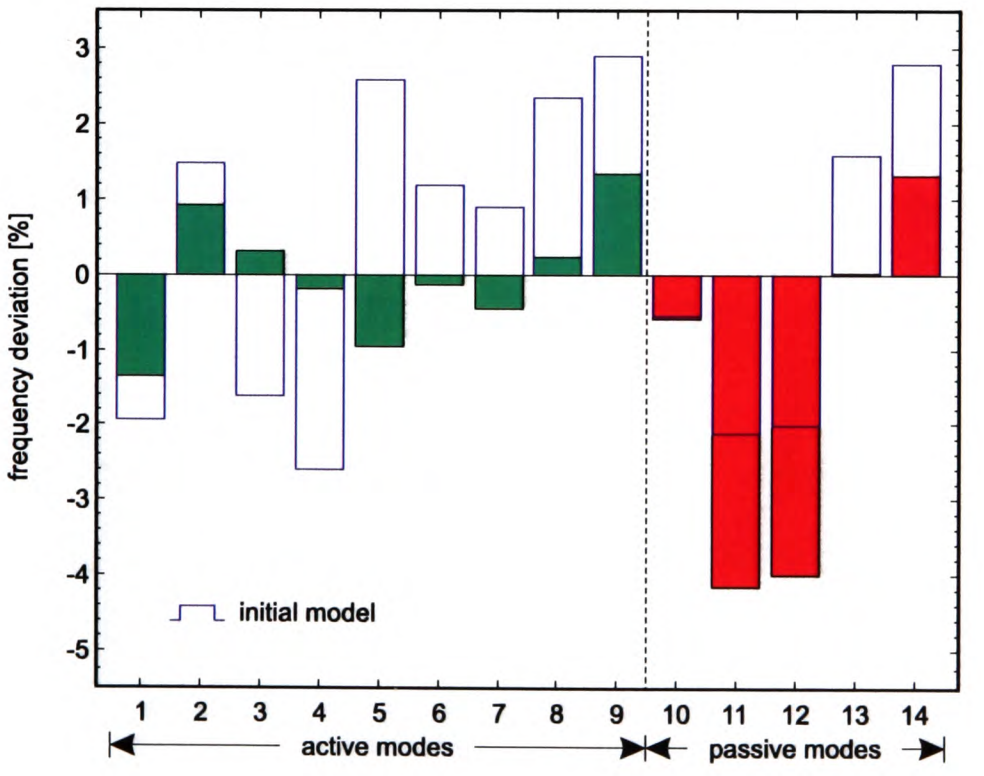

Figure 4.16: Frequency Deviations for Active and Passive Modes (Parameter Set Number 2)

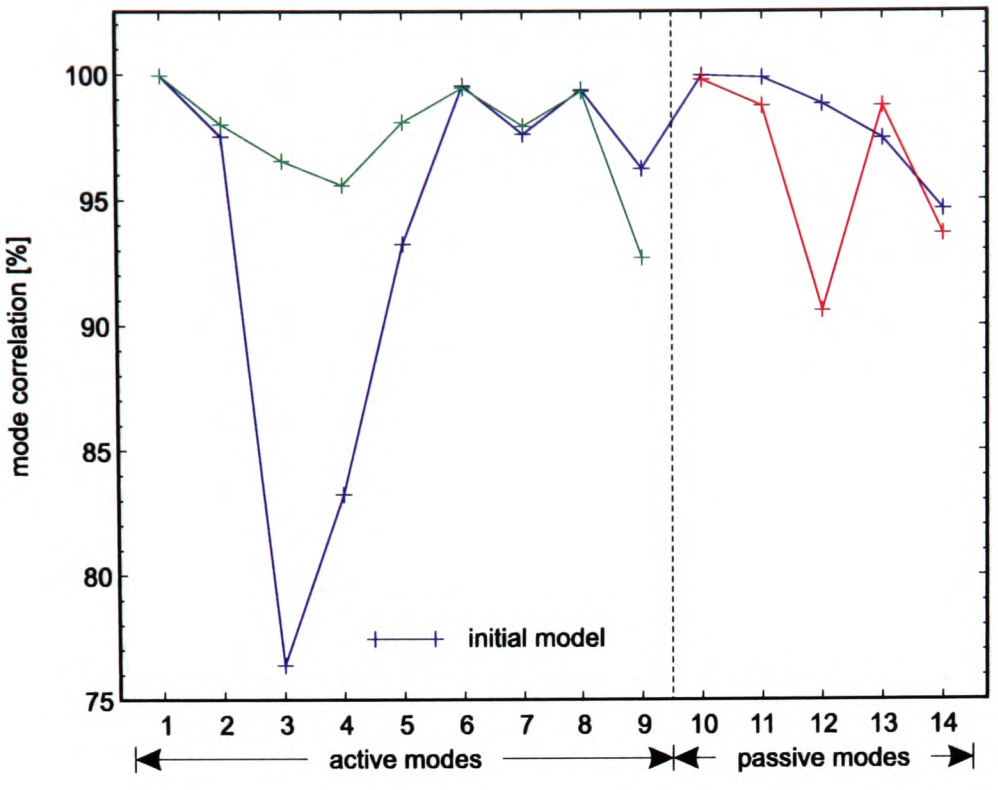

Figure 4.17: **MAC**-Values for Active and Passive Modes (Parameter Set Number 1)

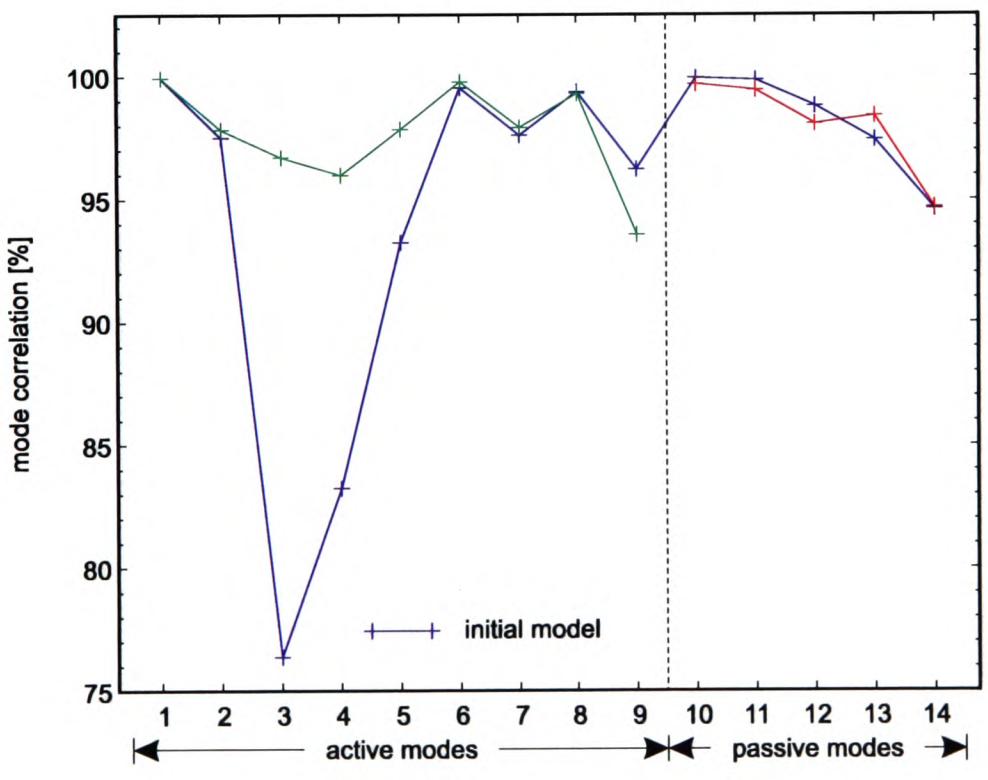

Figure 4.18: **MAC**-Values for Active and Passive Modes (Parameter Set Number 2)

The frequency for the first tail torsion mode is unchanged since none of the selected updating parameters affects this mode shape. The lateral fuselage and second tail bending are almost completely decoupled from all other modes, i.e. the deflection profiles do not appear as components in any other mode shape. Yet, the chosen correction parameters affect the corresponding eigenfrequencies but these modifications do not alter the residual vector which controls the optimisation. The frequency deviations, not being constrained by the residual, are therefore free to increase unconstrained. For the third symmetric and anti-symmetric wing bending modes the stiffness is corrected simultaneously to the first and second order wing bending modes. Here, a considerable improvement of the corresponding eigenfrequency deviations is attained.

The modal correlation results are similar but less distinct. The correlation of inactive modes generally is better for the model which is updated with parameter set number 2, i.e. in this case the predicted eigenvectors are closer to the test modes.

4.2.5.3 Frequency Response

Figure 4.20 gives some selected examples for analytical FRFs computed from the initial and validated models as compared to the measured response data. The excitation point is at the right drum tip and a sinusoidal excitation force of 1.5 N in vertical direction is used. The response is recorded at four selected sensor locations, Figure 4.19, on the left wing (108-z), left drum tip (112-x), rear fuselage (205-y), and left tailplane (303-z). Modal damping values are taken from the Ground Vibration Test [36].

Both updated models yield considerable improvements over the initial finite-element model, Figure 4.20. The differences between the two validated models, however, are not as apparent as with the modal data. The major discrepancies among the measured and analytical responses are found near the anti-resonance frequencies since the anti-resonances are not considered in the modal updating approach.

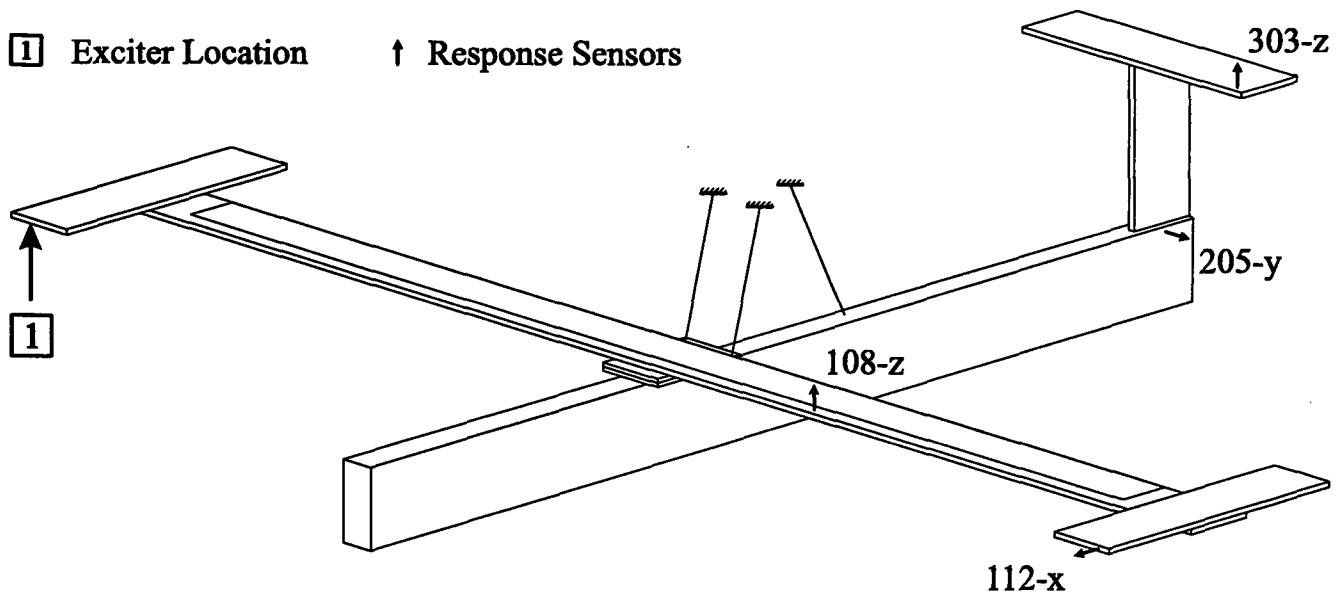

Figure 4.19: Excitation and Sensor Locations for Frequency Response Analysis

4.2.6 Concluding Remarks

In the preceding section an application of the model updating method described in Section 3.2 to an aerospace-related test case and live experimental data has been executed.

A novel iterative selection technique for correction parameters resulting in a physically correct updated analytical model, has been proposed. Unlike other systematic localisation methods suggested for finite-element modelling errors, the technique is applicable to complex structures and is insensitive to systematic experimental errors and measurement noise. The parameter selection approach allows to establish a well-conditioned optimisation problem and ensures good convergence of the updating algorithm. Also, a new technique for the correction of structural components with viscous material properties has been suggested.

Performance has been demonstrated in a numerical prediction study for modal data reaching beyond the usual model validation phase. The results show that careful parameter selection leads to an updated model that provides a realistic representation of the actual dynamic behaviour of the test structure.

The methods main drawback is that it requires physical insight and a detailed knowledge on the numerical modelling of the structure under investigation. Acquiring this knowledge may be time consuming with large models.

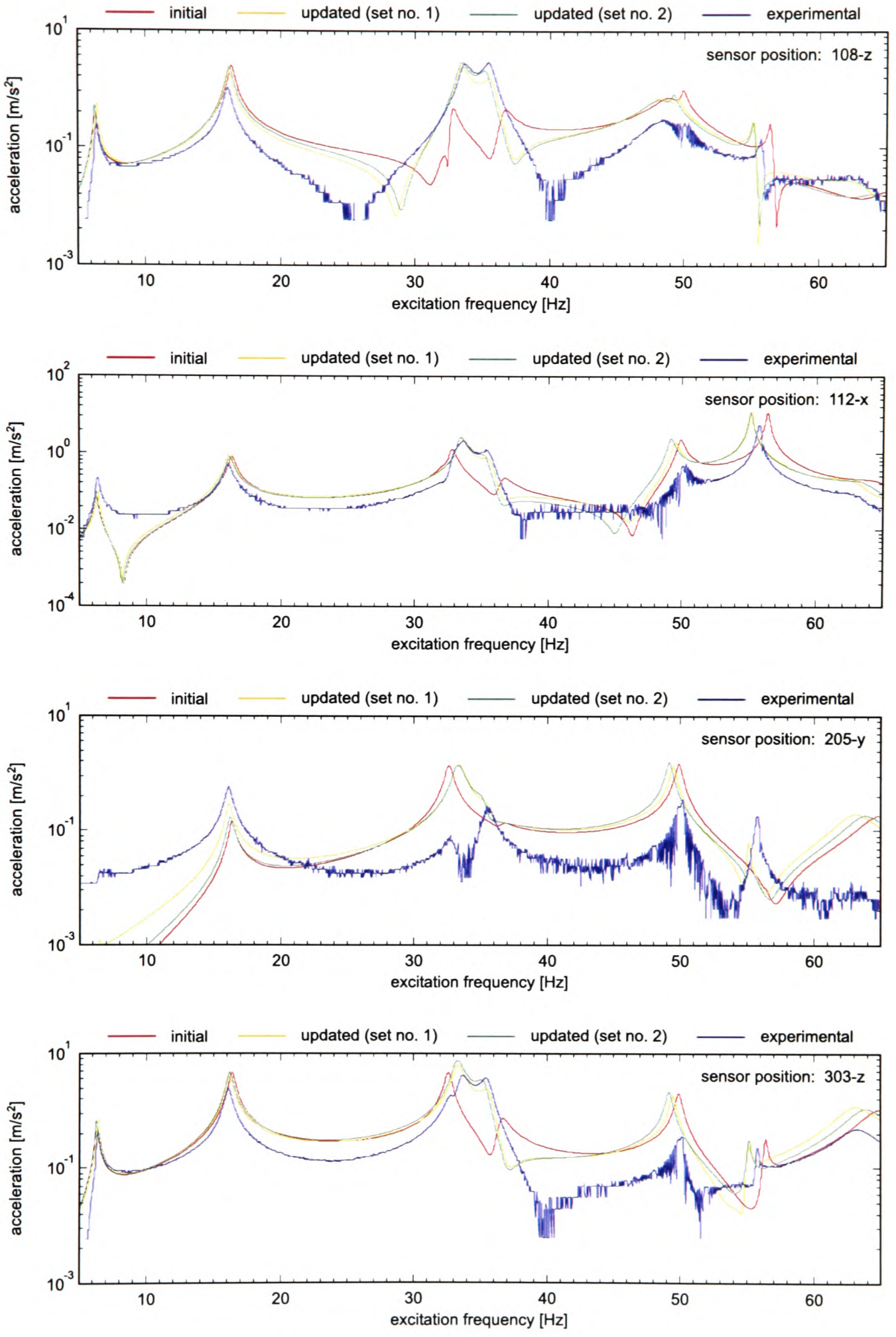

Figure 4.20: Measured and Computed Frequency Response

However, it can be used to reduce the number of mode shapes and natural frequencies needed for the model correction process and accordingly help to cut costly testing time.

4.3 The Influence of Experimental Errors

To assess the influence of errors in the experimental reference data on the accuracy of finite-element model corrections a simulation study [76] using numerically generated 'experimental' modal data and a finite-element model with artificial modelling errors is performed. Measurement uncertainties are added to the 'experimental' mode shapes and natural frequencies and their impact on the model updating results, i.e. substructure correction factors, frequency deviations, and mode shape correlation, is investigated. Different numerical models are used to evaluate the role of modelling error magnitudes and locations.

4.3.1 Introduction

The improvement of inaccurate numerical models by means of experimental vibration test data essentially depends on the measurement precision. Since errors in experimental data can be merely minimised but never be completely eliminated the respective model corrections will, to a certain extent, be inaccurate as well. This simulation study explores the influence of these errors on the accuracy of the correction factors α_i and β_j, deviations of analytical and experimental eigenfrequencies, and the correlation of computed and measured mode shapes. For useful results the measurement uncertainties in the natural frequencies and mode shape deflections should be well below the deviations observed between the experimental data and the initial finite-element model's analytical data.

From the theoretical treatment in Section 3.2 various mechanisms regarding the influence of measurement uncertainties on the updating process become apparent:

- The experimental errors directly affect the vector of residuals, eq. (3.2), which controls the optimisation. Computing the differences between experimental and analytical data makes the residual highly sensitive to measurement errors.

- The correlation of measured and analytical modes is diminished and the number of analytical eigenvectors which are allocated to experimental mode shapes is likely to decline.

- After the first iteration step the experimental uncertainties are implicitly included in the finite-element model's analytical modal data. This leads to modifications in the gradient matrix elements and constitutes a non-linear relation with respect to the correction factors, eq. (3.11).

Since the correlation of analytical and experimental mode shapes is directly linked to the individual structure's dynamic characteristics and the gradient matrix terms are a function of the choice of substructures $\mathbf{K}_i$ and $\mathbf{M}_j$ it appears to be not possible to derive general statements from theoretical considerations. Accordingly, the purpose of this simulation study is to gain a broad overview how experimental inaccuracies alter the model corrections and to provide a starting point for more detailed investigations.

The experimental uncertainties which arise from data acquisition and signal processing[9] are classified into three categories:

1. **Relative errors** (being proportional to the magnitudes of measured mode shape deflections). These errors occur due to the limited precision of transducer alignment, amplifier calibration, or analog-to-digital conversion errors.

2. **Absolute errors** (independent of the measured deflection values) which are caused by A/D-converter noise and bias, temperature effects, or external sources of interference.

3. **Natural frequency errors** mainly originating from imprecisely tuning the excitation frequency to the structure's actual resonance frequency. The accuracy of frequency measurement devices usually is far beyond the manual tuning precision and therefore will not be considered here.

Uncertainties emerging from the mode isolation quality or post-processing errors from off-line identification approaches, since they strongly depend on the

[9] cf. the discussion of experimental identification techniques in Chapter 2.

individual identification technique and test structure, are not covered here. It is further assumed that systematic errors, like a model suspension system which does not correctly reflect the boundary conditions or frequency shifts, e.g. due to the sensor masses and cabling, are carefully avoided.

4.3.2 Test Structure

The investigations are carried out on a three-dimensional tree-type laboratory test structure, see Figure 4.21, which consists of two pairs of horizontal blades (1 - 4), a central steel pylon of circular cross section (5), a supporting base plate (6), and two joint elements (7). The lower blade pair is rotated by an angle of 45 degrees relative to the upper blades. One blade in each plane (components (1) and (3)) has homogeneous material properties, whereas the others, components (2) and (4), have a thin silicone layer in their neutral planes to induce non-proportional damping. The test structure's specifications and geometric dimensions are listed in Table 4.5. For previous experimental investigations [155] the structure has been equipped with 45 acceleration sensors at 30 measurement locations. In global co-ordinates these provide 49 experimental degrees of freedom.

Again, the MATFEM [101] finite-element code is used for the numerical analysis. The numerical model, Figure 4.22, has 128 Timoshenko beam elements and 726 degrees of freedom. A rigid suspension at the base plate is assumed. The first 20 mode shapes and eigenfrequencies are used in the simulation study.

4.3.3 Simulation Procedure

For the simulation study an inaccurate numerical model and an erroneous 'experimental' modal matrix are needed to provide the necessary input data for the updating process. The modelling errors and 'experimental' uncertainties are described in Sections 4.3.3.1 and 4.3.3.2, respectively. An outline of the simulation procedure is given in Figure 4.23.

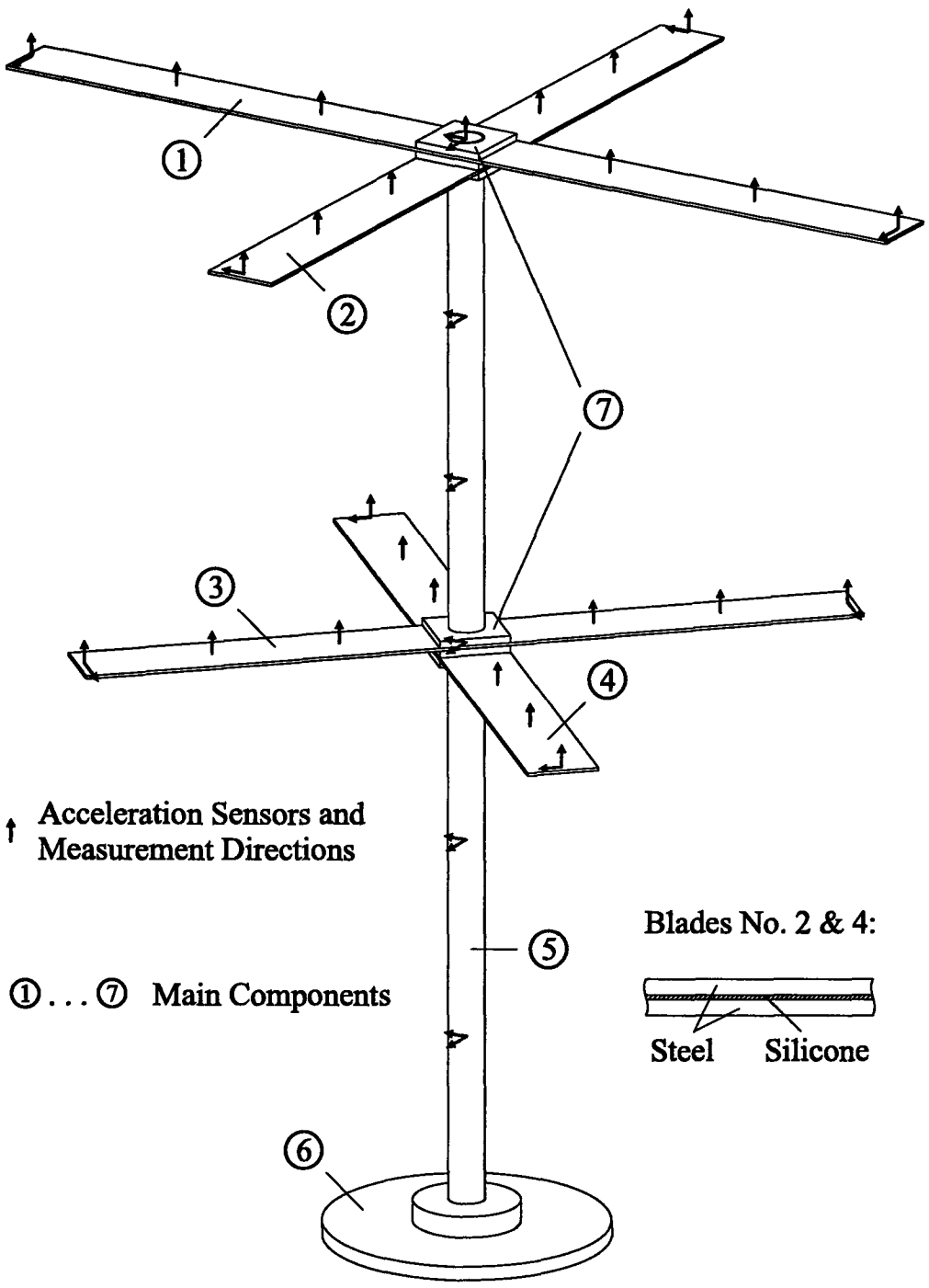

Figure 4.21: Test Structure

4.3.3.1 Model Preparation

Starting from the reference finite-element model synthetic stiffness modelling errors $\tilde{\mathbf{K}}_\xi$ are successively introduced into the stiffness matrix to generate the inaccurate numerical models[10]

$$\tilde{\mathbf{K}}_{0,\xi} = \mathbf{K}_0 + \tilde{\mathbf{K}}_\xi \ .$$

Three different modified models, Table 4.6, are created to investigate the influence of error location and magnitude. Modelling error numbered 1 is used to exemplify the effects of the different error categories listed on page 99. Then,

[10]The mass matrix is generally modelled with considerably higher accuracy. Therefore, it remains unchanged throughout this study.

General Specifications:	
Density	7.85×10^3 kg/m^3
Young's Modulus	2.06×10^{11} N/m^2
Joint Masses:	
upper Joint	2.54 kg
lower Joint	1.77 kg
Blades:	
Cross Section	0.100×0.004 m^2
Length: Blade No. 1	1.40 m
Blade No. 2	1.20 m
Blades No. 3 & 4	1.10 m
Pylon:	
Height	1.50 m
outer Diameter	0.050 m
inner Diameter	0.044 m

Table 4.5: Test Structure Specifications

a comparison between models numbered 1, 2, and 3 emphasizes the influence of modelling error magnitude and location. The system matrices $\tilde{\mathbf{K}}_{0,\xi}$ and $\mathbf{M}_0$ and the corresponding eigenvectors $\tilde{\varphi}_{a,n}$ and eigenfrequencies $\tilde{\lambda}_{a,n}$ constitute the initial numerical model for the updating process.

4.3.3.2 Simulation of Measurement Uncertainties

The 'measured' modal data needed for the model corrections are derived from the reference finite-element model's eigenvectors and eigenvalues. To achieve a realistic level of incompleteness the analytical mode shapes are reduced to

Modelling Error	**Error Location**	**Stiffness Modification**
$\tilde{\mathbf{K}}_1$	Compound Blades No. 2 & 4	-17 %
$\tilde{\mathbf{K}}_2$	Compound Blades No. 2 & 4	-7 %
$\tilde{\mathbf{K}}_3$	Pylon (between upper & lower Blade Plane)	$+10$ %

Table 4.6: Artificial Modelling Errors

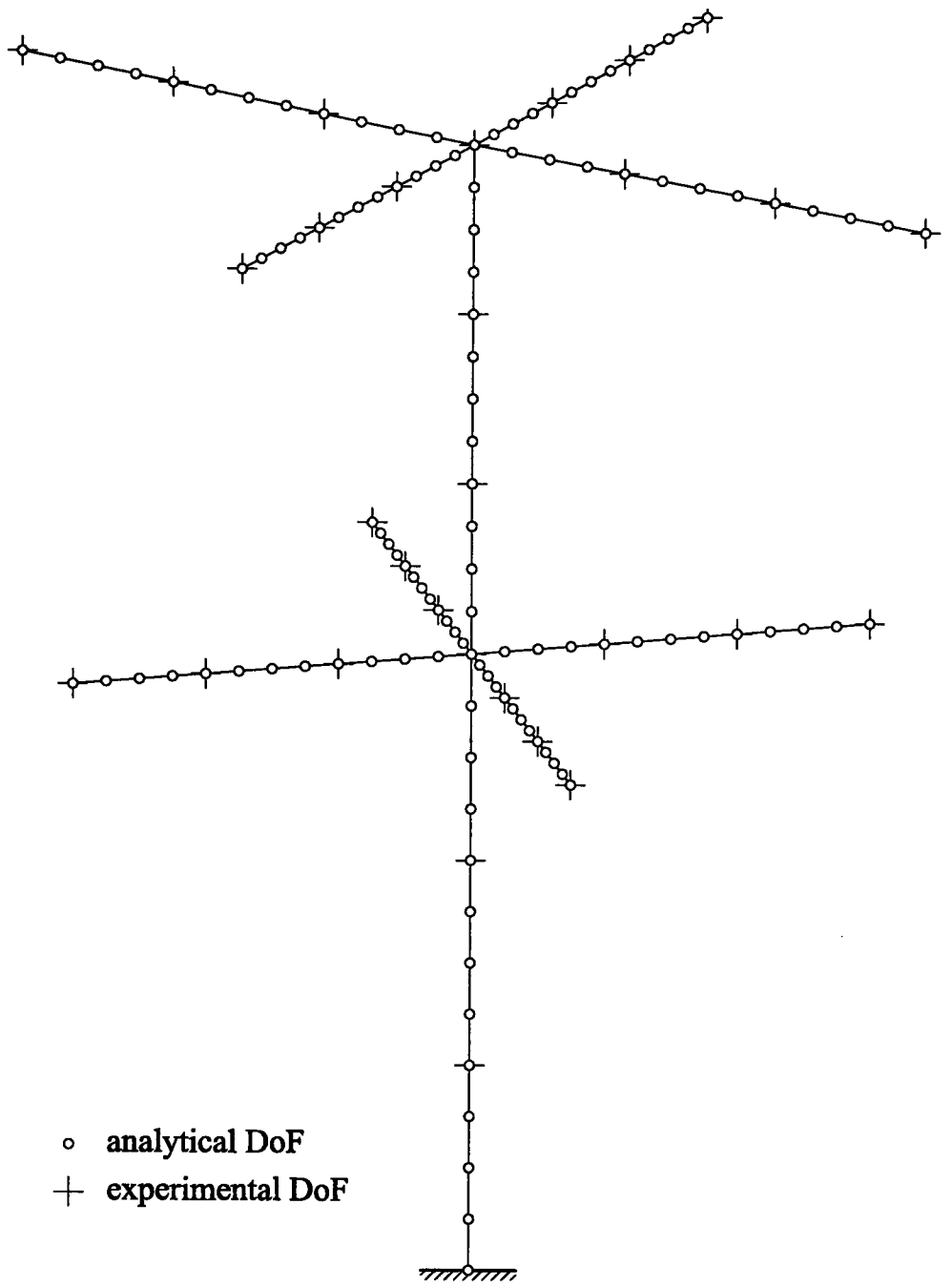

Figure 4.22: Finite-Element Model of the Test Structure

the 49 experimental degrees of freedom shown in Figure 4.22. The reduction is made by removing the surplus analytical degrees of freedom from the full eigenvectors rather than using a matrix transformation between the analytical and experimental degrees of freedom. As a result, the reduced eigenvectors only contain those deflection components which would have been actually measured in a real test.

In the second step, simulated experimental uncertainties and noise are added to the reduced mode shapes and eigenfrequencies. The different error categories are modelled by measurement error vectors of statistically distributed random numbers [60, 131], Table 4.7.

For the class of relative errors $\boldsymbol{\delta}_{rel}$ a Gaussian distribution with zero mean

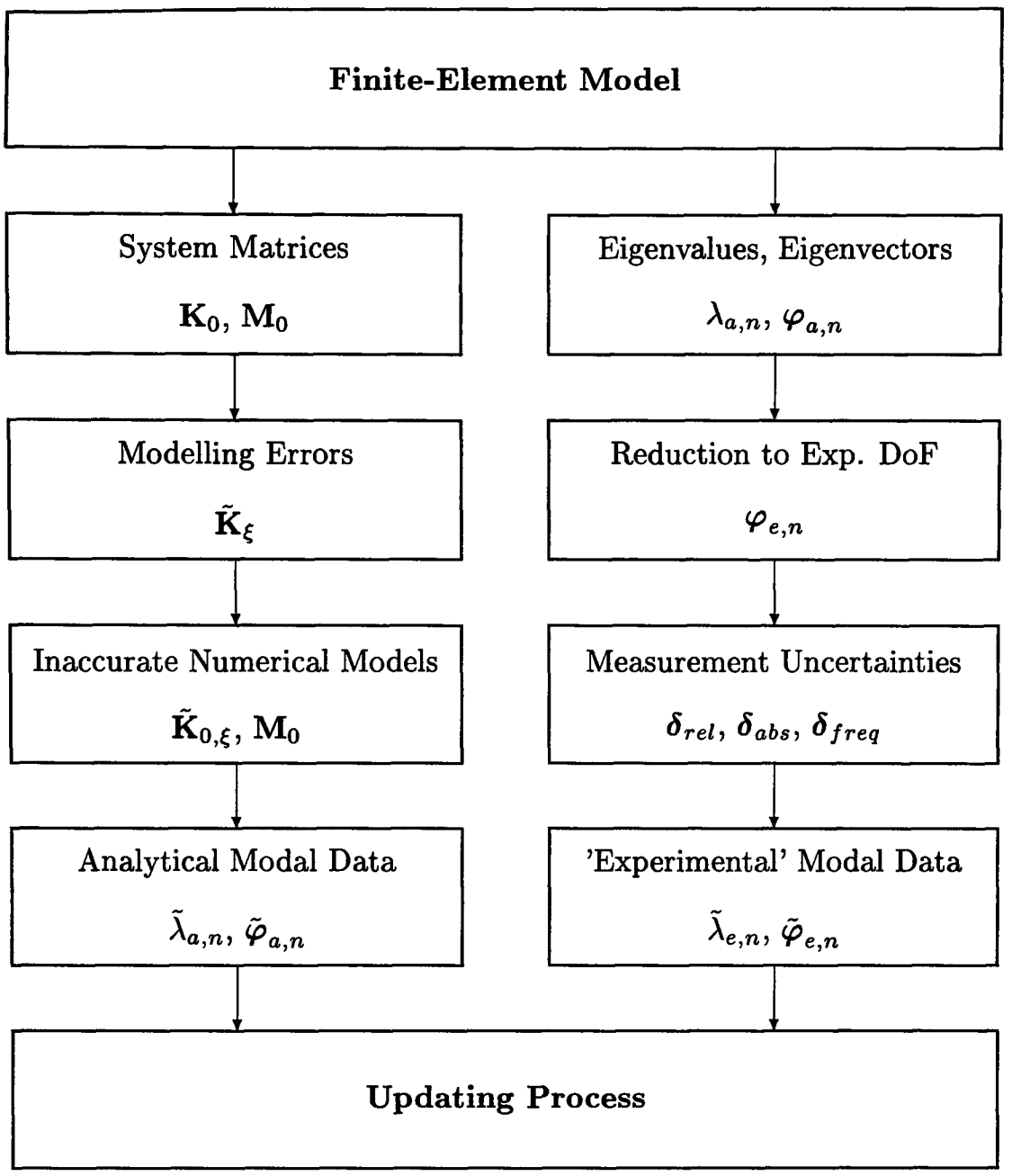

Figure 4.23: Simulation Procedure

and multiple variances between 1 % and 20 % is chosen. The errors are proportional to the individual deflection amplitudes at each 'measured' degree of freedom (DoF). The experimental mode shape vectors $\tilde{\varphi}_{e,n}$ are obtained from

$$\tilde{\varphi}_{e,n} = \varphi_{e,n} \times (1 + \delta_{rel}) \ ,$$

where $\varphi_{e,n}$ are the analytical eigenvector components at the experimental degrees of freedom (cf. Figure 4.23) and '$\times$' denotes an element-by-element multiplication of the two vectors. This error category represents all transducer alignment and amplifier calibration uncertainties as well as relative errors within the electronic signal conditioning set-up.

Absolute errors δ_{abs} are simulated by uniform distributions between 0.1 % and 2.0 % with respect to the maximum value (normalisation point) of each

Error Category	Distribution	Magnitude
δ_{rel}	Gaussian	±[1, 2, 5, 10, 20] %
δ_{abs}	Uniform	±[0.1, 0.2, 0.5, 1.0, 2.0] %
δ_{freq}	Gaussian	±[1, 2, 5] %

Table 4.7: Simulated Measurement Uncertainties

mode. The effects of noise and offsets from amplifiers and filters, temperature shifts, electromagnetic radiation, or A/D-converter noise are comprised. For this category the experimental modes are given by

$$\tilde{\varphi}_{e,n} = \varphi_{e,n} + \delta_{abs} \ .$$

Natural frequency uncertainties $\delta_{freq,n}$ are also modelled by a Gaussian distribution with zero mean and a variance of 1, 2, and 5 %, respectively. The errors are proportional to the individual frequency values, i.e.

$$\tilde{\lambda}_{e,n} = \lambda_{a,n} \cdot (1 + \delta_{freq,n})$$

with $\lambda_{a,n}$ as the analytical eigenvalues computed from the finite-element model and $\tilde{\lambda}_{e,n}$ as the simulated experimental eigenfrequencies.

4.3.3.3 Application Details

The number of mode shapes used for updating is varied between 2 and 20. No condensation or expansion of mode shapes is applied and the 'experimental' data is not averaged. Convergence is reached after 6 to 10 iteration steps. All subsequent results, i.e. correction factors, frequency deviations, and mode correlation, refer to the values after 16 iterations.

Again, measured and analytical modes are automatically allocated in each iteration step according to the Modal Assurance Criterion (**MAC**), eq. (4.2), and natural frequency deviation Δf, eq. (4.1). The necessary condition for an allocation of a measured and a computed mode shape is a minimum **MAC**-value of 65 % and a maximum difference between the associated frequencies of 30 %.

To increase the impact of frequency deviations as compared to mode shape deflection differences in the correction factor computation, eq. (3.11), the automatic eigenfrequency weighting described in Section 5.2.4 is applied here as well.

In preliminary test runs the finite-element modelling errors are tuned such that a one-to-one allocation of analytical and 'measured' mode shapes is ensured within each iteration step and for all magnitudes of simulated experimental errors. Hence, the observed correction parameter changes are directly caused by the simulated measurement errors and no secondary effects are involved.

4.3.4 Results

In this section the influence of the simulated experimental errors on the model corrections are discussed in detail. The correction factor error $\Delta\alpha$ for an experimental error $\boldsymbol{\delta}$ is defined as

$$\Delta\alpha(\boldsymbol{\delta}) = \frac{\alpha(\boldsymbol{\delta})}{\alpha(\boldsymbol{\delta}=0)} \,. \tag{4.4}$$

Likewise, the eigenfrequency deviation Δf_n and **MAC**-value error $\Delta\mathbf{MAC}_n$ for each mode n are

$$\Delta f_n(\boldsymbol{\delta}) = \frac{f_{a,n} - f_{e,n}(\boldsymbol{\delta})}{f_{e,n}(\boldsymbol{\delta})} - \frac{f_{a,n} - f_{e,n}(\boldsymbol{\delta}=0)}{f_{e,n}(\boldsymbol{\delta}=0)} \tag{4.5}$$

and

$$\Delta\mathbf{MAC}_n(\boldsymbol{\delta}) = \mathbf{MAC}_n(\boldsymbol{\delta}) - \mathbf{MAC}_n(\boldsymbol{\delta}=0) \,, \tag{4.6}$$

respectively. In eq. (4.5) $f_{e,n}$ denotes the simulated experimental natural frequencies used in the updating process and $f_{a,n}$ are corresponding analytical eigenfrequencies.

4.3.4.1 Correction Factors

Figures 4.24, 4.25, and 4.26 show the influence of the three categories of measurement inaccuracies on the substructure correction factors of finite-element model 1 (stiffness modelling error of -17 % in the steel-silicon compound

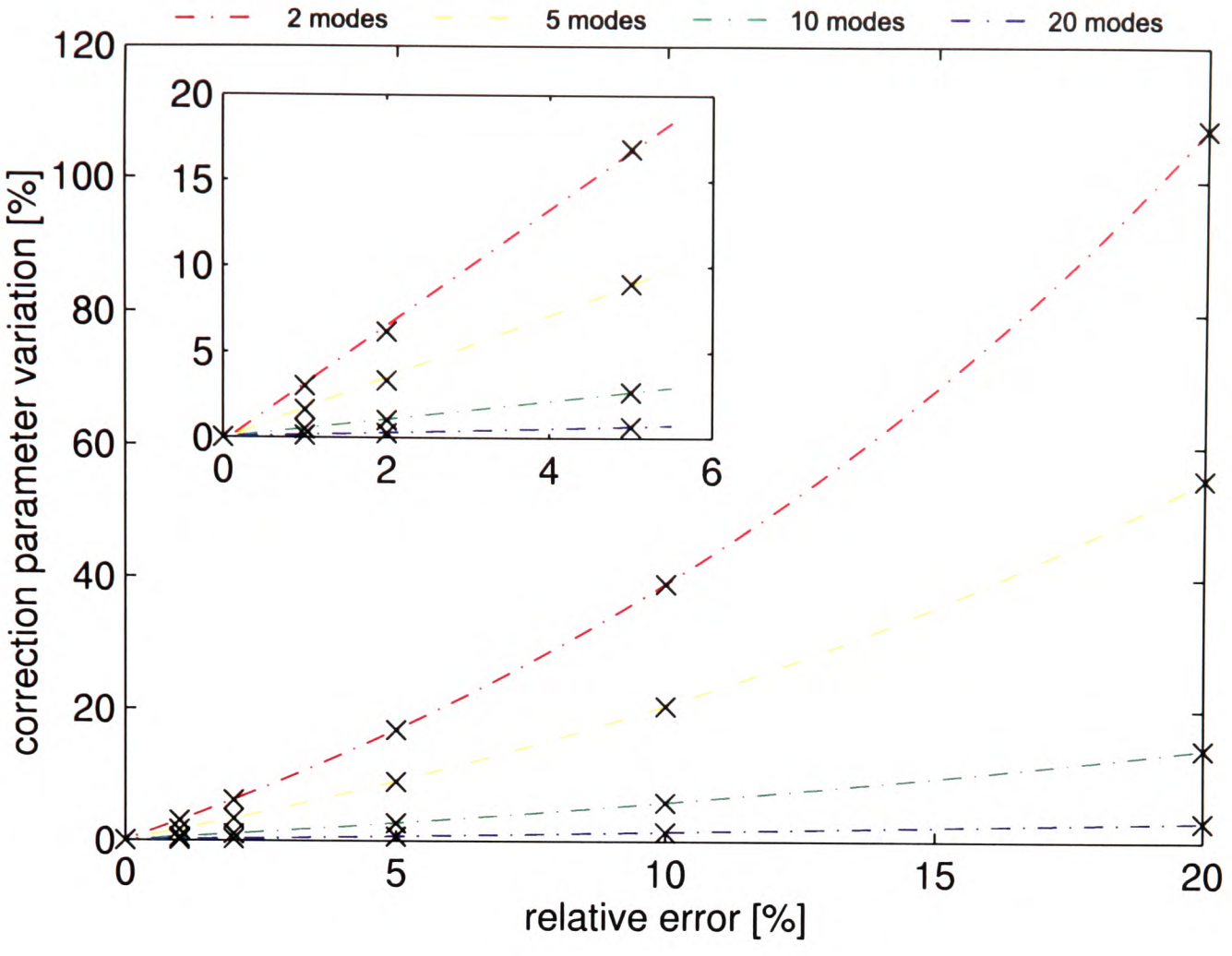

Figure 4.24: Correction Factor Deviations caused by Relative Errors

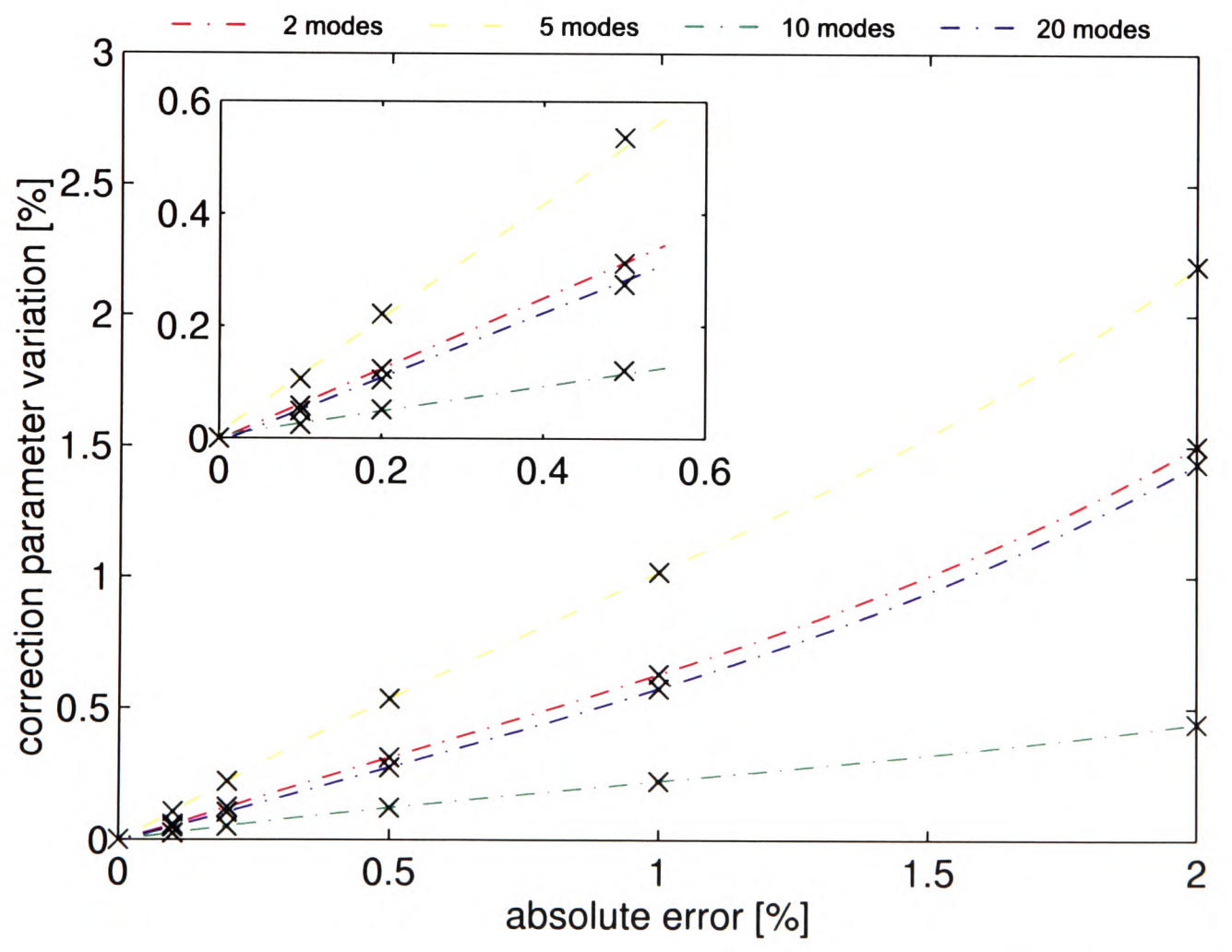

Figure 4.25: Correction Factor Deviations caused by Absolute Errors

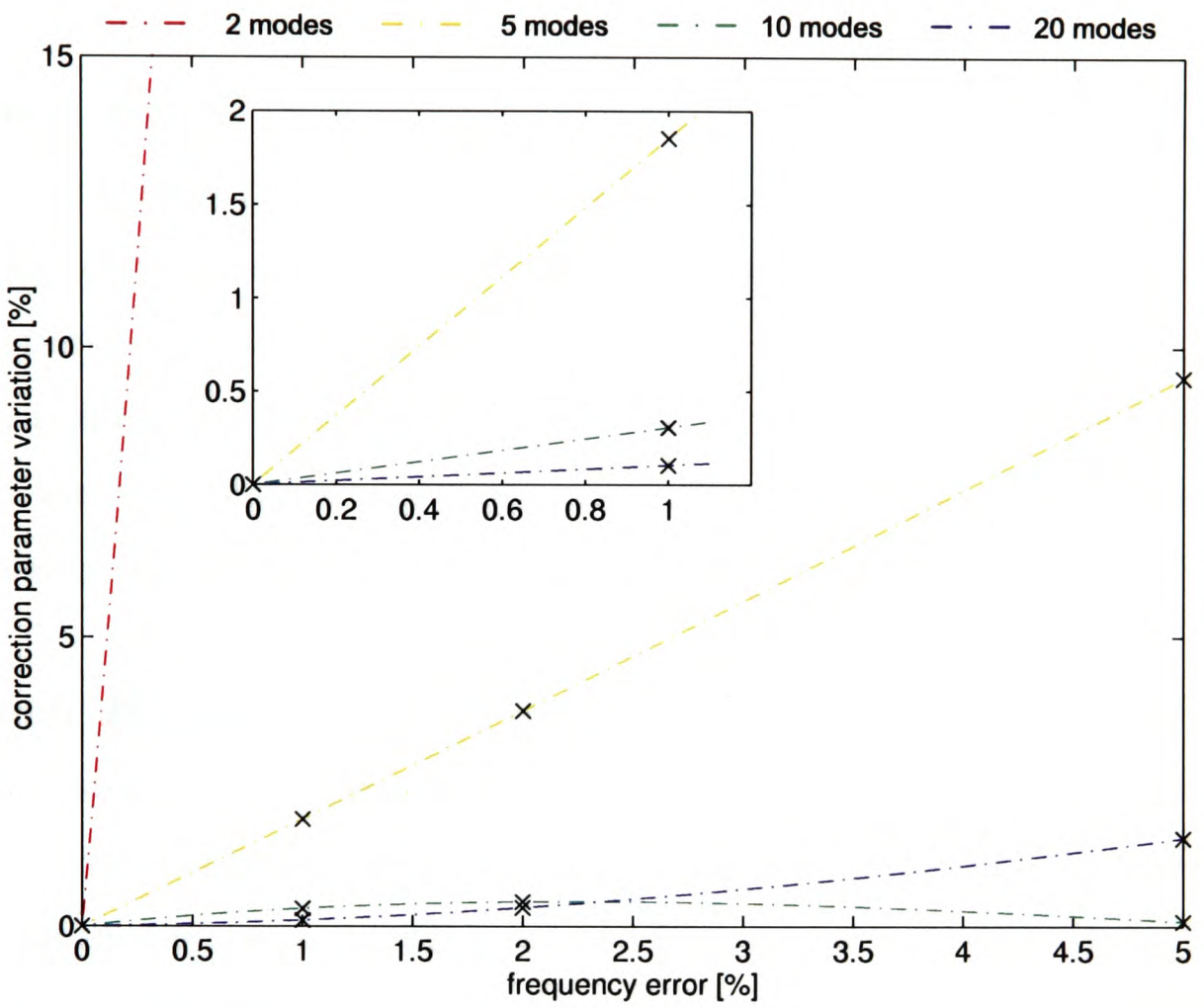

Figure 4.26: Correction Factor Deviations caused by Frequency Errors

blades). The symbols (×) mark computed data and lines represent the corresponding cubic spline interpolations.

Generally, the correction factor error $\Delta\alpha(\boldsymbol{\delta})$ increases progressively with the magnitude of the experimental errors. Still, for small values the gradients are nearly constant and a comparison to a first-order curve fitting (cf. the respective subplots in each figure) gives a good approximation. The linear ranges lie between zero and 5 % for relative errors and between zero and 1 % for absolute and frequency errors.

Relative Errors. The uncertainty $\Delta\alpha(\boldsymbol{\delta}_{rel})$, Figure 4.24, decreases with increasing number of modes used in the correction process. This is due to the fact that the correction factor is computed from an over-determined system of equations and, as a growing amount of data is processed, the statistically distributed measurement errors are averaged to a greater extent. As a result, identifying more natural modes can, within reasonable limits, compensate for low-quality measurements.

Absolute Errors. Against the tendency found with relative errors the correction results for absolute errors, Figure 4.25, are not successively improved with a higher number of mode shapes. The correction factor accuracy deteriorates as the number of modes is increased from 2 to 5 modes and also from 10 to 20 modes. Since the absolute experimental errors are independent of the individual measured deflection values they significantly alter all degrees of freedom with small deflection amplitudes. If a mode shape contains many degrees of freedom with small deflections it is likely to respond more sensitive to those errors. A detailed examination of all modes reveals that the sets of 5 and 20 modes contain a noticeably large number of degrees of freedom where the original deflection (before the experimental errors are added) is smaller than the error magnitude. This implies that the updating process is considerably affected by the amount of useful data within each individual mode. Consequently, every mode shape has to be carefully analysed before it is used for updating.

Frequency Errors. The experimental frequency errors for 2 modes, Figure 4.26, produce excessively high levels of uncertainty ($\Delta\alpha \approx 660$ % for $\delta_{freq} = 5$ %) whereas for the other sets of mode shapes the results appear more reasonable. This is possibly due to the fact that the random measurement errors for the first two natural frequencies are both > 0, i.e. with respect to the first 2 modes the error seed has a non-zero mean value. Furthermore, the uncertainty for 10 modes displays an irregular behaviour. Here, the simulated experimental frequency uncertainties and the frequency deviations due to the modelling errors partially compensate each other. It appears, that in some cases the individual constellation of experimental and modelling errors can result in irregular correction errors. Consequently, the correction factor uncertainty can not be related to the experimental error magnitude alone.

4.3.4.2 Eigenfrequencies and Mode Correlation

In a more detailed assessment the influences of measurement errors on the natural frequency and **MAC**-deviations are considered. For clarity, and because changing the number of modes used for updating does not result in significant effects, the subsequent discussion and presentation is confined to the results for corrections with a set of 10 mode shapes.

Overall, the analytical eigenfrequencies, Figures 4.27 to 4.29, and mode shapes, Figures 4.30 to 4.32, from the updated finite-element model respond less sensitively to experimental errors than the submatrix correction factor. The natural frequencies of modes numbered 5 to 8 are clearly influenced by relative and absolute errors, Figures 4.27 and 4.28, while no significant uncertainties arise in the other frequencies ($\Delta f_a(\delta) < 0.08$ %). In the initial numerical model these modes have much higher deviations between analytical and experimental eigenfrequencies (4 to 5 %) than the others (± 1 %). They yield the largest contributions to the residual vector and, as a result, experience considerable frequency modifications during the updating process. Therefore, unlike the modes with small eigenfrequency errors, they are substantially influenced by measurement noise in the experimental data.

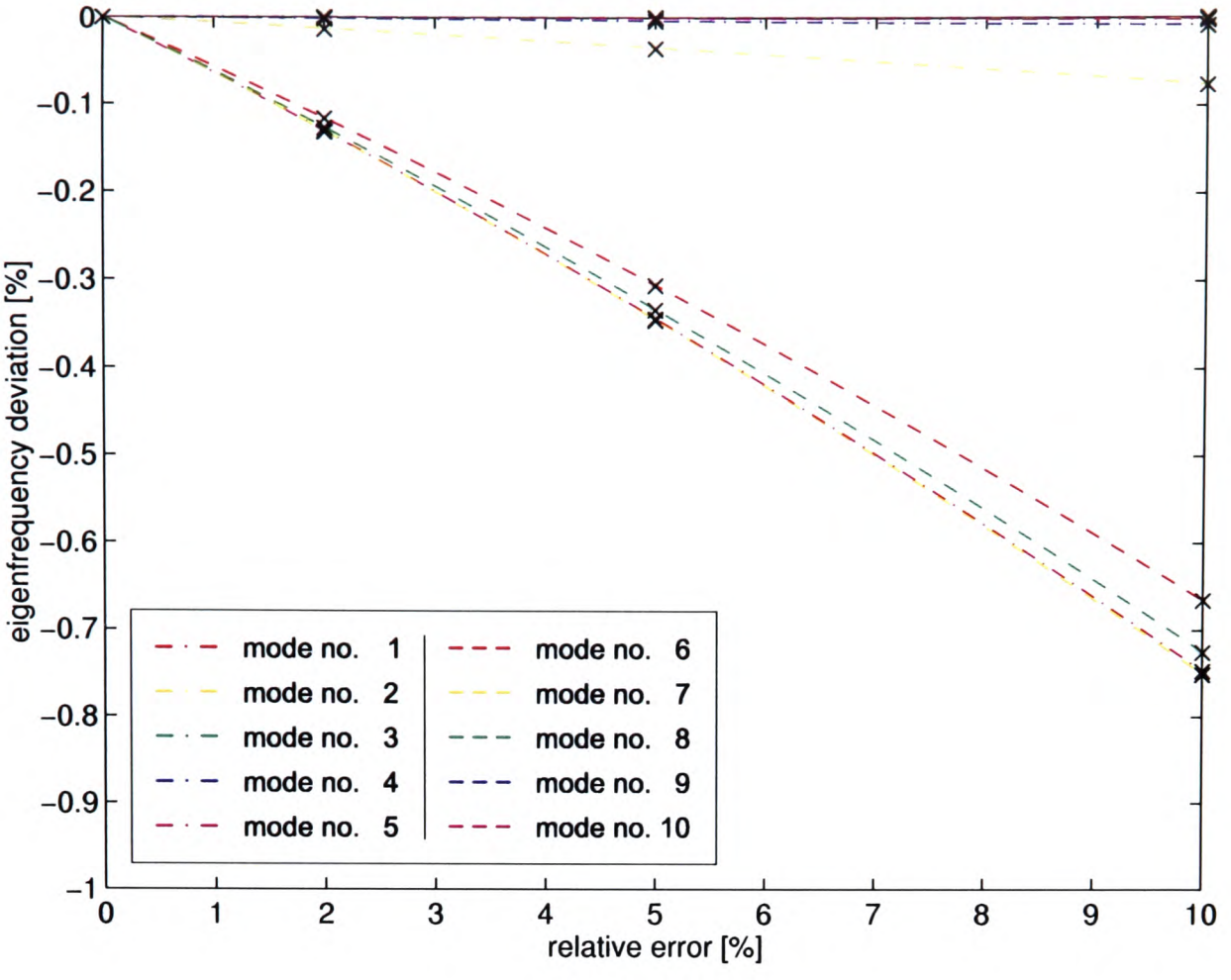

Figure 4.27: Frequency Deviations for Relative Errors

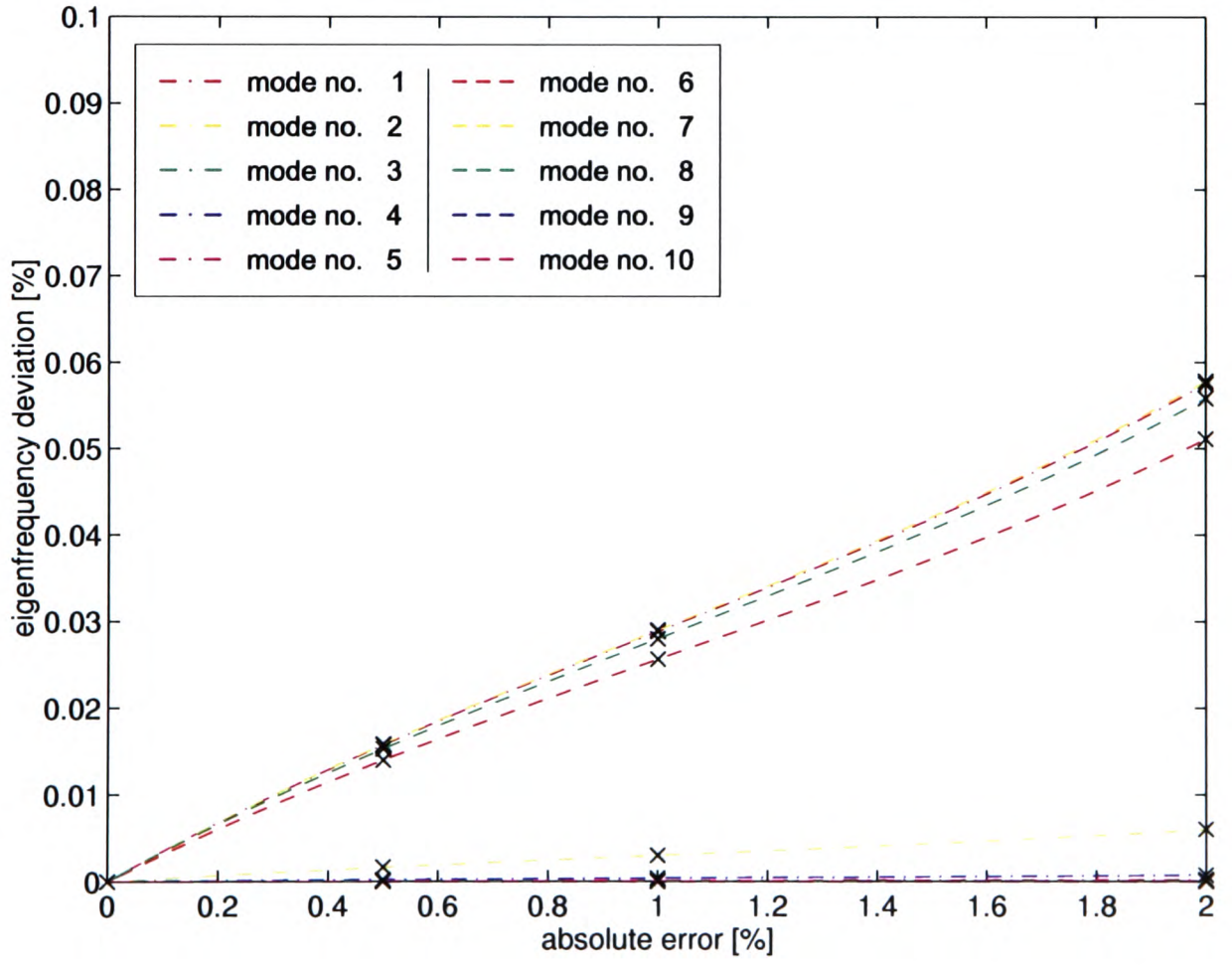

Figure 4.28: Frequency Deviations for Absolute Errors

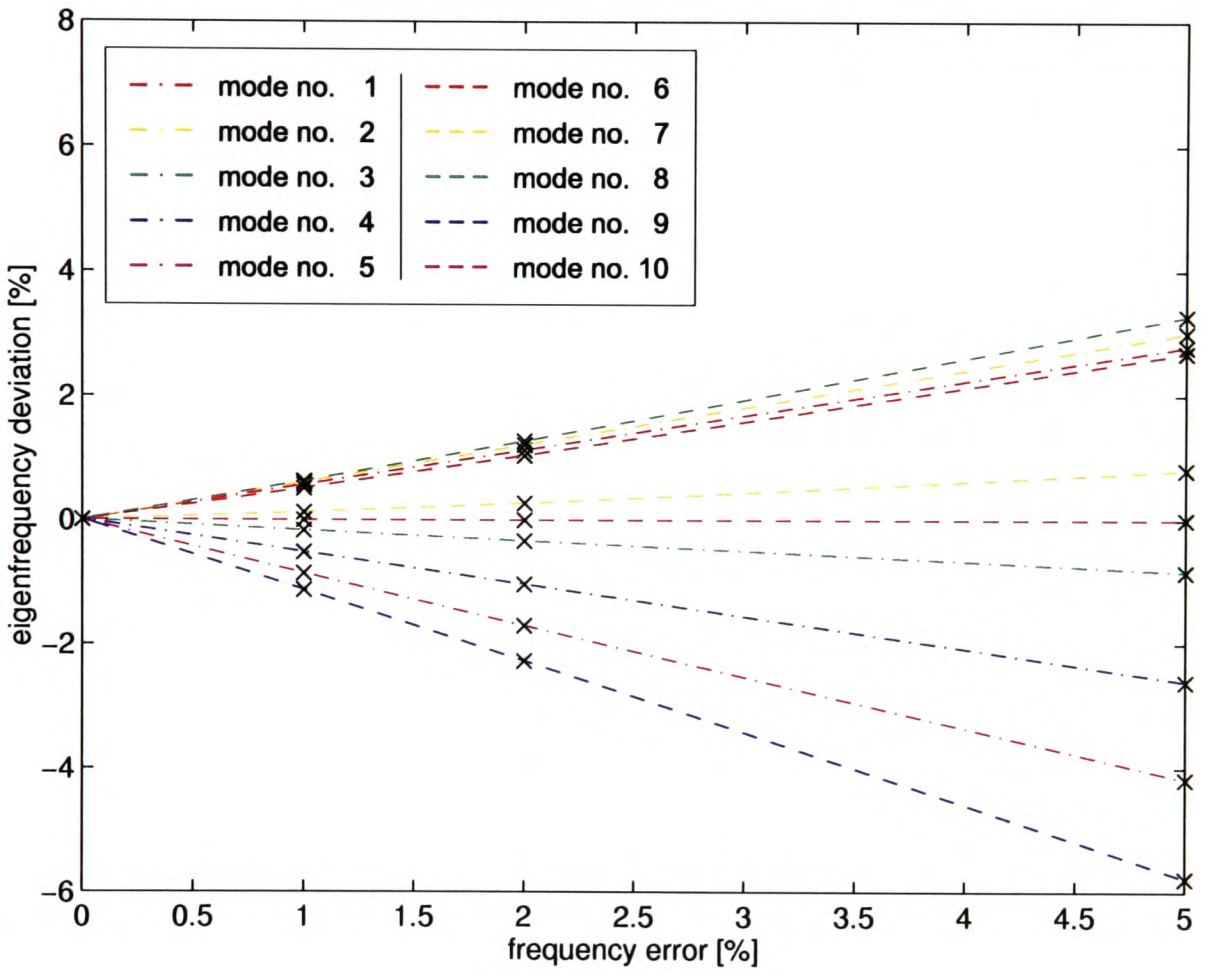

Figure 4.29: Frequency Deviations for Frequency Errors

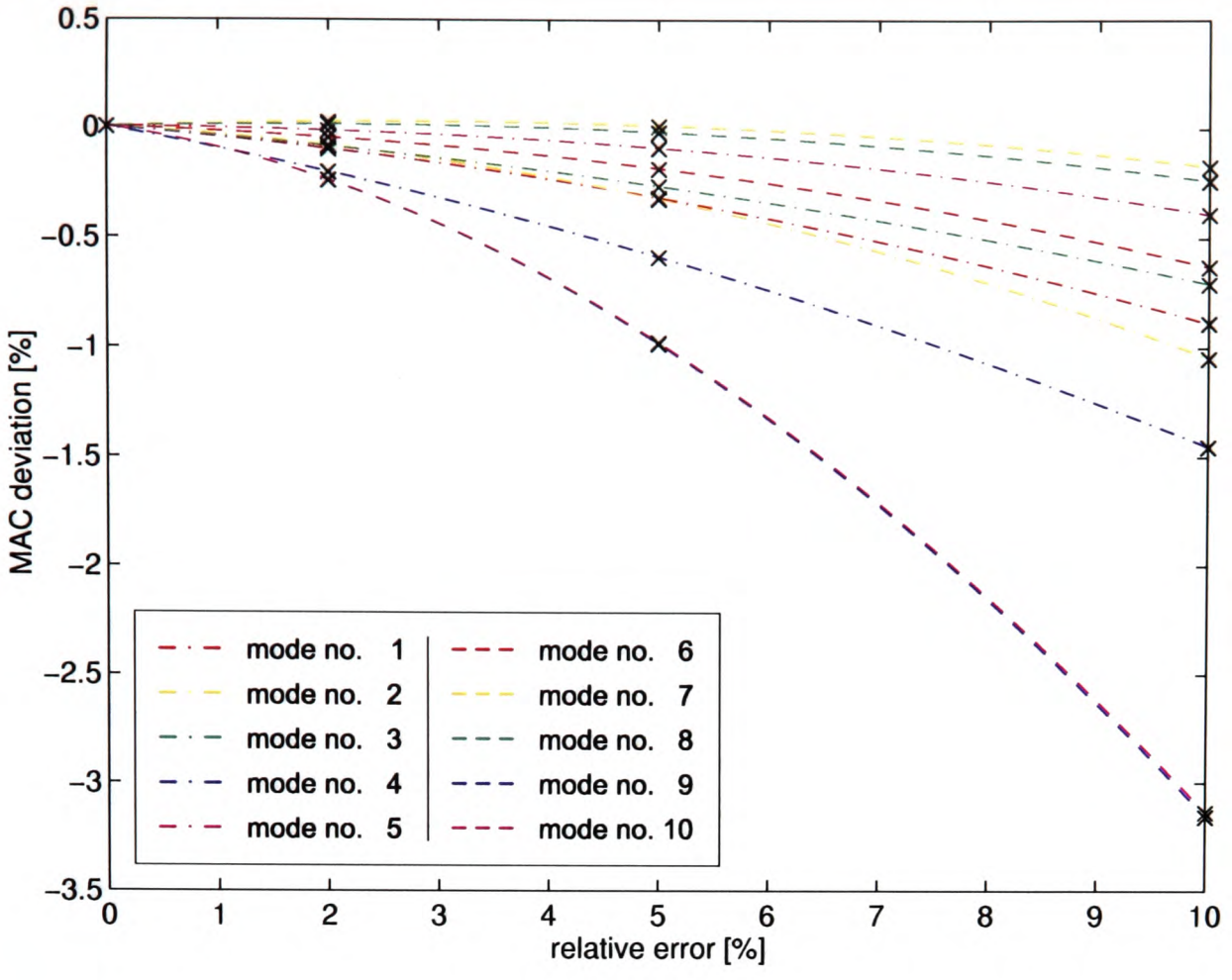

Figure 4.30: **MAC**-Value Deviations for Relative Errors

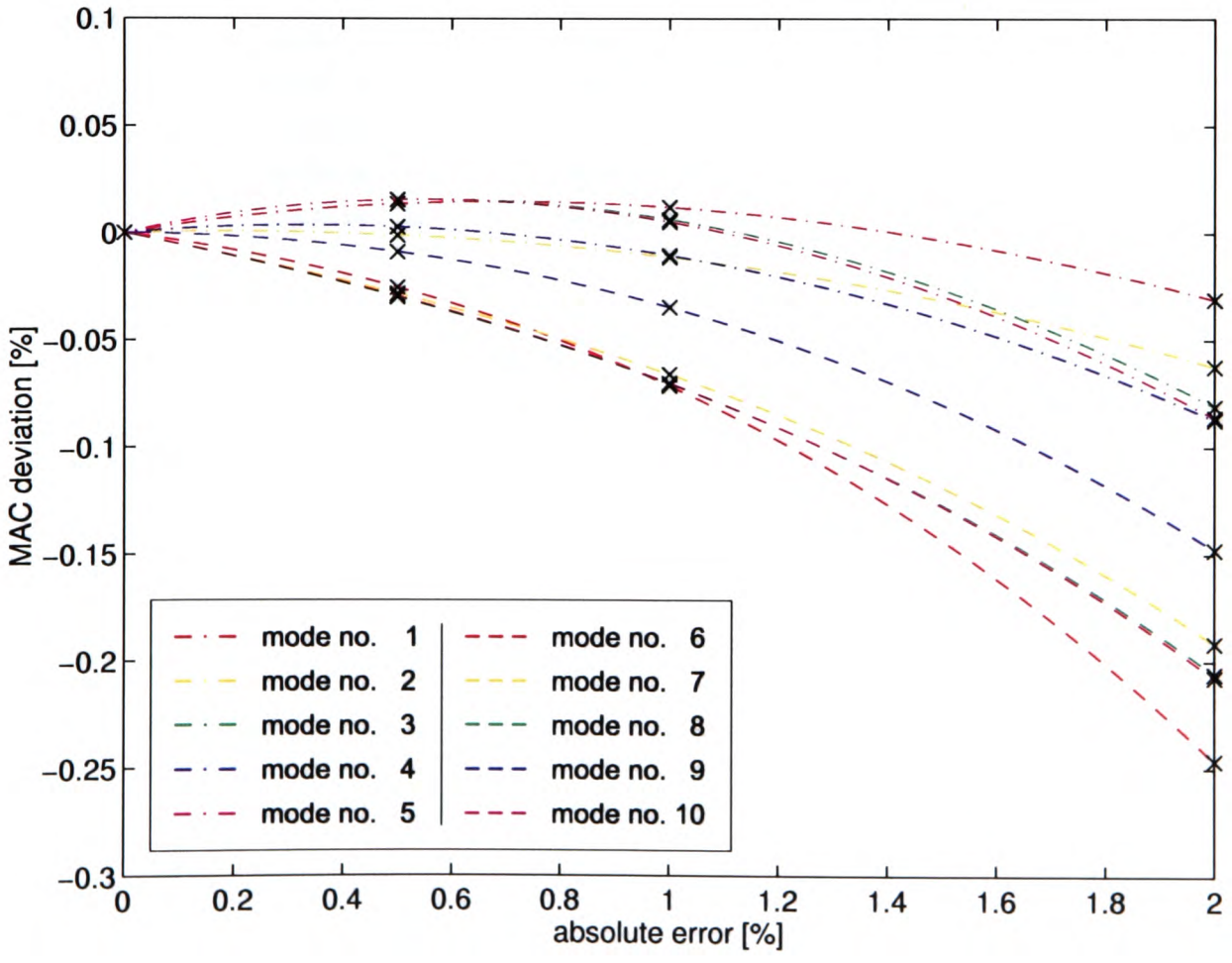

Figure 4.31: **MAC**-Value Deviations for Absolute Errors

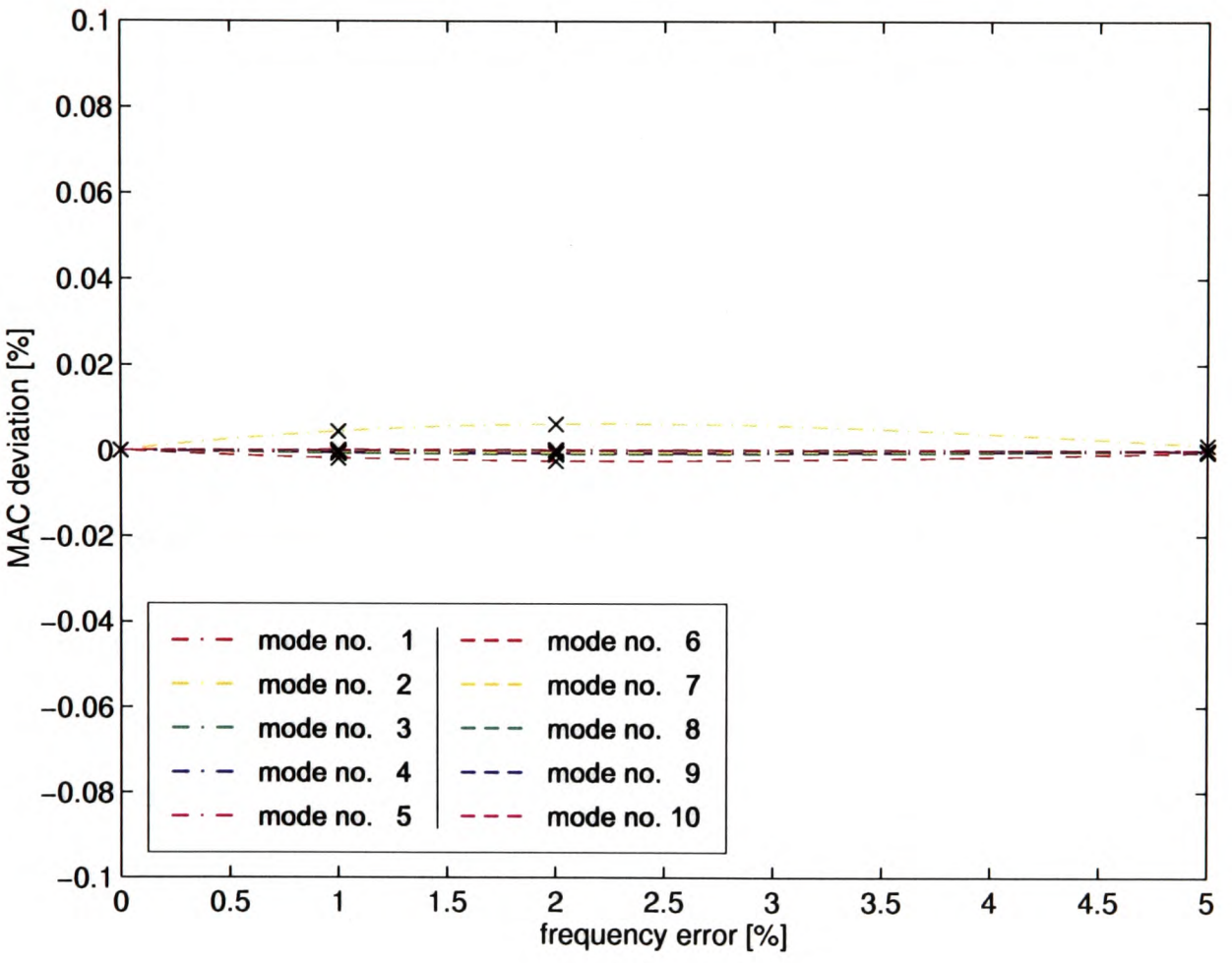

Figure 4.32: **MAC**-Value Deviations for Frequency Errors

The eigenfrequency deviations caused by experimental frequency errors basically reflect the original measurement error distribution and are not affected by the number of modes incorporated in the correction. Since reducing the analytical eigenfrequency deviations is a primary purpose in model updating a high precision in measuring the natural frequencies is required to achieve this goal.

MAC-deviations caused by experimental errors, Figures 4.30 to 4.32, are of no practical importance for updating. Even the largest correction factor inaccuracy ($\Delta\alpha_{max} = 20,56\ \%$) produces relatively small and locally confined changes in the analytical mode shapes and the errors in the experimental mode shapes are mostly averaged due to their random distribution. Therefore, the Modal Assurance Criterion, as it represents an integral measure for the correlation of experimental and analytical modes, appears to be not sensitive enough to resolve these changes.

4.3.4.3 Further Results

To emphasise the role of modelling error magnitude and location the investigations are now extended to the numerical models 2 (modelling error location identical to model 1 but smaller stiffness matrix error of $\tilde{\mathbf{K}} = -7\ \%$) and 3 (stiffness modelling error in the upper pylon section).

Influence of Modelling Error Magnitude. The correction parameter uncertainty $\Delta\alpha(\boldsymbol{\delta})$ is proportional to the ratio of modelling error magnitudes $\tilde{\mathbf{K}}_2/\tilde{\mathbf{K}}_1$ since it is related to the reference value $\alpha(\boldsymbol{\delta} = 0)$ without experimental error, eq. (4.4). The absolute differences $\alpha(\boldsymbol{\delta}) - \alpha(\boldsymbol{\delta} = 0)$, however, remain unchanged.

Eigenfrequency and deviations in **MAC** almost exactly reproduce the results for model 1. The differences are of the order 10^{-6} or less and are regarded as to originate from the limited computational accuracy.

As a result, the uncertainties caused by the erroneous experimental data are independent of the initial modelling error magnitude.

Influence of Modelling Error Location. The influence of the modelling error location is based on a comparison between the updating results for finite-element models 3 and 1. The location of a modelling error affects the analytical eigenfrequencies and eigenvectors and their derivatives with respect to the corresponding substructure correction factor, eqs. (3.13) and (3.22). Accordingly, the relation between the correction parameter and the residual vector, eq. (3.11), and likewise the influence of experimental errors on the correction parameter uncertainties, does also depend on the error location.

With the substructure correction factor accuracy consistent results are observed for both models. The general findings for model 1, as described in Sections 4.3.4.1 and 4.3.4.2, are reproduced.

The eigenfrequency deviations induced by absolute and relative errors lie below 0.03 % and are noticeably smaller than for model 1. Since in this case all modes used in the updating process (numbered 1 to 10) are flap-bending modes of the upper and lower blades the modelling error in the upper pylon section does not lead to strong frequency deviations between the initial analytical model and the experimental data. Therefore, the substructure corrections are also small and the sensitivity for measurement errors is low. For experimental frequency errors the eigenfrequency deviations again mirror the original measurement error seed and do not depend on the number of modes used.

MAC-values for the different error categories behave similarly to model 1. Again, the experimental uncertainties do not significantly modify the correlation of analytical and experimental mode shapes within the realm of this simulation study.

4.3.5 Concluding Remarks

The influence of experimental errors on the accuracy of finite-element model corrections has been investigated and the uncertainties introduced into the correction factors, updated eigenfrequencies, and mode shapes have been discussed.

Essentially, the correction parameter uncertainty is progressively increased with the magnitude of the experimental error. For small errors a linear range exists and contributions from different error categories may be superimposed. The overall uncertainty levels are reduced by the number of modes involved in the updating process.

In case of absolute errors (independent of the measured deflection value) the magnitudes with respect to the actual deflections at the particular degrees of freedom significantly affect the correction accuracy. Another observation, which is characteristic for the individual numerical model and test structure, is a partial compensation of inaccuracies of measured natural frequencies and frequency deviations due to analytical modelling errors.

Frequency deviations due to experimental errors in the mode shapes are relatively small. The deviations due to inaccurately measured frequencies, however, are of the same order as the measurement error. Consequently, model updating requires a high precision in identifying the natural frequencies of a structure.

4.4 Closure

The model updating technique introduced in Section 3.2 has been applied to different test cases and novel techniques for the selection of correction parameters and the correction of substructures with viscous material properties have been proposed. The results of both the model validation and the newly introduced numerical prediction of modal data illustrate the importance of parameter selection when a physically consistent updated model is sought.

Next, a numerical study has been performed to investigate the problem of errors in the experimental reference data. A simulation procedure has been developed and the accuracy of the model corrections has been evaluated. The uncertainty in the resulting correction parameter has been found to increase with the magnitude of the experimental errors but to be reduced as the amount of experimental data used in the updating process is expanded.

Chapter 5

Complex Applications

5.1 Introduction

Based on the experience gained to this point the Eurocopter EC 135 helicopter is selected as an example to demonstrate the capability of the developed procedures and algorithms in validating a large-scale industrial finite-element model in Section 5.2. A novel approach for a consistent correction of non-isotropic material, enabling an efficient definition of updating parameters, is proposed. While the numerical model is successfully updated using systematic computational model updating techniques the importance of experimental data quality with respect to both precision and completeness becomes clearly evident.

To emphasise the advantages of model updating in other fields of application the accuracy of the damage localisation method introduced in Section 3.3 is investigated using a rectangular fuselage panel with two stiffening stringers. The investigations in Section 5.3 prove that the updated model leads to a better indication of the damage location than the conventional analytical model. The more pronounced peak in the localisation indicator allows the actual damage to be clearly distinguished from secondary effects caused by measurement errors and modelling imperfections.

Finally, attention is focused on the quality of the experimental modal data again. An analytical eleven-degrees-of-freedom system is used in a numerical study in Section 5.4 to examine the performance of the force tuning approach

suggested in Section 3.4 in comparison to existing methods. Next, the method is applied to a simple satellite model and operation along with actual experimental data and a realistic aerospace structure is evaluated. The potential for improving the quality of the experimental modal parameters, the capability to handle non-proportional damping and restricted accessibility, and the accuracy of the theoretical predictions of Mode Indicator Function (MIF) values are investigated. In order to assess the method with respect to its performance on a complex aerospace structure and under realistic test conditions the Polar Platform satellite developed by ESA is chosen. Considerable improvements with respect to mode isolation quality are found for all test cases. The results emphasise the need for systematic tuning techniques in those situations where the complexity of the structure under investigation involves a multi-point excitation to identify the normal modes.

The topology of the existing and newly developed software components utilised within the framework of this thesis is shown in Figure 5.1.

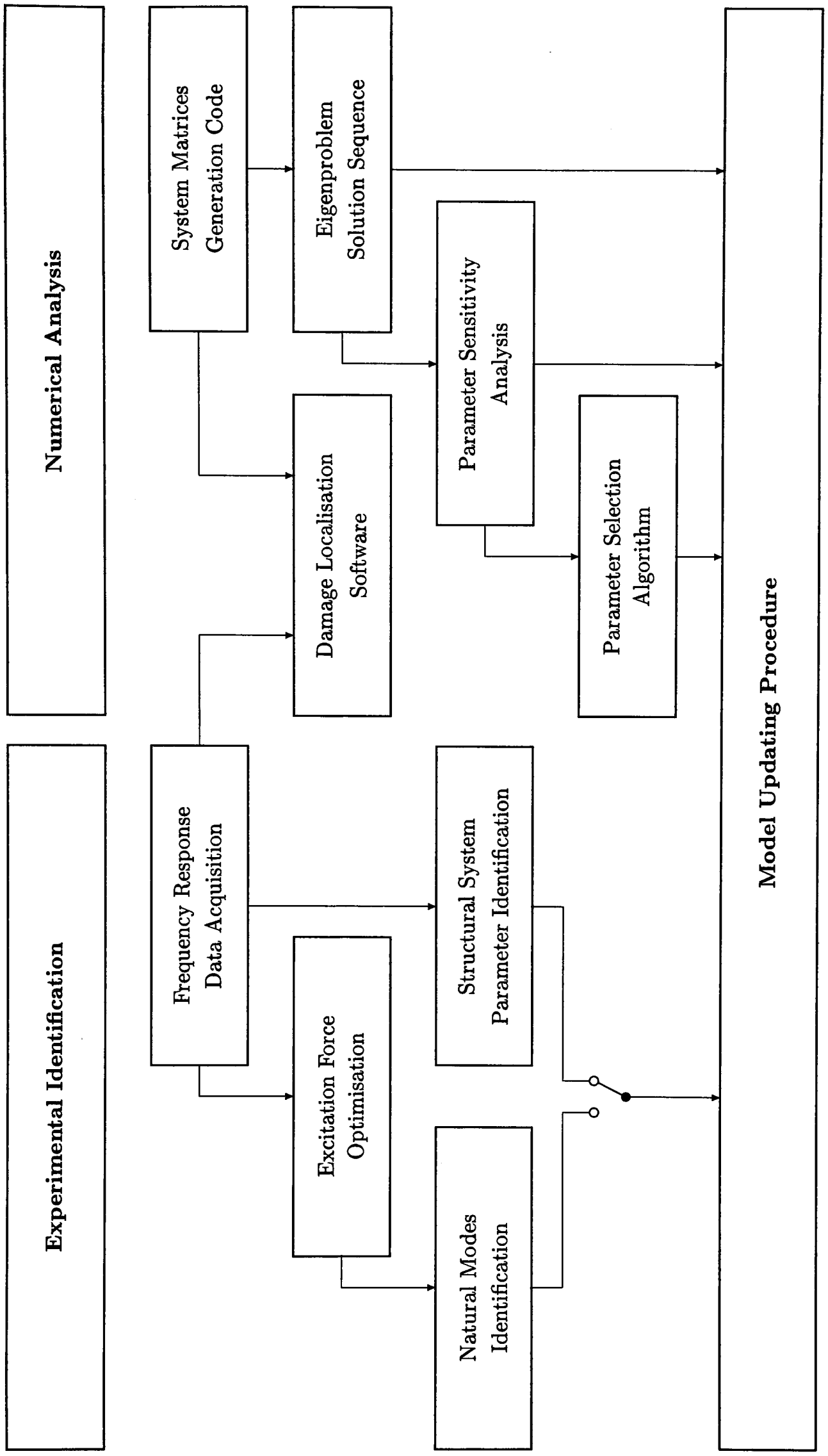

Figure 5.1: Software Technology

5.2 Updating of the EC 135 Helicopter

Following the initial application to a small laboratory test structure in the previous section the model updating technique as previously described was used to validate large-scale industrial finite-element models of the EC 135 helicopter [75, 85] and the Rosetta[1] Lander Module [81]. The application to the EC 135 helicopter is described in the following sections. Again, the objective has been to deliberately modify the finite-element model in order to achieve an improved accuracy in the analytical modal data. The validated model has been returned to Eurocopter Deutschland (ECD) for a model-based performance optimisation of a vibration suppression device which is located between the main gear box unit and the fuselage.

Experimental modal data have been extracted from frequency responses recorded during a Shake Test on the EC 135-S001 [40] prototype. The test was performed by DLR's Institute for Aeroelasticity in May 1994. The Ground Vibration Test Facility described in Section 2.4 was used to perform the test and collect the experimental reference data. Details on the test are given in [33].

The initial finite-element model, originally generated for dynamic analyses accompanying the development phase, was provided by (ECD). Based on the experience gained during the preceding validation of the analytical model for the Messerschmitt Bölkow Blohm (MBB) BO 105 helicopter the finite-element model was partially prepared for the necessary parameterisation of substructure element properties and material parameters.

5.2.1 Introduction

The EC 135, Figure 5.2, is a light, civil, twin-engine, multi-mission helicopter developed by the German/French Eurocopter S.A. group. It is designed for general passenger and cargo transport, police and air rescue services and offshore operations. The aircraft is powered by two turbine engines optionally supplied by Pratt & Whitney (PW 206B2) or Turbomeca (ARRIUS 2B2)

[1] named after the Rosetta Stone found at Rashid, Nile Delta, 196 BC.

Figure 5.2: The Eurocopter EC 135 Helicopter

and has a maximum take-off weight of 2,835 kg. The cruising speed is 141 kn (261 km/h) and the maximum range is approximately 700 km. The helicopter's overall dimensions are 12.16 m (length) by 3.51 m (height) and the main rotor diameter is 10.20 m. The EC 135 made its maiden flight on February 15th, 1994 and delivery started in 1996.

5.2.2 Finite-Element Model

A MSC/NASTRAN^{TM} Version 70.5 Bulk Data File representing the EC 135-S001 prototype was made available by ECD. The numerical model has approximately 33,000 degrees of freedom and contains 12,100 shell elements and 2,000 bar elements. No model reduction is applied to allow for a high degree of detail in the definition of correction parameters and straightforward physical interpretation of the results. To correctly model the Shake Test boundary conditions an elastic suspension, containing the effective stiffness components of the test rig, is added to the rotor head. In analogy to the Shake Test set-up, Section 5.2.3.1, the rotor blades are replaced by mass dummies.

For comparison of analytical eigenvectors and experimental mode shapes

the finite-element nodes closest in distance to the experimental acceleration sensor positions are used. Because of the fine mesh resolution in the numerical model the deviations to the actual sensor locations are in the range of millimetres which, regarding the helicopters overall dimensions, is assumed to be of no practical importance.

5.2.2.1 Definition of Correction Parameters in MSC/NASTRAN™

The mass and stiffness modifications for the substructures which are defined for correction are implemented into the MSC/NASTRAN™ Bulk Data File through property cards and material cards. The card entries are geometric properties, like thickness, cross section, or second moment of inertia and material parameters, e.g. Young's modulus, shear modulus, or density. This enables the desired physically meaningful model corrections. However, it must be ensured that no property or material card is attributed to any object outside the group of finite elements which form a single substructure, Figure 5.3. This would cause the correction to be effective to elements which do not belong to the chosen substructure. In this case the cards must be redefined in order to match the substructure boundaries. More details on the definition of substructures in MSC/NASTRAN™ were given in [150].

The correction of material parameters which are related through analytical expressions, e.g. Young's modulus, shear modulus, and Poisson's ratio, usually causes inconsistencies when just a single value in the group is modified. To avoid an over-determined system only those parameters needed to compute the full set of values should be specified in the material card. In this case the finite-element algorithm automatically calculates the missing parameters to equal the updated value.

5.2.2.2 Selection of Correction Parameters

The fundamental importance of selecting suitable updating parameters was emphasised in Section 4.2.4. In order to ensure that all correction parameters

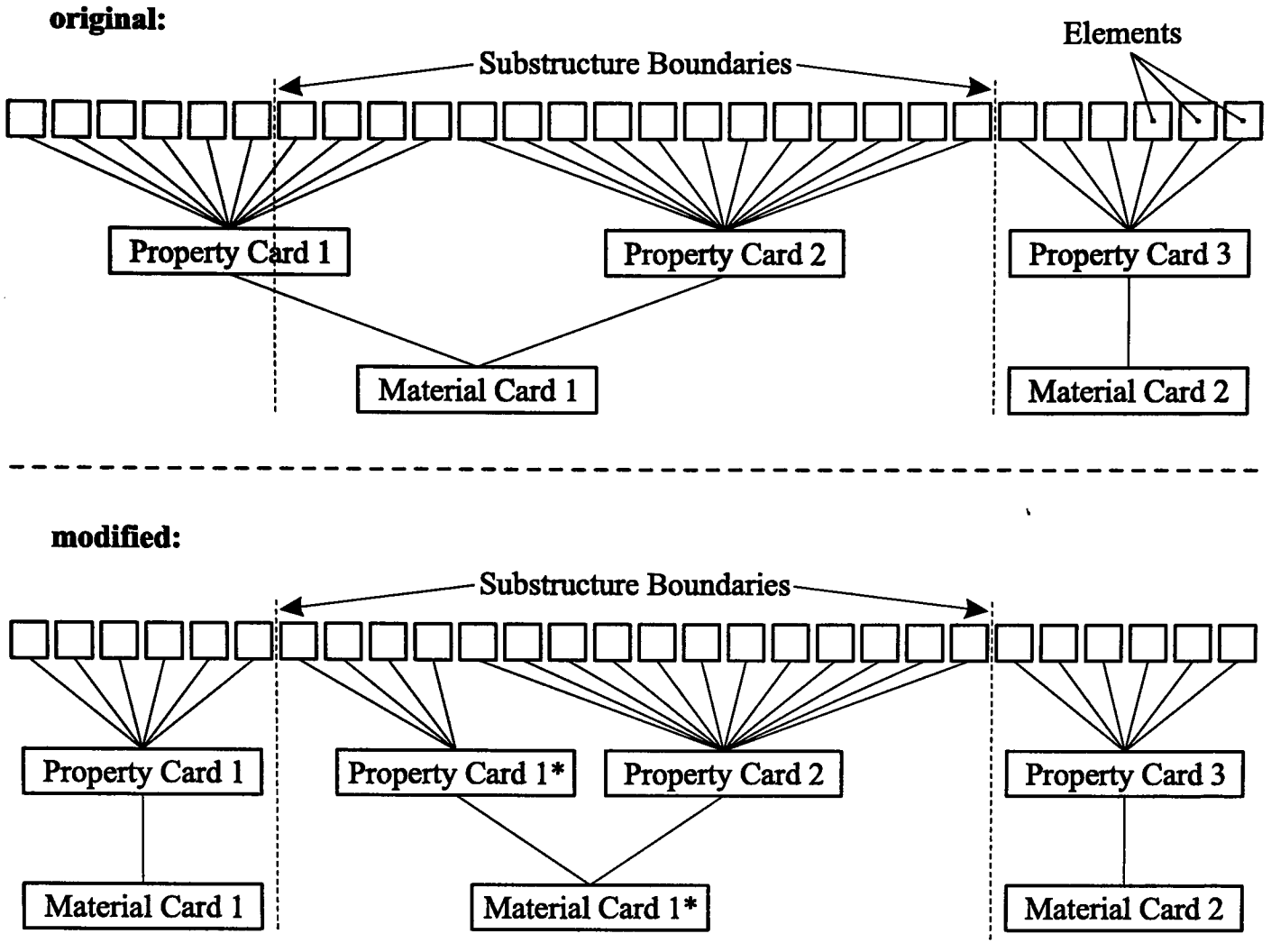

Figure 5.3: Coordination of Substructures, Property and Material Cards

have a significant influence on the helicopter's overall dynamic characteristics the selection of substructures is focused on those components which constitute the aircraft backbone structure. Specifically, the structural components intended to link the operational loads created by external aerodynamic forces (from the main rotor and Fenestron^{TM} [46] anti-torque system) and the principal inertia forces (induced by the fundamental concentrated masses, e.g. the main gear box, engines, or payload) are regarded. From these considerations the following prospective updating parameters, Figure 5.4, are chosen:

- **Frames #4, #4a, #5, #6, #7, & Rotor Deck.** The fuselage frames and rotor deck consist of grid frameworks which are reinforced with in-plane shear panels. Updating parameters are the beam longitudinal stiffness and the shell elements shear moduli.

- **Tail Boom Cone.** The tail boom cone transfers the forces and bending moments from the tail boom into the fuselage. It conceivably has a

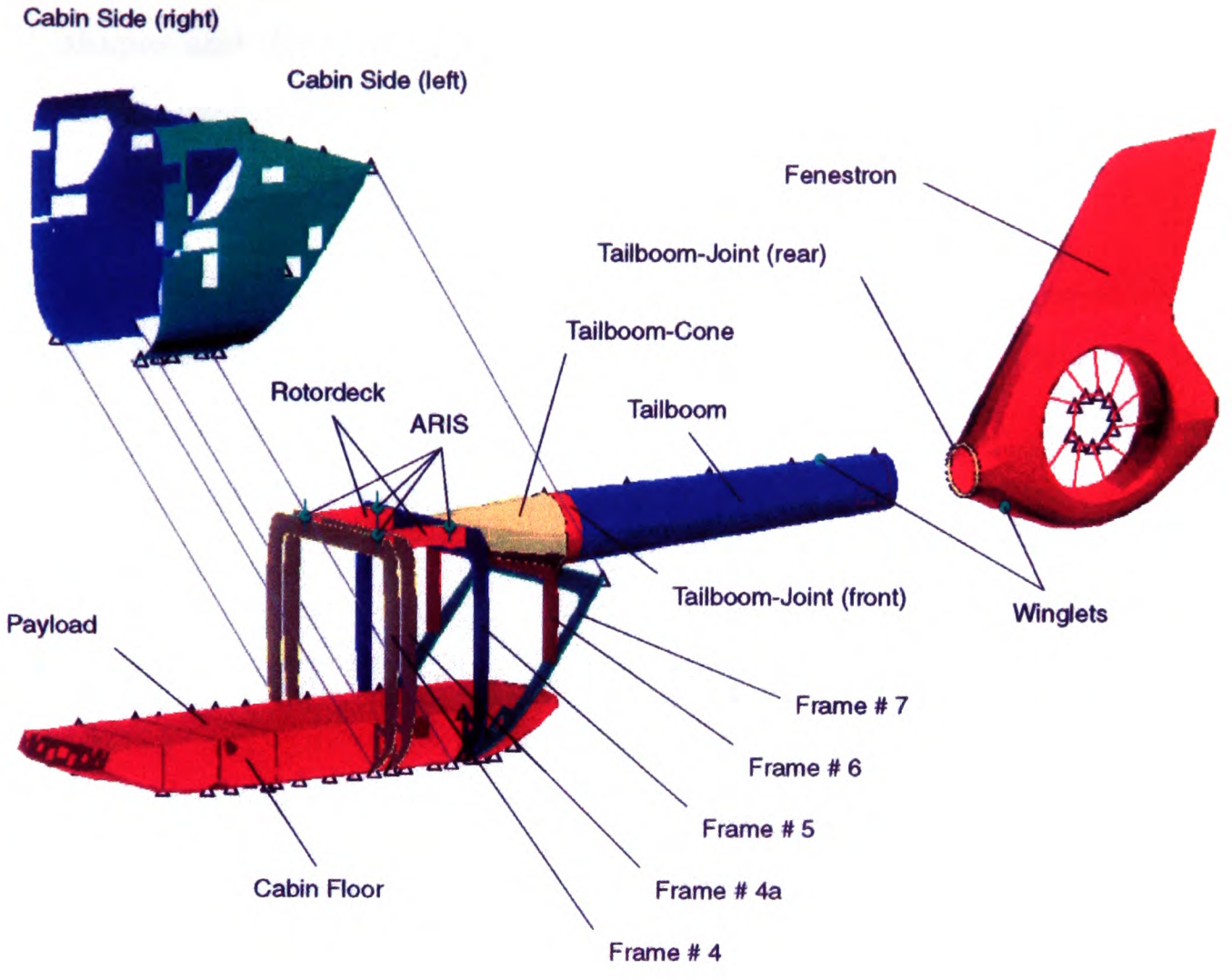

Figure 5.4: Prospective Substructures for the EC 135 Model Corrections

substantial influence on the dynamic characteristics of the tail boom and consequently the entire helicopter. Because of the principal construction being similar to the frames and rotor deck the beam stiffness and shell shear modulus are used as correction parameters.

- **Tail Boom Joints (front & rear).** The bolted ring joints between the tail boom cone and tail boom as well as the tail boom and Fenestron^{TM}, respectively, are highly uncertain with regard to the modelling of their effective stiffness and deformation behaviour. Young's modulus is updated on both joints to determine a representative substitute stiffness.

- **Cabin Sides (right & left).** With regard to the cabin side panel's function as to add shear stiffness to the fuselage the shell elements shear modulus is used for updating.

- **Tail Boom.** The tail boom considerably contributes to most mode

shapes and therefore is an important structural component with regard to the overall vibration characteristics of the helicopter. Here, Young's modulus and mass are parameterised.

- **Fenestron^{TM}.** The Fenestron^{TM} experiences comparatively small elastic deformations in all modes within the frequency range of interest. Furthermore, the number and location of available sensors is not sufficient for an acceptable identification of local deformations. Therefore, only a global mass correction is implemented here.

- **Cabin Floor & Payload.** The cabin floor rigidity is primarily provided through the applied box beam design. Considerable masses including fuel and payload are concentrated on the cabin floor and the forces from the frames are introduced in the rear segment. Therefore, the cabin floor is subjected to substantial stresses and strains. The correction parameters are Young's modulus, shear modulus, and mass.

- **Winglets.** The winglet mass is used to tune the tailplane mode.

- **Anti-Resonance Isolation System[2].** As the ARIS significantly affects the dynamics of the helicopter in general and because the transfer of vibrations from the main rotor to the fuselage is of particular interest the devices internal spring stiffness is updated.

- **Rotor Head & Gear Box[3].** The main rotor head and gear box unit represent substantial concentrated masses which are connected to the base structure via the flexible ARIS system. Together with the ARIS they form a functional unit and are considered to be extremely important for tuning the vibration suppression operation.

- **Engine Suspensions[3].** Due to the high concentrated masses in the turbine engines the engine suspension stiffness is used for tuning their rigid body modes (RBM).

[2]The Anti-Resonance Isolation System (ARIS) is a vibration damping device comprised of four isolation elements located between the main rotor gear box and fuselage.

[3]The Rotor Head, Gear Box, and Engine Suspensions are not depicted in Figure 5.4.

Following the selection strategy suggested in Section 4.2.4.1 the potential correction parameters are now evaluated as to their sensitivities with respect to the analytical modal data according to eqs. (4.3). Based on the computed eigenvalue and eigenvector sensitivities, Figure 5.5, and keeping in mind that only parameters with sufficiently high sensitivities should be preferred for further consideration, various modifications are applied to the initial group of parameters:

1. Due to their extremely low sensitivities the front and rear tail boom joints and the cabin floor shear modulus are eliminated completely.

2. In order to increase their sensitivities the frames #4 to #7 are redefined to form a single substructure. Now, all corrections of the beam longitudinal stiffness and the shell shear modulus become effective for all frames simultaneously. This move appears to be justified since any potential modelling error should be of equal nature and magnitude for all frames.

3. At this stage the helicopter used in the Shake Test exceeds the total mass of the initial finite-element model by approximately 225 kg. Although the masses of crew, passengers, and fuel were already included in the model the existence of a global mass distribution error is considered unlikely. Conversely, it is assumed that an additional loading of lead bags on the cabin floor was not taken into account in the numerical model. Because the amount of additional mass is only a coarse estimate based on an internal test notice, the payload mass parameter is used hereafter to update the additional weight that was introduced on the cabin floor.

The sensitivities for the modified set of updating parameters are plotted in Figure 5.6. Next, the new parameters are tested for their convergence behaviour and the capability to return accurate results. The test procedure outlined in Section 4.2.4.1, step three, is used and the final correction parameters are printed in bold in Figure 5.6.

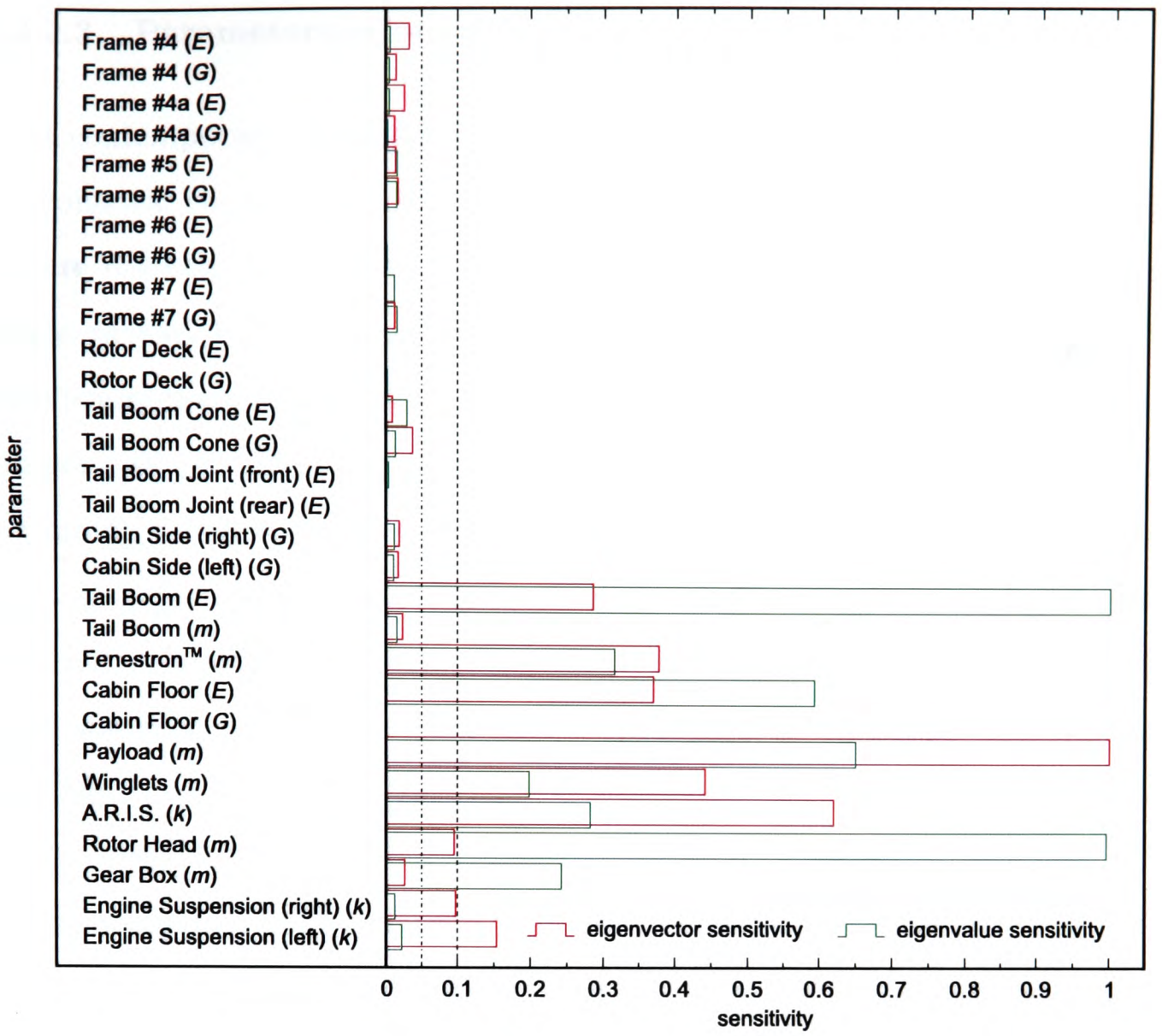

Figure 5.5: Parameter Sensitivities for First Selection of Substructures

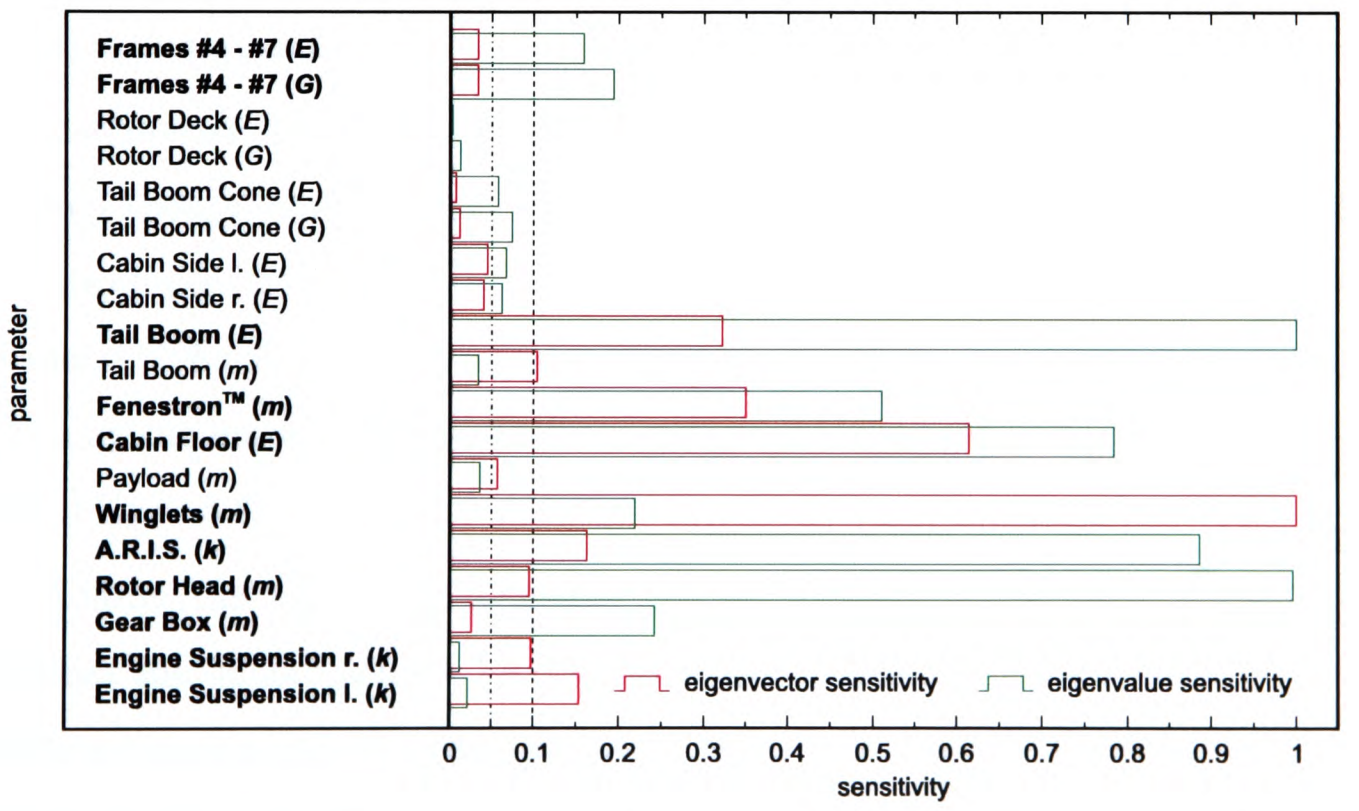

Figure 5.6: Parameter Sensitivities for Second Selection of Substructures

5.2.2.3 Parameterisation of Non-Isotropic Material Regions

Most contemporary aerospace structures do not only comprise a high degree of geometric complexity, they also consist of composite materials which often are difficult to describe in a numerical model. With the objective of a weight-saving, fail-save, and damage tolerant design many of the EC 135's main components are manufactured from non-isotropic fibre composites. These components generally consist of a multitude of individual layers, all of which containing different types of carbon fibres and having distinctive mesh patterns or fibre orientations. The complexity of the associated material laws does not encourage a direct correction of discrete parameters. In order to avoid material parameter inconsistencies, acquire an extended flexibility in the definition of updating parameters, and enable an efficient parameterisation in MSC/NASTRAN^{TM} a supplementary layer of correction elements, being superimposed to the original structure, Figure 5.7, is introduced [78, 79]. The correction elements are linked directly to the existing finite-element grid points and homogeneous isotropic material properties are assigned. Now, all necessary corrections are introduced through modifying the individual mass or stiffness parameters of the correction element layer while the original structure remains unchanged.

In the basic updating approach, eq. (3.1), the model corrections are implemented though proportional variations of the submatrices $\mathbf{K}_i$ and $\mathbf{M}_j$. This requires finite initial stiffnesses and/or masses to be specified for the correction elements. The mass and stiffness of the base substructure is modified indirectly by using the mass/stiffness of the correction element layer as updating parameter, Figure 5.8.

Adding the correction elements has an unwanted side effect in that it changes the substructure's original stiffness and mass distribution. This is likely to cause significant eigenfrequency shifts and mode shape alterations. To eliminate the undesirable correction layer influence on the structure's modal parameters a second layer of offset elements is introduced, Figure 5.9. The offset elements have negative stiffness or mass parameters equal in magnitude

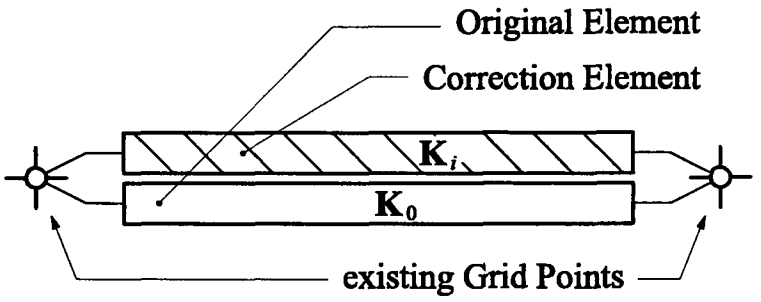

Figure 5.7: Parameterisation of Non-Isotropic Material Regions (I)

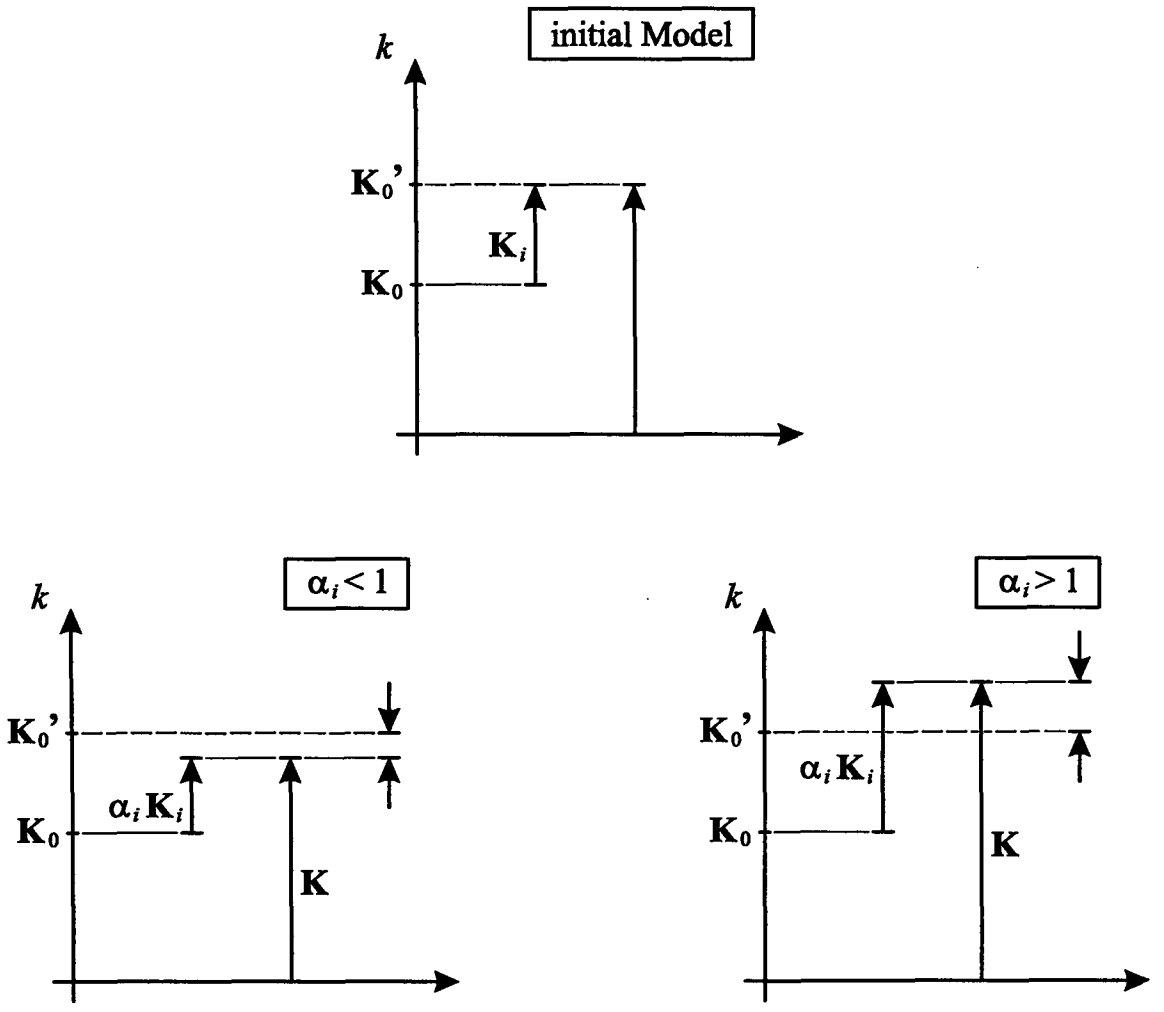

Figure 5.8: Indirect Stiffness Modification using Correction Elements

to the initial values defined for the corresponding correction elements, Figure 5.10. This balances the additional stiffness and/or mass previously added to the substructure and results in the overall system submatrices to be identical to those given in the original model.

The initial mass and stiffness parameters for the correction elements need not necessarily to be representative for the global mass and stiffness of the original substructure. For the EC 135 helicopter spatially uniform stiffness and mass distributions are used and the initial values are chosen such that suitable parameter sensitivities which enable to use the substructures in the

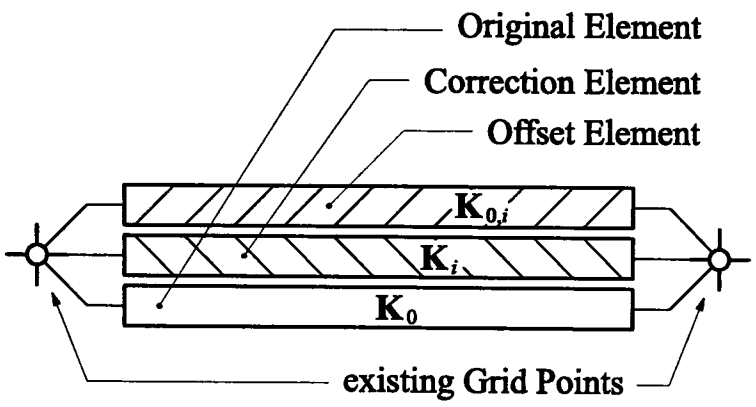

Figure 5.9: Parameterisation of Non-Isotropic Material Regions (II)

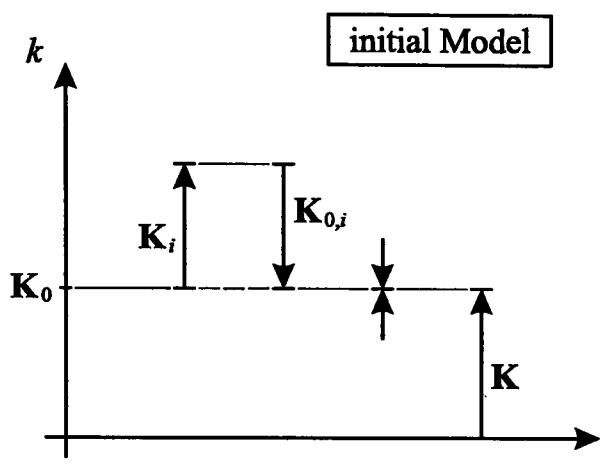

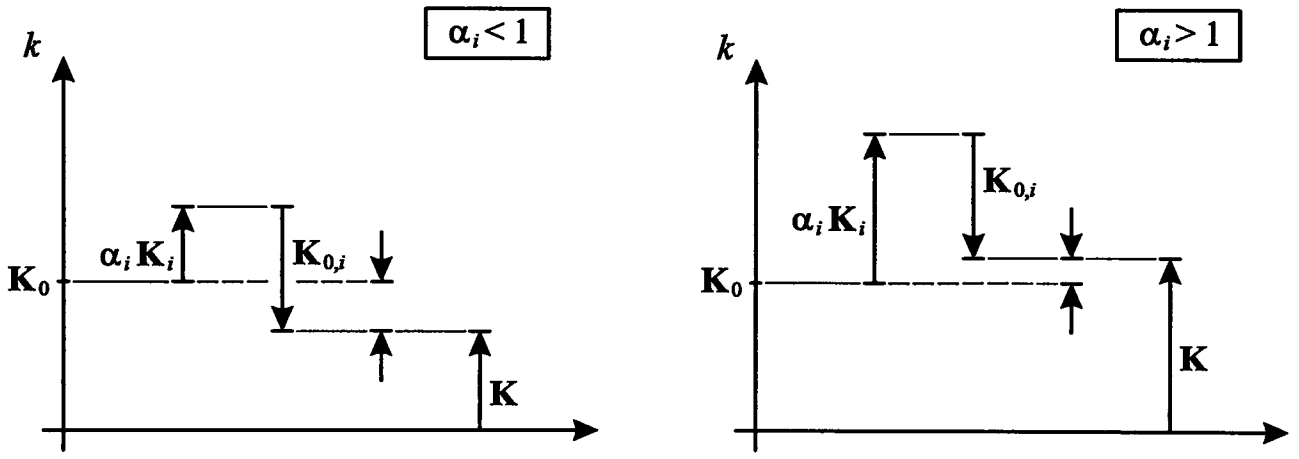

Figure 5.10: Stiffness Modification using Correction and Offset Elements

model corrections are obtained. In this situation however, only the absolute changes of mass and stiffness comprise useful information for the finite-element modelling. The main purpose of this application was to generate these data. The approach is applied to the cabin floor, tail boom, and Fenestron^{TM} substructures and the initial properties for the correction elements are given in Table 5.1.

No.	Substructure	d/[mm]	E/[N/m^2]	G/[N/m^2]	ν/[-]	ρ/[kg/m^3]
1	Cabin Floor	1.00	7.20×10^{10}	7.20×10^{10}	0.3	-
2	Tail Boom	1.00	7.20×10^{10}	-	0.3	-
3	Fenestron^{TM}	1.00	-	-	-	3.20×10^3

Table 5.1: Initial Properties for the Correction Elements

5.2.3 Processing the Experimental Data

5.2.3.1 Shake Test on the S001 Prototype

The Shake Test on the EC 135-S001 prototype [33] was performed to study various mechanisms of vibration reduction inside the fuselage and at the pilot seat. The helicopter was suspended in a test rig by means of a pneumatic suspension and a harmonic excitation was applied at the main rotor head. Excitation forces in longitudinal, transversal, and vertical direction as well as excitation moments around the pitch and roll axis were applied. Structural vibrations were recorded from 64 acceleration sensors, most of which were concentrated around the main gear box and ARIS system and on the cabin floor. Due to their high vibration amplitudes the main rotor blades were replaced by rigid mass dummies. Frequency Response Functions (FRF) were computed from the excitation forces and measured structural responses. Additionally, 7 normal modes were identified directly using the Phase Resonance Method (PRM).

It should be noted that the primary purpose of the Shake Test was to measure frequency response data for different rotor head excitations and to assess the performance of the ARIS system. This led to an acceleration sensor distribution which is not well suited for an experimental modal analysis. No appropriated multi-point excitation forces (cf. Section 3.4.2) were used to identify the normal modes and the mode shapes extracted from the frequency response measurements also suffer from the incomplete excitation. As a result, the experimental data base available for updating must be considered to be of mediocre quality.

5.2.3.2 Derivation of Modal Parameters

Modal parameters have been derived from both the results obtained with the Phase Resonance Method and the recorded frequency response data using a phase separation method. Experimental data for the test configuration equivalent to the finite-element model has been processed. To eliminate the influence of structural non-linearities only the frequency responses for the lowest excitation force levels have been considered. The direct phase separation method FDPI[4] [92] has been used to extract the modal parameters. The method is an integral part of the data acquisition and analysis software package CADA-X [109] and is based on the phase separation method ISSPA[5] which has been introduced by LINK [105]. The derivation of modal parameters from the measured frequency response data has been performed by FÜLLEKRUG [75].

Five FRFs acquired from three translational main rotor hub excitations in longitudinal, transversal, and vertical direction as well as two pith and roll excitations, respectively, have been selected for the analysis. Furthermore, seven mode shapes directly identified with the Phase Resonance Method have been available. The accumulated Frequency Response Function from all acceleration sensors and the Mode Indicator Function (MIF), eq. (3.54), have been used in the analysis. The poles, i.e. eigenfrequencies and damping values, have been determined from a stabilisation diagram and the corresponding eigenvectors have been computed. Then, the modes derived from the frequency response data and Phase Resonance Method have been correlated and the lower quality mode shapes eliminated. As a result, fifteen experimental mode shapes covering the frequency range from 5 Hz to 35 Hz have been obtained for the numerical model validation.

In Table 5.2 the Modal Assurance Criterion (**MAC**) for all combinations of experimental eigenvectors

$$\mathbf{MAC}_{rs} = \frac{|\boldsymbol{\varphi}_{e,r}^{\mathrm{T}} \cdot \boldsymbol{\varphi}_{e,s}|^2}{(\boldsymbol{\varphi}_{e,r}^{\mathrm{T}} \cdot \boldsymbol{\varphi}_{e,r})(\boldsymbol{\varphi}_{e,s}^{\mathrm{T}} \cdot \boldsymbol{\varphi}_{e,s})} \qquad \text{for } r, s = 1, \ldots, N, \tag{5.1}$$

[4] Frequency Domain Direct Parameter Identification
[5] Identification of Structural System Parameters

i.e. the cross-correlation, is shown. Assuming linearly independent eigenvectors, the auto-correlation is equal to one for $r = s$ and vanishes for $r \neq s$. However, due to unavoidable imperfections, like experimental errors and spatial incompleteness, this is rarely the case with measured data. Here, the off-diagonal values should be as small as possible. The auto-correlation in Table 5.2 reveals several strong couplings of modes (in particular between modes numbered 4 to 6, 7 to 10, and 11 to 13) which is mainly due to the insufficient number and poor spatial distribution of acceleration sensors.

Moreover, it should be kept in mind that the set of normal modes is likely to be incomplete in that not all modes in the frequency range under investigation were identified due to the inappropriate excitation. Since only a single excitation point at the rotor head was used to record the measured FRFs only those mode shapes which are significantly excited by the rotor head excitation are contained in the experimental data.

Because of the reasons mentioned the strong coupling of experimental modes and the modal incompleteness establish highly unfavourable conditions for the numerical model corrections.

5.2.4 Results

Both measured eigenfrequencies and mode shapes are used to validate the finite-element model. In each iteration step experimental and analytical eigenvectors are compared according to the Modal Assurance Criterion (**MAC**), eq. (4.2), and natural frequency deviation Δf, eq. (4.1). If the **MAC** between a measured and a computed mode is larger than 60 % and the difference between the associated eigenfrequencies is lower than 30 % the modes are considered to be identical and are allocated automatically for comparison in the error vector, eqs. (3.12) and (3.21).

In order to balance the dominating number of mode shape deflection components ($M \times N$ values) as compared to the number of frequency deviations (N values) an automatic eigenfrequency weighting is applied. Using the elements of the weighting matrix $\mathbf{W}_\varepsilon$ each eigenfrequency gradient in the Jacobian

Table 5.2: Correlation of Experimental Mode Shapes

Mode No.	1	2	3	4	5	6	7	8	9	10	11	12	13	14	15
1	100	0.28	0.27	**37.29**	7.80	8.00	1.49	0.00	0.09	0.05	0.53	0.31	1.57	0.09	0.00
2	0.28	100	7.10	0.85	0.05	0.62	0.05	0.94	1.83	1.98	0.24	0.17	0.27	0.47	**19.82**
3	0.27	7.10	100	0.05	0.51	0.04	2.84	0.13	0.93	3.18	0.01	0.04	0.31	0.09	0.27
4	**37.29**	0.85	0.05	**100**	**20.50**	**11.37**	1.58	0.11	0.01	0.26	**22.23**	3.78	4.08	0.05	0.01
5	7.80	0.05	0.51	**20.50**	**100**	**30.62**	7.69	1.10	0.07	0.02	7.77	3.33	4.28	0.03	0.00
6	8.00	0.62	0.04	**11.37**	**30.62**	**100**	9.36	0.35	0.01	0.04	5.01	1.14	0.53	0.56	0.07
7	1.49	0.05	2.84	1.58	7.69	9.36	**100**	**81.75**	**70.83**	**49.98**	0.29	0.14	0.08	0.90	**17.68**
8	0.00	0.94	0.13	0.11	1.10	0.35	**81.75**	**100**	**81.03**	**55.08**	0.01	0.26	0.05	2.51	**19.85**
9	0.09	1.83	0.93	0.01	0.07	0.01	**70.83**	**81.03**	**100**	**85.73**	0.06	1.49	0.01	3.42	**36.21**
10	0.05	1.98	3.18	0.26	0.02	0.04	**49.98**	**55.08**	**85.73**	**100**	0.22	0.41	0.23	3.47	**44.92**
11	0.53	0.24	0.01	**22.23**	7.77	5.01	0.29	0.01	0.06	0.22	**100**	**36.04**	**61.60**	0.88	0.81
12	0.31	0.17	0.04	3.78	3.33	1.14	0.14	0.26	1.49	0.41	**36.04**	**100**	**53.04**	4.02	1.09
13	1.57	0.27	0.31	4.08	4.28	0.53	0.08	0.05	0.01	0.23	**61.60**	**53.04**	**100**	0.43	0.16
14	0.09	0.47	0.09	0.05	0.03	0.56	0.90	2.51	3.42	3.47	0.88	4.02	0.43	100	3.59
15	0.00	**19.82**	0.27	0.01	0.00	0.07	**17.68**	**19.85**	**36.21**	**44.92**	0.81	1.09	0.16	3.59	100

matrix is weighted according to the norm of the corresponding eigenvector displacement gradients. The weighting procedure was described in [150]. The automatic eigenfrequency weighting assures that eigenfrequency deviations have the same impact on the model corrections as eigenvector errors. This also takes into account that reducing the frequency deviations is often considered the primary goal in model updating.

The model corrections are based on the parameters printed in bold in Figure 5.6 and the results are plotted in Figures 5.11 to 5.14. Convergence is reached after six iteration steps and between eight and nine analytical eigenvectors are allocated to experimental mode shapes, Figure 5.14. Both convergence and mode correlation suffer from the low experimental data quality discussed in Section 5.2.3.

In Figure 5.11 the correction factors are plotted as a function of iteration step. It must be noted that for the cabin floor, tail boom, and Fenestron^{TM} substructures the correction factors relate to the initial mass and stiffness parameters specified for the correction elements, Table 5.1. Since the correction elements are not modelled to match the substructure's global masses and stiffnesses the correction factors likewise do not represent actual modelling errors of these magnitudes. Here, only the absolute changes of mass and stiffness, Table 5.3, bear a physical significance.

For the conventionally updated substructures the correction factors are found to be quite modest and remaining within the magnitudes anticipated for the modelling errors by ECD's numerical modelling staff. High mass correction factors for the rotor head are observed. Apparently, the moving mass of the pneumatic suspension system is much lower than previously assumed. An

No.	**Substructure**	$\Delta E/[\mathrm{N/m^2}]$	$\Delta G/[\mathrm{N/m^2}]$	$\Delta m/[\mathrm{kg}]$
1	Cabin Floor	4.95×10^{10}	4.95×10^{10}	-
2	Tail Boom	3.21×10^{10}	-	-
3	Fenestron^{TM}	-	-	17.00

Table 5.3: Mass and Stiffness Corrections for Non-Isotropic Substructures

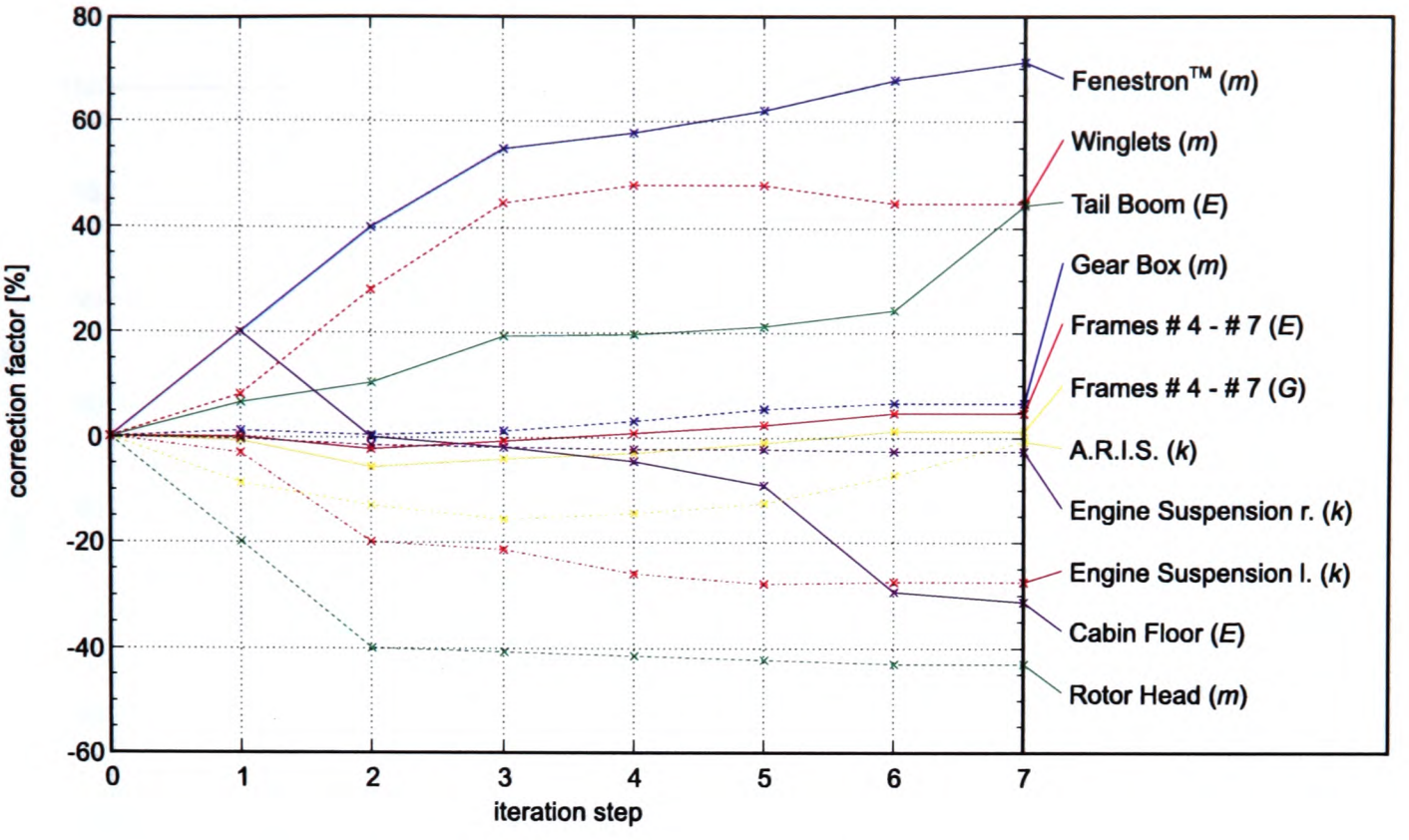

Figure 5.11: Updating Results for the EC 135, Convergence of Correction Factors

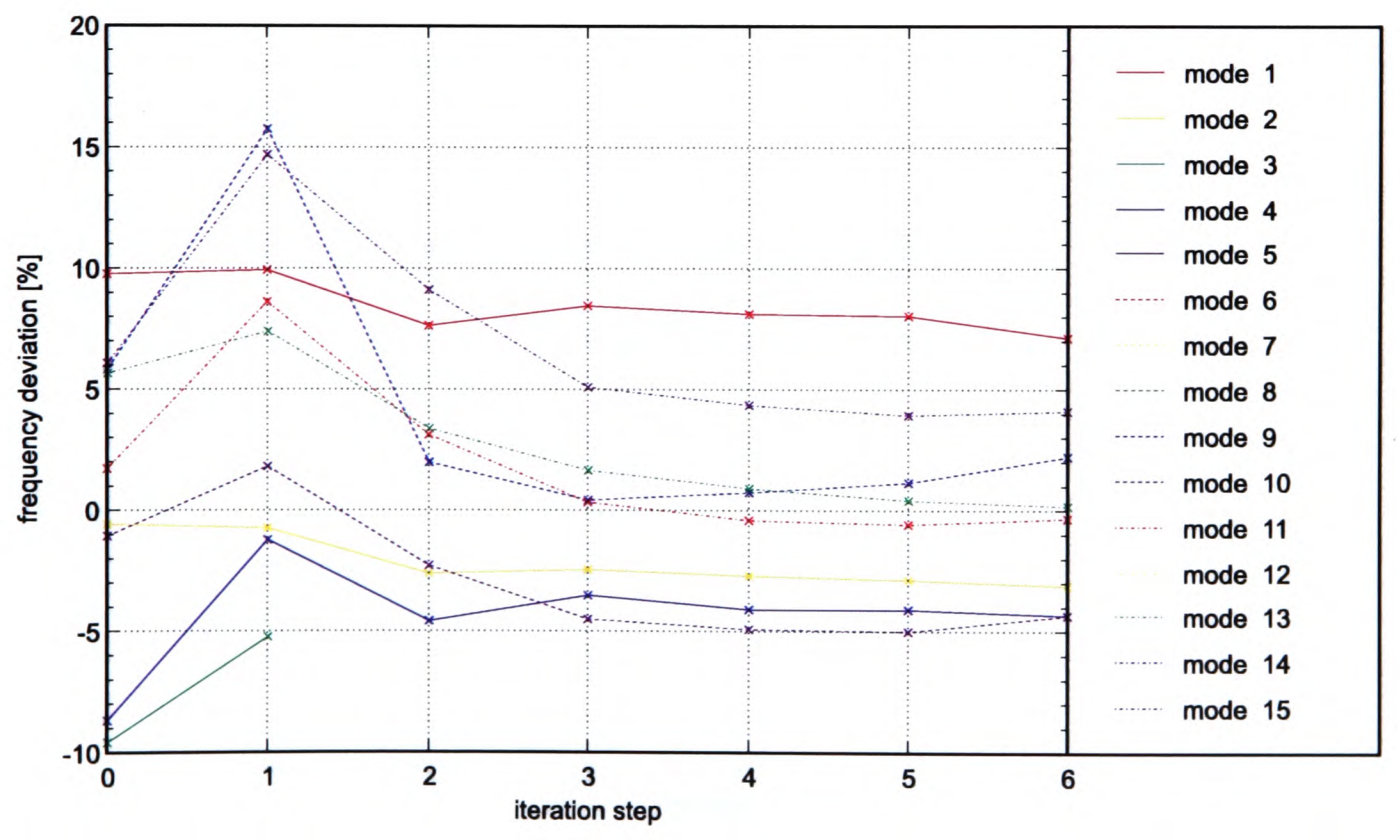

Figure 5.12: Updating Results for the EC 135, Convergence of Frequency Deviations

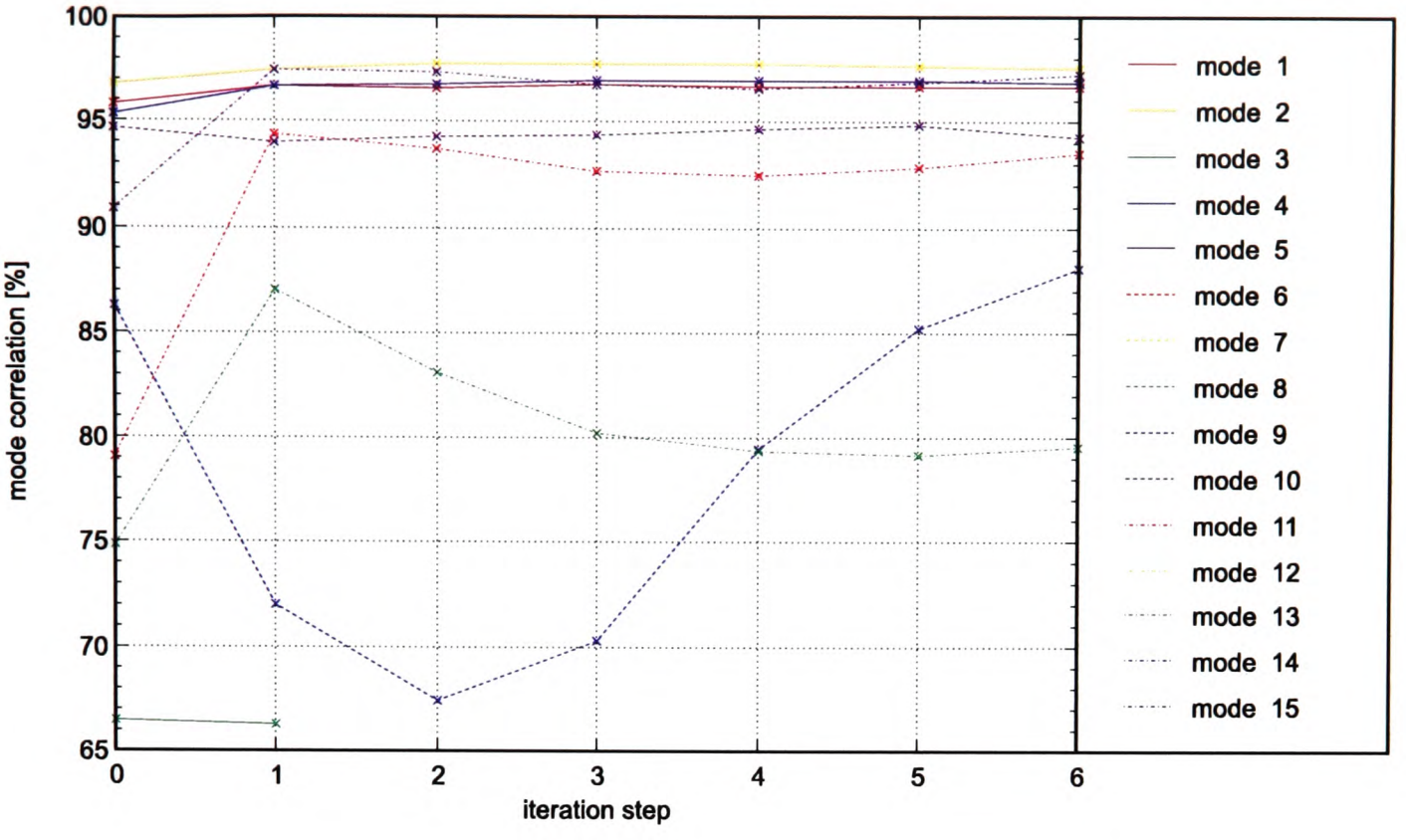

Figure 5.13: Updating Results for the EC 135, Convergence of **MAC**-Values

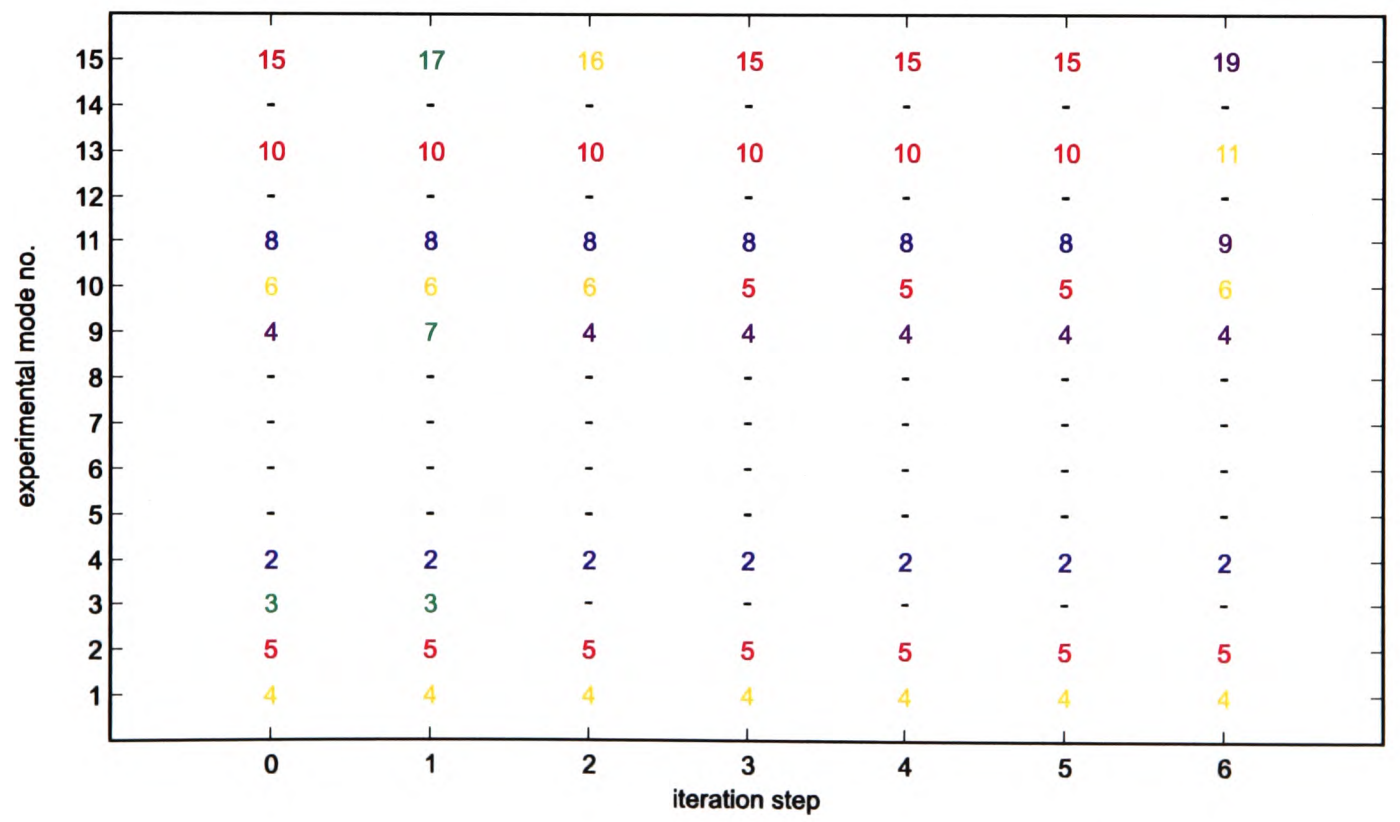

Figure 5.14: Updating Results for the EC 135, Mode Allocation

exceptionally high correction also is observed for the winglets mass. This result gives an indication that either different winglets were installed on the helicopter in the Shake Test configuration or the actual modelling error is located in the stiffness of the joint between tail boom and tailplane. However, the insufficient number of acceleration sensors in this area does not allow a detailed investigation of this subject.

Regarding the frequency deviations, Figure 5.12, the residuals are reduced from ± 10 % to $+7.1/-4.3$ %. Here, the consequences of spatial and modal incompleteness and the heavy coupling between individual modes in the experimental reference data becomes most apparent.

With the exception of modes numbered 13 ($\mathbf{MAC} = 80$ %) and 9 ($\mathbf{MAC} = 88$ %) the correlation between analytical and experimental mode shapes, Figure 5.13, is greater than 93 %.

Subsequent numerical investigations ([80], unpublished) on the effects of spatial incompleteness have revealed that neither the model updating method nor the set of correction parameters are inadequate to produce better results. Assuming a homogeneous distribution of experimental degrees of freedom the minimum number of acceleration sensors required for a good correlation of experimental and analytical data and superior model improvement has been found to be in the order of 200 to 250.

5.2.5 Concluding Remarks

An application of finite-element model updating to an authentic industrial aerospace structure has been presented. To identify the mechanically relevant correction parameters and achieve sufficient sensitivities with respect to eigenfrequencies and mode shapes the selection method proposed in Section 4.2.4 has been used. Additionally, a novel technique for the parameterisation of substructures with non-isotropic material properties has been suggested.

Experimental modal parameters have been derived from measured frequency response data using a phase separation method. Owing to the sparse acceleration sensor distribution a high degree of spatial incompleteness and

poor correlation of analytical and experimental modes has been observed. Additional problems have occurred due to apparent configuration differences between the helicopter used in the Shake Test and the one represented by the numerical model.

Yet, the results obtained under these difficult conditions are considered to be quite adequate and it may be concluded that, using the application strategies introduced in this thesis, the model updating method is well capable to work with complex aerospace structures.

5.3 Localisation of Structural Damage

In the following section the damage localisation method suggested in Section 3.3 is applied to a small representative aircraft fuselage component [83]. With the main purpose of demonstrating the advantages of model updating on the localisation accuracy the results for two cases, before and after the finite-element model is updated with experimental mode shapes and natural frequencies from the undamaged test structure, are compared.

5.3.1 Test Structure

On most existing aerospace systems the critical structural components which require monitoring are well-known, i.e. the locations where structural faults are most likely to occur are limited. Accordingly, the damage localisation method suggested in Section 3.3 is applied to a basic yet characteristic aircraft component rather than to a more complex substructure. A rectangular fuselage panel made of carbon fibre reinforced polymers (CFRP) with two stiffening stringers on the upper side, Figure 5.15, is chosen for this purpose. The base plate measures 500 by 400 mm^2 and the stringers are 40 mm high. The panel is made from 18 plies of CCC 460 bi-directional carbon fibre mesh manufactured by C. Cramer & Co., Heek-Nienborg, Germany and the total mass is approximately 1.4 kg.

A piezoelectric actuator module bonded to the top surface between the stringers is used for dynamic excitation. A second similar device mounted in the same position on the bottom surface serves as a response sensor. The piezoelectric modules consist of a $30 \times 50 \times 0.2$ mm^3 layer of PIC 151 modified lead zirconate titanate (PZT) ceramic manufactured by PI Ceramic GmbH, Lederhose, Germany, which is covered by copper-nickel mesh electrodes and thin protective glass fibre layers on the upper and lower sides. The position of actuator and sensor is chosen such that as many mode shapes as possible can be excited in the frequency range under investigation, Section 5.3.2.1.

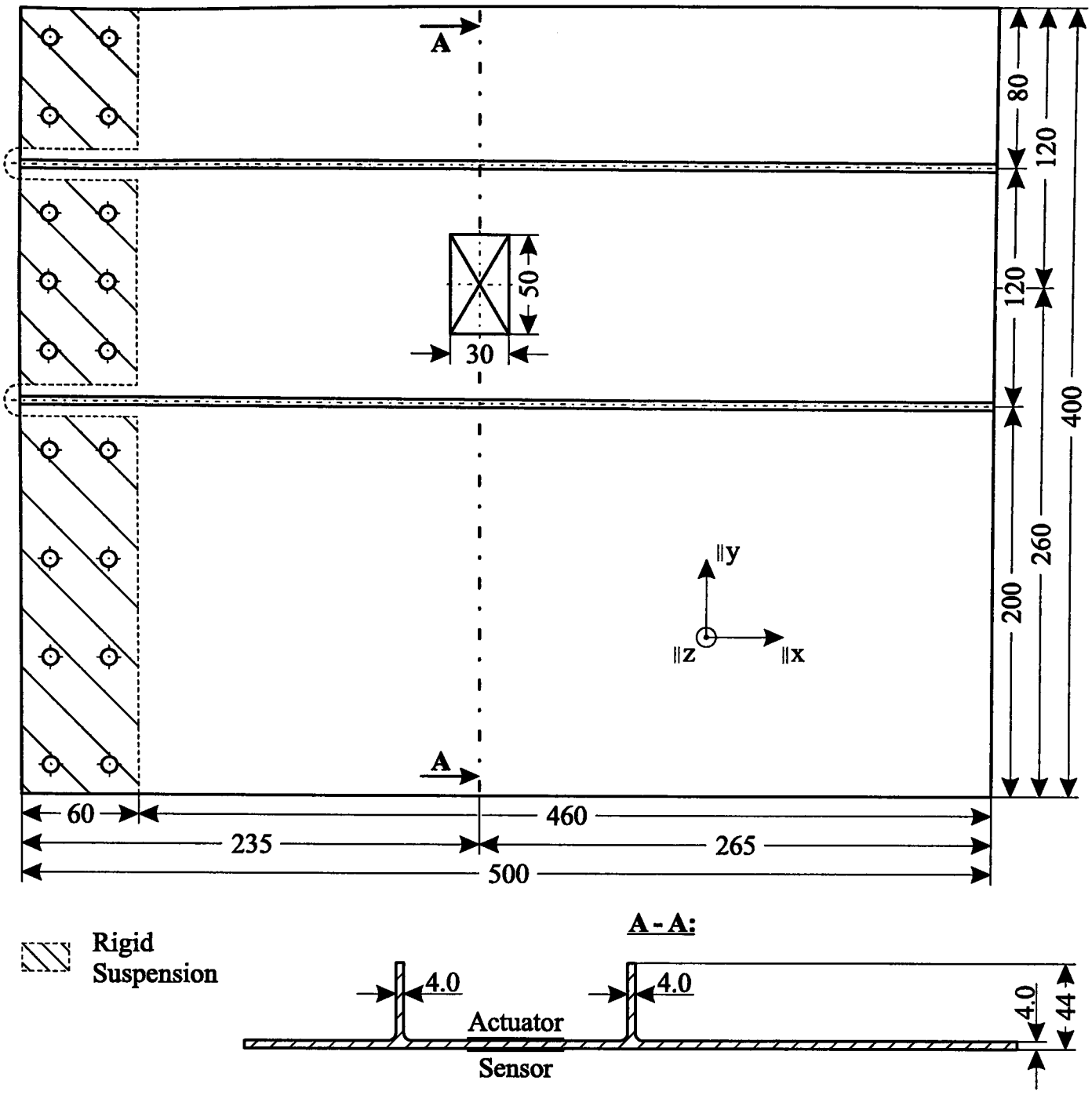

Figure 5.15: Stringer-Stiffened CFRP-Panel

5.3.2 Finite-Element Model

The finite-element analysis is executed in MSC/NASTRAN™ Version 70.5. The numerical model, Figure 5.16, consists of a total of 2,400 CQUAD4 shell elements with orthotropic material properties, Table 5.4. Such a fine mesh resolution would not be necessary for a standard dynamic analysis of a comparatively undemanding structure but is needed for a good spatial resolution in the modelling of the structural damage. A rigid suspension is assumed along the clamped boundary (represented by a dashed line in Figure 5.15).

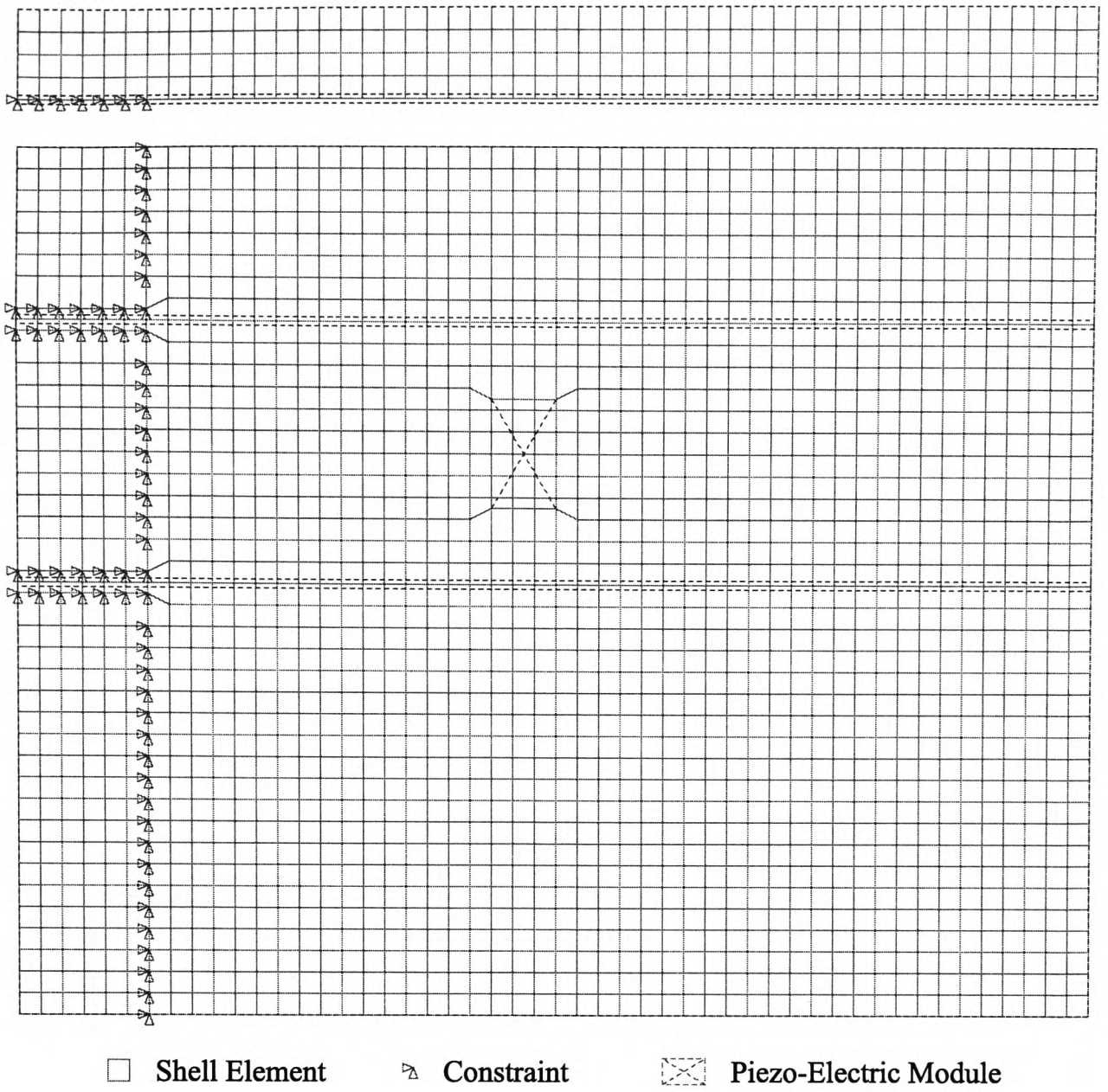

Figure 5.16: Finite-Element Mesh of the Stringer-Stiffened CFRP-Panel

Material Parameters:			
ρ	1.46×10^3 kg/m^3	G_{xy}	5.00×10^9 N/m^2
E_{xx}	5.40×10^{10} N/m^2	G_{xz}	2.00×10^9 N/m^2
E_{yy}	5.40×10^{10} N/m^2	G_{yz}	2.00×10^9 N/m^2

Table 5.4: Material Parameters for the Stringer-Stiffened CFRP-Panel

5.3.2.1 Preliminary Investigations

The main goals of the preliminary investigations are to find an optimised actuator/sensor position that allows collection of the necessary input data for the damping-based damage localisation method and to assess the method's spatial resolution using a prototype delamination model.

Modelling of Piezoelectric Modules. Within the scope of these investigations it will not be necessary to describe the behaviour of the piezoelectric material in full detail. Only the features that are relevant for a dynamic analysis are considered. Therefore, a simplified model of the piezoelectric actuator module is built which does not take into account all interactions between the elastic deformation and the electrical and thermal fields. The simplified model makes use of an analogy between the piezoelectric effect and the effect of thermal expansion permitting the use of existing standard finite-elements. In this analogy the electrical voltage applied to the electrodes of the piezoelectric module is represented by the temperature of the finite shell elements and the piezoelectric coefficients (characterising the relationship of the external electrical field and the strains) are approximated by the coefficients of thermal expansion (which quantify the relationship between the element's temperature and the strains). The mechanical excitation is realised through a homogeneous harmonically oscillating temperature load of variable frequency on the actuator shell elements resulting in a homogeneous[6] in-plane strain across the actuator's surface.

For the shell elements representing the sensor module the electrical output voltage U is assumed to be a linear function of the in-plane strain components $\frac{\partial u_x}{\partial x}$ and $\frac{\partial u_y}{\partial y}$ according to

$$\mathrm{U} = \zeta_x \cdot \frac{\partial u_x}{\partial x} + \zeta_y \cdot \frac{\partial u_y}{\partial y} \,, \tag{5.2}$$

where ζ_x and ζ_y are proportionality constants between the strains and the output voltage. Again, only qualitative information on the suitability of the sensor position to collect the required vibration data is needed here.

Hereafter, the finite-element model with integrated piezoelectric actuator and sensor modules is used for the frequency response calculations and the primary tests of the initial delamination model and localisation method.

[6]It is assumed that no thermal conductivity between the actuator shell elements and the base structure occurs.

Actuator & Sensor Position. To ensure that the largest possible amount of information is acquired from the test structure, the location which permits the piezoelectric actuator to excite the largest possible number of modes in the given frequency range must be found. From the physical point of view the in-plane surface strain components $\partial u_x/\partial x$ and $\partial u_y/\partial y$ at the chosen location must be sufficiently high to allow for the introduction of an adequate amount of energy into the structure. Simultaneously, this ensures that the co-locally mounted sensor module generates a sufficiently high output signal.

The analysis is based on the analytical eigenvectors. From the computed surface strain fields of each mode shape the location must be identified, where the strains in the actuator/sensor area are non-zero for as many modes as possible. Due to the finite dimensions of the piezoelectric modules it can not always be avoided that a nodal line comes close to or crosses the actuator/sensor area.

Two examples of surface strain fields for different mode shapes are plotted in Figures 5.17 and 5.18. The optimised actuator/sensor location is indicated by a white box. Due to the stringer stiffness the strains in y-direction are generally higher than the x-direction components. Therefore, the piezoelectric module's longer sides are oriented in y-direction in order to achieve a higher actuation efficiency and sensor output voltage.

With mode numbered 6 the actuator module lies on or very close to a nodal line for both the x- and y-component strains. Only a small amount of energy is fed into this mode shape and the resulting structural response will most likely be insufficient to process this mode for damage localisation. For mode numbered 20 an area of high strains (y- components) is located under the actuator which should allow for a good excitation of this mode in the experimental frequency response measurements.

A numerical frequency response for the chosen actuator and sensor location at 0.5 % critical damping is plotted in Figure 5.19. For some modes, e.g. at 646.4 Hz or 1,076.3 Hz, the structural response does not show individual peaks although the surface strains are high enough to yield a sufficient sensor output signal. It should be kept in mind, however, that the damping used

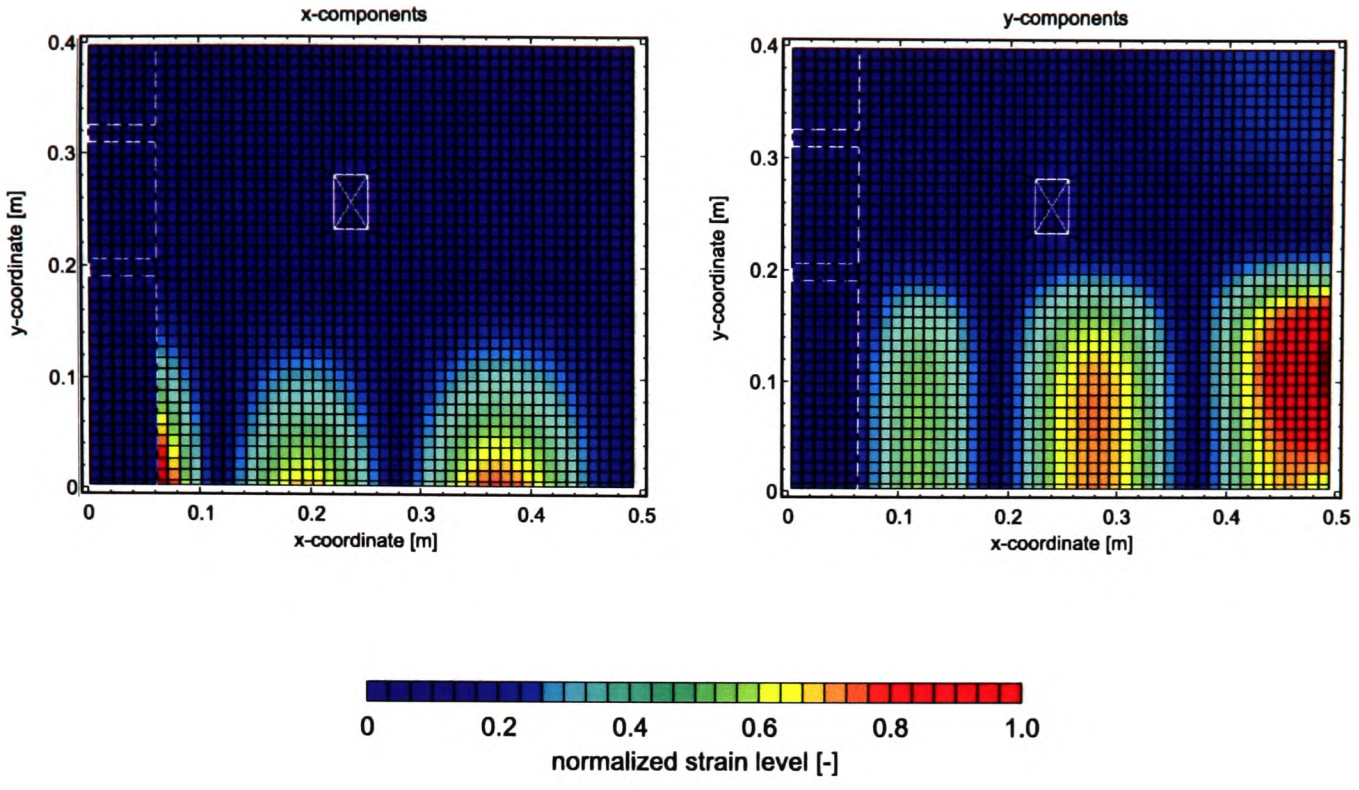

Figure 5.17: Surface Strain Fields for Mode Numbered 6

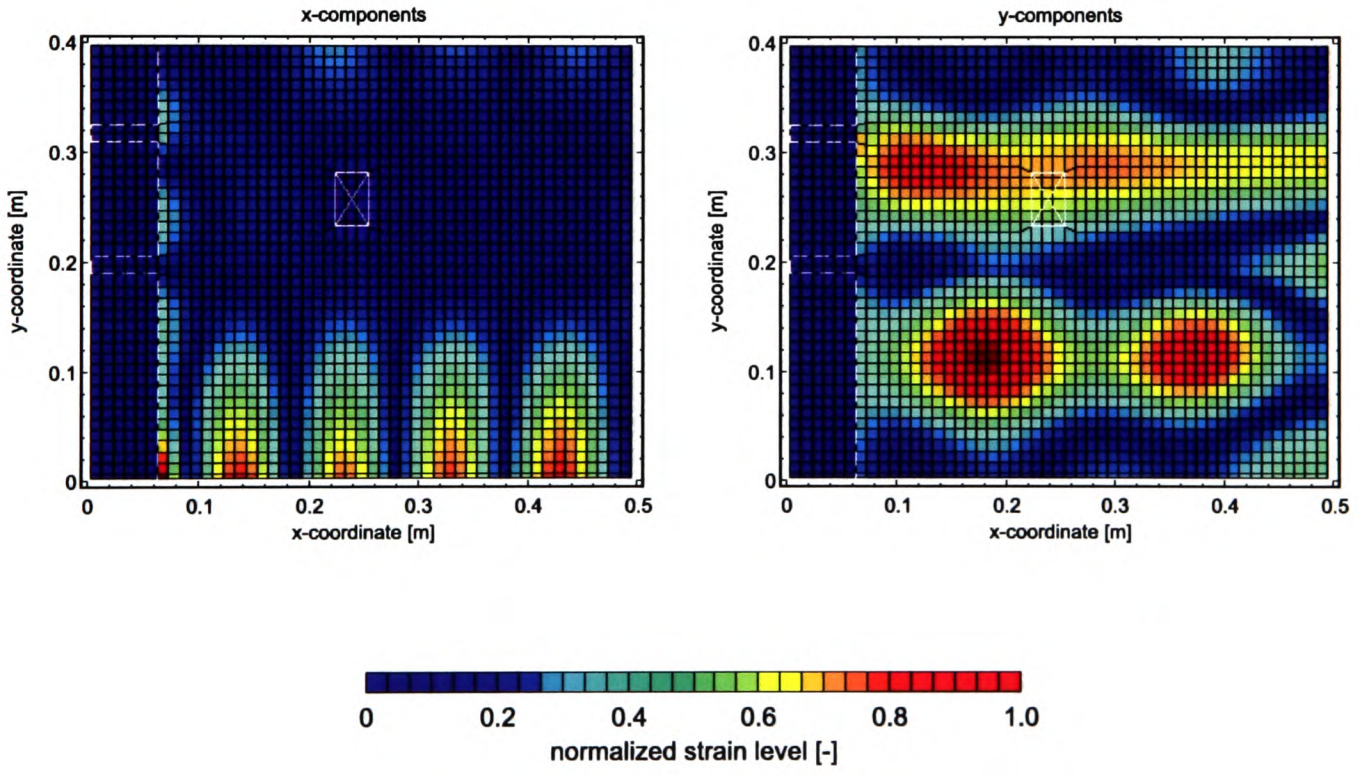

Figure 5.18: Surface Strain Fields for Mode Numbered 20

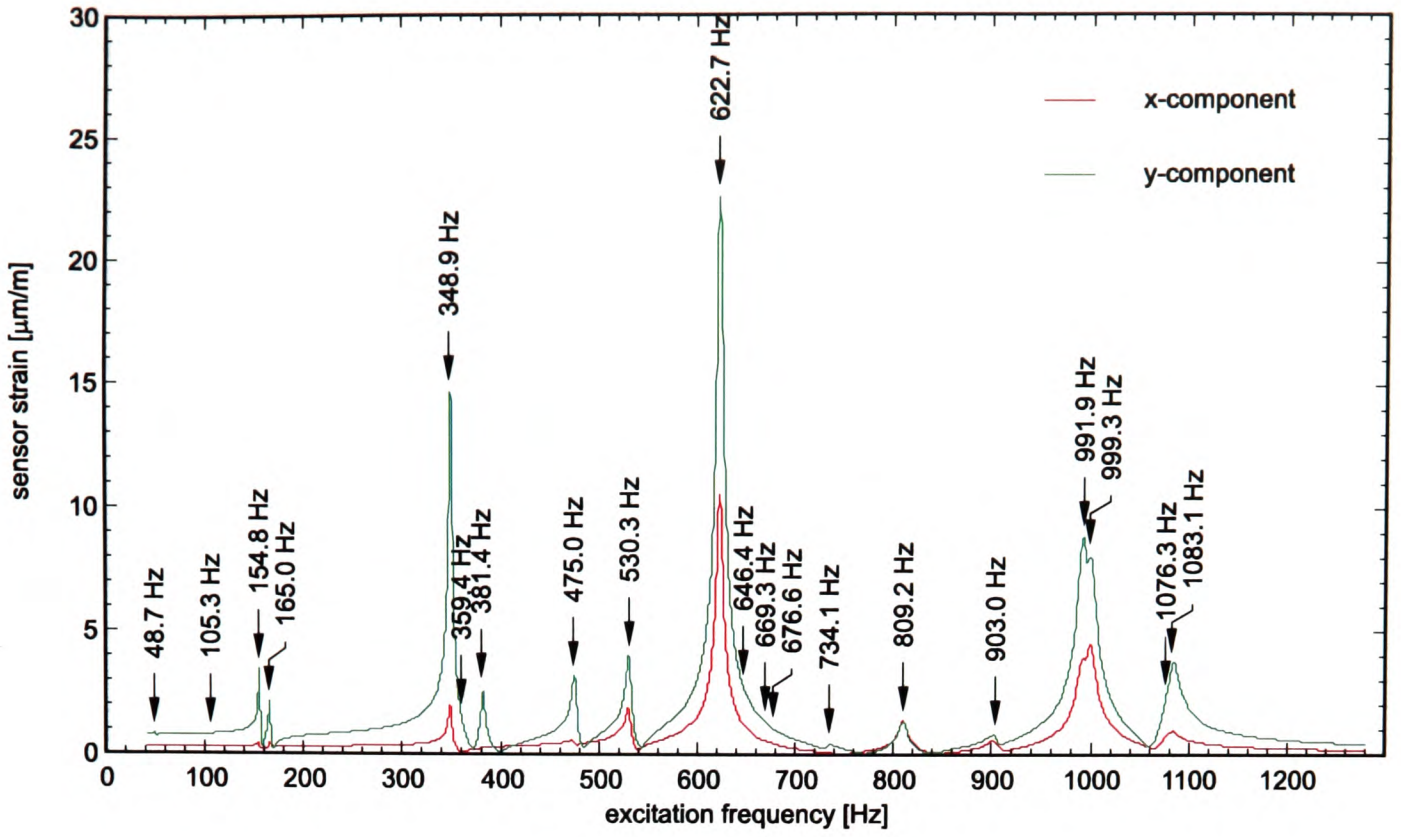

Figure 5.19: Numerical Frequency Response for Excitation at Selected Actuator/Sensor Location

in these calculations is only a coarse estimate which assumes comparatively unfavourable conditions for the later experiments.[7] With a lower damping more peaks are resolved in the frequency response spectrum.

The selected actuator and sensor module location allows the identification of 14 out of the 20 mode shapes in the frequency range between 40 Hz and 1.28 kHz.

Spatial Resolution Assessment. In this section the extent of the damage-induced damping deviations in the lower mode shapes is estimated for a characteristic delamination size and the changes of these deviations with damage location are evaluated to assess the method's spatial resolution.

A square delamination area is introduced into the finite-element model and the damping factors according to eq. (3.40) are computed for four different damage locations, Figure 5.20. The delamination is modelled by means of a 90 % reduction of the in-plane shear stiffnesses G_{xz} and G_{yz} of the shell

[7]The actual damping values of the test structure were unknown at this time. In the course of the experimental investigations the average damping in the observed frequency range was found to be as low as 0.16 %.

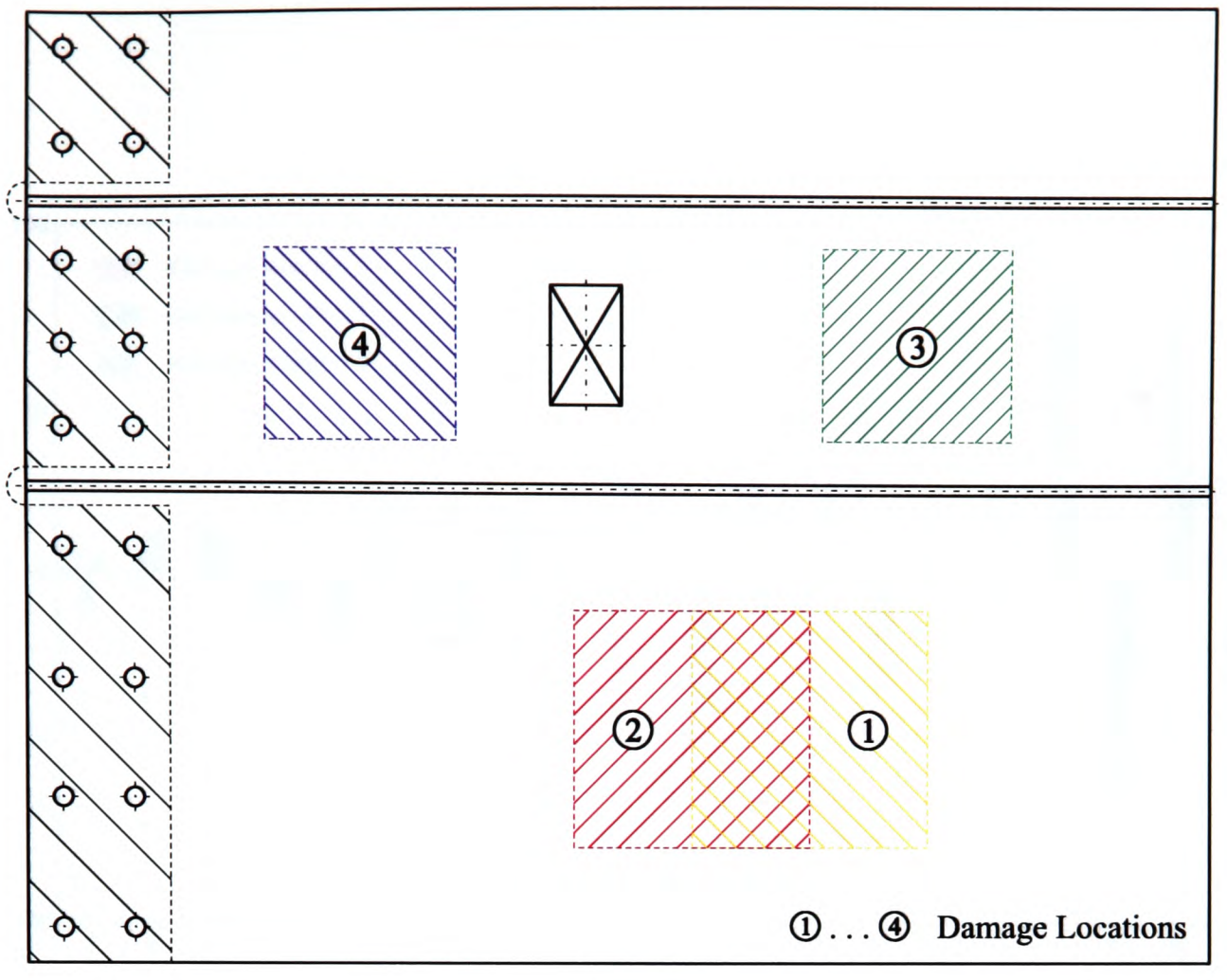

Figure 5.20: Numerical Model for Spatial Resolution Assessment

elements representing the damaged area. The deviations of the modal damping factors with respect to the values for the 'undamaged' model are plotted in Figure 5.21 for modes numbered 1 to 20.

Comparing the results for damage locations 2, 3, and 4, Figure 5.21 (top), the damping deviations display unique and easily distinguishable patterns for the different damages. This indicates that a clear separation of the various damage locations in the finite-element model from given damping deviations is possible. Some modes show a considerable response to a given damage whereas others are not significantly influenced. As a general trend, the sensitivity increases for higher mode numbers.

For the more critical case of the two overlapping damages numbered 1 and 2, Figure 5.21 (bottom), the spectrum of damping value deviations still contains some noticeable differences (e.g. for modes numbered 8, 11, 12, 17, and 20), which appear to be sufficient to distinguish the two locations.

The simulation indicates that the concept of processing modal damping for

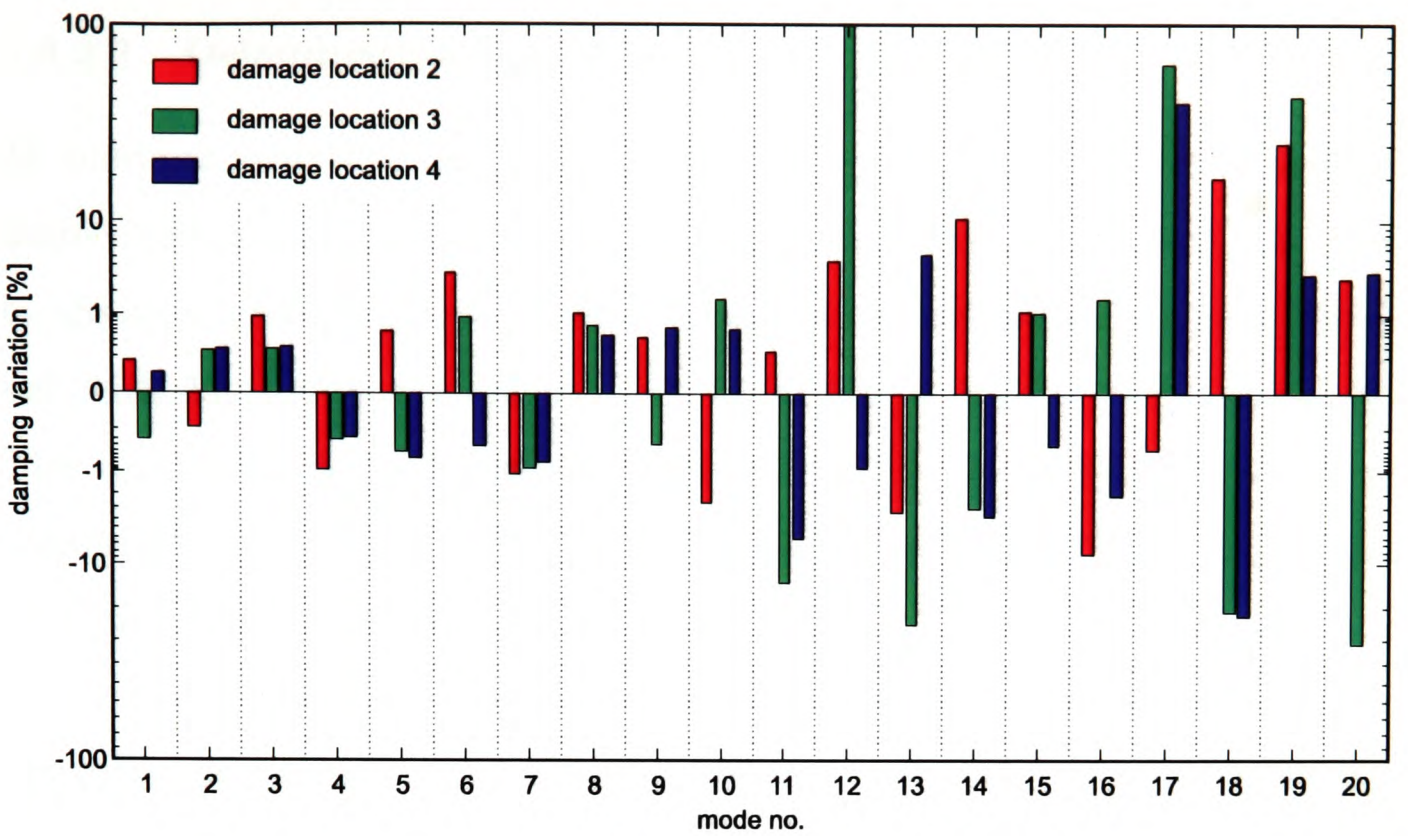

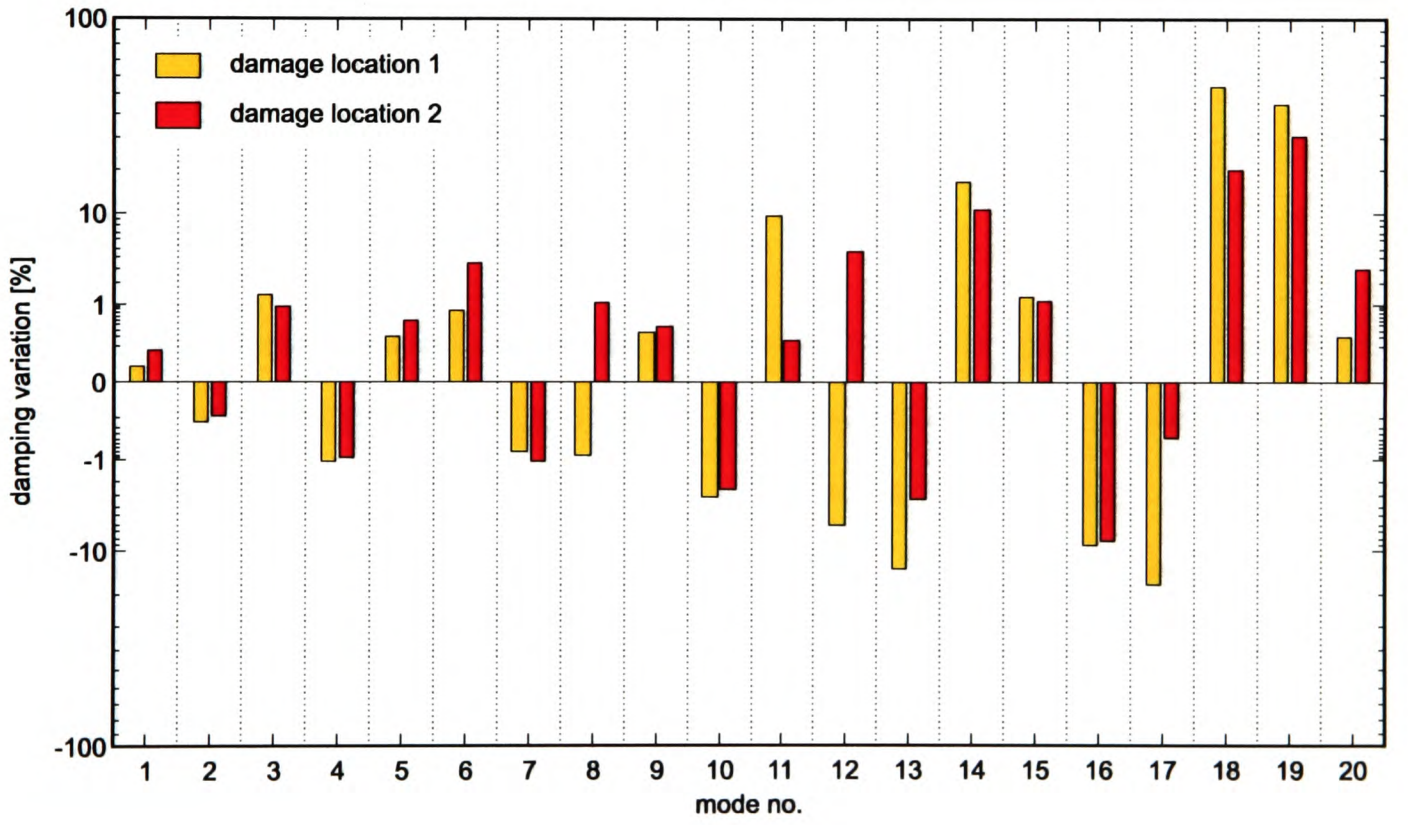

Figure 5.21: Damage-Induced Damping Variations for Different Damage Locations

damage localisation is capable of yielding a good spatial resolution and that a good localisation capability can be expected in practical application.

5.3.2.2 Delamination Modelling

To compute analytical damping factors for the damaged structure a realistic finite-element delamination model is needed. As outlined in Section 3.3.1 the localisation problem is restricted to a single concentrated damage of fixed size with damage location as the only remaining parameter to be identified. This requires to define a characteristic delamination size and shape which is obtained from ultra-sonic wave scan images of the damaged region on the test structure, Figure 5.26 in Section 5.3.4.2.

As described in the previous section the delamination is modelled by reducing the in-plane shear stiffnesses G_{xz} and G_{yz} of the involved shell elements. The modelled damage position is parameterised and is determined by two distance co-ordinates, Δx and Δy, relative to the actual damage on the test structure, Figure 5.27 in Section 5.3.5.

5.3.3 Model Corrections

The intermediate optional updating step is intended to provide an improved model for application with the damage localisation method. A brief overview of the finite-element model corrections is given here. Application-related aspects have been treated in more depth in Section 4.2. The updating process is preceded by a re-modelling phase where minor geometric adjustments are made to take into account manufacturing tolerances of the tested sample and, following an initial sensitivity analysis, the rigid suspension is modified to more accurately resemble the existing test set-up.

5.3.3.1 Modal Data for Model Updating

Mode shapes and natural frequencies were identified using a Polytec PSV 200 single-channel laser Doppler scanning vibrometer which measures the out-of-plane deflections of the base plate. All measurements were taken with the panel

clamped along one of the short sides. A harmonic excitation ranging from 40 Hz to 1.28 kHz was applied through the integrated piezoelectric actuator. This assures that no additional masses from shakers or sensors can affect the results. The number of measured degrees of freedom was 556 and 22 mode shapes and natural frequencies were identified.

5.3.3.2 Correction Results

To obtain physically reasonable and precise correction results the procedure described in Section 4.2.4 is applied. The substructures, Figure 5.22, are chosen such that they represent actual modelling uncertainties and errors and also have sufficiently high sensitivities, eq. (4.3). Table 5.5 lists the selected updating parameters and correction factors $\mathbf{p}_k$. In Figures 5.23 and 5.24 the frequency deviations and **MAC**-values are plotted for the initial and updated model.

5.3.4 Experiments

5.3.4.1 Frequency Response Data for Damage Localisation

Frequency response data has been recorded from the test structure in both the undamaged and the damaged states. Natural frequencies have been determined and experimental modal damping factors are computed from the measured sensor output signal as outlined in Section 3.3.2. Again, the integrated piezoelectric actuator was used to apply a swept-sine harmonic excitation in the frequency range from 40 Hz to 1.28 kHz. Since multiple measurements around the resonance frequency are involved in the computation of damping factors from the curve fit coefficients experimental errors are partially balanced and more accurate results than for other methods can be expected. An example for a curve fit to a measured response is shown in Figure 5.25.

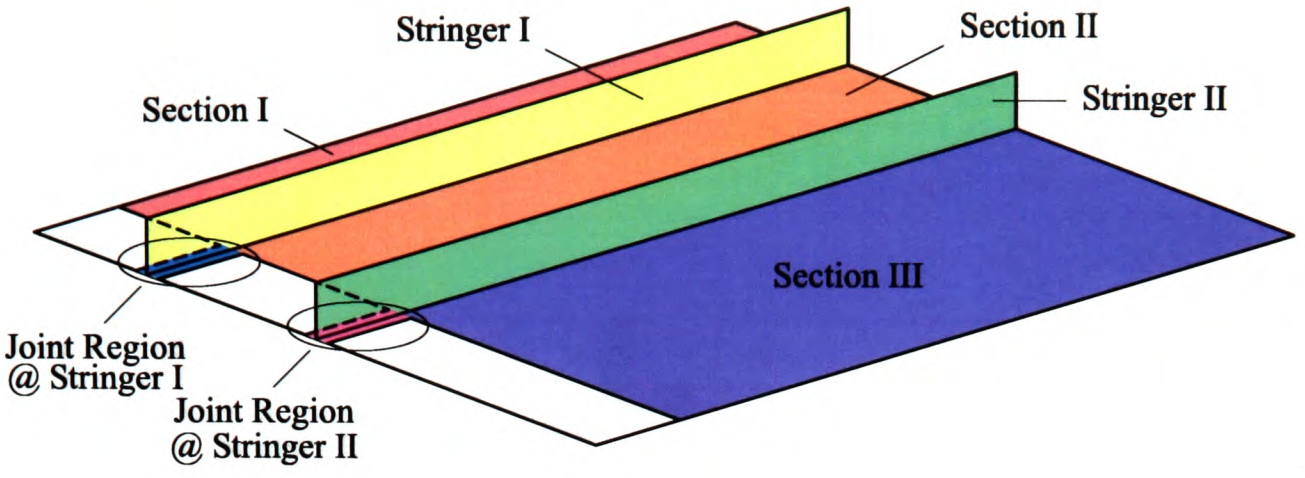

Figure 5.22: Substructures of the Stringer-Stiffened CFRP-Panel

No.	Location	Parameter	$p_k/[\%]^{*)}$
1	global	E	+12.2
2	global	G_{xy}	+22.0
3	Base Plate, Section I	ρ	−0.98
4	Base Plate, Section II	E	+6.67
5	Base Plate, Section III	E	+0.93
6	Joint Region @ Stringer I	G_{xy}	−74.2
7	Joint Region @ Stringer II	G_{xy}	−33.0
8	Stringer I	ρ	+4.45
*) after 8 iterations			

Table 5.5: Updating Parameters for the Stringer-Stiffened CFRP-Panel

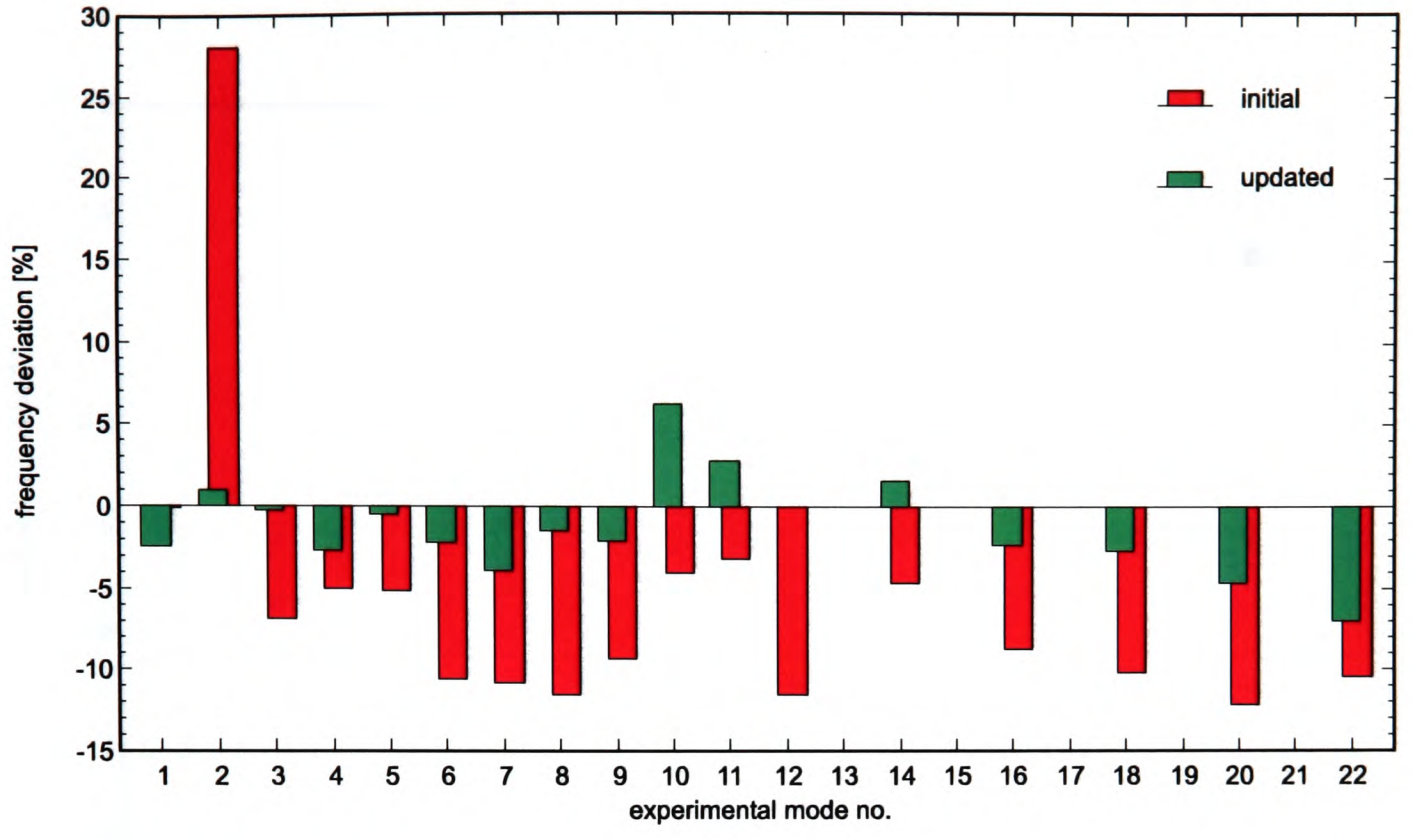

Figure 5.23: Frequency Deviations for Initial and Updated Finite-Element Model

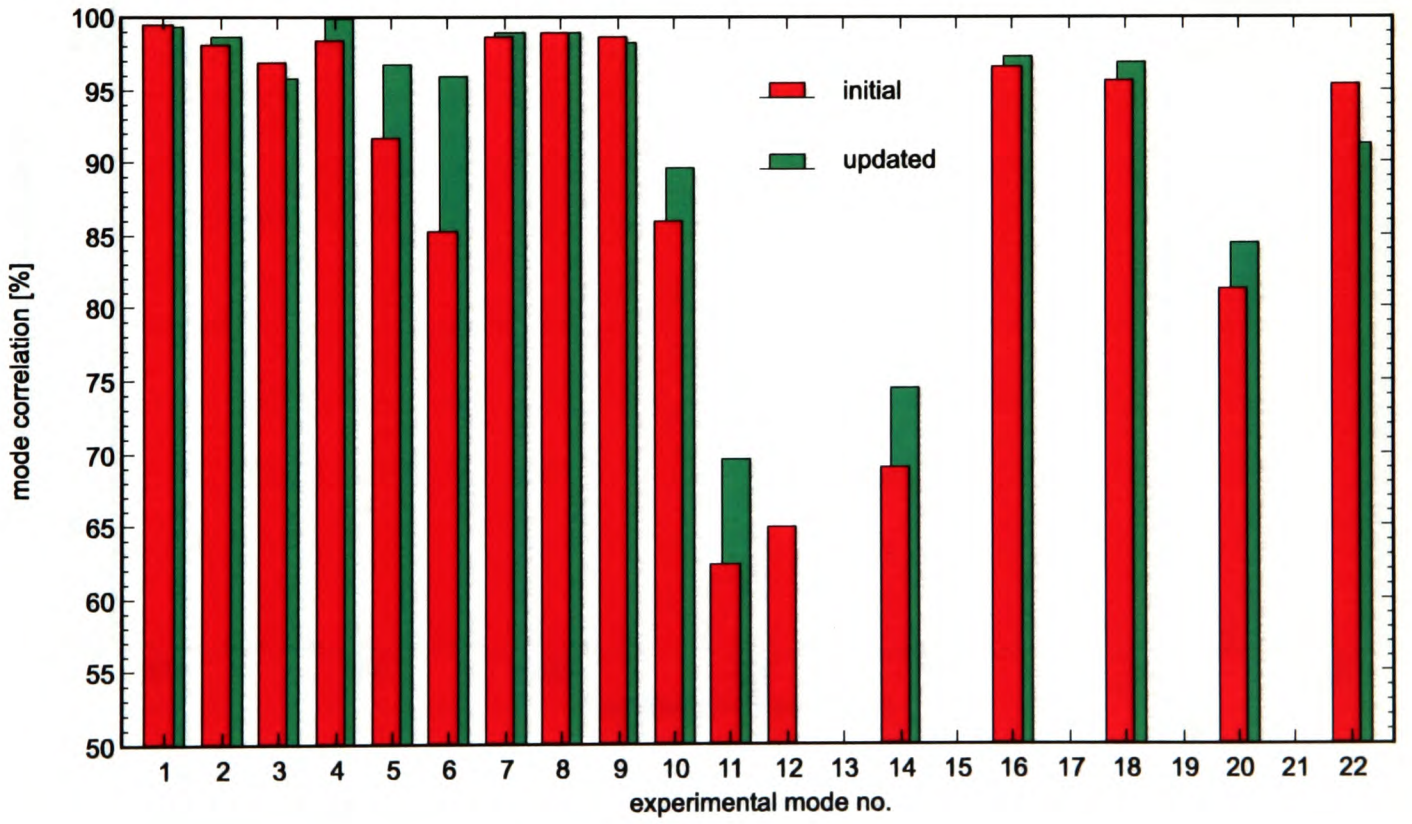

Figure 5.24: **MAC**-Values for Initial and Updated Finite-Element Model

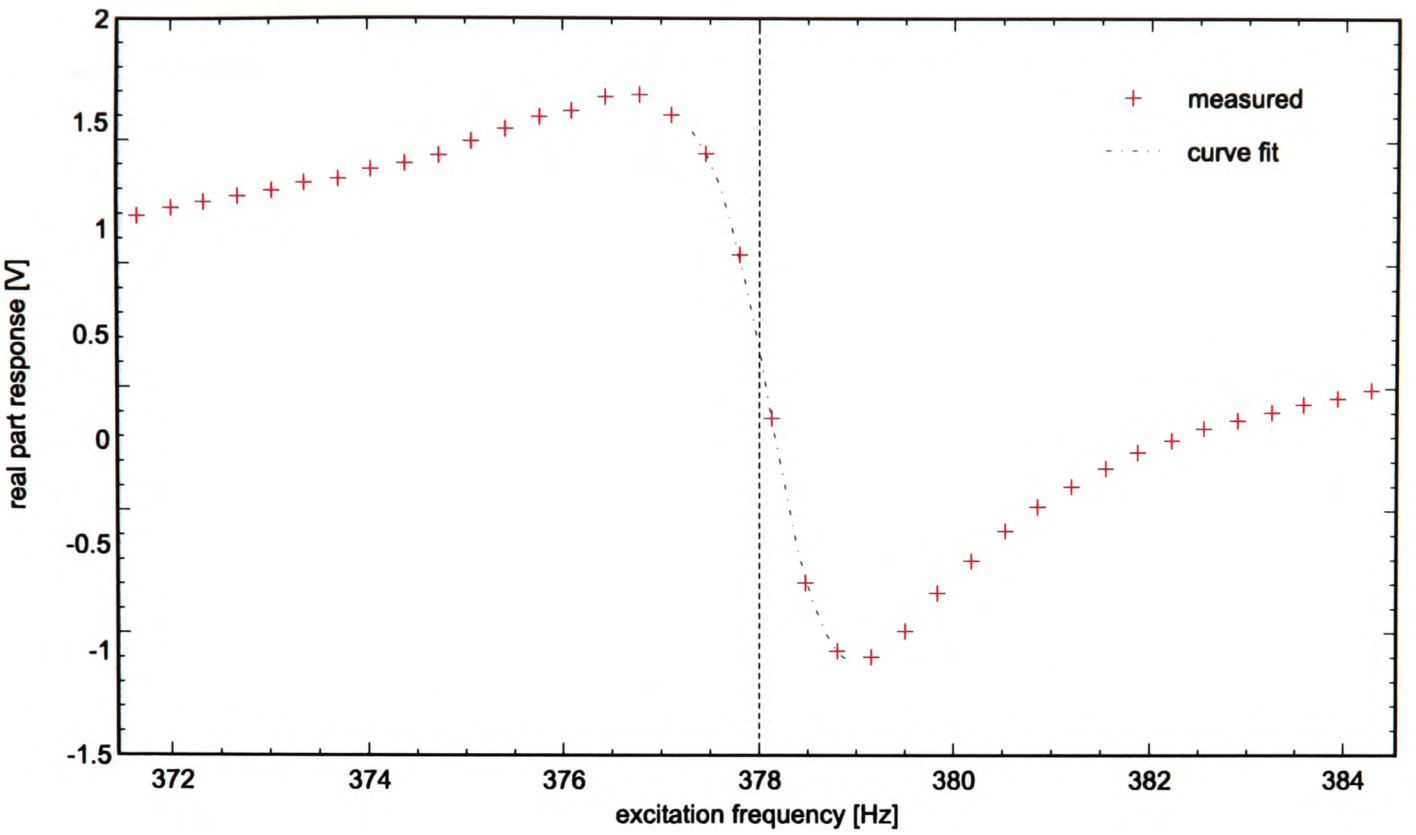

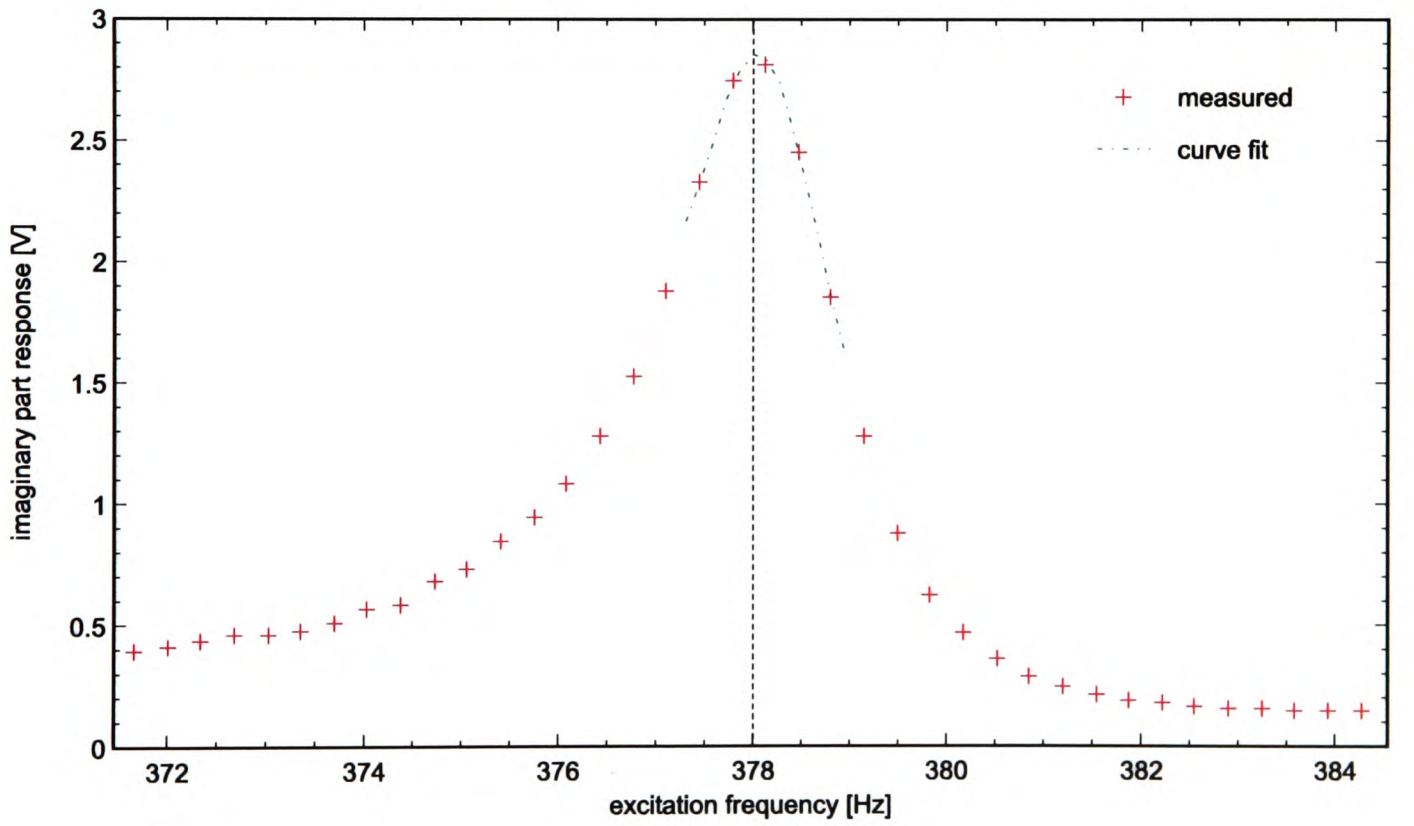

Figure 5.25: Curve Fitting of Measured Frequency Response

5.3.4.2 Generation of Delaminations

After measuring the modal data and frequency response on the undamaged[8] structure, a delamination has been produced through a steel ball impact. A damage location on the base plate between the stringers, piezoelectric modules and suspension at $x = 140$ mm and $y = 260$ mm has been chosen. The impact energy was 40 Joule and the resulting delamination size is approximately 25 mm by 44 mm. Next, the frequency response has been measured again using the same set-up and frequency resolution as for the healthy structure.

The destroyed internal bonding between adjacent layers within a delamination affects both the reflection and transmission of sound waves and the extend of damage can therefore be visualised by ultra-sonic wave scans. The method was used to identify the exact size, shape, and position of the delamination damages in order to generate a numerical model, Section 5.3.2.2, and for comparison with the modal-based localisation results. Figure 5.26 shows the reflected and transmitted Sound Pressure Levels (SPL). The notable delamination shape is believed to be due to the position of the supporting bars in the impact machine and the orthotropic material.

5.3.5 Application and Results

In order to assess the localisation capability of the new method and to investigate the effect of the numerical model quality the damage localisation method is now applied to both the initial and the updated finite-element model.

To locate the delamination on the test structure the parameterised damage location within the finite-element models is varied between $\Delta x = \pm 5$ cm and $\Delta y = \pm 7$ cm in increments of one finite element around the actual damage location, Figure 5.27, which was identified from the ultra-sonic wave scan images. The best correlation between analytical and experimental damping deviations is assumed to occur when $\Delta x = \Delta y = 0$, i.e. the modelled damage position is identical to the real delamination on the test panel.

[8]Following a popular convention within the health monitoring community the undamaged condition hereafter will be referred to as the 'healthy' state.

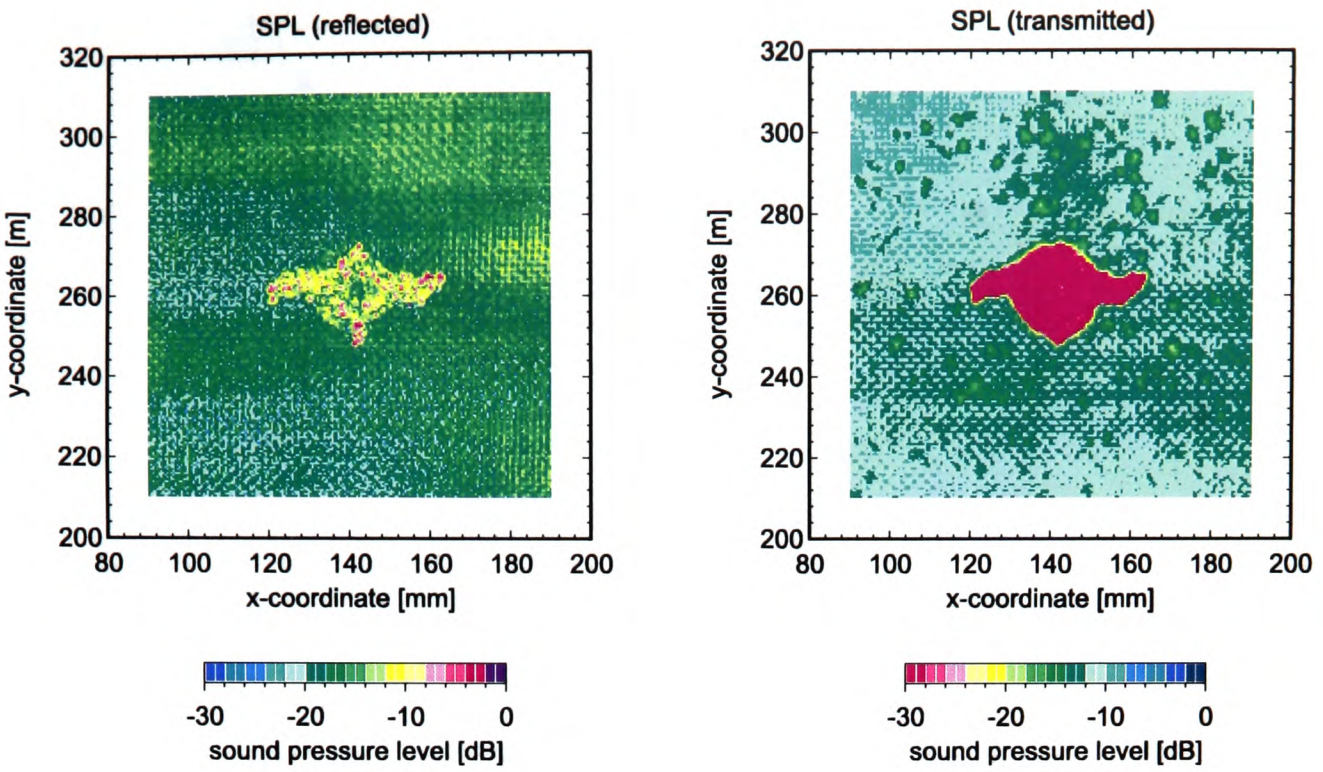

Figure 5.26: Ultra-Sonic Wave Scan Images of the Delamination Region

For each damage location the numerical damping factors $\eta^{\mathrm{D}}_{a,n}(\Delta x, \Delta y)$ are computed from eq. (3.40) and related to the corresponding values $\eta^{\mathrm{H}}_{a,n}$ from the healthy state. The damping deviation vectors $\Delta\boldsymbol{\eta}_a(\Delta x, \Delta y)$, eq. (3.44), are then compared to the corresponding experimental data obtained from the frequency response of the undamaged and damaged test panels. The correlation of damage-induced damping deviations between analytical and test data $C(\Delta x, \Delta y)$, eq. (3.45), is plotted as a function of distance between analytically modelled and real damage locations, Figure 5.28.

The number of available eigenfrequencies for comparison between test and analysis is limited by the correlation and quality of analytical and experimental mode shapes and by the suitability of individual measured resonance peaks for curve fitting (frequency spacing and peak height). Generally, the results improve when more data, i.e. a larger number of modes, is processed. For the results presented here 5 eigenfrequencies are used in the damage detection process.

With both finite-element models the delamination is clearly identified from the correlation of damage-induced damping deviations, Figure 5.28. The correlation maximum, however, is significantly higher for the updated model and

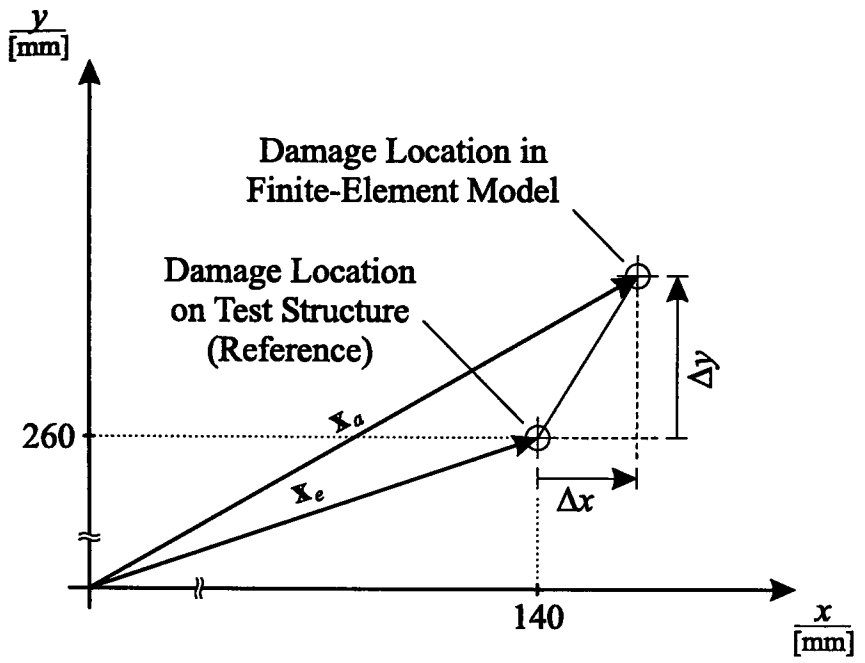

Figure 5.27: Damage Location Co-ordinates

the damage location is indicated with higher accuracy. The distinct peaks allow the actual damage to be more easily distinguished from secondary effects caused by measurement errors or modelling imperfections. These disturbances result in the correlation between analytical and experimental damping deviations to approach a non-zero base level rather than to completely vanish.

5.3.6 Concluding Remarks

The model-based damage localisation method introduced in Section 3.3 has been validated on a characteristic aircraft component and the advantages of model updating on the localisation accuracy have been investigated.

A novel criterion for the determination of optimised actuator and sensor locations and the numerical modelling of piezoelectric modules and delamination damages have been described. The correlation of damage-induced damping variations has been studied for a conventional and an updated finite-element model, the latter leading to an improved indication of the damage location as compared to the conventional analytical model.

In conclusion, the proposed method has proved to be capable of locating a concentrated structural damage from experimental data acquired from a single response sensor.

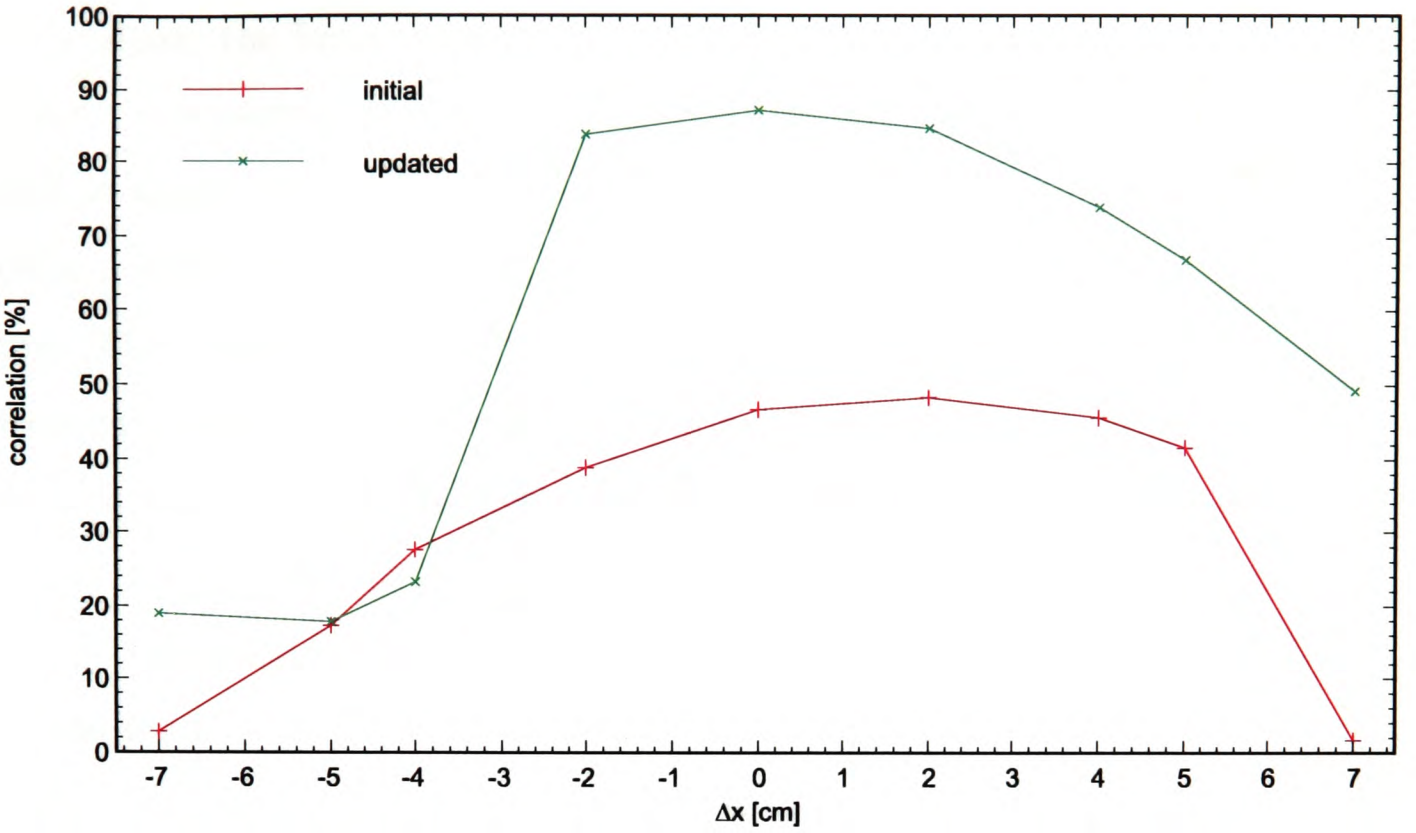

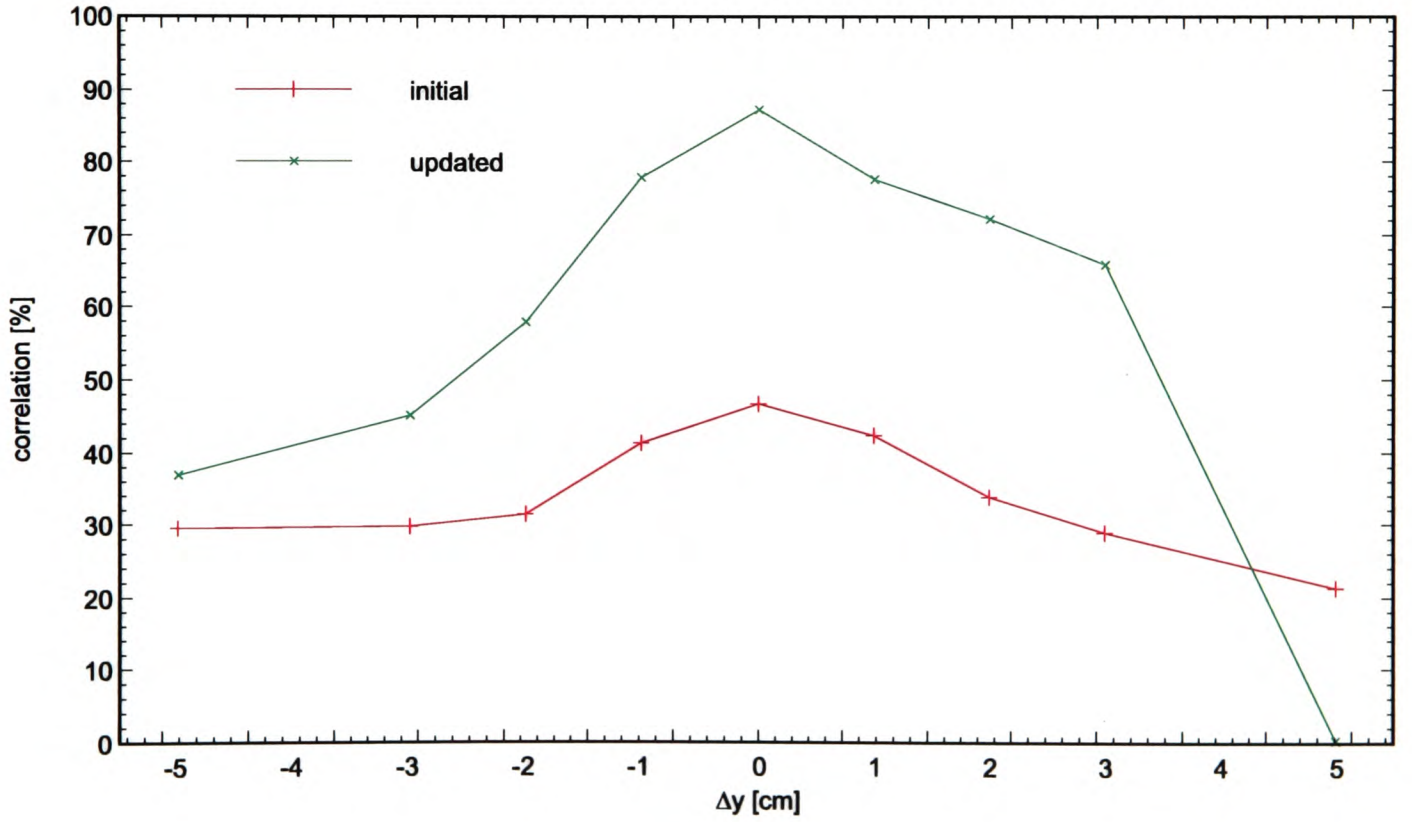

Figure 5.28: Correlation of Damage-Induced Damping Deviations

5.4 Optimisation of Modal Data Quality

5.4.1 Comparison to other Methods

To evaluate the force optimisation method introduced in Section 3.4 with respect to its performance in the field of modal testing of aerospace structures and to assess the potential for improving the quality of experimental modal data, a simulation study [72] using an analytical eleven-degrees-of-freedom system [135], Figure 5.29, is executed. The capabilities of handling close eigenfrequency spacing, non-proportional damping, and restricted accessibility are investigated and the approaches of LEWIS and WRISLEY [93], ASHER [4], and HUNT ET AL. [64] are selected for comparison. The forced dynamic response of the analytical system is numerically simulated allowing for an assessment of the force tuning methods with respect to their potential in isolating the natural modes of an elastic structure and the time and effort involved in the application during a test.

5.4.1.1 Numerical Simulation

Using the parameters in Table 5.6 and the structural damping approach

$$\mathbf{D} = 10^{-3}\,\mathrm{s} \cdot \mathbf{K}$$

the system matrices $\mathbf{M}$ and $\mathbf{K}$ are assembled and the admittance matrix

$$\mathbf{H}(i\omega) = (-\omega^2\mathbf{M} + i\mathbf{D} + \mathbf{K})^{-1} \tag{5.3}$$

is computed. The structural response to a stationary harmonic excitation force vector $\hat{\mathbf{f}}$ is given by

$$\hat{\mathbf{u}} = \mathbf{H}(i\omega) \cdot \hat{\mathbf{f}}\ . \tag{5.4}$$

The general eigenvalue problem, eq. (3.14), yields the exact eigenfrequencies and eigenvectors, Figure 5.30.

Based on the requirements listed in Section 3.4.1 four multi-point exciter configurations with two and four shakers, respectively, are defined and tested. For the two-point excitations the exciter positions are selected such that each

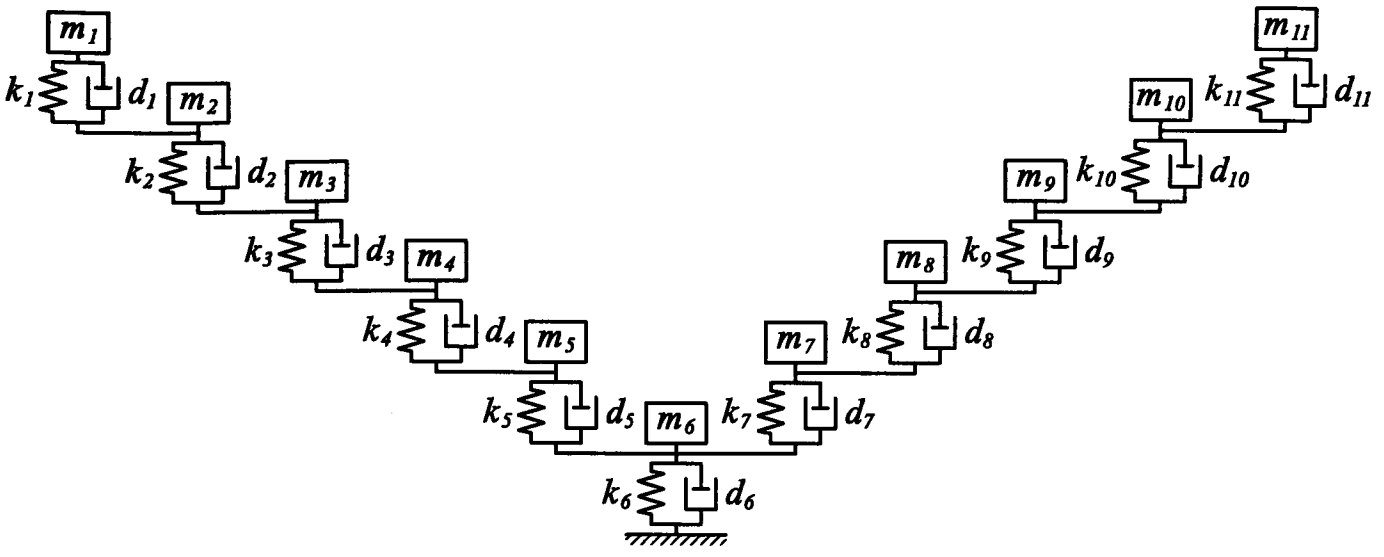

Figure 5.29: Analytical Eleven-Degrees-of-Freedom System

Physical Parameter	**Degree of Freedom**					
	1, 11	**2, 10**	**3, 9**	**4, 8**	**5, 7**	**6**
m_m/[kg]	1.0	6.0	1.0	0.6	1.0	1.0
k_m/[kg/s^2]	2421.4	2989.4	3690.6	4556.3	5625.0	18000.0

Table 5.6: Physical Parameters for the Eleven-Degrees-of-Freedom Model

mode is excited by at least one exciter configuration. The entire set of eleven mode shapes, however, can not be excited using only a single two-point exciter configuration. This takes into consideration the usual test situation that some exciter locations are not available or better positions are unknown. Predefining the excitation points additionally establishes identical starting conditions for all methods. To ensure a consistent comparison between the various methods the Mode Indicator Function (MIF), eq. (3.54), is used to assess and compare the mode isolation quality. As outlined in Section 3.4.1 the MIF increases with improved mode isolation quality. The usual requirement for a mode shape to be adequately identified is a mode indicator value of 800 or higher. A mode indicator of 1,000 would indicate that all real-part response components have vanished and the structure vibrates in a pure natural mode. This would be the best possible result for any force tuning method.

Preceding the actual Phase Resonance Test simulation structural responses from single point excitations at different degrees of freedom are computed from eq. (5.4) and the associated MIF-values are plotted as a function of excitation

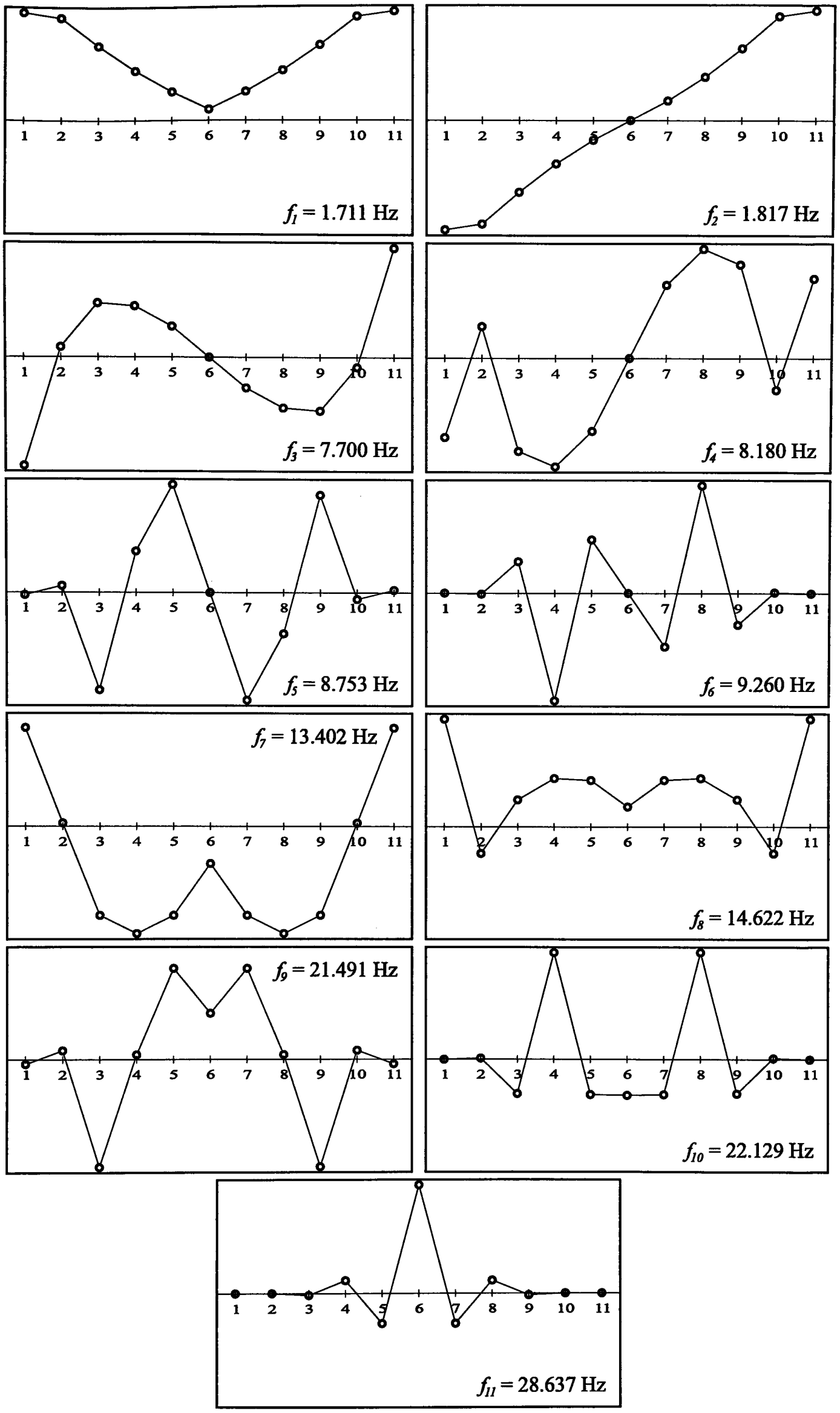

Figure 5.30: Modal Data of the Eleven-Degrees-of-Freedom System

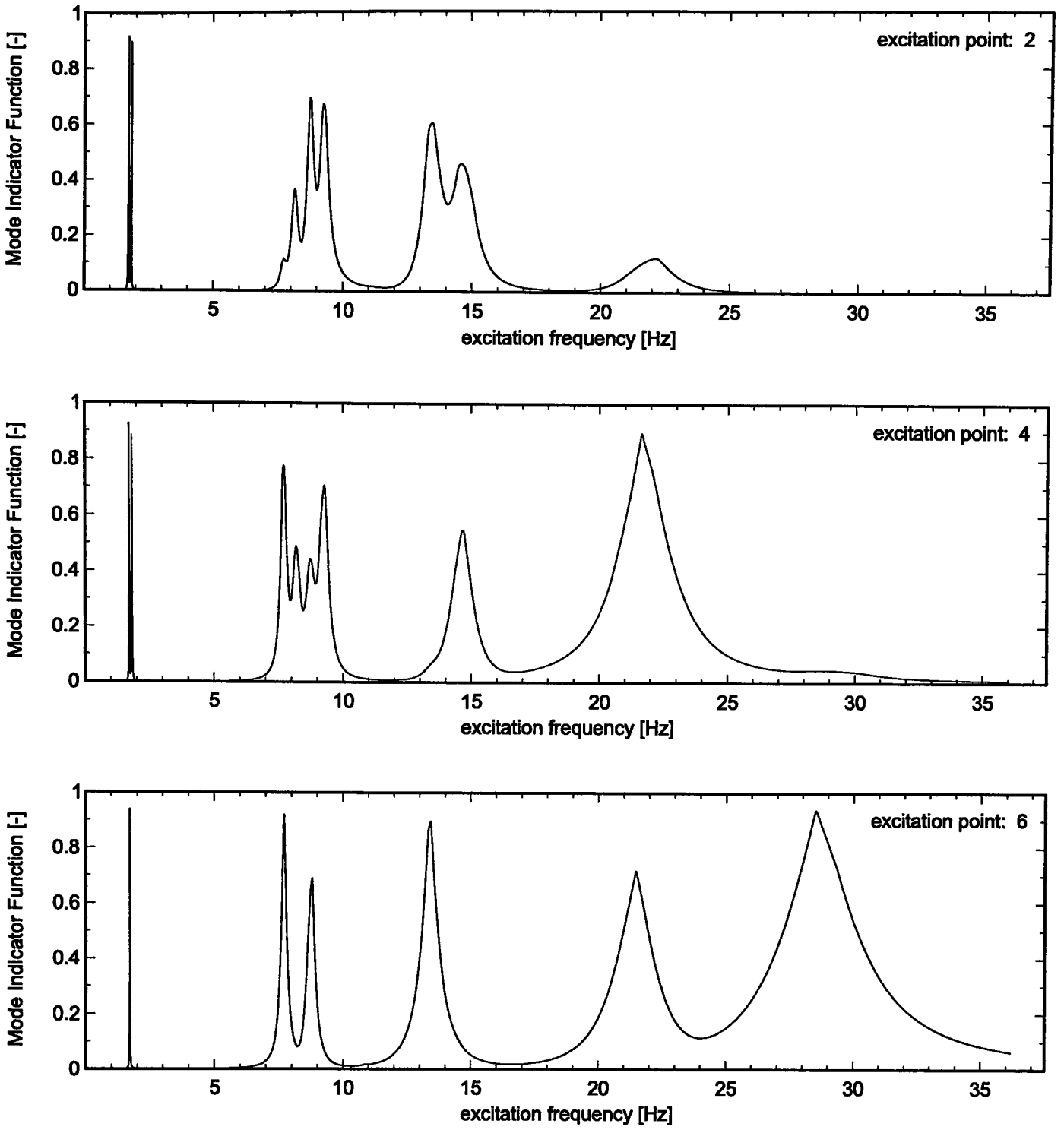

Figure 5.31: Structural Responses from Simulated Sine-Sweep Runs

frequency in Figure 5.31. The sine-sweep runs provide the approximate natural frequencies and first estimates on the mode shapes and are used as initial information by all methods.

5.4.1.2 Results

The modal identification results for the analytical eleven-degrees-of-freedom system using the excitation force tuning approaches of LEWIS and WRISLEY [93], ASHER [4], HUNT ET AL. [64], and the method proposed in Section 3.4 are summarised in Tables 5.7 to 5.10.

Excitation Points	Mode Number										
	1	**2**	**3**	**4**	**5**	**6**	**7**	**8**	**9**	**10**	**11**
2, 4	919	899	782	580	612	701	468	577	820	730	46
2, 10	980	961	143	577	926	884	813	724	140	129	1
4, 6	933	886	809	467	486	695	871	549	829	725	918
2, 4, 8, 10	980	961	916	952	859	964	821	675	921	884	66

Table 5.7: MIF-Values for Optimised Force Vectors Computed from LEWIS and WRISLEY's Method [93]

Excitation Points	Mode Number										
	1	**2**	**3**	**4**	**5**	**6**	**7**	**8**	**9**	**10**	**11**
2, 4	6	26	-	-	-	709	-	-	-	-	-
2, 10	-	-	-	-	717	884	-	-	-	-	-
4, 6	929	908	852	-	536	-	-	-	826	-	924
2, 4, 8, 10	967	-	752	-	493	907	165	-	-	-	-

Table 5.8: MIF-Values for Optimised Force Vectors Computed from ASHER's Method [4]

Excitation Points	Mode Number										
	1	**2**	**3**	**4**	**5**	**6**	**7**	**8**	**9**	**10**	**11**
2, 4	914	913	676	580	599	690	110	553	820	730	46
2, 10	941	911	143	577	926	884	813	724	140	129	1
4, 6	920	904	919	531	521	856	510	403	823	721	924
2, 4, 8, 10	965	951	961	907	852	929	124	634	921	884	66

Table 5.9: MIF-Values for Optimised Force Vectors Computed from HUNT's Method [64]

Excitation Points	Mode Number										
	1	**2**	**3**	**4**	**5**	**6**	**7**	**8**	**9**	**10**	**11**
2, 4	976	955	788	733	705	711	631	641	821	731	46
2, 10	985	960	143	577	926	884	813	724	140	131	1
4, 6	984	959	920	769	664	858	904	558	844	731	925
2, 4, 8, 10	987	964	987	964	927	969	827	841	930	889	66

Table 5.10: MIF-Values for Optimised Force Vectors Computed from the Method proposed in Section 3.4

With all four methods a considerable improvement is observed between the two-point exciter configuration at degrees of freedom 2 and 4 and the four-point configuration at DoFs 2, 4, 8, and 10. This appears reasonable because the degrees of freedom 8 and 10 embody the mirror images of 2 and 4 and the additional exciters take into account the system's symmetry allowing for a better isolation of symmetric and anti-symmetric mode shapes. From a physical viewpoint a sufficient excitation of mode numbered 11 only seems possible with exciters at 4 and 6. In fact, with each method all other exciter arrangements yield unsatisfactory identification results, i.e. mode indicator values close to zero.

The force tuning procedure introduced by LEWIS and WRISLEY [93] requires only the measured eigenfrequencies as initial information. The method involves an assumption on the structural damping and a mass model reduced to the excitation points. The force components are adjusted proportional to the deflection amplitudes and condensed masses at the selected exciter locations. With the exception of modes 4, 8, and 10 the two-point exciter configurations already lead to a sufficient mode isolation, Table 5.7. Overall, good results are obtained using this method.

ASHER's approach [4] additionally processes structural responses measured during the preliminary sine-sweep runs. An admittance matrix is computed from the real-part deflection components at the excitation degrees of freedom and associated excitation forces. Practical experience revealed that the suggested mode indicator $|\mathbf{H}| = 0$ is not a particularly reliable criterion since the

admittance matrix determinant does not necessarily become zero at the resonance frequencies. This however is the basic condition for the computation of non-trivial force vectors. Therefore, only six mode shapes were identified, Table 5.8.

HUNT's method [64] uses the real- and imaginary-part response amplitudes at the exciter locations from the initial sweep runs. A reduced mass matrix from a finite-element model is needed to generate the experimental admittance matrix. Substantial improvements compared to ASHER's method [4] and mostly similar results to LEWIS and WRISLEY's approach [93] are observed, Table 5.9.

With the force tuning method according to eqs. (3.55) to (3.61) the real- and imaginary-part responses of all measured degrees of freedom are used. A significantly higher amount of input information is available for the computation of optimised excitation force vectors than it is the case with any of the other approaches. An analytical mass matrix or estimations on the damping behaviour are not needed. The results are comprised in Table 5.10. Considerable improvements are found, especially for the higher modes which are the most difficult to identify. The average MIF-values are 47 points higher than with LEWIS and WRISLEY's method [93] and 69 points higher than with the method of HUNT [64].

5.4.2 Application to a Laboratory Test Structure

Next, a simple satellite model, Figure 5.32, is selected to test the method's performance on a realistic structure. The goal of these investigations is to assess the influence of those effects not represented within the analytical model that has been used in the previous section. Examples are frequency shifts due to incomplete excitation and non-linear behaviour in general[9], systematic errors, measurement noise, the limited resolution at low response amplitudes, A/D-converter noise, or temperature effects.

[9]These would affect the superposition of responses in eqs. (3.55) and (3.56).

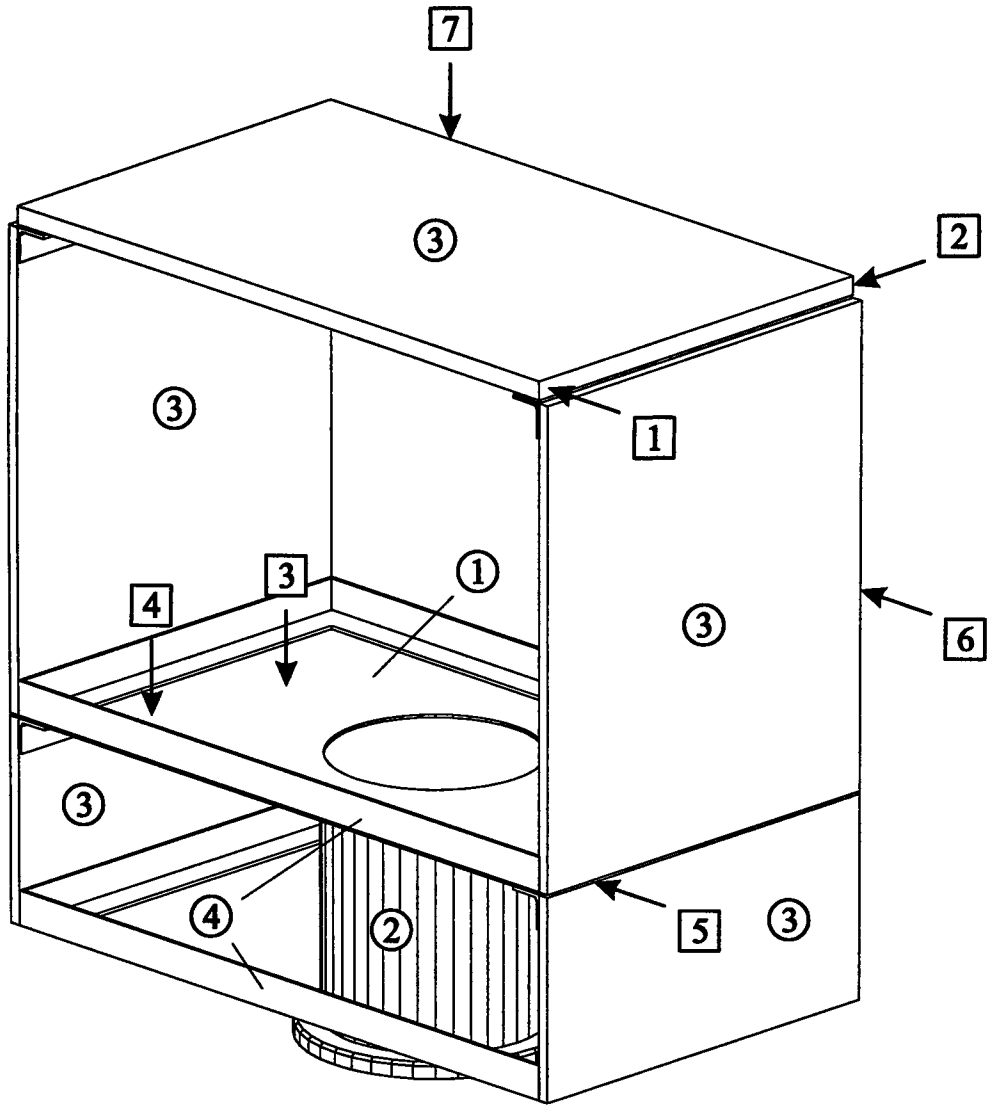

Figure 5.32: Laboratory Test Structure

5.4.2.1 Experiments

The structure is made of a steel base plate (1) attached to a cylindrical foot (2), five aluminium-honeycomb compound plates (3), and two horizontal steel frames (4) enclosing the base plate and between the lower edges of the vertical compound plates, respectively. For Ground Vibration Testing the structure is mounted on a seismic foundation and equipped with 101 acceleration sensors. Seven exciter locations (1 to 7) are available for the identification process and because of the structure's simplicity the computation of optimised multi-point excitation forces will be restricted to a maximum number of three shakers. A frequency range from 10 Hz to 200 Hz containing 18 eigenfrequencies is investigated. DLR's Ground Vibration Test Facility [32, 34] is used to collect the experimental data.

First, the experimental database required to compute optimised multi-point excitation force vectors is obtained from sine-sweep runs with single-point excitations at the exciter locations shown in Figure 5.32. Real and imaginary responses are recorded for each excitation point and resonance frequency. Next, the optimised force components and associated structural responses are determined from eqs. (3.59) to (3.61). The Mode Indicator Function (MIF), eq. (3.54), is computed for all possible combinations of three out of seven exciters and the exciter configurations with the highest theoretical mode indicators are then used to experimentally identify the structure's mode shapes. In Table 5.11 the measured MIF-values and the ones predicted from eq. (3.54) are listed for comparison.

5.4.2.2 Results

Considerable improvements with respect to mode isolation quality are achieved with the computed multi-point excitation force vectors, Table 5.11. Increases in MIF-values as high as 130 points (mode numbered 9) as compared to the single-point excitations are observed. It appears remarkable that in some cases (modes numbered 1, 14, and 17) the exciter point which has the best mode indication does not necessarily contribute to the optimised force vector. With the exception of mode numbered 17 the differences between predicted and measured values[10] of the MIF are smaller than 20 points or 2 %.

5.4.3 Ground Vibration Test on the Polar Platform

Following the successful tests under controlled laboratory conditions the force tuning method is applied to the Polar Platform (PPF) space structure, Figure 5.33, which has been developed by the European Space Agency (ESA) starting in 1988 [43]. Other applications to ESA's International Gamma Ray Astrophysics Laboratory (INTEGRAL) satellite and the Rosetta Lander Module have been reported in [35] and [56], respectively.

[10]Due to space limitations some configurations listed in Table 5.11 could not be set up. In favour of the comparability of results no alternative configurations are selected.

Table 5.11: Modal Identification Results for the Laboratory Test Structure

Mode No.	Single-Point Excitations							Excitation Points	Force Components			MIF (comp.)	MIF (meas.)
	1	2	3	4	5	6	7						
1	937	627	**984**	918	483	917	912	1 - 4 - 6	-0.447	1.871	0.838	984	967
2	569	759	889	663	915	850	**986**	3 - 4 - 7	-1.547	0.093	1.393	992	-
3	930	550	462	916	**972**	597	881	1 - 3 - 5	0.278	0.076	-2.364	992	-
4	304	609	464	**975**	943	932	909	4 - 5 - 7	0.146	2.382	0.059	991	981
5	683	**985**	87	937	933	935	932	1 - 2 - 6	-0.622	1.573	1.083	990	-
6	871	0	0	887	**937**	544	837	1 - 5 - 6	0.086	2.398	-0.134	953	-
7	934	451	859	907	841	954	**970**	1 - 6 - 7	1.424	-0.200	0.650	995	995
8	934	918	859	929	841	816	**970**	7		-		970	-
9	518	**863**	542	800	668	735	788	1 - 2 - 7	-1.254	0.463	0.709	975	993
10	833	486	879	**948**	794	847	890	3 - 4 - 5	0.910	1.776	0.823	990	-
11	833	**894**	441	677	794	517	890	2 - 3 - 4	0.674	-1.400	1.422	976	-
12	833	882	287	825	781	**960**	692	3 - 6 - 7	0.378	1.472	-0.608	966	979
13	0	814	0	875	887	**916**	839	2 - 6 - 7	1.702	0.223	0.413	984	991
14	844	814	**932**	846	703	916	533	1 - 4 - 7	1.791	-0.757	0.228	970	960
15	878	814	613	623	866	**915**	593	1 - 5 - 6	-1.609	0.857	0.459	960	-
16	522	867	437	**893**	811	819	714	2 - 4 - 6	0.021	0.016	0.002	1000	983
17	808	**867**	495	630	747	571	714	3 - 5 - 6	1.399	1.754	-0.117	879	825
18	75	778	198	**894**	454	436	834	4 - 5 - 7	1.649	1.480	0.079	954	954

The Polar Platform is a satellite backbone structure of modular design which is designed to accommodate Earth-observation instruments and to supply them with the necessary energy, attitude control, and data links to Earth. In April/May 1996 DLR carried out a Ground Vibration Test on the Polar Platform's Structural Model (STM) which was equipped with static mass dummies representing the Earth-observation instruments of the Envisat-1 payload. In its launch configuration the satellite measures 10.50 m (height) by 4.57 m (envelope diameter) and the total mass of the base structure and payload is 8,211 kg. The Polar Platform was launched from the Kourou spaceport in French Guyana by an Ariane-5 on March 1st, 2002.

5.4.3.1 Experiments

DLR's Ground Vibration Test Facility (cf. Section 2.4) was used to identify the satellite's normal modes and eigenfrequencies. The structure was equipped with 575 acceleration sensors and 99 excitation points were available. Two configurations (with and without mass dummies for the solar array) were investigated and 109 modes were measured in a frequency band ranging from zero to 180 Hz.

The force tuning method is applied to a mode shape which previously had not been isolated satisfactorily using manual exciter force tuning strategies. Based on the corresponding eigenfrequency single-point sine-sweep runs from eight exciter locations containing the wanted mode are found. The **MAC**-matrix, Table 5.12, shows a good correlation between the selected modes. With the structural responses from the eight single-point excitations the force components for a three- and four-point excitation are computed, Table 5.13. It should be noted that in both configurations the exciter point with the lowest mode indication (number 8) has the second-largest component in the optimised force vectors.

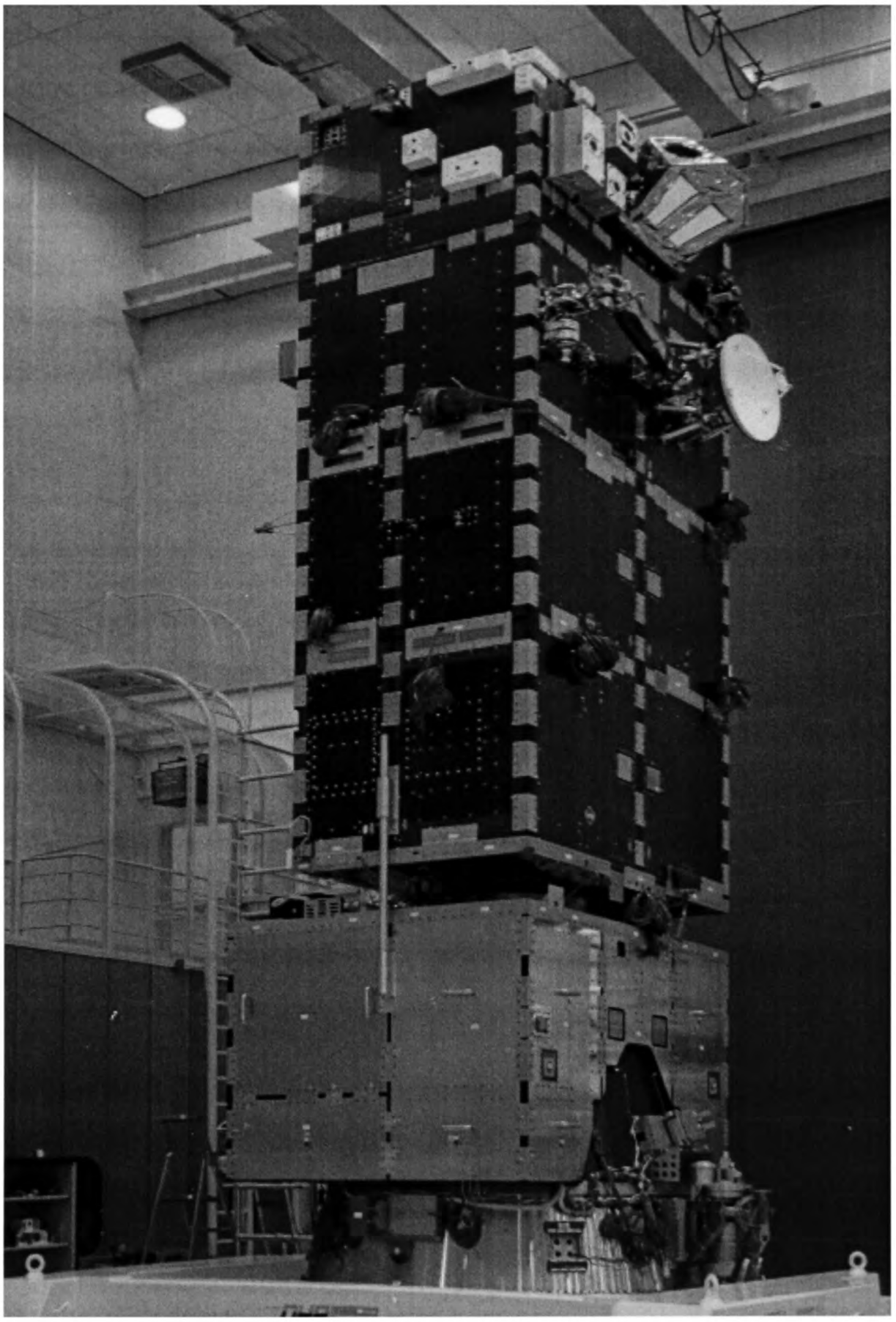

Figure 5.33: The Polar Platform Satellite Structure

Excitation Point	1	2	3	4	5	6	7	8
1	1000	838	840	799	774	770	600	793
2	838	1000	919	970	943	938	712	916
3	840	919	1000	861	825	819	616	870
4	799	970	861	1000	973	971	824	855
5	774	943	825	973	1000	1000	844	850
6	770	938	819	971	1000	1000	851	840
7	600	712	616	824	844	851	1000	549
8	793	916	870	855	850	840	549	1000

Table 5.12: Correlation of Selected Structural Responses

	Excitation Point							
	1	**2**	**3**	**4**	**5**	**6**	**7**	**8**
MIF (Sweep)	**634**	592	465	613	615	617	547	462
$\hat{\mathbf{f}}_{r,opt}$/[N]	17.34	-	13.62	-	-	41.78	-	22.35
$\hat{\mathbf{f}}_{r,opt}$/[N]	16.98	-	-	-	-	43.50	-	22.92

Table 5.13: Optimised Excitation Forces for the Polar Platform

5.4.3.2 Results

In Table 5.14 the pre-computed mode indicators, measured MIF-values employing the optimised excitation forces from Table 5.13, and improvements with respect to the best single-point excitation are listed for both the three-point and four-point configuration.

A satisfactory mode identification (MIF $>$ 800) is predicted only with the four-point configuration but was achieved experimentally with both optimised

Exciter Configuration	MIF (comp.)	MIF (meas.)	Deviation (comp. - meas.)	Improvement w.r.t. Sweep
Four-Point	805	806	+1	+172
Three-Point	792	801	+9	+167

Table 5.14: Modal Identification Results for the Polar Platform

excitation force vectors. The deviations between computed and measured MIFs remain within acceptable margins. The slightly higher deviation for the three-point excitation is assumed to be caused by structural non-linearities. Due to time limitations, however, no further investigations were made.

Similar to the observations made with the laboratory test structure in Section 5.4.2 neither the exciter locations used in the optimised force vector nor the computed force component magnitudes are associated with the mode isolation quality obtained in the single-point excitations. This emphasises the need for systematic tuning techniques when the complexity of the structure under investigation involves a multi-point excitation to identify the normal modes.

5.4.4 Concluding Remarks

In the previous section the method for the computation of optimised multi-point excitation force vectors, Section 3.4, has been applied to various test cases. Encouraging results have been obtained in comparison to existing methods in a numerical study and in processing life experimental data on a simple satellite model. In addition, a successful application to a complex aerospace structure under realistic test conditions has been described.

With all test cases a considerable potential for improving the phase purity of the experimental mode shapes has been found.

5.5 Closure

A finite-element model of the Eurocopter EC 135 helicopter has been updated to demonstrate the capabilities of the procedures and algorithms developed in Sections 4.2 and 4.3 with respect to the validation of a representative industrial aerospace structure. Experimental data from a Shake Test on the EC 135-S001 prototype has been used and a novel technique for a consistent correction of non-isotropic material which enables an efficient definition of updating parameters has been proposed. The numerical model has been successfully updated. The results, however, have revealed the importance of precision and completeness of the experimental reference data.

The advantages of model updating in the fields of structural damage localisation have been emphasised in Section 5.3. A stringer-stiffened rectangular fuselage panel has been chosen as a test structure and it has been shown that an updated model yields a better indication of the damage location as compared to a conventional analytical model.

A numerical study has been carried out to evaluate the force tuning technique suggested in Section 3.4 and the performance with respect to the isolation of the structure's normal modes has been assessed in comparison to existing methods. Then, the method has been applied to a satellite model and realistic experimental data. Additionally, an application to a complex aerospace structure in a real life Ground Vibration Test has been described. In all test cases the method has yielded significant improvements with respect to the phase purity of the identified mode shapes.

Chapter 6

Conclusions and Further Work

This thesis discusses different aspects of experimental identification techniques for structural dynamic systems and the correction of the corresponding numerical models using results of the experimental investigations.

The finite-element model of a laboratory test structure is updated using experimental eigenfrequencies and mode shapes from a Ground Vibration Test. The problem of selecting suitable updating parameters for the model corrections is discussed in detail. Two sets of correction parameters are investigated and the capabilities of the updated model to predict modal data beyond the frequency range used in the validation process is investigated. In addition, analytical Frequency Response Functions are computed from the validated models and compared to the measured response data.

The investigations show that a good consistency between the selected updating parameters and the errors in the finite-element model is most important for the success of the correction process. This ensures that the introduced modifications bear a physical meaning and that reliable predictions of modal and frequency response data which were not used for updating can be achieved.

The influence of experimental errors on the accuracy of finite-element model corrections is investigated in a simulation study. The uncertainties introduced into the correction parameter values, updated eigenfrequencies, and mode shapes are discussed.

Primarily, the correction parameter uncertainty is progressively increased

with the magnitude of the experimental error. For small errors a linear domain exists and contributions from different error categories may be superimposed. The overall uncertainty levels are reduced by the number of modes involved in the updating process.

In case of absolute errors which are independent of the measured value the magnitudes with respect to the actual deflections at the particular degrees of freedom significantly affect the correction accuracy. Another observation characteristic for the individual numerical model and test structure is the partial compensation of inaccuracies of measured natural frequencies and frequency deviations due to analytical modelling errors.

Analytical frequency deviations from experimental errors within the mode shapes are relatively small. The deviations due to inaccurately measured frequencies, however, are of the same order as the measurement error. As a result, model updating requires high precision in identifying the natural frequencies of a structure.

The model updating method is applied to a large-scale finite-element model of the EC 135 helicopter. Experimental reference data is obtained from a Shake Test on the EC 135-S01 prototype. Modal parameters are derived from the Frequency Response Functions using a phase separation technique. To ensure sufficiently high parameter sensitivities the selection of correction parameters is focussed on those components which constitute the aircraft backbone structure. The model corrections are partially carried out by means of supplementary correction elements.

Encouraging improvements as to the correlation of experimental and analytical natural frequencies and mode shapes are achieved. The quality of the model corrections, however, notably suffers from the modal and spatial incompleteness of the measured data.

A new method of localising delamination damages in CFRP is introduced and the influence of the analytical model quality on the method's accuracy is investigated. A single delamination damage is located in a stringer-stiffened CFRP panel using two different analytical models. For the first model only

standard finite-element modelling techniques are used. An improved second model is obtained from updating the first model with experimental data from the test structure.

Compared to the initial model damage detection using the updated model provides more accurate and apparent results on the damage location and is less sensitive to distressing effects.

A new approach for the computation of optimised excitation force vectors for Phase Resonance Testing is proposed. The performance of the method is compared to other methods by using an analytical eleven-degrees-of-freedom system. The results of applications to a laboratory testing model and a large space structure are presented. The new method provides significant improvements with respect to the identification accuracy and helps reduce test duration and costs. The method exhibits considerable advantages in the course of modal testing using the Phase Resonance Method.

Regarding model updating techniques in general, further work should be directed towards including anti-resonance frequencies and the direct processing of Frequency Response Functions in the residual vector.

With large-scale finite-element models the correction of global modal parameters does not necessary result in an improvement of individual local structural responses. A more detailed dynamic representation of the real structure can be achieved through starting modal testing and model validation on the sub-component level.

Further work with respect to the detection of delamination damages should strive for an improved finite-element modelling of delaminations, including the use of model updating techniques, the investigation of alternate analytical damping approaches, and the development of a sensitivity analysis of the individual modes with respect to the damage location.

In the optimisation of multi-point excitation forces the selection of single-point exciter locations is still based on engineering judgement. A more systematic procedure, e.g. the use of a-priori knowledge from an analytical model, could yield further improvement to the modal data quality.

Bibliography

[1] ALLEMANG, R.J.; BROWN, D.L.: *A Correlation Coefficient for Modal Vector Analysis.* 1st International Modal Analysis Conference, Orlando, Florida, pp. 110–116, 1982.

[2] ALLEMANG, R.J.; BROWN, D.L.; ROST, R.W.: *Experimental Modal Analysis and Dynamic Component Synthesis: Volume II Measurement Techniques for Experimental Modal Analysis.* Wright Aeronautical Laboratories, Report AFWAL-87-3069, 1987.

[3] ANDERSON, J.E.: *Another Look at Sine-Dwell Mode Testing.* AIAA/ASME/ASCE/AHS 22nd Structures, Structural Dynamics, and Materials Conference, Atlanta, Georgia, pp. 358–365, 1981.

[4] ASHER, G.W.: *A Method of Normal Mode Excitation Utilizing Admittance Measurements.* National Specialists' Meeting on Dynamics and Aeroelasticity, Fort Worth, Texas, pp. 69–76, 1958.

[5] AVITABILE, P.; O'CALLAHAN, J.C.; MILANI, J.: *Comparison of System Characteristics Using Various Model Reduction Techniques.* 7th International Modal Analysis Conference, Las Vegas, Nevada, pp. 1109–1115, 1989.

[6] AVITABILE, P.; PECHINSKY, F.; O'CALLAHAN, J.C.: *Study of Vector Correlation Using Various Techniques for Model Reduction.* 10th International Modal Analysis Conference, San Diego, California, pp. 572–583, 1992.

[7] BARUCH, M.: *Optimization Procedure to Correct Stiffness and Flexibility Matrices Using Vibration Tests.* AIAA Journal, **16**(11), pp. 1208–1210, 1978.

[8] BARUCH, M.: *Methods of Reference Basis for Identification of Linear Dynamic Structures.* AIAA Conference Paper 82-0769, 1982.

[9] BERGER, H.; BARTHE, L.; OHAYON, R.: *Parametric Updating of a Finite Element Model from Experimental Modal Characteristics.* Mechanical Systems and Signal Processing, 4(3), pp. 233–242, 1990.

[10] BERMAN, A.: *Limitations on the Identification of Discrete Structural Dynamic Models.* 2nd International Conference on Recent Advances in Structural Dynamics, Southampton, Great Britain, pp. 427–435, 1984.

[11] BERMAN, A.: *System Identification of Structural Dynamic Models - Theoretical and Practical Bounds.* AIAA Conference Paper 84-0929, 1984.

[12] BERMAN, A.; FLANNELLY, W.G.: *Theory of Incomplete Models of Dynamic Structures.* AIAA Journal, **9**(8), pp. 1481–1487, 1971.

[13] BERMAN, A.; WEI, F.S.: *Automated Dynamic Analytical Model Improvement.* National Aeronautics and Space Administration (NASA), CR-3452, 1981.

[14] BLEVINS, R.D.: *Flow Induced Vibration.* Van Nostrand Rheinholt Co., 1977.

[15] BREITBACH, E.: *Neuere Entwicklungen auf dem Gebiet des Standschwingungsversuchs an Luft- und Raumfahrkonstruktionen.* Deutsche Forschungsanstalt für Luft- und Raumfahrt (DLR), IB 253 - 74 J 08, 1974.

[16] BRUGHMANS, M.; LEURIDAN, J.; BLAUWKAMP, K.: *The Application of FEM-EMA Correlation and Validation Techniques on a Body-in-White.* 11th International Modal Analysis Conference, Kissimmee, Florida, pp. 646–654, 1993.

[17] BRUGHMANS, M.; LEURIDAN, J.; HRYCKO, G.; WYZYKOWSKI, J.: *Application of FEM Model Correction and Updating Techniques on an Aircraft Using Test Data of a Ground Vibration Survey.* 15th International Seminar on Modal Analysis, Leuven, Belgium, pp. 589–606, 1990.

[18] CAESAR, B.; BAIER, H.; BADENHAUSEN, H.; LINK, M.; HÜNERS, H.; ERBEN, E.: *Procedures for Updating Dynamic Mathematical Models.* Dornier Rep. EMSB 23/86, Final Report for ESTEC, Contract 5597/83/NL/PB (SC), 1985.

[19] CAESAR, B.; ECKERT, L.; HOPPE, A.: *Design Parameter Update of Dynamic Mathematical Models in Presence of Test Noise and Mode Pairing Problems.* International Conference on Spacecraft Structures and Mechanical Testing, ESA/ESTEC, Noordwijk, The Netherlands, 1991.

[20] CAESAR, B.; ECKERT, L.; WÖHLER, H.: *Parametric Identification of Conservative Self Adjoint Structures.* International Conference on Spacecraft Structures and Mechanical Testing, Paris, France, 1994.

[21] CAUGHEY, T.K.; OKELLY, M.M.J.: *Classical Normal Modes in Damped Linear Dynamic Systems.* Transactions ASME, Journal of Applied Mechanics, **32**, pp. 583–588, 1965.

[22] CAWLEY, P.; ADAMS, R.D.: *The Location of Defects in Structures from Measurements of Natural Frequencies.* Journal of Strain Analysis, **14**(3), pp. 49–57, 1979.

[23] CHEN, J.C.: *Analytical Model Accuracy Refinements for Structural Dynamic Systems.* AIAA Conference Paper 82-0734, 1982.

[24] CHEN, J.C.; GARBA, J.A.: *Analytical Model Improvement Using Modal Test Results.* AIAA Journal, **18**(6), pp. 684–690, 1980.

[25] CHEN, J.C.; GARBA, J.A.; KUO, C.P.: *Direct Structural Parameter Identification by Modal Test Results.* AIAA Conference Paper 83-0812, 1983.

[26] COLLINS, J.D.; HART, G.C.; HASSELMANN, T.K.; KENNEDY, B.: *Statistical Identification of Structures.* AIAA Journal, **12**(2), pp. 185–190, 1974.

[27] COOPER, J.E.; HAMILTON, M.J.; WRIGHT, J.R.: *Experimental Evaluation of Normal Mode Force Appropriation Methods Using a Rectangular Plate.* 10th International Modal Analysis Conference, San Diego, California, pp. 1327–1333, 1992.

[28] COPPOLINO, R.N.; RUBIN, S.: *Detectability of Structural Failures in Offshore Platforms by Ambient Vibration Monitoring.* 12th Offshore Technology Conference, **1**, OTC 3865, pp. 101–110, 1980.

[29] COTTIN, N.; FELGENHAUER, H.P.; NATKE, H.G.: *On the Parameter Identification of Elastomechanical Systems Using Input and Output Residuals.* Ingenieur Archiv, **54**, pp. 378–387, 1984.

[30] CRAIG, R.R. JR.: *Structural Dynamics.* John Wiley & Sons, 1981.

[31] DAILEY, R.L.: *Eigenvector Derivatives with Repeated Eigenvalues.* AIAA Journal, **27**(4), pp. 486–491, 1989.

[32] DEGENER, M.: *A Large Multi-Channel Measurement Facility for Both Modal Survey and Multi-Axis Vibration Testing.* International Conference on Spacecraft Structures and Mechanical Testing, Paris, France, 1994.

[33] DEGENER, M.: *Shake Test on the "EC 135" Helicopter.* Deutsche Forschungsanstalt für Luft- und Raumfahrt (DLR), IB 232 - 94 C 17, 1994.

[34] DEGENER, M.: *Ground Vibration Testing for Validation of Large Aircraft Structural Dynamics.* International Forum on Aeroelasticity and Structural Dynamics, Manchester, Great Britain, pp. 70.1–70.12, 1995.

[35] DEGENER, M.; GLOTH, G.; KEYE, S.: *Modal Survey Test on the INTEGRAL Satellite.* Deutsche Forschungsanstalt für Luft- und Raumfahrt (DLR), IB 232 - 98 C 09, 1998.

[36] DEGENER, M.; HERMES, M.: *Ground Vibration Test and Finite Element Analysis of the GARTEUR SM-AG19 Testbed.* Deutsche Forschungsanstalt für Luft- und Raumfahrt (DLR), IB 232 - 96 J 08, 1996.

[37] DEMCHAK, L.; HARCROW, H.: *Analysis of Structural Dynamic Data from Skylab.* Martin-Marietta Corp., National Aeronautics and Space Administration (NASA), CR-2727, 1976.

[38] http://www.eurocopter.com/site/FO/home.html. *Internet Homepage.*

[39] http://www.eurocopter.com/site/FO/scripts/siteFO_contenu.php?lang=EN&noeu_id=37. *Product Description.*

[40] http://www.helionline.de/EC13500.htm. *EC 135 Website.*

[41] ECKERT, L.; CAESAR, B.: *Model Updating under Incomplete and Noisy Modal Test Data.* 9th International Modal Analysis Conference, Schenectady, New York, pp. 563–571, 1991.

[42] ECKERT, L.; CAESAR, B.: *Update of Dynamic Mathematical Models using Incomplete and Noisy Modal Test Data.* International Forum on Aeroelasticity and Structural Dynamics, Aachen, West Germany, 1991.

[43] http://www.esa.int/export/esaCP/ESAJZA8VTTC_index_0.html. *ESA Info 11-2001.*

[44] EWINS, D.J.: *Modal Testing: Theory and Practice.* Research Studies Press Ltd., John Wiley, 2000.

[45] FARRAR, C.R., ET AL.: *Dynamic Characterization and Damage Detection in the I-40 Bridge over the Rio Grande.* Los Alamos National Laboratories, Technical Report LA-12767-MS, 1994.

[46] http://www.enae.umd.edu/AGRC/Aero/tailrotors.html. *Internet Course on Helicopter Aerodynamics.*

[47] FENNER, R.T.: *Engineering Elasticity:Applications of Numerical and Analytical Techniques.* Ellis Horwood, 1986.

[48] FISSETTE, E.; IBRAHIM, S.: *Error Location and Updating of Analytical Dynamic Models Using a Force Balance Method.* 6th International Modal Analysis Conference, Kissimmee, Florida, pp. 1063–1070, 1988.

[49] FOX, R.L.; KAPOOR, M.P.: *Rates of Change of Eigenvalues and Eigenvectors.* AIAA Journal, **6**(12), pp. 2426–2429, 1968.

[50] FRISWELL, M.I.: *Updating Physical Parameters from Frequency Response Function Data.* 12th Biennial ASME Conference on Mechanical Vibration and Noise, DE-Vol **18-4**, pp. 393–400, Montreal, Canada, 1989.

[51] FRISWELL, M.I.; PENNY, J.I.T.: *Is Damage Location Using Vibration Measurements Practical ?.* Euromech 365: DAMAS 97, Structural Damage Assessment Using Advanced Signal Processing Procedures, Sheffield, Great Britain, 1997.

[52] FRITZEN, C.P. : *Identification of Mass, Damping and Stiffness Matrices of Mechanical Systems.* Transactions ASME, Journal of Vibration, Acoustics, Stress and Reliability in Design, **108**(1), pp. 9–16, 1986.

[53] FÜLLEKRUG, U.: *Grundlagen der Strukturdynamik.* Lecture Manuscript, Technische Universität Clausthal, Germany, 1994.

[54] FUHR, P.L.; HUSTON, D.R.; KAJENSKY, P.J.; AMBROSE, T.P.: *Performance and Health Monitoring of the Stafford Medical Building Using Embedded Sensors.* Smart Materials and Structures, **1**, pp. 63–68, 1992.

[55] GASCH, R.; KNOTHE, K.: *Strukturdynamik.* Springer-Verlag Berlin, Heidelberg, New York, London, Paris, Tokyo, 1987.

[56] GSCHWILM, J.; KEYE, S.: *Modal Identification Tests of the ROSETTA Lander (Demonstration Model).* Deutsche Forschungsanstalt für Luft- und Raumfahrt (DLR), IB 232 - 99 C 02, 1999.

[57] GUYAN, R.J.: *Reduction of Stiffness and Mass Matrices.* AIAA Journal, **3**(2), p. 380, 1965.

[58] GYSIN, H.: *Comparison of Expansion Methods for FE Model Localisation.* 8th International Modal Analysis Conference, Kissimmee, Florida, pp. 195–204, 1990.

[59] HALL, B.M.; CALKIN, E.D.; SHOLAR, M.S.: *Linear Estimation of Structural Parameters from Dynamic Test Data.* AIAA/ASME 11th Structures, Structural Dynamics, and Materials Conference, Denver, Colorado, pp. 193–197, 1970.

[60] HOGG, R.V.; CRAIG, A.T.: *Introduction to Mathematical Statistics.* Macmillan, 1978.

[61] HONG, S.W.; LEE C.W.: *Identification of Linearised Joint Structural Parameters by Combined use of Measured and Computed Frequency Responses.* Mechanical Systems and Signal Processing, **5**(4), pp. 267–277, 1991.

[62] HÜNERS, H.; NIEDBAL, N.: *Modal-Survey Testing for System Identification and Dynamic Qualification of Spacecraft Structures.* ESA Journal, **6**, pp. 21–34, 1982.

[63] HUGHES, T.J.R.: *The Finite Element Method, Linear Static and Dynamic Finite Element Analysis.* Prentice-Hall, 1987.

[64] HUNT, D.L.; VOLD, H.; PETERSON, E.L.; WILLIAMS, R.: *Optimal Selection of Excitation Methods for Enhanced Modal Testing.* Structures, Structural Dynamics, and Materials Conference, Palm Springs, California, pp. 549–553, 1984.

[65] IBRAHIM, S.R.: *Computation of Normal Modes from Identified Complex Modes.* AIAA Journal, **21**(3), pp. 446–451, 1983.

[66] IBRAHIM, S.R.: *Correlation of Analysis and Test in Modelling of Structures: Assessment and Review.* Journal of the Society of Environmental Engineers, **27-1**, Issue 116, pp. 39–44, 1988.

[67] IMREGUN, M.; EWINS, D.J.: *An Investigation into Mode Shape Expansion Techniques.* 11th International Modal Analysis Conference, Kissimmee, Florida, pp. 168–175, 1993.

[68] http://www.ae.go.dlr.de:8088/. *Internet Homepage.*

[69] KAISER, S.; ET AL.: *Structural Dynamic Health Monitoring of Adaptive CFRP-Structures.* 6th Annual International Symposium on Smart Structures and Materials, Newport Beach, California, 1999.

[70] KENLEY, R.M.; DODDS, J.D.: *West Sole WE Platform: Detection of Damage by Structural Response Measurements.* 12th Offshore Technology Conference, **1**, OTC 3866, pp. 111–118, 1980.

[71] KEY, S.W.: *Transient Response by Time Integration.* In: *Advanced Structural Dynamics*, J. Donéa ed., pp. 71–95, Applied Science Publishers, 1978.

[72] KEYE, S.: *Vergleichende Untersuchung von Methoden zur Erregerkraftanpassung im Phasenresonanzverfahren.* Deutsche Forschungsanstalt für Luft- und Raumfahrt (DLR), IB 232 - 95 J 05, 1995.

[73] KEYE, S.: *Ein neues Verfahren zur Berechnung optimaler Erregerkräfte im Phasenresonanzverfahren.* Deutsche Forschungsanstalt für Luft- und Raumfahrt (DLR), IB 232 - 96 J 05, 1996.

[74] KEYE, S.: *Die Korrektur der Systemmatrizen analytischer Modelle am Beispiel der CLUMOD-Teststruktur.* Deutsche Forschungsanstalt für Luft- und Raumfahrt (DLR), IB 232 - 96 J 09, 1996.

[75] KEYE, S.: *Die Korrektur des FE-Modells des EC135-Helikopters auf der Basis experimenteller Modaldaten.* Deutsche Forschungsanstalt für Luft- und Raumfahrt (DLR), IB 232 - 97 J 09, 1997.

[76] KEYE, S.: *The Influence of Experimental Errors on the Correction Parameters of Finite Element Models.* ASME Design Engineering Technical Conferences, Sacramento, California, VIB-4148, 1997.

[77] KEYE, S.: *Anwendungsaspekte eines auf Modaldaten basierenden Korrekturverfahrens für Finite-Elemente-Modelle.* DGLR Aeroelastik-Tagung, Göttingen, Germany, 1998.

[78] KEYE, S.: *Prediction of Modal and Frequency Response Data from a Validated Finite Element Model.* 2nd International Conference on Identification in Engineering Systems, Swansea, Great Britain, 1999.

[79] KEYE, S.: *A Procedure to Improve Convergence and Accuracy of Iterative Model Updating Methods.* International Forum on Aeroelasticity and Structural Dynamics, Williamsburg, Virginia, NASA/CP-1999-209136/PT1, pp. 81–88, 1999.

[80] KEYE, S.: *Numerische Studie zum Einfluß der Unvollständigkeit experimenteller Modaldaten auf die Korrektur von Finite Elemente Modellen am Beispiel des EC135-Helikopters.* Deutsche Forschungsanstalt für Luft- und Raumfahrt (DLR), Internal Note, 1999.

[81] KEYE, S.: *Finite Element Model Updating Report.* European Space Agency (ESA), Technical Note RO-LST-TN-3620, 1999.

[82] KEYE, S.: *Ein Verfahren zur Lokalisation von Delaminationsschäden in CFK.* Deutsche Forschungsanstalt für Luft- und Raumfahrt (DLR), IB 131 - 2001/19, 2001.

[83] KEYE, S.: *Locating Delamination Damages in CFRP Using an Updated Numerical Model.* 3rd International Workshop on Structural Health Monitoring, Stanford University, Stanford, California, 2001.

[84] KEYE, S.; FÜLLEKRUG, U.: *A new Method for Computing Optimized Exciter Forces for Phase Resonance Testing.* International Forum on Aeroelasticity and Structural Dynamics, Rome, Italy, Vol. III, pp. 269–274, 1997.

[85] KEYE, S.; FÜLLEKRUG, U.; LINK, M.: *Die Korrektur des Finite Elemente Modells der EC135 auf der Basis experimenteller Modaldaten.* Deutsche Forschungsanstalt für Luft- und Raumfahrt (DLR), IB 232 - 99 C 04, 1999.

[86] KEYE, S.; ET AL.: *A Localization Concept for Delamination Damages in CFRP.* IUTAM-Symposium on Smart Structures and Structronic Systems, Magdeburg, Germany, pp. 57–64, 2000.

[87] KEYE, S.; ET AL.: *Localizing Delamination Damages in Aircraft Panels from Modal Damping Parameters.* 19th International Modal Analysis Conference, Kissimmee, Forida, pp. 412–417, 2001.

[88] KIDDER, R.L.: *Reduction of Structural Frequency Equations.* AIAA Journal, **11**(6), p. 892, 1973.

[89] LALLEMENT, G. ; PIRANDA, J.: *Localisation Methods for Parameter Updating of Finite Element Models in Elastodynamics.* 8th International Modal Analysis Conference, Orlando, Florida, pp. 579–585, 1990.

[90] LALLEMENT, G.; PIRANDA, J.; FILLOD, R.: *Parametric Identification of Conservative Self Adjoint Structures.* International Conference on Spacecraft Structures and Mechanical Testing, ESA/ESTEC, Noordwijk, The Netherlands, 1989.

[91] LAWSON, C.L.; HANSON, R.J.: *Solving Least Squares Problems.* Prentice-Hall, 1974.

[92] LEMBREGTS, F; LEURIDAN, J; BRUSSEL, H: *Frequency Domain Direct Parameter Identification for Modal Analysis: State Space Formulation.* Mechanical Systems and Signal Processing, **4**(1), pp. 65–75, 1990.

[93] LEWIS, R.C.; WRISLEY, D.L.: *A System for the Excitation of Pure Natural Modes of Complex Structure.* Journal of the Aeronautical Sciences, **17**(11), pp. 705–722, 735, 1950.

[94] LIEVEN, N.A.J.: *Spatial Correlation of Mode Shapes, the Coordinate Modal Assurance Criterion.* 6th International Modal Analysis Conference, Kissimmee, Florida, pp. 690–695, 1988.

[95] LIEVEN, N.A.J.; EWINS, D.J.: *Error Location and Updating Finite Element Models Using Singular Value Decomposition.* 8th International Modal Analysis Conference, Kissimmee, Florida, pp. 768–773, 1990.

[96] http://www.uni-kassel.de/fb14/leichtbau/Welcome.html. *Internet Homepage.*

[97] LINK, M.: *Localisation of Errors in Computational Models Using Dynamic Test Data.* European Conference on Structural Dynamics - EURODYN 90, Bochum, West Germany, 1990.

[98] LINK, M.: *Requirements for the Structure of Analytical Models Used for Parameter Identification.* IUTAM Symposium on Inverse Problems in Engineering Mechanics, Tokyo, Japan, pp. 133–146, 1992.

[99] LINK, M.: *Updating of Analytical Models - Procedures and Experience.* Conference on Modern Practice in Stress and Vibration Analysis, J.L. Wearing ed., Sheffield Academic Press, pp. 35–52, 1993.

[100] LINK, M.: *UPDATE. Software for Updating Finite Element Model Parameters using Experimental Vibration Test Data.* Fachgebiet Leichtbau, Fachbereich 14, Universität Gesamthochschule Kassel, Mönchebergstraße 7, 34109 Kassel, Germany, 1996.

[101] LINK, M.; GRUBER, J.; ZOU, Z.; SCHEDLINSKI, C.: *MATFEM Finite Element Code including Pre- and Post-Processing, Version 5/95.* Fachgebiet Leichtbau, Fachbereich 14, Universität Gesamthochschule Kassel, Mönchebergstraße 7, 34109 Kassel, Germany, 1995.

[102] LINK, M.; GRUBER, J.; ZOU, Z.; SCHEDLINSKI, C.: *MATFEM Finite Element Code including Pre- and Post-Processing, Version 5/96.* Fachgebiet Leichtbau, Fachbereich 14, Universität Gesamthochschule Kassel, Mönchebergstraße 7, 34109 Kassel, Germany, 1996.

[103] LINK, M.; HANKE, G.: *Model Quality Assessment and Model Updating.* NATO Advanced Study Institute, Sesimbra, Portugal, 1998.

[104] LINK, M.; SANTIAGO, O.F.: *Updating and Localizing Structural Errors Based on Minimisation of Equation Errors.* International Conference on Spacecraft Structures and Mechanical Testing, ESA/ESTEC, Noordwijk, The Netherlands, 1991.

[105] LINK, M.; VOLLAN, A.: *Identification of Structural System Parameters form Dynamic Response Data.* Zeitschrift für Flugwissenschaften und Weltraumforschung, **2**(3), pp. 165–174, 1978.

[106] LINK, M.; ZHANG, L.: *Experience with Different Procedures for Updating Structural Parameters of Analytical Models Using Test Data.* 10^{th} International Modal Analysis Conference, San Diego, California, pp. 730–738, 1992.

[107] LINK, M.; ZHENG, Q.: *Updating Substructure Models with Dynamic Boundary Conditions.* ASME Conference on Noise & Vibration, Boston, Massachusetts, 1995.

[108] LIPKINS, J.; VANDEURZAN, U. : *The Use of Smoothing Techniques for Structural Modification Applications.* 12th International Seminar on Modal Analysis, Leuven, Belgium, S1-3, 1987.

[109] LMS: *CADA-X Modal Analysis Manual, Revision 3.3.* Leuven, Belgium, 1994.

[110] LOLAND, O.; DODDS, C.J.: *Experiences in Developing and Operating Integrity Monitoring System in North Sea.* 8th Offshore Technology Conference, **2**, OTC 3865, pp. 313–319, 1976.

[111] MESSINA, A.; WILLIAMS, E.J.: *Use of Changes in Resonance and Anti-Resonance Frequencies for Damage Detection.* 2nd International Conference on Identification in Engineering Systems, Swansea, Great Britain, 1999.

[112] MILLS-CURRAN, W.C.: *Calculation of Eigenvector Derivatives for Structures with Repeated Eigenvalues.* AIAA Journal, **26**(7), pp. 867–871, 1988.

[113] MILLS-CURRAN, W.C.: *Comment on 'Eigenvector Derivatives with Repeated Eigenvalues'.* AIAA Journal, **28**(10), p. 1846, 1990.

[114] MILNE, R.R.; SIMPSON, A.: *Reconciliation of Calculated and Measured Natural Frequencies and Normal Modes.* Journal of Sound and Vibration, **30**(1), pp. 45–63, 1973.

[115] MITCHELL, L.D.: *Complex Modes: a Review.* 8th International Modal Analysis Conference, Kissimmee, Florida, pp. 891–899, 1990.

[116] MOTTERSHEAD, J.E.: *Theory for the Estimation of Structural Vibration Parameters from Incomplete Data.* AIAA Journal, **28**(7), pp. 1326–1328, 1990.

[117] MOTTERSHEAD, J.E.; FOSTER, C.D.: *An Instrumental Variable Method of the Estimation of Mass, Stiffness and Damping Parameters from Measured Frequency Response Functions.* Mechanical Systems and Signal Processing, **2**(4), pp. 379–390, 1988.

[118] MOTTERSHEAD, J.E.; FOSTER, C.D.: *On the Treatment of Ill-Conditioning in Spatial Parameter Estimation from Measured Vibration Data.* Mechanical Systems and Signal Processing, **5**(2), pp. 139–154, 1991.

[119] MOTTERSHEAD, J.E.; FRISWELL, M.I.: *Model Updating in Structural Dynamics: A Survey.* Journal of Sound and Vibration, **167**(2), pp. 347–375, 1993.

[120] MOTTERSHEAD, J.E.; FRISWELL, M.I.: *Finite Element Model Updating in Structural Dynamics.* Kluwer Academic Publishers, 1995.

[121] MOTTERSHEAD, J.E.; FRISWELL, M.I.; NG, G.H.T.; BRANDON, J.A.: *Experience in Mechanical Joint Model Updating.* 19th International Seminar on Modal Analysis, Leuven, Belgium, pp. 481–492, 1994.

[122] NATKE, H.G.: *Die Korrektur des Rechenmodells eines elastomechanischen Systems mittels gemessener erzwungener Schwingungen.* Ingenieur Archiv, **46**, pp. 169–184, 1977.

[123] NATKE, H.G.: *Vergleich von Algorithmen für die Anpassung des Rechenmodells einer schwingungsfähigen elastomechanischen Struktur an Versuchswerte.* Zeitschrift für Angewandte Mathematik und Mechanik, **59**, pp. 257–268, 1979.

[124] NATKE, H.G.: *Updating Computational Models in the Frequency Domain Based on Measured Data: A Survey.* Probabilistic Engineering Mechanics, **3**(1), pp. 28–35, 1988.

[125] NATKE, H.G.: *Error Localisation within Spatially Finite-Dimensional Models.* Computational Mechanics, **8**, pp. 153–160, 1991.

[126] NATKE, H.G.: *Einführung in die Theorie und Praxis der Zeitreihen und Modalanalyse.* Vieweg Verlag, Braunschweig/Wiesbaden, 1992.

[127] NATKE, H.G.; CEMPEL, C.: *Fault Detection and Localisation in Structures: A Discussion.* Mechanical Systems and Signal Processing, **5**(5), pp. 345–356, 1991.

[128] NATKE, H.G.; COLLMANN, D.; ZIMMERMANN, H.: *Beitrag zur Korrektur des Rechenmodells eines elastomechanischen Systems anhand von Versuchsergebnissen.* VDI Fortschritt-Berichte, Nr. 221, pp. 23–32, 1974.

[129] NATKE, H.G.; COTTIN, N.: *Updating Mathematical Models on the Basis of Vibration and Modal Test Results - a Review of Experience.* 2nd International Forum on Aeroelasticity and Structural Dynamics, Aachen, West Germany, DGLR 85-02, pp. 625–631, 1985.

[130] NELSON, R.B.: *Simplified Calculation of Eigenvector Derivatives.* AIAA Journal, **14**(9), pp. 1201–1205, 1976.

[131] NEWLAND, D.E.: *An Introduction to Random Vibrations and Spectral Analysis.* 2nd Edition, Longman Group Ltd., 1985.

[132] NIEDBAL, N.: *Survey of the State of the Art in Modern Ground Vibration Testing.* International Symposium on Aeroelasticity, Nürnberg, West Germany, DGLR 82-01, pp. 143–150, 1982.

[133] NIEDBAL, N.: *Die experimentell-rechnerische Ermittlung der reellen Eigenschwingungsgrößen bei begrenzter Zugänglichkeit der Struktur.* Deutsche Forschungsanstalt für Luft- und Raumfahrt (DLR), FB 83-26, 1983.

[134] NIEDBAL, N.: *Analytical Determination of Real Normal Modes from Measured Complex Responses.* AIAA/ASME 25th Structures, Structural Dynamics, and Materials Conference, Palm Springs, California, pp. 292–295, 1984.

[135] NIEDBAL, N.: *Advances in Ground Vibration Testing Using a Combination of Phase Resonance and Phase Separation Methods.* 2nd International Forum on Aeroelasticity and Structural Dynamics, Aachen, West Germany, DGLR 85-02, pp. 523–528, 1985.

[136] NIEDBAL, N.; KLUSOWSKI, E.: *Die Verknüpfung strukturdynamischer Rechenmodelle mit gemessenen Eigenschwingungs-Kenngrößen.* Zeitschrift für Flugwissenschaften und Weltraumforschung, **12**, pp. 99–110, 1988.

[137] NIEDBAL, N.; KLUSOWSKI, E.: *Optimal Exciter Placement and Force Vector Tuning Required for Experimental Modal Analysis.* International Conference on Spacecraft Structures and Mechanical Testing, ESA/ESTEC, Noordwijk, The Netherlands, 1991.

[138] NIEDBAL, N.; KLUSOWSKI, E.; LUBER, W.: *Updating a Finite-Element Model by means of Normal Mode Parameters.* International Conference on Spacecraft Structures and Mechanical Testing, ESA/ESTEC, Noordwijk, The Netherlands, 1988.

[139] O'CALLAHAN, J.C.: *A Procedure for an Improved Reduced System (IRS) Model.* 7th International Modal Analysis Conference, Las Vegas, Nevada, pp. 17–21, 1989.

[140] O'CALLAHAN, J.C.; AVITABILE, P.; RIEMER, R.: *System Equivalent Reduction Expansion Process.* 7th International Modal Analysis Conference, Las Vegas, Nevada, pp. 29–37, 1989.

[141] O'CALLAHAN, J.C.; LIEU, I.W.; AVITABILE, P.; MADDEN, R.: *An Efficient Method of Determining Rotational Degrees of Freedom from Analytical and Experimental Modal Data.* 4th International Modal Analysis Conference, Los Angeles, California, pp. 50–58, 1986.

[142] OJALVO, I.U.: *Effective Computation of Mode Shape Derivatives for Large Dynamic Systems.* AIAA Journal, **25**(10), pp. 1386–1390, 1987.

[143] OÑATE, E.; CERVERA, M.; ZIENKIEWICZ, O.C.: *A Finite Volume Format for Structural Mechanics.* International Journal for Numerical Methods in Engineering, **37**, pp. 181–201, 1994.

[144] http://www.aerospace-technology.com/projects/envisat/index.html. *Aerospace Technology Website.*

[145] RAYLEIGH, J.N.S.: *The Theory of Sound.* Volume 1 & 2, Dover Publications, 1945.

[146] RODDEN, W.P.: *A Method for Deriving Structural Influence Coefficients from Ground Vibration Tests.* AIAA Journal, **5**(5), pp. 991–1000, 1967.

[147] SALAWU, O.S.: *Non-Destructive Assessment of Structures Using the Integrity Index Method Applied to a Concrete Highway Bridge.* Journal of the British Institute of Non-Destructive Testing, **37**(1), pp. 875–878, 1995.

[148] SAS, P.: *4^{th} Workshop on Modal Updating and Modal Optimization Techniques.* 11^{th} International Seminar on Modal Analysis, Leuven, Belgium, pp. 943–951, 1986.

[149] SCHEDLINSKI, C.: *Computational Model Updating of Large Scale Finite Element Models.* 18^{th} International Modal Analysis Conference, San Antonio, Texas, pp. 476–482, 2000.

[150] SCHEDLINSKI, C.; LINK, M.; HANKE, G.: *Handbuch UPDATE.* Fachgebiet Leichtbau, Fachbereich 14, Universität Gesamthochschule Kassel, Mönchebergstraße 7, 34109 Kassel, Germany, 2000.

[151] SCHEDLINSKI, C.; LINK, M.; SCHÖNROCK, A.: *Application of Computational Model Updating to Aeroengine Components.* 23^{rd} International Seminar on Modal Analysis, Leuven, Belgium, pp. 1095–1102, 1998.

[152] SESTIERI, A.; D'AMBROGIO, W.: *Why be Modal: How to Avoid the use of Modes in the Modification of Vibrating Systems.* International Journal of Analytical and Experimental Modal Analysis, **4**(1), pp. 25–30, 1989.

[153] SESTIERI, A.; IBRAHIM, S.R.: *Analysis of Errors and Approximations in the Use of Modal Co-ordinates.* Journal of Sound and Vibration, **177**(2), pp. 145–157, 1994.

[154] SHEPARD, G.D.; MILANI, J.: *Frequency Based Localisation of Structural Discrepancies.* Mechanical Systems and Signal Processing, **4**(2), pp. 173–184, 1990.

[155] SINAPIUS, J.M.: *Die experimentelle Umsetzung der Modalkraftsimulation verteilter dynamischer Lasten unter besonderer Berücksichtigung struktureller Nichtlinearitäten.* PhD-Thesis, Rheinisch-Westfälische Hochschule Aachen, Germany, 1994.

[156] SNOEYS, R.; SAS, P.; HEYLEN, W.; VAN DER AUWERAER, H.: *Trends in Experimental Modal Analysis.* Mechanical Systems and Signal Processing, **1**(1), pp. 5–27, 1987.

[157] TIMOSHENKO, S.P.: *On the Correction for Shear of the Differential Equation for Transverse Vibrations of Prismatic Bars.* Philisophical Magazine, **41** (Series 6), pp. 744–746, 1921.

[158] TIMOSHENKO, S.P.: *On the Transverse Vibrations of Bars of Uniform Cross Section.* Philisophical Magazine, **43** (Series 6), pp. 125–131, 1921.

[159] TIMOSHENKO, S.P.; GOODIER, J.N.: *Theory of Elasticity.* McGraw-Hill, 1982.

[160] TO, W.M.; LIN, R.M.; EWIND, D.J.: *A Criterion for the Localization of Structural Modification Sites Using Modal Data.* 8th International Modal Analysis Conference, Kissimmee, Florida, pp. 961–967, 1990.

[161] TRAILL-NASH, R.W.: *On the Excitation of Pure Natural Modes in Aircraft Resonance Testing.* Journal of the Aero/Space Sciences, **25**, pp. 775–778, 1958.

[162] VAN DER AUWERAER, H.; LEURIDAN, J.: *Multiple Input Orthogonal Polynomial Parameter Estimation.* Mechanical Systems and Signal Processing, **1**(3), pp. 259–272, 1987.

[163] VANDIVER, J.K.: *Detection of Structural Failure on Fixed Platforms by Measurements of Dynamic Response.* 7th Offshore Technology Conference, **2**, OTC 2267, pp. 243–252, 1975.

[164] VESTRONI, F.; CAPECCHI, D.; CERRI, M.N.: *Damage Identification Based on Measured Frequency Changes.* 2nd International Conference on Identification in Engineering Systems, Swansea, Great Britain, 1999.

[165] VESTRONI, F.; CERRI, M.N.; ANTONACCI, E.: *The Problem of Damage Detection in Vibrating Beams.* European Conference on Structural Dynamics - EURODYN 96, Balkema, Rotterdam, The Netherlands, 1996.

[166] WADA, B.K.; CHEN, J.C.: *Test and Analysis Correlation for Structural Dynamic Systems.* 2nd International Forum on Aeroelasticity and Structural Dynamics, Aachen, West Germany, DGLR 85-02, pp. 632–647, 1985.

[167] WANG, J.H.; LIOU, C.M.: *Experimental Identification and Mechanical Joint Parameters.* Transactions ASME, Journal of Vibration and Acoustics, **113**(1), pp. 28–36, 1991.

[168] WOJNAROWSKI, M.E.; STIANSEN, S.G.; REDDY, N.E.: *Structural Integrity Evaluation of a Fixed Platform Using Vibration Criteria.* 9th Offshore Technology Conference, **2**, OTC 2909, pp. 247–256, 1977.

[169] ZHANG, D.W.; ZHAO, L.C.: *A Minimum Norm Perturbation Method for the Modification of Structural Analysis Model.* 4th International Modal Analysis Conference, Los Angeles, California, pp. 541–548, 1986.

[170] ZIENKIEWICZ, O.C.; TAYLOR, R.L.: *The Finite Element Method, Basic Formulation and Linear Problems.* Volume 1, McGraw-Hill, 1989.

[171] ZIMMERMANN, H.; COLLMANN, D.; NATKE, H.G.: *Erfahrungen zur Korrektur des Rechenmodells mit gemessenen Eigenfrequenzen am Beispiel des Verkehrsflugzeugs VFW 614.* Zeitschrift für Flugwissenschaften und Weltraumforschung, **1**(4), pp. 278–285, 1977.

[172] ZURMÜHL, R.: *Matrizen und ihre technischen Anwendungen.* Springer-Verlag Berlin, Göttingen, Heidelberg, New York, 1964.